Searches for new phenomena involving top quarks and Higgs bosons with the ATLAS detector

Mirkoantonio Casolino

Searches for new phenomena involving top quarks and Higgs bosons with the ATLAS detector

Ph.D. dissertation

Mirkoantonio Casolino

Institut de Física d'Altes Energies
Universitat Autònoma de Barcelona
Departament de Física
Facultat de Ciències
Edifici Cn E-08193 Bellaterra (Barcelona)

Thesis director
Aurelio Juste Rozas
ICREA / Institut de Física d'Altes Energies
Universitat Autònoma de Barcelona
Edifici Cn E-08193 Bellaterra (Barcelona)

Thesis tutor
Maria Pilar Casado Lechuga
Universitat Autònoma de Barcelona / Institut de Física d'Altes Energies
Universitat Autònoma de Barcelona
Edifici Cn E-08193 Bellaterra (Barcelona)

Abstract

In this thesis, searches for new phenomena involving top quarks and Higgs bosons in proton-proton collisions at CERN's Large Hadron Collider are presented. The first search targets a variety of signals, including the pair production of a vector-like top quark (T) with a significant branching ratio to a top quark and either a Standard Model Higgs boson or a Z boson; four-top-quark production, both within the Standard Model and in several new physics scenarios; and heavy Higgs bosons (neutral and charged) produced in association with, and decaying into, third generation quarks. The second search targets the production of the Standard Model Higgs boson in association with top-quark pairs, $t\bar{t}H$, with $H \to b\bar{b}$, aiming at a direct measurement of the top-Higgs Yukawa coupling.

The searches are based on 13.2 fb^{-1} of proton-proton collision data at a centre-of-mass energy $\sqrt{s} = 13$ TeV collected with the ATLAS detector. Data are analysed for both searches in the lepton-plus-jets final state, characterised by an isolated electron or muon with high transverse momentum, large missing transverse momentum and multiple jets. For the first search data are analysed as well as in the jets+$E_{\mathrm{T}}^{\mathrm{miss}}$ final state, not exploited in Run 1, characterised by multiple jets and large missing transverse momentum. Both searches exploit the high multiplicity of jet and b-jets characteristic of signal events. In the first search the high scalar sum of transverse momenta of all final-state objects, and the presence of boosted, hadronically-decaying resonances reconstructed as large-radius jets are used to discriminate between signal and background events, while in the second search multivariate techniques are employed. Background events for both searches are dominated by $t\bar{t}$+jets production, in particular by the $t\bar{t}+ \geq 1b$ process, for which detailed studies have been performed.

For the first search, in the absence of a significant excess above the Standard Model expectation, 95% CL upper limits are derived for the signal models in a number of benchmark scenarios, in most cases significantly extending the reach of previous searches. For the second search the data are consistent with either the background-only hypothesis or with the Standard Model $t\bar{t}H$ prediction. The ratio of the measured $t\bar{t}H$ signal cross section to the Standard Model expectation is found to be $\mu = 2.1^{+1.0}_{-0.9}$, assuming a Higgs boson mass of 125 GeV.

Keywords: particle physics, CERN, LHC, ATLAS, top quark, Higgs boson, standard model, search, new phenomena, Monte Carlo.

Contents

Introduction

We shall not cease from exploration
And the end of all our exploring
Will be to arrive where we started
And know the place for the first time.
T.S. Eliot

The "Zeptospace Odyssey" by G. Giudice begins with this quote. It is an invitation to explore and understand the universe and, even in case of no discovery, the journey will expand the knowledge compared to where it started. The explorations at the Large Hadron Collider (LHC) started with the discovery of a Higgs boson with a mass of ∼125 GeV, announced by the ATLAS and CMS Collaborations, making the journey even more exciting and with new questions coming up. Is this Higgs boson really the elementary scalar predicted by the Standard Model? Are there any hints of new physics in its properties? Therefore, the attention quickly shifted towards measuring its properties in order to determine whether it is the Standard Model Higgs boson or whether it has a completely different (e.g. composite) nature. Of particular interested are the Yukawa couplings, which in the Standard Model can be inferred from the measured fermion masses. At the LHC only the Yukawa couplings to third-generation fermions can be measured directly because of their high values. With the largest Yukawa coupling, $y_t \sim 1$, the top quark may play a central role in the underlying electroweak symmetry breaking dynamics and any deviation of its Yukawa coupling can point to the presence of new physics. This is the motivation to focus, in this dissertation, on processes involving top quarks and Higgs bosons.

Firstly, the observation of the $t\bar{t}H$ process, from which the top Yukawa coupling can be extracted directly, is a stepping stone towards answering the key question about the nature of the Higgs boson. But with the discovery of the Higgs boson, is the Standard Model the end of the story in particle physics? Or is it just the start of a wonderful journey? Assuming the Standard Model as the final theory valid up to the Planck scale, it is not possible to explain the presence of a Higgs boson at the electroweak scale (∼100 GeV) without invoking a fine tuning over 30 orders of magnitude, making the theory highly unnatural (*naturalness problem*). Furthermore, the Standard Model does not include gravity and it explains only 4% of the energy density of the universe, lacking a candidate to explain the six times larger contribution from non-luminous matter (dark matter) present in the universe. Those are just few arguments on the fact that the Standard Model cannot be the final theory, but rather a successful low-energy description of a more complete theory at higher energy scales. Theories "Beyond the Standard Model" try to overcome some of these shortcomings, e.g. by postulating new particles that can solve the problem of the unnatural mass of the Higgs boson and, in some cases, provide as well a dark matter candidate. Some of the proposed solutions introduce extra spatial dimensions, compositeness or new strong sectors leading to the introduction of vector-like top-quark partners, which address the naturalness problem. Such particles can decay, through flavour-changing neutral-currents interactions, in a top quark and a Higgs boson. These models predict as well an enhancement in the production of four-top-quark production, a rare process in the Standard Model.

This dissertation presents searches for $t\bar{t}H$ production, with $H \to b\bar{b}$, as well as new phenomena involving multiple top quarks and/or Higgs bosons, covering several extensions of the Standard Model discussed above. These searches use early Run 2 data collected with the ATLAS detector and share a final state characterised by the presence of high jet and b-jet multiplicities. The main background is $t\bar{t}+ \geq 1b$ production, which is very challenging to model. Sophisticated analyses are developed to maximize the sensitivity of the searches, through a combination of powerful discriminating variables between signal and background, and the determination of the background with high precision by

exploiting high-statistics subsidiary data samples.

The content of this dissertation is organised as follows. Chapter 1 gives an introduction to the Standard Model, its shortcomings and proposed solutions, with particular attention to the BSM theories predicting new phenomena involving top quarks and Higgs bosons. The experimental setup used to produce and collect the data for these analyses are presented in Chapter 2. Chapter 3 describes the Monte Carlo techniques used to obtain simulated samples to compare with the data. Starting from the computation of the matrix element for a particular physics process, Monte Carlo tools try to provide a complete picture for how. The validation of these tools is of crucial importance in the ATLAS Collaboration and the author was an active member of the team involved in this task. Chapter 4 outlines the reconstruction and identification of physics objects, such as charged leptons, jets and weakly-interacting particles. Chapter 5 summarizes the details of the collider data and simulated data samples used in this dissertation, as well as some useful tools for the analyses presented. Finally, the main topic of this dissertation, the search for new phenomena involving top quarks and Higgs bosons is discussed in Chapter 6 and 7, where two different analyses are presented.

The results presented in this dissertation have led to the following publications, in which the author has been one of the main analysers:

- ATLAS Collaboration, *Search for production of vector-like top quark pairs and of four top quarks in the lepton-plus-jets final state in pp collisions at* $\sqrt{s} = 13$ *TeV with the ATLAS detector*, ATLAS-CONF-2016-013 (2016).
- ATLAS Collaboration, *Search for the associated production of a Higgs Boson with a top quark pair decaying into* $H \to b\bar{b}$ *pairs with the ATLAS detector*, ATLAS-CONF-2016-080 (2016).
- ATLAS Collaboration, *Search for new phenomena in* $t\bar{t}$ *final states with additional heavy-flavour jets in pp collisions at* $\sqrt{s} = 13$ *TeV with the ATLAS detector*, ATLAS-CONF-2016-104 (2016).

Being involved in detailed studies of the $t\bar{t}+ \geq 1b$ background modelling, a key aspect for these analyses, the author has also contributed significantly to the following publications:

- ATLAS Collaboration, *Studies of Monte Carlo generators in Higgs boson production for ATLAS Run 2*, ATLAS-PHYS-PUB-2014-022 (2014).
- ATLAS Collaboration, *Additional studies of MC generator predictions for top quark production at the LHC*, ATLAS-PHYS-PUB-2016-016 (2016).
- LHC Higgs Cross Section WG, *Handbook of LHC Higgs Cross Sections: 4. Deciphering the Nature of the Higgs Sector*, arXiv:1610.07922 [hep-ex].

The author was also a primary author of a phenomenological study proposing a novel search for a light CP-odd scalar (see appendix A):

- M. Casolino *et al.*, *Probing a light CP-odd scalar in di-top associated production at the LHC*, Eur. Phys. J. C **75** (2015) 498, arXiv:1507.07004 [hep-ph].

Finally, the author has also contributed to the following results as part of the ATLAS Monte Carlo validation team:

- ATLAS Collaboration, *Validation of Monte Carlo event generators in the ATLAS Collaboration for LHC Run 2*, ATLAS-PHYS-PUB-2016-001 (2016)

1 Theoretical framework

It is wrong to think that the task
of Physics is to find out how Nature is.
Physics concerns what We can say about Nature.
Niels Bohr

Contents

The current understanding of the fundamental structure of matter and its interactions is summarised in the Standard Model of particle physics. This theory, developed in the 1960s, has turned out to be extremely valid in describing a large variety of observed phenomena and in predicting new ones that have found experimental confirmation. The discovery of the Higgs boson at the LHC in July 2012 was only the most recent proof of a tremendous successfully theory. The Standard Model is a very elegant and successful theory but there are several indications that cannot be the final theory of Nature. This chapter introduces the main ingredients of the Standard Model, describes its experimental tests, and provides a discussion of some of its limitations as the ultimate theory. Finally, an overview of some of the most promising theories beyond the Standard Model is provided.

1.1 The Standard Model

The Standard Model (SM) [1–3] is a renormalizable quantum field theory describing the interactions between the elementary constituents of matter through the fundamental forces. The matter particles, described as fields with half-integer spin (fermions), are subdivided in six leptons and six quarks. Leptons and quarks are respectively categorised in three families of particles with the same quantum numbers but with different mass. Each of these particles has an associated antiparticle with the same mass and opposite quantum numbers. The fundamental forces are described in terms of exchange of mediator fields with integer spin (bosons). Tables 1.1 and 1.2 show the elementary particles of the Standard Model, classified as matter particles and force carriers.

Matter particles and force carriers obey equations of motion derived from the principle of minimal action from a Lagrangian density. Fermions are described by the free Lagrangian:

$$\mathcal{L} = \bar{\Psi}(i\gamma^\mu \partial_\mu - m)\Psi, \tag{1.1}$$

where Ψ is the fermion field, γ^μ are the Dirac matrices and m is the mass of the fermion. Fundamental forces are introduced in the Lagrangian imposing invariance under local transformations of a given symmetry group. The number of associated boson fields is equal to the number of generators of the symmetry group. The SM Lagrangian is invariant under the gauge group:

$$SU(3)_C \otimes SU(2)_L \otimes U(1)_Y, \tag{1.2}$$

where $SU(3)_C$ is the gauge group for strong interactions mediated by gluons, while $SU(2)_L \otimes U(1)_Y$ is the unified gauge group for electromagnetic and weak interactions mediated by photons, $W^\pm$ and Z bosons.

	Leptons		Quarks	
	Spin 1/2			
Electric charge (q/e)	$q=-1$	$q=0$	$q=+2/3$	$q=-1/3$
I family	e^-	ν_e	u	d
Mass	0.51 MeV	<2 eV	2.3 MeV	4.8 MeV
II family	μ^-	ν_μ	c	s
Mass	105.66 MeV	<2 eV	1.275 GeV	95 MeV
III family	τ^-	ν_τ	t	b
Mass	1.77 GeV	<2 eV	173.5 GeV	4.65 GeV

Table 1.1: Table of quark and lepton families with their mass and charge according to the Particle Data Group [4].

The SM Lagrangian can be split in two terms,[1] one describing strong interactions, known as Quantum Chromodynamics (QCD) and a second one describing electroweak (EW) interactions:

$$\mathcal{L}_{\text{SM}} = \mathcal{L}_{\text{QCD}} + \mathcal{L}_{\text{EW}}. \tag{1.3}$$

[1] This splitting simplifies the discussion, but it introduces a small caveat: the kinetic term of the quarks will be present in both terms even if in the reality there is only a single kinetic term.

Force	Electromagnetism	Weak		Strong	Gravity
Carrier boson	γ	$W^{\pm}$	Z	g(× 8)	G
Spin	1	1	1	1	2
Electric charge (q/e)	0	±1	0	0	0
Mass (GeV)	0	80.385	91.1876	0	$< 6 \cdot 10^{-35}$

Table 1.2: Table of gauge bosons in the SM with their mass and charge according to the Particle Data Group [4]. Gravity is added for completeness.

1.1.1 Quantum Chromodynamics

The introduction of the strong interaction arose from the need to explain what keeps protons together inside nuclei and quarks bound inside hadrons. The postulation of colour as fundamental charge of the strong interaction was motivated by the need to achieve a description of the Δ^{++} baryon consistent with Fermi-Dirac statistics. Being a spin-3/2 fermion composed of three identical quarks (uuu), an additional feature was required in order to build a wavefunction fully antisymmetric under the interchange of quarks. At the same time, an explanation was needed for the lack of experimental observations of free quarks or qq states. The proposed solution was the existence of a new quantum number, C, the colour charge with three different possible values: red (R), blue (B) and green (G). A quark can carry one colour at the time, while anti-quarks carry anti-colours. Only colour-singlet states exist as bound states. The carriers of the strong interaction, called gluons, are massless spin-1 bosons, carrying one of eight bi-colour combinations, i.e. a superposition of colour-anti-colour states, but no electric charge.

Quantum ChromoDynamics (QCD) is a gauge theory of strong interactions between quarks and gluons based on the symmetry group $SU(3)_C$. Quarks are colour triplets and for each flavour three fields with different colour index (i) are present, q_i. Under a local gauge $SU(3)_C$ transformation, the quark field q transforms as follows:

$$q \rightarrow q' = e^{ig_S T_a \cdot \theta^a(x)} q, \text{ with a=1,...,8 }, \tag{1.4}$$

where $\theta_a(x)$ is an arbitrary phase that is a-priori different for each point in space-time, $T_a = \frac{\lambda_a}{2}$ refers to the group generators of $SU(3)_C$, with λ_a being the eight Gell-Mann matrices, which are 3×3 generalisations of the Pauli matrices, and $g_s = \sqrt{4\pi\alpha_s}$ is the strong coupling. The group is non-abelian and the commutation rules are the following:

$$[T_a, T_b] = i f_{abc} T_c \tag{1.5}$$

where f_{abc} are the structure constants of the group. To ensure the local gauge invariance of the Lagrangian the covariant derivative is introduced:

$$D_\mu \equiv \partial_\mu + i g_s T_a G^a_\mu, \tag{1.6}$$

where G^a_μ are the gluon fields, which transform as $G^a_\mu \rightarrow G^a_\mu{}' = G^a_\mu - \frac{1}{g_s}\partial_\mu \theta^a$. The interactions between quarks and gluons are enclosed in the definition of the covariant derivative.

After introducing the covariant derivative and a kinetic term for the gluon fields, the QCD Lagrangian is given by:

$$\mathcal{L}_{\text{QCD}} = \bar{q}(i\gamma^\mu D_\mu - m)q - \frac{1}{4} G^\alpha_{\mu\nu} G^{\mu\nu}_\alpha, \tag{1.7}$$

where the $G^{\alpha}_{\mu\nu}$ tensor field is defined as:

$$G^{\alpha}_{\mu\nu} = \partial_{\mu} G^{a}_{\nu} - \partial_{\nu} G^{a}_{\mu} - g_s f_{abc} G^{b}_{\mu} G^{c}_{\nu}. \tag{1.8}$$

Being carriers of colour charge, gluons can self-interact. This self-interaction is described by the third term of equation 1.8 and has an effect on the way the strong coupling evolves as a function of the energy scale Q at which the interaction takes place. At the leading order, the strong coupling constant can be expressed as:

$$\alpha_s(Q^2) = \frac{12\pi}{(33 - 2n_f) \log\left(Q^2/\Lambda^2_{\mathrm{QCD}}\right)}, \tag{1.9}$$

where n_f is the number of active quark flavours (i.e. with $m_q < Q$) and Λ_{QCD} is an infrared cut-off scale ($\Lambda_{\mathrm{QCD}} \sim 200\mathrm{MeV}$) below which the perturbative approximation is no longer valid. The strong coupling constant is decreasing with increasing energy (or decreasing distance), as shown in figure 1.1.

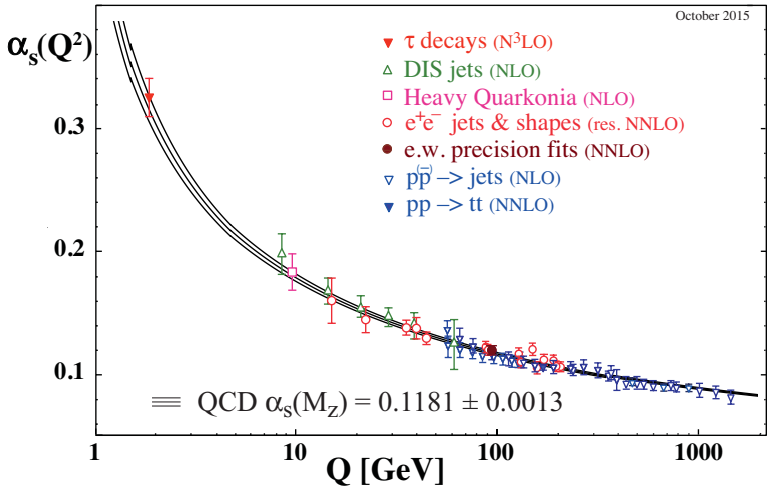

Figure 1.1: Evolution of the strong coupling constant α_s with energy scale Q, as probed by different measurements. From Ref. [5].

In the high-energy (i.e. short-distance) regime, α_s is sufficiently small that perturbation theory fully applies, and asymptotically quarks and gluons can be considered as free particles. This property is referred to as "asymptotic freedom" [6, 7], and it is particularly important for the computability of cross sections at hadron colliders. On the other hand, at lower energies (i.e. longer distances) α_s increases to the point of diverging; i.e. quarks and gluons cannot be found as free particles. This property is known as "confinement": when trying to separate two quarks, the potential energy increases enough that a quark-antiquark pair is created from the vacuum and colorless hadrons are eventually formed. Therefore, quarks and gluons produced as the result of interactions among particles at high energy will manifest themselves in the detector as collimated sprays of colorless hadrons called "jets". At low energies ($Q < \Lambda_{\mathrm{QCD}}$), where the perturbative approximation is no longer valid, numerical (lattice QCD) or phenomenological (hadronisation models) approaches have to be used in order to describe this regime.

1.1.2 Electroweak theory

The gauge invariance of electromagnetism was already introduced in Maxwell's formulation of Electrodynamics [8]. It was later extended to the invariance under a local phase transformation, which accommodated the explanation of the interaction in terms of Quantum ElectroDynamics (QED). The weak interaction was first identified by studying β-decays of atomic nuclei in the late 19th century. The experiments regarding these decays also lead to the postulation of neutrinos by Wolfgang Pauli [9], introduced to ensure the energy, momentum and spin conservation in these processes. After the parity violation of the weak processes was confirmed in the experiment conducted by C.-S. Wu [10], a new gauge theory formulation was constructed. The Wu experiment showed that the decay particles were travelling in a direction opposite to their spin, which suggested that the weak interaction had a form of a difference of a vector (representing the particle momentum) and an axial vector (representing the particle spin), i.e. a V-A form. The weak interaction is thus not the same for a particle and its mirror symmetric partner. This feature is referred to as the parity violation (P violation) of the weak interaction. It was shown later that the weak interaction violates as well the CP (charge conjugation and parity) symmetry [11] and the T (time reversal) [12], but conserves CPT [13].

The electroweak theory describes the weak and the electromagnetic interactions, using a Lagrangian invariant under transformations of the symmetry group $SU(2)_L \otimes U(1)_Y$. The $SU(2)_L$ group introduces the weak isospin quantum number (T). The group is non-abelian and the commutation rules for the generators of the group are the following:

$$[T_i, T_j] = i\varepsilon_{ijk} T_k, \tag{1.10}$$

where ε_{ijk} is the totally-antisymmetric Levi-Civita tensor and $T_i = \frac{\sigma_i}{2}$ $(i = 1, 2, 3)$, where σ_i are the Pauli matrices. Three bosons are introduced for $SU(2)_L$ according to the number of group generators. The fermions have different $SU(2)_L$ representation according to their chiral structure, defined as $f_{L,R} = \frac{1}{2}(1 \mp \gamma_5) f$, with $\gamma_5 = i\gamma_0\gamma_1\gamma_2\gamma_3$. Left-handed fermions are weak-isospin doublets ($T_3 = \pm 1/2$) while right-handed fermions are singlets ($T_3 = 0$), where T_3 is the third component of the weak isospin. Only left-handed components participate in weak interaction, thus explaining the subscript in $SU(2)_L$. The abelian group $U(1)_Y$ introduces the hypercharge quantum number, Y, defined using the Gell-Mann-Nishijima formula:

$$Q = T_3 + \frac{Y}{2}, \tag{1.11}$$

where Q is the electric charge. Electric charge and hypercharge are quantities absolutely conserved. Table 1.3 shows the multiplets of fermions fields and their T, T_3, Y and Q quantum numbers.

Under a local gauge transformation of the $SU(2)_L \otimes U(1)_Y$ group a fermionic field $\Psi(x)$ transforms as:

$$\Psi(x) \to \Psi'(x) = e^{\frac{i}{2}\vec{\sigma}\cdot\vec{\alpha}(x)} e^{i\frac{Y}{2}\beta(x)} \Psi(x). \tag{1.12}$$

To ensure local gauge invariance of the lagrangian the covariant derivative is introduced:

$$D_\mu^L \equiv \partial_\mu + igT_i W_\mu^i + ig'\frac{Y}{2} B_\mu, \qquad D_\mu^R \equiv \partial_\mu + ig'\frac{Y}{2} B_\mu, \tag{1.13}$$

where D_μ^L acts on weak-isospin doublets and D_μ^R, instead, on singlets. The coupling constants g and g' are associated with the $SU(2)_L$ and $U(1)_Y$ gauge groups respectively, and W_μ^i, B_μ denote the gauge fields of the respective gauge groups. The $SU(2)_L$ gauge fields transform as $\vec{W}_\mu \to \vec{W}_\mu - \frac{1}{g}\partial_\mu\vec{\alpha} - \vec{\alpha}\times\vec{W}_\mu$, while the $U(1)_Y$ gauge field transforms as $B_\mu \to B_\mu - \frac{1}{g'}\partial_\mu\beta$.

After introducing the covariant derivative and a kinetic term for the gauge fields, the EW Lagrangian is:

$$\mathcal{L}_{\text{EW}} = i\bar{f}_L\gamma^\mu D_\mu^L f_L + i\bar{f}_R\gamma^\mu D_\mu^R f_R - \frac{1}{4}W^i_{\mu\nu}W_i^{\mu\nu} - \frac{1}{4}B_{\mu\nu}B^{\mu\nu}, \tag{1.14}$$

where $i = 1, 2, 3$, and $W^i_{\mu\nu}$ and $B_{\mu\nu}$ are the field tensors for $SU(2)_L$ and $U(1)_Y$ respectively, defined as:

$$W^i_{\mu\nu} = \partial_\mu W^i_\nu - \partial_\nu W^i_\mu - g\varepsilon_{ijk}W^j_\mu W^k_\nu, \qquad B_{\mu\nu} = \partial_\mu B_\nu - \partial_\nu B_\mu. \tag{1.15}$$

The introduction of mass terms for gauge fields ($\frac{1}{2}M_V^2 W_\mu W^\mu$) or fermion fields ($-mf_Lf_R$) in equation 1.14 would violate the local gauge invariance under $SU(2)_L \otimes U(1)_Y$, since those terms couple left- and right-handed components. Breaking gauge invariance would consequently break the renormalizability of the SM. Therefore, a mechanism for generating non-zero masses while preserving the renormalizability of the theory needs to be introduced to be consistent with the experimental observation of massive fermions and vector bosons.

1.1.3 The Brout-Higgs-Englert mechanism

The Brout-Higgs-Englert (BEH) mechanism [16,17] solves the apparent contradiction between massive particles and the requirement of gauge invariance. This mechanism triggers a Spontaneous Symmetry Breaking (SSB), $SU(2)_L \otimes U(1)_Y \rightarrow U(1)_{\text{EM}}$, where $U(1)_{\text{EM}}$ denotes the gauge group describing electromagnetism. The SSB is triggered by introducing a complex scalar field. This field, referred to as "Higgs field", must have the form of a $SU(2)_L \otimes U(1)_Y$ multiplet in order to satisfy the SM gauge invariance. In the so called "minimal" Higgs sector, the Higgs field is an $SU(2)_L \otimes U(1)_Y$-isodoublet with isospin $T = 1/2$ and the hypercharge $Y = 1$:

$$\Phi = \begin{pmatrix} \phi^+ \\ \phi^0 \end{pmatrix}, \tag{1.16}$$

containing one positively-charged component ϕ^+ and one neutral component ϕ^0.

The dynamics of this field, which will be added to the $\mathcal{L}_{\text{EW}}$, is given by the Lagrangian:

$$\mathcal{L}_{\text{Higgs}} = (D_\mu\Phi)^\dagger D^\mu\Phi - V(\Phi), \tag{1.17}$$

where D_μ is the covariant derivative (see equation 1.13) and the potential $V(\Phi)$ is:

	Fermions multiplets			T	T_3	Y	Q
Leptons	$\begin{pmatrix} e \\ \nu_e \end{pmatrix}_L$	$\begin{pmatrix} \mu \\ \nu_\mu \end{pmatrix}_L$	$\begin{pmatrix} \tau \\ \nu_\tau \end{pmatrix}_L$	$1/2$	$+1/2$ $-1/2$	-1	0
	e_R	μ_R	τ_R	0	0	-2	-1
Quarks	$\begin{pmatrix} u \\ d' \end{pmatrix}_L$	$\begin{pmatrix} c \\ s' \end{pmatrix}_L$	$\begin{pmatrix} t \\ b' \end{pmatrix}_L$	$1/2$	$+1/2$ $-1/2$	$+1/3$	$+2/3$ $-1/3$
	u_R	c_R	t_R	0	0	$+4/3$	$+2/3$
	d_R	s_R	b_R	0	0	$-2/3$	$-1/3$

Table 1.3: Weak isospin multiplets. Here d', s', and b' denote flavour eigenstates, each of which can be expressed as a linear combination of the mass eigenstates (d, s, and b) weighted by CKM matrix elements [14,15].

$$V(\Phi) = \mu^2 \Phi^\dagger \Phi + \lambda (\Phi^\dagger \Phi)^2. \tag{1.18}$$

In order for $V(\Phi)$ to have at least one stable minimum λ is required to be positive. For $\lambda > 0$, two possibilities arise: $\mu^2 > 0$ and $\mu^2 < 0$, which are illustrated in figure 1.2. In the first case, $\mu^2 > 0$,

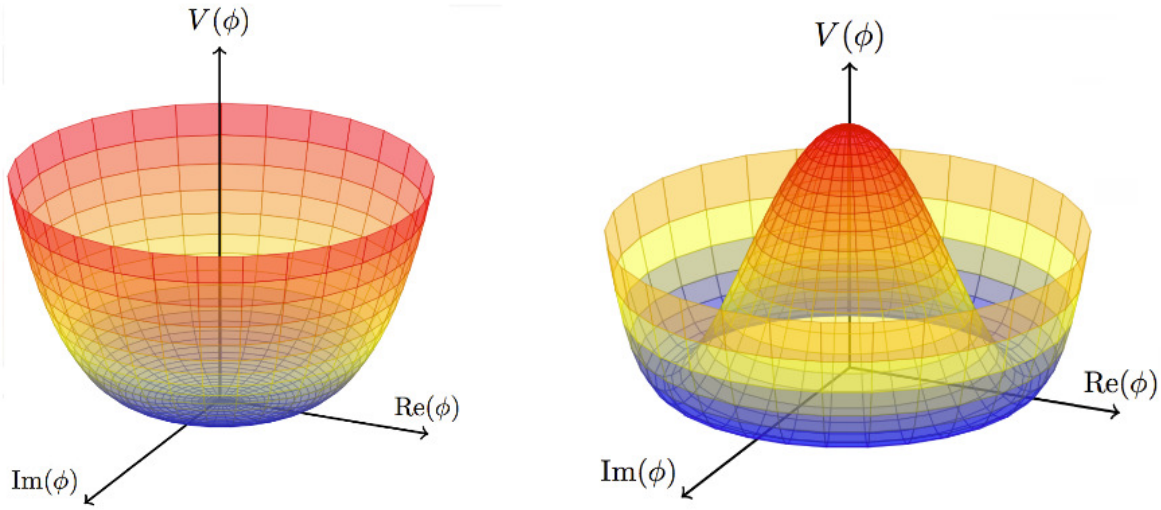

(a) (b)

Figure 1.2: Vacuum potential for $\lambda > 0$ and (a) $\mu^2 > 0$ or (b) $\mu^2 < 0$, with the typical shape of a Mexican hat.

there is a single solution to the minimisation which corresponds to $|\Phi| = 0$ and provides a vacuum expectation value (VEV), $\langle \Phi \rangle_0 = \langle 0|\Phi|0\rangle = 0$. If $\mu^2 < 0$, there is no unique minimum with a VEV, $\langle \Phi \rangle_0 = \langle 0|\Phi|0\rangle = v/\sqrt{2}$ and the potential $V(\Phi)$ presents a "Mexican hat" shape (figure 1.2b) with its minimum at:

$$\Phi^\dagger \Phi = -\frac{\mu^2}{2\lambda} = \frac{v^2}{2}, \tag{1.19}$$

where $v = \sqrt{-\mu^2/\lambda}$. In this case, the fundamental vacuum state is no longer invariant under $SU(2)_L \otimes U(1)_Y$, meaning that these two symmetries are now broken. When a continuous symmetry is broken Goldstone bosons, massless scalars, are present (Goldstone theorem [18]) and they can be absorbed by a gauge field as a longitudinal polarisation component, resulting in the gauge field acquiring mass. Since the photon is the only electroweak boson known to be massless, the minimum of the potential is chosen so that the Higgs field that acquires a VEV is the one with zero electric charge in order to not break $U(1)_{\text{EM}}$:

$$\Phi_0 = \frac{1}{\sqrt{2}} \begin{pmatrix} 0 \\ v \end{pmatrix}. \tag{1.20}$$

An infinitesimal $SU(2)_L$ transformation around the vacuum can then be expressed as:

$$\Phi'(x) = \frac{e^{i\vec{\sigma}\cdot\vec{\theta}(x)/v}}{\sqrt{2}} \begin{pmatrix} 0 \\ v + H(x) \end{pmatrix}, \tag{1.21}$$

with $H(x)$ denoting a real scalar field associated to a physical degree of freedom, the Higgs boson particle, and θ denoting the three fields which will be absorbed by the gauge fields. With this choice of the vacuum and the gauge, the Lagrangian of the physical Higgs field reads:

$$\mathcal{L}_{\text{Higgs}} = (D_\mu H)^\dagger D^\mu H - \frac{1}{2}(-2\mu^2)H^2 - \lambda v H^3 - \frac{1}{4}\lambda H^4, \tag{1.22}$$

where the second term corresponds to the tree-level mass term of the $H(x)$ field, $m_H = \sqrt{-2\mu^2} = \sqrt{2\lambda}v$, and the last two terms describe interactions among Higgs fields. Since the value of λ is unknown, m_H is not predicted by the theory and must be determined experimentally.

Furthermore, this procedure has also generated the masses of the gauge bosons. This becomes obvious from the development of $|D_\mu \Phi'|^2$, which provides terms of the form:

$$\begin{aligned}
&\left|\left(-ig\frac{\vec{\sigma}}{2}\vec{W}_\mu - i\frac{g'}{2}B_\mu\right)\Phi\right|^2 = \frac{1}{8}\left|\begin{pmatrix} gW_\mu^3 + g'B_\mu & g(W_\mu^1 - iW_\mu^2) \\ g(W_\mu^1 + iW_\mu^2) & -gW_\mu^3 + g'B_\mu \end{pmatrix}\begin{pmatrix} 0 \\ v \end{pmatrix}\right|^2 \\
&= \frac{1}{8}v^2 g^2\left[(W_\mu^1)^2 + (W_\mu^2)^2\right] + \frac{1}{8}v^2(g'B_\mu - gW_\mu^3)(g'B^\mu - gW^{3\mu}) \\
&= \left(\frac{1}{2}vg\right)^2 W_\mu^+ W^{-\mu} + \frac{1}{8}v^2\left(W_\mu^3, B_\mu\right)\begin{pmatrix} g^2 & -gg' \\ -gg' & g'^2 \end{pmatrix}\begin{pmatrix} W_\mu^3 \\ B_\mu \end{pmatrix},
\end{aligned} \tag{1.23}$$

defining the charged fields as $W^\pm = (W^1 \mp iW^2)/\sqrt{2}$. The mass eigenstates can be obtained diagonalizing the mass matrix, and expressed as a function of W_μ^3 and B_μ:

$$\begin{aligned}
\frac{1}{8}v^2\left[g^2\left(W_\mu^3\right)^2 - 2gg'W_\mu^3 B^\mu + g'^2 B_\mu^2\right] &= \frac{1}{8}v^2\left[gW_\mu^3 - g'B_\mu\right]^2 \\
&\quad + 0\left[g'W_\mu^3 + gB_\mu\right]^2 \\
&= \frac{1}{2}\left(v\frac{\sqrt{g^2+g'^2}}{2}\right)^2 Z_\mu^2 \\
&\quad + 0 \cdot A_\mu^2,
\end{aligned} \tag{1.24}$$

where Z_μ and A_μ can be defined as:

$$Z_\mu = \frac{gW_\mu^3 - g'B_\mu}{\sqrt{g^2+g'^2}} = \cos\theta_W W_\mu^3 - \sin\theta_W B_\mu \tag{1.25}$$

$$A_\mu = \frac{g'W_\mu^3 + gB_\mu}{\sqrt{g^2+g'^2}} = \sin\theta_W W_\mu^3 + \cos\theta_W B_\mu, \tag{1.26}$$

representing the fields associated with the Z boson and the photon respectively, and θ_W is the Weinberg angle, $\tan\theta_W = g'/g$. From equations 1.23 and 1.24, the tree level predictions for masses of the gauge bosons and the relation between the coupling constants can be derived:

$$m_W = \frac{vg}{2} = m_Z \cos\theta_W, \tag{1.27}$$

$$m_Z = v\frac{\sqrt{g^2+g'^2}}{2}, \tag{1.28}$$

$$m_\gamma = 0. \tag{1.29}$$

The BEH mechanism can provide as well mass to the fermions, by postulating their coupling to the Higgs boson via a Yukawa interaction:

$$\mathcal{L}_{\text{Yukawa}} = \sum_{f=\ell,q} y_f \left[\bar{f}_L \Phi f_R + \bar{f}_R \bar{\Phi} f_R\right], \tag{1.30}$$

where the matrices y_f describe the Yukawa couplings between the Higgs doublet and the fermions. The Yukawa Lagrangian is gauge invariant since the combinations $\bar{f}_L \Phi f_R$ and $\bar{f}_R \bar{\Phi} f_R$ are $SU(2)_L$ singlets. The y_f matrices can be diagonalised to obtain the eigenvalues of the Yukawa couplings using unitary transformations that will redefine the fermion fields. In the leptonic sector this transformation has no effect given the absence of right-handed neutrinos, while in the quark sector, the rotation to the mass eigenstate basis introduces a mixing among fermion families that is manifest in the weak interactions. The mixing between the weak eigenstates of the down-type quarks,[2] d', s' and b', and the corresponding mass eigenstates d, s and b, is described by the Cabibbo-Kobayashi-Maskawa (CKM) matrix [15]. Off-diagonal elements of the CKM matrix have the result that W bosons can couple to two quark belonging to two different families. The CKM matrix is fully specified by four parameters: three mixing angles controlling the mixing between each family pair and one complex phase responsible for CP-violating phenomena.

The tree level predictions for the mass of the fermions are obtained introducing the expansion of the Higgs doublet in equation 1.30:

$$m_f = \frac{y_f v}{\sqrt{2}}. \tag{1.31}$$

While the gauge-boson masses can be determined from the known values of the coupling constants g and g', the fermion masses are free parameters, since their Yukawa couplings y_f are not predicted by the SM.

1.1.4 Higgs boson production and decay in the Standard Model

The most important production modes for the SM Higgs boson at the LHC are displayed in figure 1.3, with their cross sections shown in figure 1.4a. The dominant production mechanism is gluon-gluon fusion (ggF) mediated by a virtual quark loop, where the main contribution is from the top quark, owing to its large Yukawa coupling. The ggF production mode gives access to the top-quark Yukawa coupling under the assumption that no new particles are contributing to the loop. The vector-boson fusion (VBF) mode, whose cross section is about one order of magnitude smaller than ggF, is an important Higgs-boson production mechanism due to the two forward jets that can be exploited to suppress backgrounds. The associated production with a vector boson (VH) which, like VBF, allows to measure the Higgs boson couplings to weak gauge bosons, is suppressed compared to ggF and VBF since it needs an antiquark in the initial state.[3] The $b\bar{b}H$ and $t\bar{t}H$ production modes have the lowest cross sections but they can provide direct access to the third generation quark Yukawa couplings in production mode.

The branching ratios for the different SM Higgs boson decay modes [19] as function of its mass are shown in figure 1.4b. For a mass of about 125 GeV the $H \to b\bar{b}$ decay mode is dominant. The channels with the cleanest experimental signature are $H \to \gamma\gamma$ and $H \to ZZ^* \to 4\ell$ and, despite their small branching ratio, played a crucial role in the Higgs boson discovery.

[2] By convention, the mixing takes place between down-type quarks only, while the up-type mass matrix is diagonal.
[3] VH was the second leading production mode at the Tevatron, after ggF.

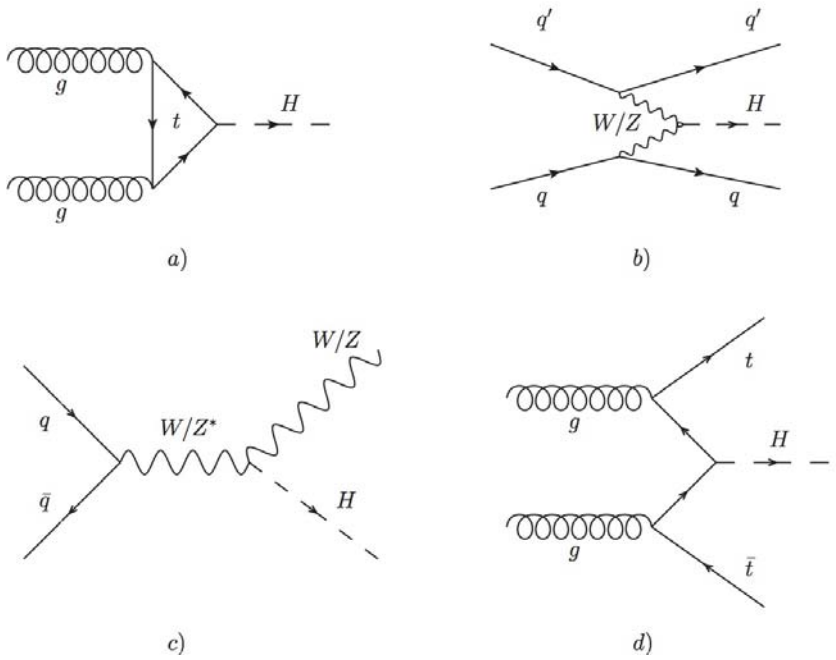

Figure 1.3: Representative Feynman diagrams for the most important production modes for the SM Higgs boson at the LHC (a) gluon-gluon fusion (b) vector-boson fusion (c) associated production with a vector boson and (d) $t\bar{t}H$ production.

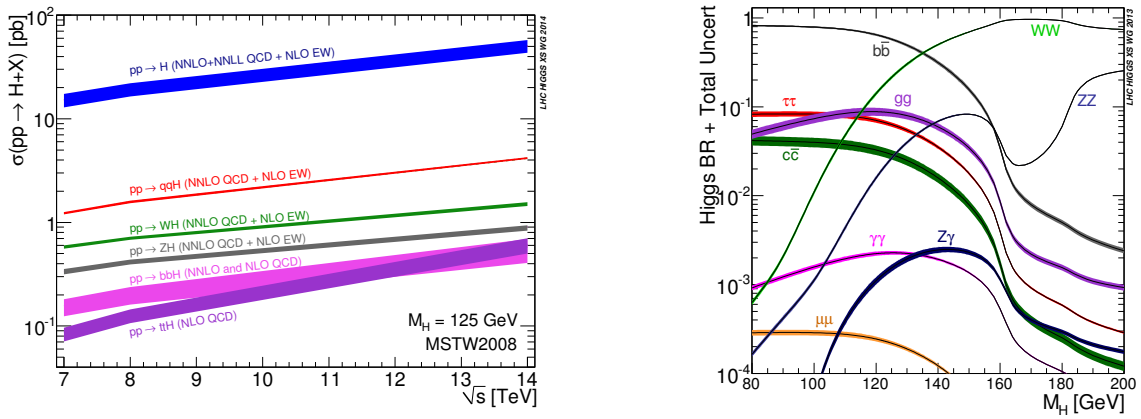

Figure 1.4: (a) Higgs boson production cross sections as a function of centre-of-mass energy and (b) branching ratios as a function of the Higgs boson mass. The SM-like Higgs boson is assumed to have a mass of m_H=125 GeV. From Ref. [19].

1.1.5 Experimental tests and limitations of the Standard Model

The SM has so far shown a remarkable success. It is a mathematically-consistent theory accommodating most experimental findings, with an excellent predictive power due to its renormalisability. During the 1970s and 1980s many discoveries set the scene for the success of the Standard Model: the discovery of neutral current processes [20], the discovery of the charm [21,22] and bottom [23] quarks, the τ lepton and its neutrino [24,25], the discovery of the gauge bosons of the weak interaction W and Z [26–29]. In the 1990s the precision era of the electroweak sector started at CERN's Large Electron

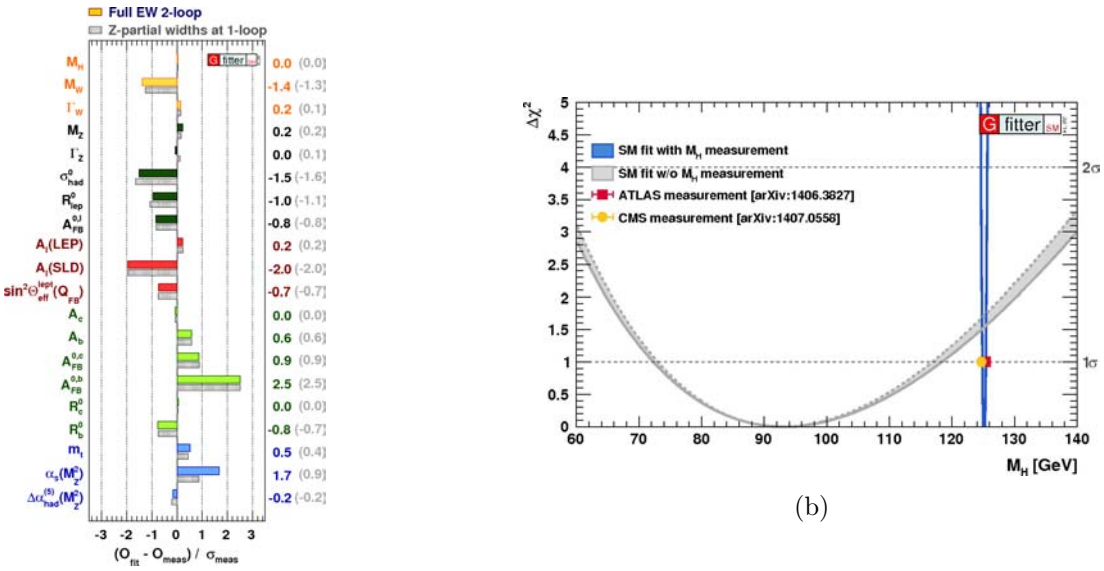

(a) (b)

Figure 1.5: (a) Pull values for the SM fit, i.e. deviations between experimental measurements and theoretical calculations in units of the experimental uncertainty. (b) χ^2 as a function of Higgs boson mass M_H, with (blue band) and without the M_H measurements (gray band). From Ref. [38].

Positron (LEP) Collider. Many precision measurements of SM quantities were performed and, together with accurate theoretical calculations of radiative corrections, allowed to check the consistency of the model at permille level, which in turn allowed to derive indirect constraints on unknown parameters. In this context, the top-quark mass was precisely predicted from radiative corrections to the W boson mass and the $Z \to b\bar{b}$ branching ratio, prior to the discovery of the top quark in 1995 by the CDF and D0 Collaborations [30, 31] at Fermilab's Tevatron Collider. The discovery of the Higgs boson in July 2012 by the ATLAS and CMS Collaborations [32, 33] allowed to measure the last free parameter of the SM, the Higgs boson mass of about 125 GeV [34]. Further measurements of the spin and CP of this particle confirmed that it is a scalar with positive CP eigenstate [35, 36]. As of today, the couplings to the SM particles [37] have been found to be in agreement with those of the SM Higgs boson.

The validity of the SM can be tested performing a global electroweak fit using as input many precision measurements. The fit results, performed by the GFitter collaboration [38], are shown in figure 1.7a. Good consistency between measured and expected quantities is found and none of the observed differences exceeds three standard deviations. From this fit, leaving the mass of the Higgs boson as free parameter, it was predicted to be 94.1^{+25}_{-22} GeV, within 1.5 standard deviation from the current measurement (see figure 1.7b).

Despite its tremendous success, a number of theoretical and experimental arguments suggest that the SM is not the ultimate theory of Nature, but more likely just a low-energy manifestation, i.e. an effective theory, of a more general theory. Gravity is not accommodated in this model, since no renormalizable quantum gravity theory is available. The SM is not a complete unified theory, but rather describes three of the four forces present in Nature using a convolution of different symmetries and not as a single symmetry group. Grand Unified Theories (GUTs) try to unify these three symmetry groups in a single symmetry group G, $G \supset SU(3)_C \otimes SU(2)_L \otimes U(1)_Y$, while Theories of Everything try to add gravity as well. An additional indication of the SM not being complete unified theory, besides the ones already discussed, is that the forces are expected to unify at high energy since their

couplings depend on the energy scale but, as shown in figure 1.6, there is no convergence of the three couplings to a common value.

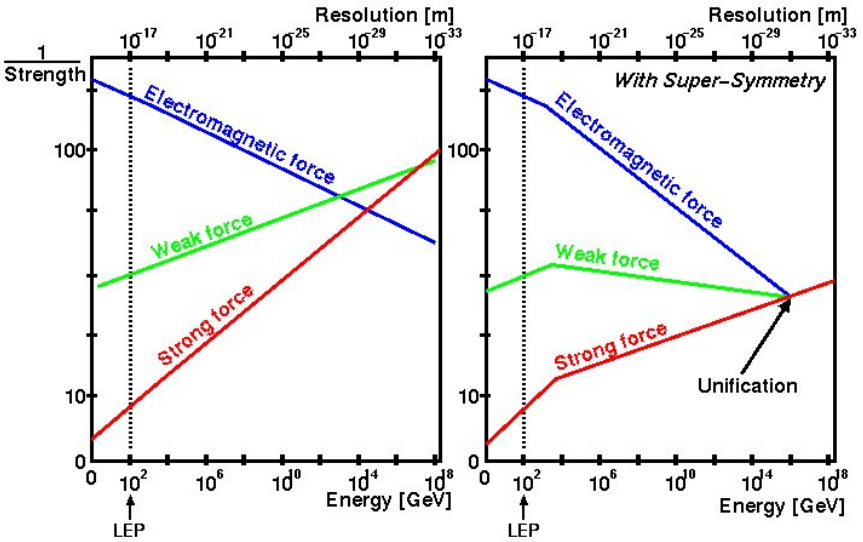

Figure 1.6: Running of couplings (a) in the SM and (b) in a hypothetical Supersymmetric Model as function of the energy scale.

The SM provides no explanation for the baryon (i.e. matter-antimatter) asymmetry in the universe [39], which is connected to CP violation, since the amount of CP violation predicted by the SM is not enough to explain such asymmetry. The energy density of the universe made by ordinary baryonic matter according to several astronomical observations, from rotation curves of galaxies [40] to gravitational lensing [41], is only for a $\sim 5\%$, the remaining component being dark matter ($\sim 25\%$) and dark energy ($\sim 70\%$). The SM does not provide a particle candidate to explain the large amount of dark matter in the universe. Also, it does not explain dark energy. The observation of neutrino oscillations and hence the fact that neutrinos are massive [42] cannot be explained in the SM. Extending the SM Lagrangian to accomodate massive neutrinos can be achieved by introducing right-handed neutrinos or by describing them as Majorana particles. The SM has already 19 arbitrary parameters, out of them nine fermion masses, and it would have even more if neutrinos masses were added. There is no explanation for why there are exactly three generations of chiral fermions and why their masses are so different, i.e. which mechanism generates their Yukawa couplings. The arbitrariety of parameters in the SM, and in particular of the fermion masses, introduces the naturalness problem [43]. A "natural" theory is characterised by free parameters with values of the same order of magnitude. This does not happen in the SM, where some masses differ by several orders of magnitude. If the SM is assumed as the "final theory" valid up to the Planck scale, it exhibits an additional problem known as the "hierarchy problem" coming from the huge difference between the electroweak and the Planck scales ($M_{\mathrm{Pl}}/m_W \sim 10^{17}$) and its effect on the Higgs boson mass. Unlike fermion and gauge boson masses, which are protected by chiral or gauge symmetries, the mass of an elementary scalar receives radiative corrections from vacuum polarisation diagrams (see figure 1.7) of the order of the largest energy scale involved in the theory:

$$m_H^2 = (m_H)_0^2 + \delta m_H^2 = (m_H)_0^2 - \frac{|y_f|^2}{16\pi^2}\left[\Lambda^2 + \mathcal{O}\left(m_f^2 \ln\left(\frac{\Lambda}{m_f}\right)\right)\right], \tag{1.32}$$

where $(m_H)_0$ is the bare Higgs boson mass, y_f and m_f are the Yukawa coupling and the mass,

respectively, of the fermion f involved in the loop, and Λ is the energy scale up to which the SM is still valid. The top quark is responsible for the largest correction due to its large Yukawa coupling, $y_t \sim 1$; thus the top quark might have a special role in the electroweak symmetry breaking mechanism and the mass hierarchy pattern. If Λ is set to M_{Pl}, the quantum corrections to the Higgs boson mass can be up to 30 orders of magnitude larger than the measured Higgs boson mass squared. To recover the measured mass, the value of the bare Higgs boson mass and the corrections have to cancel with an incredible precision, referred to as "fine tuning". Although this lucky cancellation could in principle happen in Nature, it is considered highly "unnatural" and several extensions of the SM have been proposed to stabilise the Higgs boson mass.

(a) (b)

Figure 1.7: Examples of one-loop quantum corrections to the Higgs boson mass due to (a) fermions and (b) vector bosons.

1.2 Beyond the Standard Model

Over the years, many theories have been developed to solve one or more of the SM shortcomings, but so far none of these theories have found experimental support yet. In the following sections, some of these scenarios for physics beyond the SM are reviewed, with a focus on those predicting new phenomena of interest for this dissertation.

1.2.1 Supersymmetry

Supersymmetric models introduce a new symmetry, referred to as "supersymmetry" (SUSY), which transforms a bosonic state into a fermionic state and viceversa, being the last possible extension of the Lorentz group [44, 45]. This symmetry introduces a superpartner for each SM particle. The existence of those partners can stabilise the Higgs boson mass, solving the hierarchy problem. In fact, if a new boson S, which couples to the Higgs boson, is introduced for each fermion f the correction to the Higgs boson mass due to this boson will be:

$$\delta m_H^2 = \frac{y_S^2}{16\pi^2}\left[2\Lambda^2 + \mathcal{O}\left(m_S^2 \log\left(\frac{\Lambda}{m_S}\right)\right)\right]. \tag{1.33}$$

Bose-Einstein statistics implies an opposite sign with respect to the fermion mass correction shown in equation 1.32. Therefore, if $y_S = |y_f|$, each of the fermion terms have a counter term that naturally cancels the quadratic divergence introduced. The residual correction left, ignoring the logarithmic contribution, is proportional to the quadratic mass difference between the fermion and the boson:

$$\delta m_H^2 = \frac{y_f^2}{16\pi^2}|m_S^2 - m_f^2|. \tag{1.34}$$

According to the the "naturalness" argument, these corrections must not be much greater than m_H in order to avoid too much fine tuning. This argument, not strict but quite desirable, sets the scale of the

SM validity around the TeV, where the supersymmetric theory would replace the SM up to the Plank scale. Supersymmetry naturally predicts superpartners with the same mass as the SM particles but, since no supersymmetric particles have been observed yet, supersymmetry must be a broken symmetry at low energy [46, 47] and so the masses of the superpartners have to be beyond the reach of current experiments.

Supersymmetry is not a fixed model but rather a framework that allows many SM extensions depending on the number of generators in the symmetry group, as well as the composition and arrangement of the SM particles into supermultiplets. The Minimal Supersymmetric SM (MSSM) is a model that introduces the minimal number of new particles. It obeys to the same gauge symmetry of the SM, but it doubles the spectrum of particles, since for every partner of the SM, a superpartner is postulated, differing by half a unit of spin. Spin-0 superpartners of the fermions are denoted starting with an extra "s" (e.g. the selectron is the superpartner of the electron) while the spin-1/2 superpartners of the bosons are added the suffix "ino" (e.g. the gluino is the superpartner of the gluon). Table 1.4 summarises the MSSM particle content.

Names	**Spin**	P_R	**Gauge eigenstates**	**Mass Eigenstates**
Higgs bosons	0	+1	$H_u^0\ H_d^0\ H_u^+\ H_d^-$	$h^0\ H^0\ A^0\ H^\pm$
Squarks	0	−1	$\tilde{u}_L\ \tilde{u}_R\ \tilde{d}_L\ \tilde{d}_R$ $\tilde{s}_L\ \tilde{s}_R\ \tilde{c}_L\ \tilde{c}_R$ $\tilde{t}_L\ \tilde{t}_R\ \tilde{b}_L\ \tilde{b}_R$	same same $\tilde{t}_1\ \tilde{t}_2\ \tilde{b}_1\ \tilde{b}_2$
Sleptons	0	−1	$\tilde{e}_L\ \tilde{e}_R\ \tilde{\nu}_e$ $\tilde{\mu}_L\ \tilde{\mu}_R\ \tilde{\nu}_\mu$ $\tilde{\tau}_L\ \tilde{\tau}_R\ \tilde{\nu}_\tau$	same same $\tilde{\tau}_1\ \tilde{\tau}_2\ \tilde{\nu}_\tau$
Neutralinos	1/2	−1	$\tilde{B}^0\ \tilde{W}^0\ \tilde{H}_u^0\ \tilde{H}_d^0$	$\tilde{\chi}_1^0\ \tilde{\chi}_2^0\ \tilde{\chi}_3^0\ \tilde{\chi}_4^0$
Charginos	1/2	−1	$\tilde{W}^\pm\ \tilde{H}_u^+\ \tilde{H}_d^-$	$\tilde{\chi}_1^\pm\ \tilde{\chi}_2^\pm$
Gluino	1/2	−1	$\tilde{g}$	same

Table 1.4: The predicted particle spectra in the MSSM (sfermion mixing for the first two families is assumed to be negligible).

The Higgs sector is enlarged in the MSSM with the introduction of an additional complex doublet, leading to five physical Higgs bosons after the SSB mechanism. Baryonic and leptonic number violating terms are included in the most general MSSM, but strong constraints on those terms come from the fact that no such violations have been observed. A new discrete symmetry, R-parity, is added to avoid such terms and the conserved quantum number is defined as:

$$P_R = (-1)^{3(B-L)+2s}, \tag{1.35}$$

where B and L refer to the baryon and lepton quantum numbers respectively, and s is the spin of the particle. This definition sets all the SM particles and the Higgs bosons to have $P_R = +1$, while their SUSY partners have $P_R = -1$. R-parity is not necessarily conserved but, when is imposed as a discrete symmetry, it has the consequence that SUSY particles are always produced in pairs. Furthermore, the lightest supersymmetric particle must be stable since, due to the conservation of $R-$parity, it cannot decay into ordinary particles, thus providing a good candidate for dark matter. The MSSM solves in an elegant way the hierarchy problem, provides a candidate for dark matter, can predict enough

CP violation to explain baryon asymmetry and, finally, predicts the unification of the three SM gauge couplings. On the other hand, it introduces 105 new parameters, to be added to the 19 parameters of the SM. In order to reduce the number of parameters to be considered, several simplifications and assumptions are introduced in collider searches. Usually, only the sparticles that contribute to a particular final state are considered. The rest of the superpartners are considered heavy enough so that they can be completely decoupled.

1.2.1.1 The Two-Higgs-doublet model

In supersymmetric theories the scalars belong to chiral multiplets and their complex conjugates belong to multiplets of the opposite chirality; a single Higgs doublet is unable to give mass simultaneously to the charge $+2/3$ and charge $-1/3$ quarks since multiplets of different chiralities cannot couple together in the Lagrangian. Thus, the MSSM contains two Higgs doublets.

A simple possible extension of the SM, without invoking the presence of supersymmetry, is the introduction of two complex Higgs doublets instead of one:

$$\Phi_1 = \begin{pmatrix} \phi_1^+ \\ \phi_1^0 \end{pmatrix}, \qquad \Phi_2 = \begin{pmatrix} \phi_2^- \\ \phi_2^0 \end{pmatrix}, \tag{1.36}$$

where Φ_1 and Φ_2 have positive hypercharge like the SM doublet, and the superscripts $\pm$ and 0 denote the electric charge of the scalar fields ϕ. The class of models that include two Higgs doublets are referred to as Two-Higgs-doublet models (2HDM) [48]. These models can explain the baryon asymmetry in the universe due to the flexibility of their scalar mass spectrum [49] and the existence of additional sources of CP violation [50]. Those models can as well rotate away the CP-violating term in the QCD Lagrangian. Assuming that CP is conserved in the Higgs sector and that discrete symmetries eliminate from the potential all quartic terms odd in either of the doublets, the most general scalar potential is:

$$\begin{aligned} V = {} & m_{11}^2 \Phi_1^\dagger \Phi_1 + m_{22}^2 \Phi_2^\dagger \Phi_2 - m_{12}^2 (\Phi_1^\dagger \Phi_2 + \Phi_2^\dagger \Phi_1) + \frac{\lambda_1}{2} (\Phi_1^\dagger \Phi_1)^2 + \\ & + \frac{\lambda_2}{2} (\Phi_2^\dagger \Phi_2)^2 + \lambda_3 \Phi_1^\dagger \Phi_1 \Phi_2^\dagger \Phi_2 + \lambda_4 \Phi_1^\dagger \Phi_2 \Phi_2^\dagger \Phi_1 + \frac{\lambda_5}{2} \left[(\Phi_1^\dagger \Phi_2)^2 + (\Phi_2^\dagger \Phi_1)^2 \right], \end{aligned} \tag{1.37}$$

where all parameters are real. The minimisation of the potential gives:

$$\langle \Phi_1 \rangle = \begin{pmatrix} 0 \\ \frac{v_1}{\sqrt{2}} \end{pmatrix}, \qquad \langle \Phi_2 \rangle = \begin{pmatrix} 0 \\ \frac{v_2}{\sqrt{2}} \end{pmatrix}, \tag{1.38}$$

and excitations of the different Higgs fields around their VEVs can be expressed as:

$$\Phi_1 = \begin{pmatrix} \phi_1^+ \\ (v_1 + \rho_1 + i\eta_1)/\sqrt{2} \end{pmatrix}, \qquad \Phi_2 = \begin{pmatrix} \phi_2^- \\ (v_2 + \rho_2 + i\eta_2)/\sqrt{2} \end{pmatrix}, \tag{1.39}$$

with $\rho_i = \mathrm{Re}(\phi_i^0) - v_i$ and $\eta_i = \mathrm{Im}(\phi_i^0)$, $i = 1, 2$. From these eight fields three of them are absorbed to generate the mass of the W and Z bosons and the remaining five correspond to physical Higgs fields: two CP-even scalars h and H with $m_h < m_H$, a pseudoscalar (CP-odd) A, and two charged scalars $H^\pm$. The angles α and β are the rotation angles that diagonalise the mass-squared matrix of the scalars, and the one of the charged scalars and of the pseudoscalars respectively. The single most important parameter of the 2HDM is:

$$\tan\beta \equiv \frac{v_2}{v_1}, \tag{1.40}$$

the ratio of the VEVs of both Higgs doublets. The two parameters α and β determine the interactions of the various Higgs fields with the vector bosons and with the fermions; they are thus crucial in discussing the phenomenology of a 2HDM. A feature of 2HDMs is the possibility of tree-level flavour-changing neutral currents (FCNC) [48]. It is possible to remove FCNCs from the theory by forcing (with the introduction of discrete symmetries) any given type of fermions to couple to not more than one doublet [51]. Table 1.5 shows the possible combinations usually denoted as Type I to Type IV.

	Type I	Type II	Type III	Type IV
$q^i_{R_u}$	ϕ_2	ϕ_2	ϕ_2	ϕ_2
$q^i_{R_d}$	ϕ_2	ϕ_1	ϕ_2	ϕ_1
ℓ^i_R	ϕ_2	ϕ_1	ϕ_1	ϕ_2

Table 1.5: 2HDM Types defined using the fermions fields $q^i_{R_u}$, $q^i_{R_d}$ and ℓ^i_R and their coupling to the Higgs doublets Φ_1 and Φ_2.

1.2.2 Extra dimensions

Several theories propose a spacetime with more than 3+1 dimensions to address some of the shortcomings of the SM. The idea is sketched in figure 1.8: the vertical dimension stands for the 3+1 (infinitely large) dimensions and the fifth dimension is finite, being compactified on a circle of radius R. Our world would correspond to the surface of the cylinder, usually referred to as the "brane". These extra-dimensional models are built to be consistent with all aspects of the SM and the presence of the extra dimension can explain, for example, the apparent weakness of the gravitational force, making gravity diluted in the extra dimensions. The higher-dimensional space is usually referred to as the "bulk" and particles propagating in the compactified extra dimension manifest in a four-dimensional brane as an infinite number of Kaluza-Klein (KK) modes. Extra-dimensional models are classified according to the geometry of the extra dimension: flat or warped.

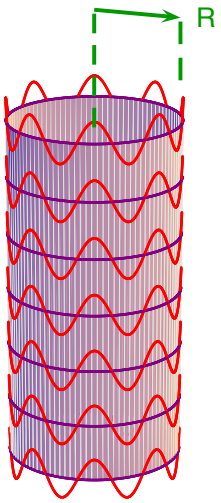

Figure 1.8: Representation of an extra spatial dimension with radius R. From Ref. [52].

1.2.2.1 Flat-extra-dimensions models

In this category of models there are Arkani-Hamed-Dimopoulos-Dvali (ADD) models [53] in which the extra dimension is accessible only to gravity; therefore, the only particle propagating in the bulk is the graviton. It requires two or more extra dimensions with a size R that can range between ~ 1 mm and ~ 1 TeV^{-1}. The "effective" $4D$ Planck mass as a function of the D-dimensional parameters can be expressed as:

$$M_P^2 = M_D^{2+n} R^n, \tag{1.41}$$

where M_D is Planck scale in $D = 4 + n$ dimensions. Fixing M_D at around the electroweak scale to avoid introducing a new scale in the model, many options for the number and the size of the extra dimensions are possible. However, experimental lower bounds on the M_D scale for ADD models are in the range of $4 - 6$ TeV for $2 - 6$ extra dimensions [54], pushing M_D away from the electroweak scale.

Allowing SM particles to propagate in the bulk is a feature of Universal Extra-Dimensional (UED) models [55]. The main challenge for these theories is recovering the SM behavior after compactification of the extra dimensions. One possibility is the existence of two extra dimensions, which are compactified under the real projective plane geometry (RPP) [56, 57], referred to as 2UED/RPP model. In this case, new states can be produced only in pairs and the lightest KK state is stable, leading to a candidate for dark matter.

1.2.2.2 Warped-extra-dimension models

Randall and Sundrum (RS) [58, 59] models use a warped geometry in a five-dimensional Anti-de Sitter (AdS) spacetime with a compactification scale ∼TeV. The origin of the huge difference between the electroweak scale and the Planck scale is explained by the gravitational redshift factor present in the warped AdS metric. The "warp" factor determines how $4D$ scales change as a function of the position in the extra dimension: energy scales for $4D$ fields localised on the infrared (IR) brane are red-shifted compared to the ones on the ultraviolet (UV) brane. Therefore, a natural solution to the hierarchy problem [60] can be achieved in this framework if the Higgs field is localised on the IR brane where the effective mass scales are of order TeV, while SM gauge bosons and fermions can propagate in the $5D$ bulk. In warped-extra-dimensions models the Higgs boson appears as the fifth component of a $5D$ gauge boson and its mass is protected by the $5D$ gauge invariance. In these models there is a light Higgs boson whose mass can be around 125 GeV, but it behaves as a composite pseudo-Nambu-Goldstone boson (see section 1.2.3) with couplings that deviate from those of the SM Higgs boson.

1.2.3 Compositeness

Several times a particle that was believed elementary revealed its composite nature when studied at higher energy scales, e.g. pions, protons and even atoms were considered elementary at some point. Nowadays the idea that some of the SM particles may be composite is a fascinating one, as the discovery of compositeness would radically redefine most of the fundamental questions in particle physics.

This idea developed starting from the not exact (i.e. broken) chiral symmetry in QCD, which produces three Goldstone bosons with a mass, usually referred to as pseudo-Nambu-Goldstone Bosons (PNGB). The three PNGBs are the pions, which are not elementary particles and have a naturally low mass compared to other mesons. Before it was established as a meson, i.e. a quark-antiquark bound state of the strong interaction, the neutral pion was considered an elementary particle, responsible for mediating the strong interaction. The low mass (∼100 MeV) of the neutral pion could, however, not be explained without interpreting it as a meson. This in turn required new particles at the GeV scale,

which were indeed found thereafter. This is the result of strong dynamics that can be reinterpreted in terms of more fundamental degrees of freedom, the quarks.

Some new theories propose that the Higgs boson is a composite PNGB [61–64]. In these theories, a new strongly-interacting sector with a new global symmetry is present at the compositeness scale, usually $\sim$ TeV. A composite light Higgs boson emerges, much like the pion of QCD, as the PNGB of a global symmetry breaking of that sector. The explicit symmetry breaking is induced by interactions of the SM gauge bosons and fermions with the strong sector. Loops of SM fermions and gauge bosons generate a Higgs potential that eventually breaks the electroweak symmetry at scale v, generated dynamically and lower than the strong sector (compositeness) breaking scale. In this scenario the radiative corrections to the Higgs boson mass do not reach the Planck scale since the Higgs boson will reveal its composite nature at the energy scale of the new strong sector. Strongly-interacting theories usually are subject to strong constraints from precision electroweak data, but weakly-coupled models such as the one in section 1.2.2.2 can satisfy such bounds.

Some other theories propose instead that the top quark is composite [65], made of some new constituent particles ("preons") bound together by a new confining force, or a condensed state. Most of those models [66, 67] focus on right-handed top quarks to avoid strong constraints from precision electroweak data.

1.2.4 Vector-like quarks

A fermion is vector-like if left- and right-handed chiralities belong to the same representation of the symmetry group of the underlying theory. Vector-like quarks (VLQs) are triplets under the $SU(3)_C$ gauge group, and so their left- and right-handed components carry the same colour and electroweak quantum numbers [68–71]. VLQs have been introduced in many different BSM scenarios; in composite Higgs models VLQs are part of the condensate that drives the EW symmetry breaking, the excited partners of SM quarks in extra-dimensional models are also vector-like. The presence of VLQs can introduce new sources of CP violation to solve the baryon asymmetry [72] and can also explain the observed A_{FB}^{b} asymmetry through mixing with the bottom quark [73, 74]. The introduction of VLQs also stabilises the Higgs boson mass since the quadratic divergences cancel and only a logarithmic divergence remains. The one-loop contributions to the Higgs boson mass are shown in figure 1.9.

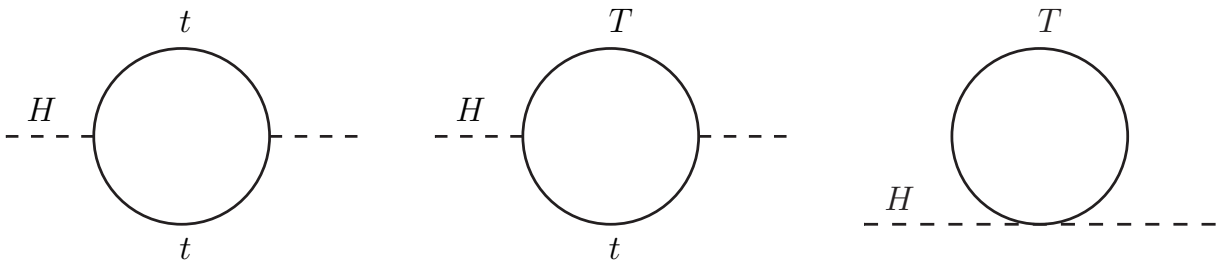

Figure 1.9: One-loop contributions to the Higgs boson mass tern from (a) the top quark and (b, c) a vector-like top-quark partner T.

The mass term $m_f \bar{\Psi}_f \Psi_f$ of a VLQ f is gauge invariant under $SU(2)_L \otimes U(1)_Y$, i.e. its mass is generated without the need for a Yukawa interaction with the Higgs boson. Therefore, there are no constraints on the existence of VLQs arising from the measured Higgs boson production cross section,

since the contribution to loop-induced Higgs boson couplings, ggH and $\gamma\gamma H$, is suppressed by the heavy quark mass. Classifying VLQs in multiplets of $SU(2)_L$, it is possible to write gauge-invariant interaction terms only for singlets, doublets and triplet representations, shown in table 1.6.

	Singlets		Doublets			Triplets	
	(U)	(D)	$\begin{pmatrix} X \\ U \end{pmatrix}$	$\begin{pmatrix} U \\ D \end{pmatrix}$	$\begin{pmatrix} D \\ Y \end{pmatrix}$	$\begin{pmatrix} X \\ U \\ D \end{pmatrix}$	$\begin{pmatrix} U \\ D \\ Y \end{pmatrix}$
$Y/2$	$2/3$	$-1/3$	$7/6$	$1/6$	$-5/6$	$2/3$	$-1/3$
$\mathcal{L}_{\text{Yukawa}}$	$-\lambda_u^i \bar{q}_L^i H^c U_R$ $-\lambda_d^i \bar{q}_L^i H D_R$		$-\lambda_u^i \psi_L H^{(c)} u_R^i$ $-\lambda_d^i \psi_L H^{(c)} d_R^i$			$-\lambda_i \bar{q}_L^i \tau^a H^{(c)} \psi_R^a$	

Table 1.6: VLQs in different $SU(2)_L$ representations with hypercharge quantum number and Yukawa mixing terms in the Lagrangian. Depending on the chosen representation, the Higgs boson may be H or H^c; therefore, it has been noted as $H^{(c)}$ when necessary.

The mass eigenstates are labelled as X, T, B, and Y with an electric charge of $+5/3$, $+2/3$, $-1/3$, $-4/3$ respectively. The left-right symmetry of VLQs allows for tree-level flavour changing neutral currents, which are their distinctive feature. In order to be consistent with precision electroweak data, a small mass splitting between VLQs belonging to the same $SU(2)_L$ multiplet is required [68], which forbids cascade decays such as $T \to WB$, and leaves direct decays into SM particles as the only possibility. VLQs interact with SM quarks and the Higgs boson through Yukawa couplings. VLQs can mix with the SM quarks; the mixing occurs in the left-handed sector for the singlet and triplet representations and in the right-handed sector for the doublet representation. The mixing of a VLQ and a SM quark is of the order $\sim m_q/M_Q$, where M and m are the masses of the VLQ and the SM quark respectively. Thus VLQs are expected to predominantly mix with the third SM generation, while mixing with lighter SM generations is mass suppressed. Under this assumption, the only possible decays for VLQs are into top / bottom quark plus a W, Z or Higgs boson. For the quarks with exotic charges the only decay channels are $X \to W^+ t$ and $Y \to W^- b$, while the heavy quarks with charges $+2/3$ and $-1/3$ the possible channels are respectively:

$$T \to W^+ b,\ Zt,\ Ht \quad \text{and} \quad B \to W^- t,\ Zb,\ Hb. \tag{1.42}$$

The branching ratios for different channels have some dependence on the heavy quark masses and on the $SU(2)_L$ representation. For singlets all decay modes are possible, while for doublets the branching ratio depend on the relative size of the mixing factor of the extended CKM matrix V_{Tb} and V_{tB}. In this dissertation the scenario where $V_{Tb} \ll V_{tB}$ is assumed. Thus the mixing of the heavy quarks with the SM top quark is much stronger, and the $T \to Wb$ decay is suppressed, as well as $B \to Hb$ and $B \to Zb$. Table 1.7 summarises the possible decays modes for VLQs. Figure 1.10 shows the decay branching ratios of the vector-like top and bottom partners for singlets and doublets as a function of the heavy-quark mass.

VLQs can be produced either in pairs through the strong interaction or as single quarks in association with SM quarks or bosons through the weak interaction [75]. Pair production is model independent since it just depends on the VLQ mass, while single production depends on the strength of VLQ coupling to SM quarks, and thus is model dependent. However, pair production suffers from a

Singlets	Decay modes	Doublets	Decay modes	Triplets	Decay modes
X	W^+t	$\begin{pmatrix} X \\ T \end{pmatrix}$	W^+t $Ht,\ Zt$	$\begin{pmatrix} X \\ T \\ B \end{pmatrix}$	W^+t $W^+b,\ Ht,\ Zt$ $Hb,\ Zb$
T	$W^+b,\ Ht,\ Zt$				
B	$W^-t,\ Hb,\ Zb$	$\begin{pmatrix} T \\ B \end{pmatrix}$	$Ht,\ Zt$ W^-t	$\begin{pmatrix} T \\ B \\ Y \end{pmatrix}$	$Ht,\ Zt$ $W^-t,\ Hb,\ Zb$ W^-b
Y	W^-b	$\begin{pmatrix} B \\ Y \end{pmatrix}$	$Hb,\ Zb$ W^-b		

Table 1.7: Allowed decay modes for vector-like singlets, doublets and triplets.

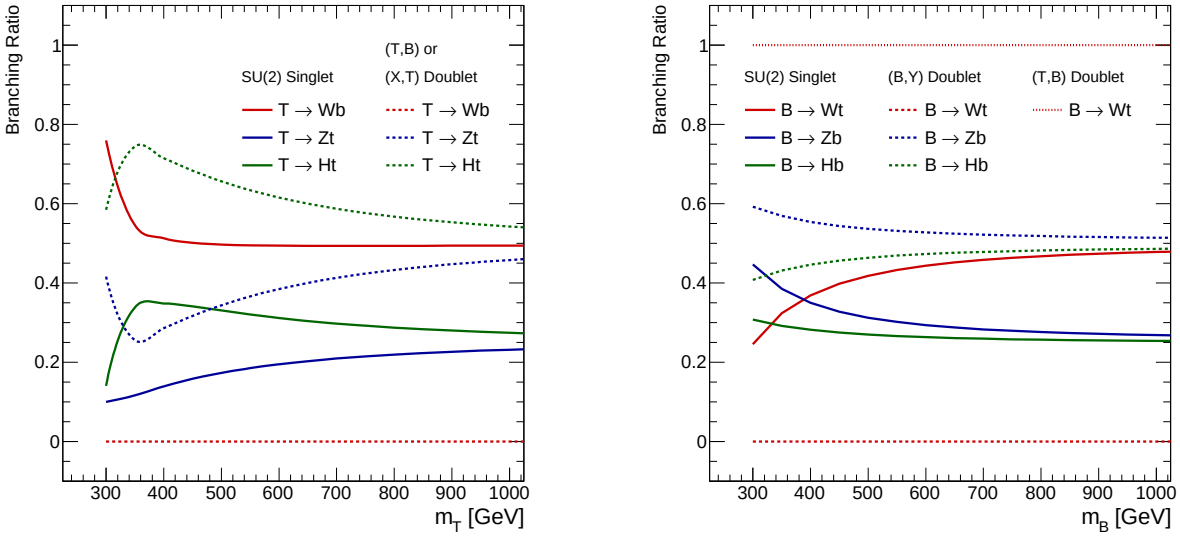

(a) (b)

Figure 1.10: Branching ratios for vector-like (a) top and (b) bottom partners as function of the heavy quark mass m_T and m_B respectively for singlets and doublets. From Ref. [68]

larger phase-space suppression with respect to single production, and if the VLQ mass is large enough ($\sim$ TeV), single production may dominate over pair production. Example Feynman diagrams at the tree level for pair and single production of vector-like T-quark are shown in figure 1.11. Figure 1.12 shows the cross section for pair production and single production in the t-channel as a function of VLQ mass.

1.2.5 Anomalous four-top-quark production

The cross section of four-top-quark events predicted by the SM (see figure 1.13a) is extremely small, $\sigma_{t\bar{t}t\bar{t}} = 9.2$ fb at $\sqrt{s} = 13$ TeV [76]. However, in many BSM models, the four-top-quark production is enhanced, usually through the pair production of a new particle decaying to a top-antitop pair.

For example, a possible source of enhancement of the $t\bar{t}t\bar{t}$ cross-section appears in extra-dimensional models. In this framework the four-top-quark signal is an important probe for low-scale warped extra

(a) (b)

Figure 1.11: Representative leading-order Feynman diagrams for vector-like top (a) pair-production and (b) single-production modes.

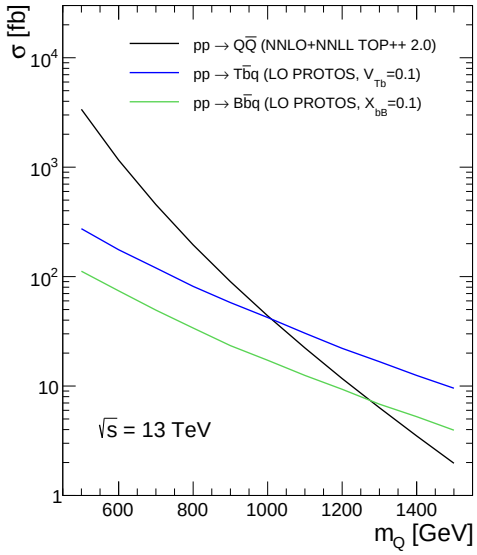

Figure 1.12: Production cross sections for pair and single production of VLQs in pp collisions at $\sqrt{s}$ =13 TeV. Pair production is computed at NNLO+NNLL order in QCD using Top++ 2.0 while single production is computed at LO in QCD with Protos assuming $V_{Tb} = 0.1$ and $X_{bB} = 0.1$.

dimensions [77]; the enhancement comes from a heavy gluon that can be pair produced and decay into $t\bar{t}$ or via associate production of the heavy gluon with $t\bar{t}$. In flat-extra-dimensions models, such as 2UED/RPP, the enhancement is caused by the lightest particle of the tier (1,1), i.e. the vector photon $A_\mu^{(1,1)}$. In these models to each SM fields corresponds a tower of massive resonances organised in tiers, labelled by two integers (ℓ, k) that correspond to the discretised momenta along the extra dimensions. At leading order, all the states in each tier are degenerate with mass determined by the two integers:

$$m^2 = \frac{\ell^2}{R_5^2} + \frac{k^2}{R_6^2} \tag{1.43}$$

where R_5 and R_6 are respectively the size of the two extra dimensions. For the tier (1,1) its mass is given by $M^{(1,1)} = \sqrt{1/R_5^2 + 1/R_5^2} \sim \sqrt{2}M_{KK}$; assuming the two extra dimensions have the same size, and where $M_{KK} = M^{(0,1)} = M^{(1,0)}$. The production of any heavy state of the tier (1,1) contributes

to the production of vector photons since it will undergo chain decays until the lightest state[4] (see figure 1.13b). Therefore, the production cross section of vector photons can be sizeable even though their couplings to quarks and gluons are small. The branching ratios of $A_\mu^{(1,1)}$ into SM particles are not predicted by the model, although the decay into $t\bar{t}$ is expected to be dominant [78].

It is also possible to parametrise new physics, maybe not accessible at LHC, leading to four-top-quark production using the language of effective field theory with higher-dimensional operators. This approach is used by composite top quark scenarios or RS models, in which, below the new physics scale, phenomena are described by an effective field theory containing the bound states of the new sector. A dimension-six Lorentz-invariant operator with a four-point interaction (see figure 1.13c) that involves only right-handed top quarks, t_R, can be considered:

$$\mathcal{L}_{4t} = \frac{C_{4t}}{\Lambda^2}(\bar{t_R}\gamma_\mu t_R)(\bar{t_R}\gamma_\mu t_R) \tag{1.44}$$

where Λ is the scale where new physics will manifest, and C_{4t} is the effective coupling. The effective field theory approach is valid for $|C_{4t}| < 4\pi$. In this framework right-handed top quarks are chosen because of the strong constraints coming from precision electroweak data on operators involving left-handed ones.

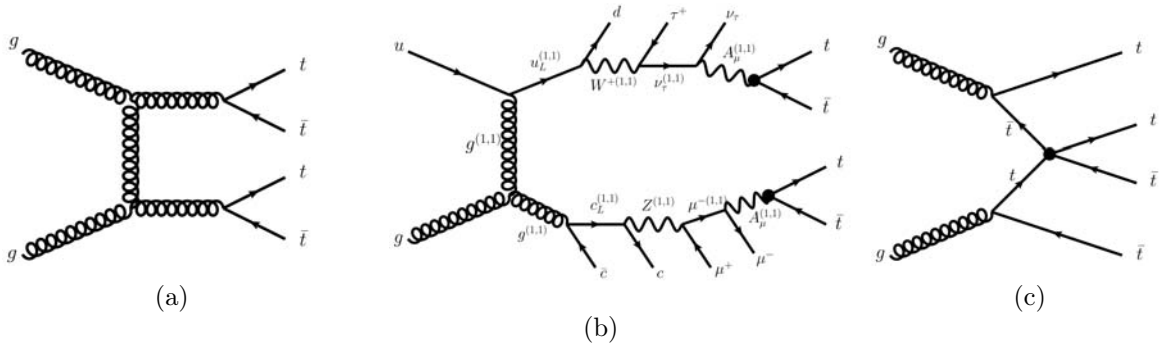

Figure 1.13: Representative leading-order Feynman diagrams for four-top-quark production within (a) the SM and several BSM scenarios: (b) via cascade decays from Kaluza-Klein excitations in a universal extra dimensions model with two extra dimensions compactified using the geometry of the real projective plane, and (c) via an effective four-top-quark interaction in an effective field theory model.

[4]The SM particles radiated in the chain decay are soft due to the typically small mass differences between states in the tier, and therefore they will easily escape detection.

2

The ATLAS experiment at the Large Hadron Collider

Nos esse quasi nanos gigantium humeris insidentes.
Bernardus Carnotensis

Contents

Exploring the TeV energy scale requires particle accelerators and the corresponding experiments to be designed and built for this purpose. The first part of this chapter describes the world's largest and most powerful particle accelerator, the Large Hadron Collider (LHC), with a particular emphasis on the evolution of the running parameters over the past years of operation. The second part of this chapter is focused on the ATLAS detector, one of the four large experiments studying the high-energy

collisions produced by the LHC. An overview of its subdetector components and their performance is also provided.

2.1 The Large Hadron Collider

The LHC [79] is a circular proton-proton collider located at the European Council for Nuclear Research (CERN). The machine is hosted in a 27 km circumference tunnel built between 50 m and 170 m underneath the French-Swiss countryside outside Geneva. Not only it is the world's largest collider but, with the current operation at a beam energy of 6.5 TeV and its expected upgrade to the design energy of 7 TeV, it is also the most powerful. It was designed to extend the reach of previous accelerators in the study of SM processes and searches for new phenomena.

The centre-of-mass energy increased by an order of magnitude with respect to the Tevatron collider at Fermilab [80], while the high instantaneous luminosity (up to 10^{34} cm^{-2}s^{-1}) allows access to very rare processes and precision measurements. These considerations ultimately motivated the choice of a proton-proton collider. For protons the energy loss in a curved trajectory due to synchrotron radiation[1] is considerably smaller than for electrons and this allows accelerating protons more efficiently in a circular machine. At the same time, a hadron collider probes multiple energy scales simultaneously due to the momentum distribution of partons inside the protons. A proton-antiproton collider alternative was rejected due to the difficulties of producing and operating high-intensity anti-proton beams, which would have resulted in a lower peak luminosity. The LHC is also able to accelerate and collide lead ions at the nominal energy of 2.76 TeV/nucleon, for a total centre-of-mass energy of 1.15 PeV.

2.1.1 CERN accelerator complex

As for any other large particle collider, the energy of the colliding particles is gradually increased by subsequent acceleration steps; this solution has high flexibility and allows for a more efficient beam production. At the same time, intermediate accelerator machines provide beams that are used in other lower-energy experiments. A sequence of accelerators, shown in figure 2.1, is involved in the preacceleration of the protons before they are injected into the LHC ring [81].

Protons are obtained from hydrogen gas by breaking the molecules and stripping the electrons from hydrogen atoms. Protons are accelerated in the Linear Accelerator 2 (LINAC2) to 50 MeV and grouped in bunches. They are then transferred to the 157 m long Proton Synchrotron Booster (PSB), where they reach an energy of 1.4 GeV. After the PSB, protons are injected into the 628 m long Proton Synchrotron (PS), where their energy is ramped up to 25 GeV. In both the PSB and the PS protons are squeezed in very tight bunches that are the base bunch structure of the LHC. The last stage of preacceleration is done in the 7 km long Super Proton Synchrotron (SPS), where the protons are brought to an energy of 450 GeV before injection into the LHC ring in two opposite directions. The connection between the LHC and the SPS is done through two 2.5 km long transfer lines.

2.1.2 LHC design and machine parameters

One of the main contraints to reduce the cost of the LHC construction was the need to reuse the tunnel previously hosting the Large Electron Positron Collider (LEP). The technological challenge of the LHC was the mass production of magnets necessary to maintain 7 TeV protons in a circular trajectory with

[1] The energy emission per turn is proportional to $(E/m)^4$, where E and m are the energy and mass of the particle respectively.

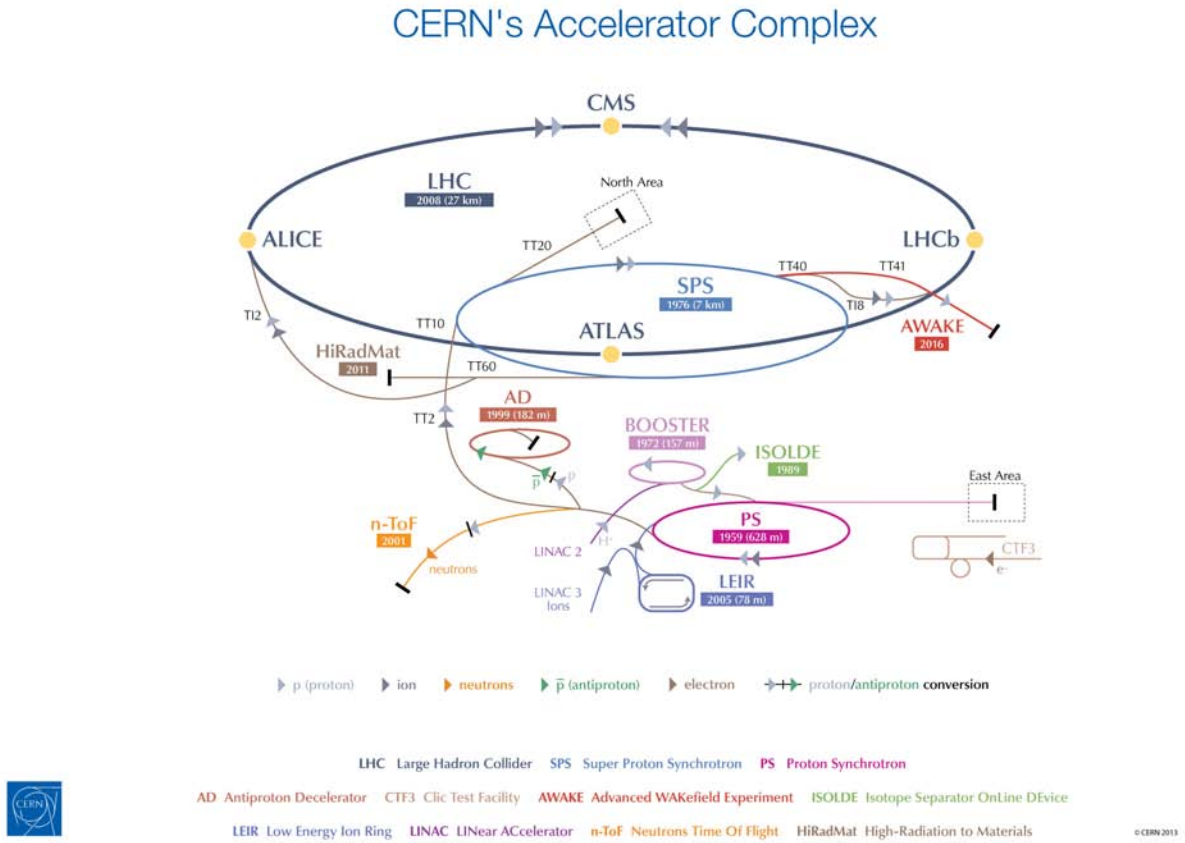

Figure 2.1: Schematic view of the CERN accelerator complex. The four main LHC experiments are shown at the interaction points.

a radius of 4.3 km. A total of 1232 dipole magnets have been assembled in the LHC. Each magnet produces a bending field of up to 8.33 T thanks to superconducting coils made of niobium-titanium (NbTi) kept at a temperature of 1.9 K by superfluid helium. This makes the LHC the largest cryogenic system in the world. Each dipole contains two vacuum chambers in one single cryostat with magnetic fluxes that go in opposite directions, which allows the acceleration of two proton beams in opposite directions. This structure was needed to reduce the size of the cryostat and the cost of the cryogenic system. The main acceleration from 450 GeV to a maximum of 7 TeV happens in the LHC with eight resonant Radio-Frequency (RF) cavities per beam. The electric field of those RF cavities oscillates at 400 MHz and increases the beam energy by 0.5 MeV/ turn. The field intensity at the maximum energy is around 5.5 MV/m.

One of the important aspects in the design of an accelerator is the overall interaction rate that the LHC, in our case, can provide to the experiments. The cross section, σ, describes the likelihood for a certain reaction - the effective area that one particle presents to another particle for that reaction to occur. The instantaneous luminosity, $\mathcal{L}(t)$, describes how frequently particles encounter each other, per unit of area and time. The overall interaction rate is equal to $\sigma \times \mathcal{L}(t)$. The total number of interactions for a certain process in a time interval $[t_1,t_2]$, is given by:

$$N_{\text{proc}} = \int_{t_1}^{t_2} \sigma_{\text{proc}} \times \mathcal{L}(t)dt = \sigma_{\text{proc}} \times \mathcal{L}_{\text{int}}(t_1, t_2) \tag{2.1}$$

where it is assumed that the cross section σ_{proc} does not depend on time and where $\mathcal{L}_{\text{int}}(t_1, t_2)$ is the integrated luminosity for the time interval $[t_1,t_2]$. The requirement of high statistical accuracy of the data is translated into a requirement of high integrated luminosity of the accelerator. The instantaneous luminosity of the LHC at any Interaction Point (IP) depends on the beam bunch structure, the beam parameters and how well they can be controlled. For beams with equal parameters and approximately Gaussian spatial distributions, the instantaneous luminosity can be expressed as:

$$\mathcal{L} = N_b \cdot F \frac{n^2 f_{\text{rev}}}{4\pi\sigma_{xy}}, \sigma_{xy} = \sqrt{\frac{\varepsilon\beta^*}{\gamma}} \tag{2.2}$$

where N_b is the number of bunches present in each beam, n is the number of protons in each bunch, σ_{xy} is the transverse beam size at the IP, f_{rev} is the revolution frequencies of the bunches, γ is the Lorentz factor, β^* is the betatron function at the collision point, ε the normalised beam emittance and F is a geometric luminosity reduction factor that takes into account the beam crossing angle at the IP. The LHC beam parameters have been optimised to maximise the instantaneous luminosity at each IP taking into account various performance limitations and machine boundary conditions.

Due to the high frequency of collisions and the high density of the bunches necessary to achieve high luminosity, there is a non-zero probability that several events, originating from different pp collisions, may occur simultaneously. These events are referred to as *pileup* and are categorised as in-time or out-of-time pileup. In-time pileup events are caused by additional pp interactions in the same bunch crossing. The out-of-time pileup occurs when traces from an event in a different bunch crossing are recorded. The mean number of interactions per bunch crossing $\langle\mu\rangle$, which is taken as measure of the pileup activity, is shown in figure 2.2. The instantaneous luminosity is not constant over time, slowly degrading due to the bunch collisions, multiple Coulomb scattering within each bunch, and the scattering of protons against residual gas atoms inside the beam pipe. Therefore, the integrated luminosity depends on the luminosity lifetime, defined as the time that the beams are left orbiting in the LHC, and the beam turn-around time, defined as the time that passes between the beams being dumped and the beams being stable and ready for collisions again. More details about the LHC performance can be found in Ref. [82].

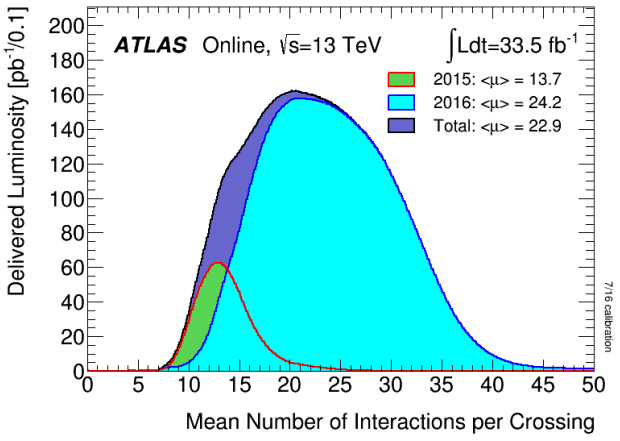

Figure 2.2: Average number of interactions per beam crossing during the 2015 and 2016 LHC runs.

2.1.3 LHC experiments

The LHC beams cross in four IPs, in each of which a particle detector is installed to record the collisions. Earlier infrastructures, with some modifications to accommodate the LHC, were reused in order to further reduce the costs. Two of them are hosted in sites where before there were LEP experiments, while for the other two IPs new sites were needed. ATLAS [83] and CMS [84] are general-purpose experiments located at opposite IPs in the LHC ring. The independent design of the two experiments is of primary importance since it allows for cross-confirmation of measurements and possible new discoveries. LHCb [85] is a single-arm spectrometer designed to cover the forward region to perform dedicated studies of CP violation in B-meson decays and other studies of flavour physics, while ALICE [86] is designed to explore the formation of quark-gluon plasma in collisions of heavy ions. In addition to these four large experiments, three smaller experiments, LHCf [87], TOTEM [88] and MoEDAL [89], are placed in the LHC ring. The LHCf experiment has been designed to study neutral hadrons emitted at low angles with respect to the beam pipe and it has been installed in the vicinity of ATLAS. CMS hosts TOTEM, which measures the total cross section through elastic and diffractive scattering of protons. The MoEDAL experiment is placed near LHCb and its purpose is to search for massive long-lived particles and magnetic monopoles.

2.1.4 From first beam to world's record energy and luminosity

After almost 15 years of prototyping the required technologies and an additional eight years of installation and commissioning of collider components, the LHC was officially completed and ready to start on the 10th of September 2008. Unfortunately, a serious accident occurred on the 19th of September, and the LHC operation had to be postponed and rescheduled. A faulty electrical connection between two magnets ceased to be superconducting, causing mechanical failure of the cryogenic vessel followed by the leakage of around six tonnes of liquid helium. A total of 53 magnets were damaged and vacuum conditions in the beam pipe were lost. A total of 20 dipoles were replaced with spares, and new techniques to prevent a similar incident were developed. In December 2009 the LHC delivered first beams at the world energy record of 1.18 TeV. The new plan established that the LHC should provide proton beams of 3.5 TeV during its initial operation from 2010 until 2012, and that it would be prepared to operate with proton beams of 7 TeV only after a long shut-down period in 2013 and 2014.

In March 2010, Run 1 of the LHC started with the first collisions at a beam energy of 3.5 TeV, setting a new record for the energy achieved at a particle collider. The centre-of-mass energy was kept at 7 TeV also during all of 2011. For the 2012 data taking the beam energy was increased to 4 TeV, for a center-of-mass energy of 8 TeV. In early 2010 the peak luminosity reached 2×10^{32} $\mathrm{cm}^{-2}\mathrm{s}^{-1}$ obtained with 348 colliding bunches of approximately 0.9×10^{11} protons each with a bunch spacing of 150 ns. In 2011 the peak luminosity reached 3.7×10^{33} $\mathrm{cm}^{-2}\mathrm{s}^{-1}$, increasing the number of bunches to 1380 with a minimum separation of 50 ns and the number of protons per bunch to 1.45×10^{11}. A further increase in luminosity was achieved by reducing the beam transverse size at the IP in order to increase the probability of pp collisions per crossing. In 2012 a further reduction of the beam transverse size and an increase to the bunch intensity to 1.3 times the designed value allowed to reach a peak luminosity of 7.7×10^{33} $\mathrm{cm}^{-2}\mathrm{s}^{-1}$. During the long shutdown (LS1), started on the 16th of February 2013, all electrical connections between superconducting magnets were consolidated allowing LHC to reach higher energy and luminosity during Run 2. In figure 2.3 a summary of LHC maintenance carried out during LS1 is shown.

In June 2015 LHC Run 2 started recording the first collisions at a beam energy of 6.5 TeV, setting a new record. During the year the number of bunches was increased up to 2244 with a minimum separation of 25 ns. For 2016 data taking the LHC achieved the current luminosity record for a

hadron machine of 1.1×10^{34} cm^{-2}s^{-1} by further reducing the beam transverse size. Table 2.1 shows the values of the beam parameters for the design operation, as well as those used during Run 1 and early Run 2 data taking.

Figure 2.3: The main LHC consolidations during LS1.

2.2 The ATLAS experiment

ATLAS (A Toroidal Lhc ApparatuS) [83], is a multi purpose detector designed to measure particles produced in pp collisions at unprecedented energies and instantaneous luminosities. The guidelines in the detector construction and specifications were driven by the goals of maximising the discovery potential for new phenomena while keeping the ability to perform precise measurements of known processes [90]. Among the priorities of the experiment was the search for the Higgs boson (and the measurement of its properties) as well as the search for new exotic (e.g. supersymmetric) particles that might be part of possible extensions of the SM. Furthermore the luminosity delivered by the LHC allows to collect a very large sample of vector bosons (W and Z), B-mesons and top quarks which gives the possibility to perform detailed studies on QCD, CP violation and top quark properties. At the same time, the possibility to observe unexpected phenomena demanded a very flexible design, not excessively tied to a specific physics model. For this reason, the detector is required to identify and measure the kinematic properties of a large spectrum of particles that are produced in pp collisions over a wide energy range (from few GeV to TeV). This includes charged leptons (electrons, muons, taus), photons, jets produced by the hadronisation of quarks and gluons, as well as particles that escape

Parameter	Design value	Run 1	2015	2016
Beam energy (TeV)	7	3.5–4	6.5	6.5
Beta function β^* (m)	0.55	1.5–0.6	0.8	0.4
Maximum num. bunches/beam	2808	1380	2244	2220
Max. num. protons/bunch	1.15×10^{11}	$(1.45 - 1.7) \times 10^{11}$	1.15×10^{11}	1.3×10^{11}
Bunch spacing (ns)	25	75–50	50–25	25
Peak luminosity ($\mathrm{cm}^{-2}\mathrm{s}^{-1}$)	1×10^{34}	7.7×10^{33}	6×10^{33}	1.4×10^{34}
Emittance $\varepsilon_n(\mu\mathrm{rad})$	3.75	2.5	2.5	2.5
Max. $\langle\mu\rangle$	19	37	30	50

Table 2.1: Overview of the LHC beam parameters comparing the design values with their time evolution during Run 1 and early Run 2 operations.

'direct' detection like neutrinos and other new weakly-interacting particles. These latter are identified through the measurement of transverse-momentum imbalance in the event, the missing transverse energy ($E_{\mathrm{T}}^{\mathrm{miss}}$).

A schema of the ATLAS detector is shown in figure 2.4 . It measures 44 m in length and 25 m in diameter for a total weight of 7000 tons. Like most collider detectors, ATLAS has a cylindric geometry to cover the full solid angle around the interaction point with the various subdetectors arranged in concentric layers. Starting from the centre, the Inner Detector (ID) is designed to reconstruct the trajectories of charged particles (tracks) and measure their momenta from the radius of curvature in a solenoidal magnetic field. The ID is surrounded by an electromagnetic and a hadronic calorimeter that measure the energies of electrons/photons and hadrons by detecting the showers produced by the particles' interactions with their absorber materials. Muons are the only directly-detectable particles that pass through the thick calorimeter. They are detected with a spectrometer embedded in a toroidal magnetic field.

The following specifications have been taken into account in the construction of the detector :

- efficient track reconstruction and good track momentum resolution;
- precise measurement of track quantities and secondary vertices for the identification of jets produced by b-/c-quarks and τ-leptons;
- an electromagnetic calorimeter with excellent angular and energy resolution for the measurements of electrons and photons;
- a hermetic hadronic calorimeter with large angular coverage for the measurement of jets and missing transverse energy;
- good muon identification and momentum reconstruction up to highest luminosity with the possibility to determine the charge of high-p_{T} muons;
- large acceptance in pseudorapidity (η) with almost full azimuthal angle (ϕ) coverage;
- a flexible trigger system capable of maintaining high selection efficiency and sufficient background rejection even for low-/medium-p_{T} objects.

In addition to these requirements, specific conditions from the LHC operation pose additional constraints on the detector design. Due to the high interaction rate of 40 MHz, fast electronics is employed in the readout of all sub detectors, while the large number of interactions per crossing and the consequent large particle flux requires sensors resistant to high-radiation doses. At the same time, highly-granular detectors are required to reduce the impact of overlapping interactions.

2.2.1 Coordinate system

The ATLAS coordinate system is right-handed in which x-axis points to LHC's center, the z-axis follows the beam direction and the y-axis points upwards away from the centre of the Earth. The origin of the coordinate system is defined by the nominal interaction point of the beams. The region delimited by positive values of the z coordinate, is referred to as "A side", while the region with negative values is referred to as "C side". At hadron colliders spherical coordinates are commonly used. The azimuthal angle ϕ is measured around the beam axis, ranging between $-\pi$ and $+\pi$ with respect to the x-axis. The polar angle θ is measured with respect to the z-axis and ranges between 0 and π. Since the momentum of the colliding partons along the z-axis is unknown, it is useful to define the transverse component of variables of interest, like energy and momentum, defined as the projection on the xy plane, which are boost-invariant along the z-axis:

$$p_T = \sqrt{p_x^2 + p_y^2} = \vec{p}\sin\theta\,, E_T = E\sin\theta. \tag{2.3}$$

Another angular quantity, boost-invariant along the z-axis as well, known as pseudorapidity η is defined as:

$$\eta = -\ln\left(\tan\frac{\theta}{2}\right). \tag{2.4}$$

The angular separation in the η-ϕ plane between particles is defined as:

$$\Delta R = \sqrt{(\Delta\eta)^2 + (\Delta\phi)^2}. \tag{2.5}$$

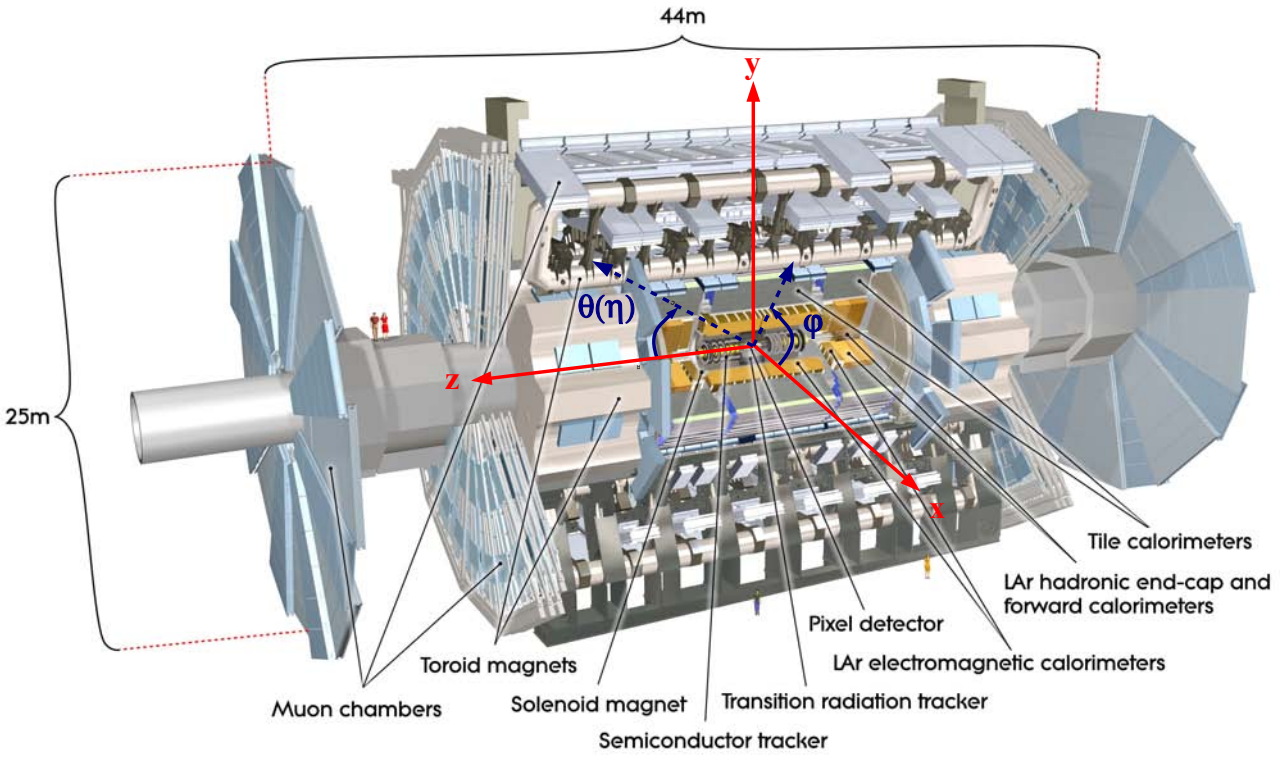

Figure 2.4: View of the ATLAS detector along with the coordinates system.

2.2.2 Magnet system

The magnet system [90] represents a particular characteristic of the ATLAS experiment that has a peculiar design compared to other high-energy physics experiments. It is composed of four large superconducting magnets, cooled with liquid helium at 4.5 K, designed to provide a field mostly orthogonal to the particle trajectory. It consists of a central solenoid and three open-air toroids, as shown in figure 2.5. This hybrid solution has the advantage of extending the pseudorapidity coverage ($|\eta| < 3$), and having no magnetic field inside the calorimeters in order not to degrade their performances. Furthermore, The open-air design for the toroids reduces the impact of multiple scattering on the momentum resolution and improves the muon reconstruction without relying on the Inner Detector.

The central solenoid (CS) provides a magnetic field to the Inner Detector parallel to the beam axis bending particles in the ϕ direction. The CS is 5.3 m long and it has a radius of 2.5 m. The coil of the CS was designed to be the thinnest possible to limit the amount of material in front of the calorimeters, but still thick enough to ensure safety and reliability during operation. Also to minimise the amount of material in front of the calorimeter, one cooling cryostat is shared between the CS and the Liquid Argon Calorimeter. The magnetic field is 2 T with a peak of 2.6 T on the superconductor. As the distance from the interaction point increases in the z direction, the field strength decreases as result of the finite size of the solenoid.

The toroidal system generates the field necessary to bend particles in the muon spectrometer. The system is composed by two End-Cap Toroids (ECT) at the extremities of the detector and a Barrel Toroid (BT) centrally located around the calorimeters. The ECT are 5 m long and have an external diameter of 10.7 m, while the BT is 26 m long with a diameter of 20 m. Each toroid is composed of eight rectangular coils arranged in the radial direction from the beam axis. The ECT are rotated by 22.5° with respect to the BT in order to generate a radial overlap for a higher magnetic field uniformity and to optimise the bending power in the transition regions. Each coil of the BT has its own cryostat, while for the end-cap toroids all the coils are in the same cryostat that is shared with the forward calorimeter. The magnetic fields generated by the BT and ECT are 3.9 T and 4.1 T respectively.

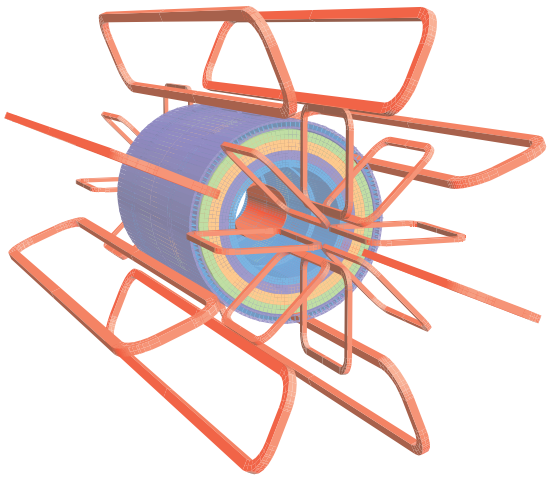

Figure 2.5: The ATLAS magnet system. The eight coils of the barrel and end-cap toroids are visible. The solenoid is inside the calorimeter and it is shown as four layers with different magnetic properties.

2.2.3 Inner detector

The ATLAS Inner Detector (ID) [90] is designed to provide efficient pattern recognition and good momentum resolution for charged particles in the range $|\eta| < 2.5$ from p_T as low as 0.4 GeV up to a few TeV. At the same time, its capability of precisely reconstructing primary and secondary vertices and measuring the track parameters is of primary importance for identifying the decays of short-lived particles. A precise measurement of the particle curvature in the solenoidal magnetic field requires a good spatial resolution. In presence of a high density of particles emerging from the interaction point, this can be achieved only with high granularity. The chosen configuration results from a compromise between high performance, economical budget and amount of material used in the tracker. A large amount of material can in fact degrade the intrinsic momentum resolution due to multiple scattering, as well as the performance of the calorimeter. The overall thickness of the ID is about 0.4 radiation lengths (X_0) and increases up to 1.5 X_0 in the forward region due to the presence of services (e.g. cables for the electronic boards and the cooling system). The structure of the ID is shown is figure 2.6. It combines three different technologies reflecting the different track densities that can be found when increasing the distance from the interaction point. High-resolution detectors are located in the innermost region using semiconductor technology. At larger distance from the interaction point, a detector with lower intrinsic resolution, a transition radiation detector based on drift tubes, allows to collect a larger number of measurements working in a continuous tracking mode. The three components are:

- Pixel Detector,
- SemiConductor Tracker (SCT),
- Transition Radiation Tracker (TRT).

In the barrel the layers of each subdetector are composed of concentric cylinders oriented in the direction of the beam axis while in the forward region are composed of disks/wheels arranged orthogonally to the beam direction. The ID is 7 m long and it has an external radius of 1.15 m, fully contained in the CS. The relative precision of the three subdetectors is comparable so that no single measurements dominates the momentum resolution. This redundancy also guarantees high efficiency even in case a part of one of the subdetectors is malfunctioning. Combining the information from the three subdetectors, the ID reaches a designed resolution of the track momentum of:

$$\frac{\sigma_{p_T}}{p_T} = 0.05\% \times p_T(\text{GeV}) \oplus 0.1\%. \tag{2.6}$$

2.2.3.1 Pixel detector

The silicon pixel technology is the only solution that guarantees good pattern recognition performance in a very dense track environment such as the one close to the LHC interaction point. The ATLAS Pixel detector has been designed to provide at least four precise hits for the track reconstruction in the proximity of the interaction point; the precise reconstruction of the primary vertex makes use as well of those hits. The pixel detector with its design and location is also important for measurement of the track impact parameter, which is defined as the minimum distance of the track to the primary vertex. This is one of the main quantities used in the identification of B/D-hadrons and τ-leptons. The resolution on the track impact parameter is completely dominated by the performance of the pixel detector. The detector is organised in a barrel and two end-caps. The barrel is composed of four cylinders: the layer closest to the beam pipe is 62 cm long and has a radius of 3.325 cm (Insertable

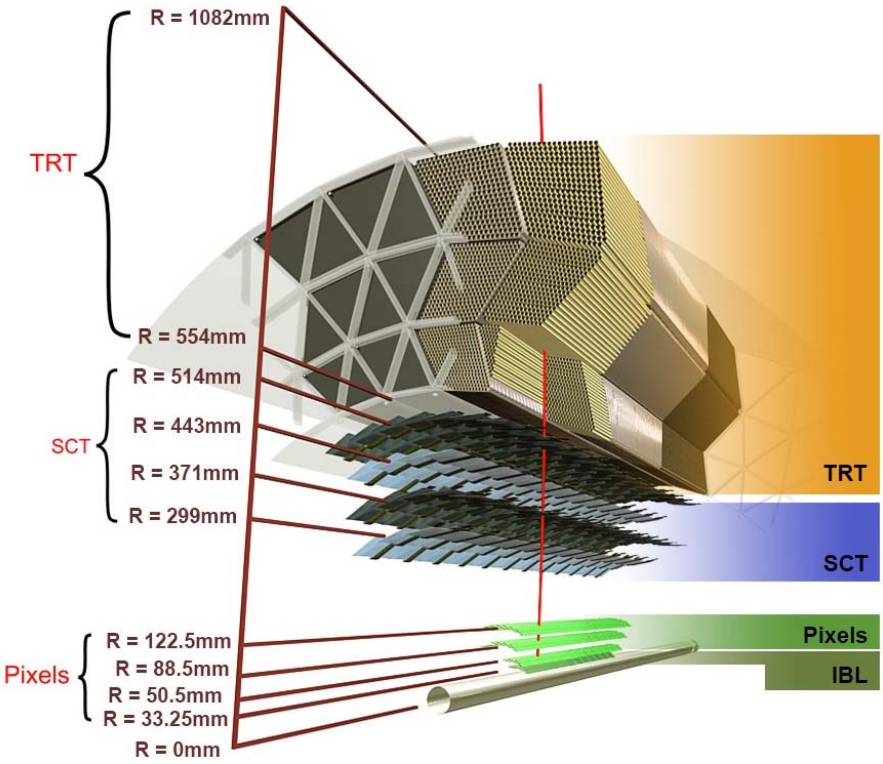

Figure 2.6: Representation of the structure of the Inner Detector and its three subdetectors.

B-Layer) [91], installed during the long shutdown (LS1), and the three outer cylinders are 80 cm long and have radii of 5.05 cm (B-Layer), 8.85 cm (Layer 1) and 12.25 cm (Layer 2). Each end-cap contains three disks with a radius of 34 cm placed at distances of $|z| = 49.5$, 58.0 and 65.0 cm from the centre of the detector. To obtain high granularity the silicon chips are segmented in a matrix of pixels allowing simultaneous measurements of the two spatial coordinates. The dimension of the single pixel is 50×250 μm^2 and 50×400 μm^2 respectively for the IBL and the other layers. The shortest dimension of the sensor is aligned in the direction of the bending plane of the particle in order to achieve the best performance. The average position resolution is equal to 10 μm in the direction of the short pixel pitch and 65 (115) μm in the direction of the long pixel pitch for the IBL (three outer layers). The basic unit of the detector is the module, which contains the silicon sensor and the required electronics. The matrix in each module has 80 pixels and 144×328 pixels respectively in the IBL and the other layers. In total ~ 2500 modules were assembled in the barrel and endcap for a total of 92 million channels. The pixel detector needs high thermal stability to keep good performance and a low temperature to minimise radiation damage. The IBL temperature during 2015 and 2016 was kept between $-15\,^{\circ}$C and $5\,^{\circ}$C. The other layers are kept at temperature between $-10\,^{\circ}$C and $-15\,^{\circ}$C.

2.2.3.2 Semiconductor tracker

The SCT has been designed to provide at least eight precise points per track. Thanks to its high granularity, it contributes to the track reconstruction and momentum measurement. The detector is organised in a barrel with four cylinders and two end-caps with nine disks. The cylinders have a structure in carbon fibre with radii of 30.0, 37.3, 44.7 and 52.0 cm, on which several longitudinal staves are mounted and equipped with the semiconductor modules. In the end-caps the disks have the modules arranged in the radial direction. The basic unit of the detector is the module and contains

two single-sided silicon microstrip sensors mounted back-to-back. Each sensor has an active area of 6.36×6.40 cm^2 and contains 768 microstrips with 80 μm width. In the barrel the $R-\phi$ coordinate of the hit is determined by the strip position, while a precise measurement of the z-coordinate is obtained exploiting the stereoscopic effect: the back-to-back sensors are mounted with a 40 mrad 'tilt' angle, so the crossing point of the strips on both sensors on each module is used to determine the space-point position. In the end-cap, the ϕ coordinate of the track is determined using the strip position and the R-coordinate with the 'stereo' effect. The spatial resolution achieved is 17 μm in the direction of the strip pitch, and 580 μm in the direction determined by the strip crossing. For the same reasons as in the Pixel Detector, the SCT is kept at a temperature between $-5\,^{\circ}$C and $-15\,^{\circ}$C.

2.2.3.3 Transition radiation tracker

The TRT, the outermost part of the three tracking subsystems of the ID, is a straw-tube tracker particularly well suited to LHC conditions due to its resistance to radiation. The barrel region contains 52544 straw tubes with a length of 1.5 m arranged parallel to the beam axis. Barrel tubes have the central wires electrically split and read out at both ends of the straw. Each end-cap contains 122880 straw tubes with a length of 0.4 m arranged perpendicularly to the beam axis, and read out at their outer end. Each drift tube has a diameter of 4 mm that is made from wound Kapton and carbon fibre; in the centre of each tube there is a gold-plated tungsten wire of 31 μm diameter and the tube is filled with a gas mixture. Most of the TRT is filled with a mixture of 70 % Xe, 27 % CO_2 and 3 % O_2. Due to large irreparable gas leaks that developed in the gas system, part of the TRT detector is now flushed with a gas mixture composed primarily of much cheaper argon, 80 % Ar and 20 % CO_2 (see figure 2.7).

The spaces between the straws are filled with polymer fibres (barrel) and foils (end-caps) to create transition radiation, which is emitted by highly-relativistic charged particles as they traverse a material boundary. This effect depends on the Lorentz boost γ (E/m) and is strongest for electrons, which means it can be used for particle identification. X-rays coming from the transition radiation process can be absorbed by the noble gas, resulting into additional energy being deposited into the gas. This design makes the TRT complementary to the silicon-based tracking devices. Each channel, through the tube drift time measurement, has an intrinsic single-point resolution of 120 μm, larger than that of the silicon trackers, but this is compensated by the large number of hits per track (typically more than 30) and the long lever arm. Furthermore, the high sampling frequency of the wire signals enables the TRT to provide timing information on the nanosecond level.

2.2.4 Calorimeters

The ATLAS calorimeter system [90] surrounds the ID and it consists of an inner electromagnetic calorimeter and an outer hadronic calorimeter. It was designed to fully cover the ϕ space and to measure a wide range of energy deposits over the entire pseudorapidity coverage of $|\eta| < 4.9$ from both neutral and charged particles. The structure of the ATLAS calorimeter is shown in figure 2.8. In the acceptance region covered by the ID, the granularity of the EM calorimeter is finer in the η and ϕ directions in order to provide precision measurements of electrons and photons. The rest of the calorimeter system has coarser granularity, yet appropriate for a precise measurement of jet kinematics, and provides sufficient longitudinal containment of the showers in order to calculate the missing transverse energy. All of the ATLAS calorimeters are sampling calorimeters; they consist of absorber sheets, which initiate particle showers, alternated with layers of active medium material to perform energy measurements. When a particle reaches the calorimeter, it produces showers in stages, loosing more and more energy until the shower is completely absorbed. The energy of the

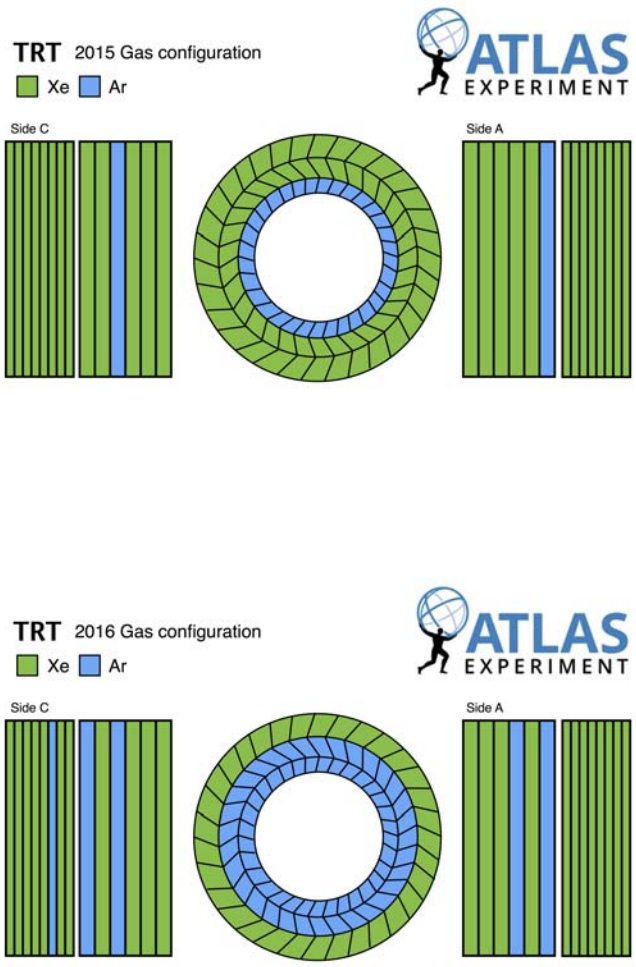

Figure 2.7: TRT gas configuration used in the year 2015 (top) and 2016 (bottom).

initial particle is then obtained by summing up all energy deposits within the active material of the calorimeter. The calorimeter is designed to fully absorb the particle energy to avoid losses caused by escaping particles. It also reduces possible punch-through to the muon chambers by energetic hadrons.

2.2.4.1 Electromagnetic calorimeter

The Electromagnetic CALorimeter (ECAL) is divided into a barrel part ($|\eta| < 1.475$) and two end-caps ($1.375 < |\eta| < 3.2$). The barrel calorimeter consists of two identical half-barrels, separated by a small gap (6 mm) at $z = 0$. Each end-cap calorimeter is mechanically divided into two coaxial wheels: an outer wheel covering the region $1.375 < |\eta| < 2.5$, and an inner wheel covering the region $2.5 < |\eta| < 3.2$. The ECAL uses liquid argon (LAr) as active material with accordion-shaped Kapton electrodes and lead absorber plates over its full coverage. The LAr solution was adopted for its intrinsic linear behaviour, high ionisation yield and stability. The LAr gas is constantly flowing and does not suffer from radiation damage; LAr is therefore preferable in the region close to the interaction

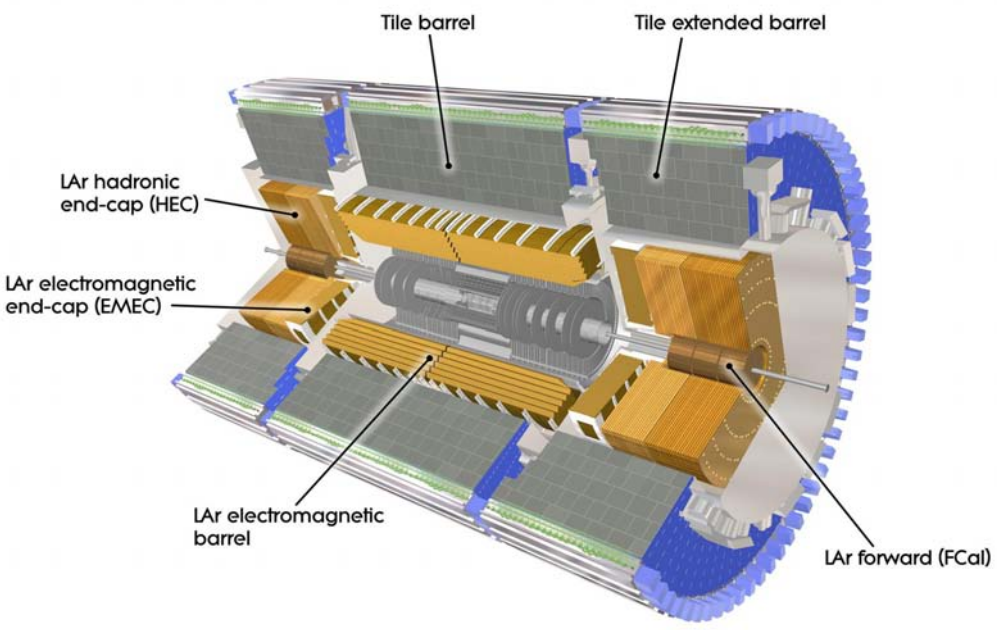

Figure 2.8: Schematic view of the ATLAS calorimeter system.

point, as well as in the very forward regions. The accordion geometry provides complete ϕ symmetry without azimuthal cracks. The lead thickness in the absorber plates has been optimised as a function of η in terms of EM energy resolution. High voltage is applied between absorber plates to collect ionisation electrons from the interaction with the LAr as well as to produce signal amplification. The total thickness of the ECAL is >24 X_0 in the barrel and >26 X_0 in the end-caps. This ensures the absorption of electron and photon showers up to few TeV of energy and around 2/3 of typical hadronic showers. Over the region devoted to precision physics ($|\eta| < 2.5$), the ECAL is segmented into three longitudinal sections with different cell structure in the $\eta - \phi$ plane. The first layer, which has a constant thickness of $\sim 6\, X_0$ (upstream material included) as a function of η, is equipped with narrow readout strips of $\Delta\eta \times \Delta\phi = 0.0031 \times 0.098$. This section acts as a "preshower" detector, enhancing particle identification ($\gamma/\pi^0, e/\pi$ separation, etc) and providing a precise position measurement in η. The second layer is transversally segmented into square towers of size $\Delta\eta \times \Delta\phi = 0.025 \times 0.025$ ($\sim 4{\times}4$ cm^2 at $\eta = 0$). The total calorimeter thickness up to the end of the second section is ~ 24 X_0, tapered with increasing rapidity (this includes also the upstream material). Combining the information from the first two layers provides a precise measurement of a photon's production vertex. The third layer has a granularity of 0.05 in η and a thickness varying between 2 X_0 and 12 X_0. For $|\eta| > 2.5$, i.e. for the end-cap inner wheel, the calorimeter is segmented in two longitudinal sections and has a coarser lateral granularity than for the rest of the acceptance. The calorimeter cells point towards the interaction region over the complete eta coverage. In the region where the amount of material exceeds ~ 2 X_0 (as is the case for $|\eta| < 1.8$), a presampler is used to correct for the energy lost by electrons and photons upstream of the calorimeter. The presampler consists of an active LAr layer of thickness 1.1 cm (0.5 cm) in the barrel (end-cap) region. In figure 2.9a the structure of the ECAL is shown. The total number of channels for the entire ECAL is ∼190 000. The design energy resolution is:

$$\frac{\sigma_E}{E} = \frac{9\%}{\sqrt{E\,(\mathrm{GeV})}} \oplus 0.3\%, \tag{2.7}$$

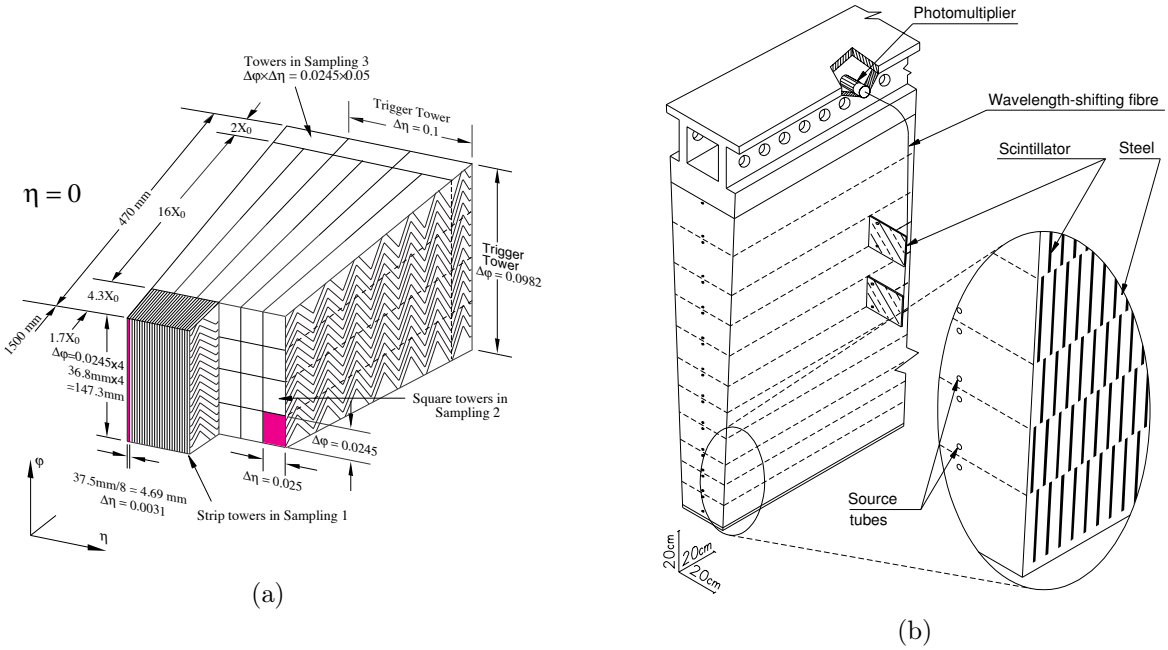

Figure 2.9: Schema of different modules of the ATLAS calorimeters: (a) electromagnetic calorimeter and (b) hadronic calorimeter.

while the angular resolution is ~ 50 mrad$/\sqrt{E(\mathrm{GeV})}$.

2.2.4.2 Hadronic calorimeter

The ATLAS hadronic calorimeters cover the range $|\eta| < 4.9$ using different techniques best suited for the widely-varying requirements and radiation environment over the large η range. An important parameter in the design of the hadronic calorimeter is its thickness: it has to provide good containment for hadronic showers and reduce punch-through into the muon system to a minimum. The total thickness is 11 interaction lengths (λ) at $\eta = 0$, including about 1.5 λ from the outer support, which has been shown both by measurements and simulation to be sufficient to reduce the punch-through well below the irreducible level of prompt or decay muons. Close to 10 λ of active calorimeter are adequate to provide good energy resolution for high-energy jets. Together with the large η coverage, this also guarantees a good $E_{\mathrm{T}}^{\mathrm{miss}}$ measurement. In the central region the Tile calorimeter covers the range $0 < |\eta| < 1.7$ (11.4 m long cylinder with an inner radius 2.28 m and an outer radius of 4.25 m). The Tile calorimeter is composed of one barrel and two extended barrels. It consists of a sampling calorimeter that uses scintillating tiles as the active material and steel as the absorber arranged in three layers. Scintillator tiles, approximately 3 mm in thickness, are arranged radially along the beam pipe with the tile face along the z-axis, with steel absorbers sandwiched between the tiles in this orientation. The scintillation light induced in a tile upon the passage of radiation is read out by optical fibres and sent into two separate photomultiplier tubes. Azimuthally, the barrel and extended barrels are divided into 64 modules. In η, the readout cells, built by grouping fibres into PMTs, are "pseudo-projective" towards the interaction region. The resulting granularity is $\Delta\eta \times \Delta\phi = 0.01 \times 0.01$ (0.2×0.1 in the last layer). The region $1.5 < |\eta| < 3.2$ is covered by the Hadronic End-cap Calorimeter (HEC), which uses copper plates as absorbers and LAr as active material for its superior radiation resistance. It consists of two independent wheels with an outer radius of 2.03 m. Each wheel is built out of 32 identical modules, assembled with fixtures at the periphery, and a central ring. As for the electromagnetic

calorimeter, the electric signal produced in the LAr is collected by cathodes on the plates. Finally, in the most forward part ($3.1 < |\eta| < 4.9$) a Forward Calorimeter (FCAL) is present. It is assembled with tungsten rod absorbers embedded in a copper matrix. Between the two, a thin gap filled with LAr provides the active material. The radial depth of the hadronic calorimeter is approximately 7.4 λ with minimal variation across the η range. The resolution achieved in this configuration is:

$$\frac{\sigma_E}{E} = \frac{50\%}{\sqrt{E\,\mathrm{GeV}}} \oplus 3\% \text{ for Tile and HEC, and} \tag{2.8}$$

$$\frac{\sigma_E}{E} = \frac{100\%}{\sqrt{E\,\mathrm{GeV}}} \oplus 10\% \text{ for FCAL.} \tag{2.9}$$

2.2.5 Muon spectrometer

The ATLAS Muon Spectrometer (MS) [90] was designed to provide a high-resolution measurement of the muon momentum up to very high energy (few TeV) in the pseudorapidity range $|\eta| < 2.7$. The muon momentum measurement is based on the muon deflection in the toroidal magnet. The MS can perform measurements in stand-alone mode being independent from other subdetectors; this feature is important for fast event triggering as well as for the redundancy of the pattern recognition. The MS employs four different technologies in order to fulfil the different needs of the detector: two different precision tracking chambers for precise momentum measurements and two different triggering chambers (with fast response time <25 ns) used to provide a trigger signal and timing calibration to the event. Different technologies have been also adopted in order to keep similar performance in terms of radiation hardness, low occupancy and detector efficiency since the particle flux from the interaction point has a large variation according to the position of the muon chambers. In the barrel region, chambers are arranged in three cylindrical layers around the beam axis, one layer being inside the magnet. In the end-caps these three layers are placed on four wheels perpendicularly to the beam axis. The conceptual layout of the MS is shown in figure 2.10. The total number of channels for the entire MS is ∼1 million.

2.2.5.1 Tracking chambers

- **MDT** (Monitored Drift-Tube Chambers): MDTs are proportional chambers based on the drift tube technology. The tubes of 30 mm diameter are made of aluminium with a 50 μm diameter central W-Re wire. The tubes are operated with a non-flammable mixture of 93 % Ar and 7 % CO_2 at 3 bar absolute pressure; the chosen working point provides for a non-linear space-time relation with a maximum drift time of 700 ns, a small Lorentz angle, and excellent ageing properties. To improve the resolution of a chamber beyond the single-wire limit (80 μm) and to achieve adequate redundancy for pattern recognition, the MDT chambers are constructed from 2×4 monolayers of drift tubes for the inner station, and 2×3 monolayers for the middle and outer stations. The tubes are arranged in multilayer pairs of three or four monolayers, respectively, on opposite sides of a rigid support structure and placed transverse to the beam axis. A chamber provides a resolution of 40 μm, while the resolution for three layers of MDTs is 30 μm. Due to their reliability, mechanical robustness and simpler operation, MDT chambers are employed to cover the larger area of the spectrometer ($|\eta|$<2.7, 2.0 for the innermost layer).

- **CSC** (Cathode Strip Chambers): CSCs are multiwire proportional chambers with cathode strip readout and with a symmetric cell in which the anode-cathode spacing is equal to the anode wire pitch. The precision coordinate is obtained by measuring the charge induced on the segmented

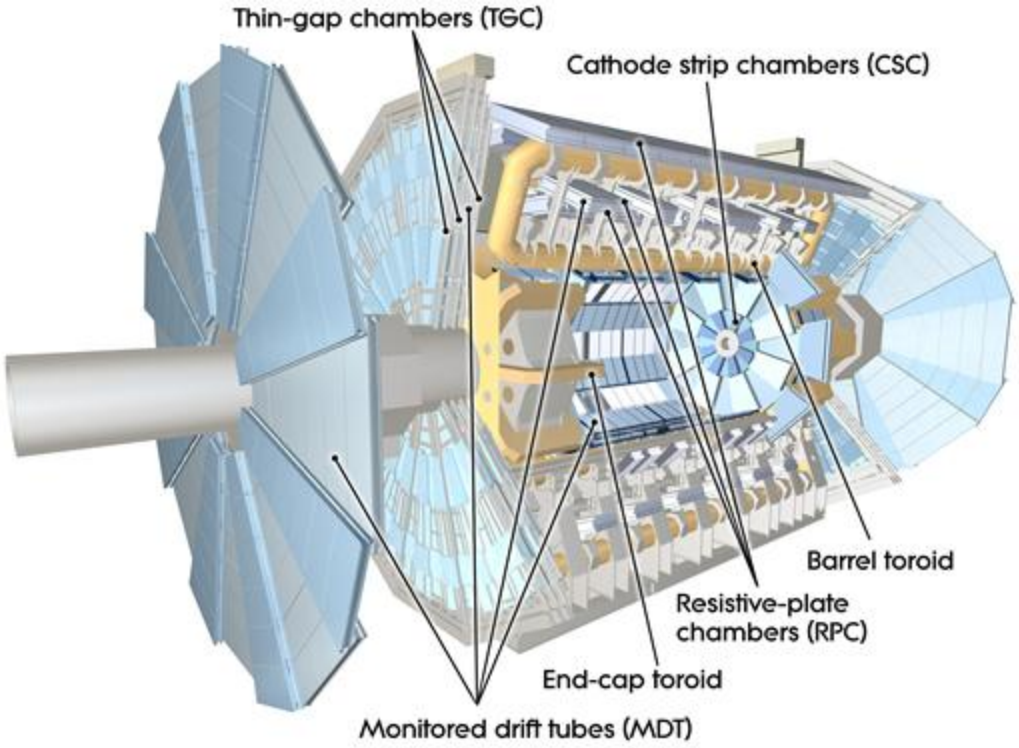

Figure 2.10: Schematic view of the ATLAS muon spectrometer.

cathode by the avalanche formed on the anode wire. The spatial resolution is $\sim$ 40 μm in the bending plane and $\sim$5 mm in the non-bending one. The maximum drift time for signal collection is 40 ns compared to the 700 ns of the MDTs; this gives the possibility to achieve higher acquisition rates. Due to this capability, together with the high radiation resistance, CSCs are used in the range $2.0 < |\eta| < 2.7$. The baseline CSC gas is a non-flammable mixture of 30 % Ar, 50 % CO_2, and 20 % CF_4; the fact that this gas contains no hydrogen explains the low sensitivity to neutron backgrounds.

2.2.5.2 Triggering chambers

- **RPC** (Resistive Plate Chambers): RPCs are gaseous detectors providing a space-time resolution of 1 cm$\times$1 ns allowing single bunch-crossing discrimination. The basic RPC unit is a narrow gas gap filled with a gas mixture (94.7 % $C_2H_2F_4$, 5 % Iso-C_4H_{10}, and 0.3 % SF_6) and formed by two parallel resistive bakelite plates. The signal is read out via capacitive coupling by metal strips on both sides of the detector. A trigger chamber is made from two rectangular detector layers, each one read out by two orthogonal series of pick-up strips, one parallel to MDT wires and the other orthogonal to the MDT wires. RPCs provide also the ϕ coordinate for the tracks in the final analysis since MDTs only give the η coordinate.

- **TGC** (Thin Gap Chambers): TGCs are similar to multiwire chambers with the only difference being that the anode wire pitch is larger than the cathode-anode distance. The chambers operate with a highly-quenching gas mixture of 55 % CO_2 and 45 % n-pentane (n-C_5H_{12}) and with wires arranged parallel to the MDT wires provide the trigger information. They are assembled in the end-cap wheels, covering the region $1.05 < |\eta| < 2.7$ ($1.05 < |\eta| < 2.4$ for triggering). The timing

resolution is comparable to the RPC's one while the spatial resolution is in the range of 2-7 mm for both coordinates.

In the barrel region, muon tracks are measured with MDT chambers and RPCs assembled on three cylindrical layers: the coordinate in the bending plane is provided by the MDT chambers, while the coordinate in the non-bending plane is provided by the RPCs (together with timing information). In the end-cap region, MDT and CSC provide the coordinate in the bending plane while the non-bending coordinate is provided by the TGCs. The muon spectrometer is designed to measure in standalone mode muons with p_{T} down to 3 GeV (softer muons are stopped) and up to a few TeV. The momentum resolution achieved is $\sim 10\%$ at $p_T = 1$ TeV. At lower energies the resolution is improved substantially by combining the track reconstructed in the muon spectrometer with a track reconstructed in the ID. During LS1 the MS was improved targeting an increased muon acceptance. Completion of the spectrometer acceptance was already foreseen for this shutdown period, with new resistive plate chambers (RPC) placed in the barrel holes due to the toroid feet and elevators (+2.8% acceptance) and extra end-cap chambers.

2.2.6 Luminosity detectors

A good determination of the integrated luminosity is of particular importance to reach the ultimate precision in measurement of processes of interest. The luminosity in a pp collider, $\mathcal{L}$, defined in equation 2.2, can be expressed as well as:

$$\mathcal{L} = \frac{\mu_{\mathrm{vis}} n_b f_{\mathrm{rev}}}{\sigma_{\mathrm{vis}}}, \tag{2.10}$$

where f_{rev} is the collider revolution frequency, n_b the number of colliding bunches and σ_{vis} is the visible inelastic cross section (total inelastic cross section times the detector acceptance and efficiency). The visible interaction rate per bunch crossing is denoted by μvis. It is extracted primarily from the signals coming from specific luminosity detectors. The simplest algorithm consists in simple counting of "bunch crossings" where detectors reported a signal, but more refined algorithms are used, in particular when the pileup contamination is no longer negligible. In order to use the measured μ_{vis} for luminosity determination, each detector and algorithm must be calibrated by determining its visible cross section σ_{vis}. Van der Meer scans allow to determine the effective beam size as well as the maximum achievable collision rate. These are special low-intensity LHC runs where the beam separation in the transverse planes is varied (scanned) in order to determine the beams' overlap profile.

The main detectors for luminosity measurement are listed below:

- **LUCID-2** (LUminosity measurements using Cherenkov Integrating Detector): It consists of 16+16 10 mm diameter Cerenkov detectors for luminosity measurements. LUCID-2 uses the thin quartz windows of photomultipliers as Cherenkov medium. To monitor the gain stability of the photomultipliers, small sources of radioactive Bi-207 are deposited on to the quartz windows. The luminosity is measured by not only counting hits (signals over threshold) in the detectors but also by integrating the signals. LUCID-2 is the only detector in ATLAS that can measure luminosity for individual bunches by charge integration.

- **BCM** (Beam Conditions Monitor): It consists of 1 cm^2 diamond detectors located at $z = 184$ cm around the beam pipe. Their fast readout and good time resolution (0.7 ps) allow them to provide luminosity information for each bunch crossing. At the same time, they are also employed to trigger on beam losses and induce the dump of the beam, thus protecting the silicon detectors from damage that might result from an uncontrolled beam.

- **ALFA** (Absolute Luminosity For ATLAS): It consists of eight scintillating fibers detectors placed at 240 m from the interaction point inside roman pots, above and below the beam pipe. It is a subdetector that is only activated during special runs.

In addition, cross-checks of the luminosity measurement have been performed using information from other standard subdetectors: counting of primary vertices reconstructed by the ID, and integrated signals from the Tile and forward calorimeters. The precision achieved is of a few % depending on the data-taking year.

2.2.7 Trigger and data acquisition system

Due to technical and practical limitations, not every LHC collision can be recorded by the ATLAS detector. The goal of the ATLAS trigger and data acquisition (DAQ) system is to select in real time and to record efficiently events with interesting characteristics for physics analyses. The implementation results in a multi-level system optimised to cope with the very high interaction rate and short bunch spacing of the LHC. The ATLAS trigger system is shown schematically in figure 2.11.

The trigger system consists of a hardware Level 1 (L1) and a single software-based high-level trigger (HLT). This two-stage system will reduce the event rate from the bunch-crossing rate of 40 MHz to 100 kHz at L1 and to an average recording rate of 1 kHz at the HLT. During Run 1, this was a three-stage system with two stages in the HLT. In Run 2 the Event Builder and Event Filter farms are merged into a unique HLT farm for simplification and dynamic resource sharing [92]. At L1, fast custom-made electronics find regions of interest (RoI) using the calorimeter and muon data with coarse information within a latency of 2.5 μs and keeps the information in pipeline memories. High-p_{T} muons are identified using only the trigger chambers, RPCs in the barrel, and TGCs in the end-caps. The calorimeter selections are based on reduced-granularity information from all the calorimeters. The L1 system in Run 2 consists of the L1 calorimeter trigger system (L1Calo), the L1 muon trigger system (L1Muon), new L1 topological trigger modules (L1Topo) that allow to select events on topological quantities between L1 objects within the L1 latency, and the Central Trigger Processors (CTP). At the HLT, fast algorithms accessing data from an RoI, or offline-like algorithms using the full-event information, run on a unique PC farm within a processing time of 0.2 s on average. At the end of 2016, a hardware track finder (FTK) is planned to be fully integrated and will provide tracks to the HLT at the L1 rates.

Most of the trigger chains used for physics are unscaled, meaning that all the events passing the selection are kept. Other trigger chains that contain either too many events or events considered not physically interesting are prescaled. These are characterised by a prescaling value, P, meaning that of all the events that activated the trigger, only $1/P$ are accepted. These trigger chains are usually used for checks or calibration rather than physics analysis. The term trigger chain refers to the sequence of selections that define a certain trigger object. The naming convention is:

$$[\text{LEVEL}][\text{N}][\text{TYPE(S)}][\text{THRESHOLD}][\text{ISOLATION}][\text{QUALITY}], \tag{2.11}$$

where the components, from left to right, are: the trigger level used, the multiplicity of the type, the object candidate, the threshold applied to the transverse momentum or energy of the object candidate, the object isolation, and the severity of the final algorithm requirements. Trigger chains define a trigger menu, where they are associated to their prescale value, and which is chosen based on the physics program of the data-taking period and depending on the LHC instantaneous luminosity.

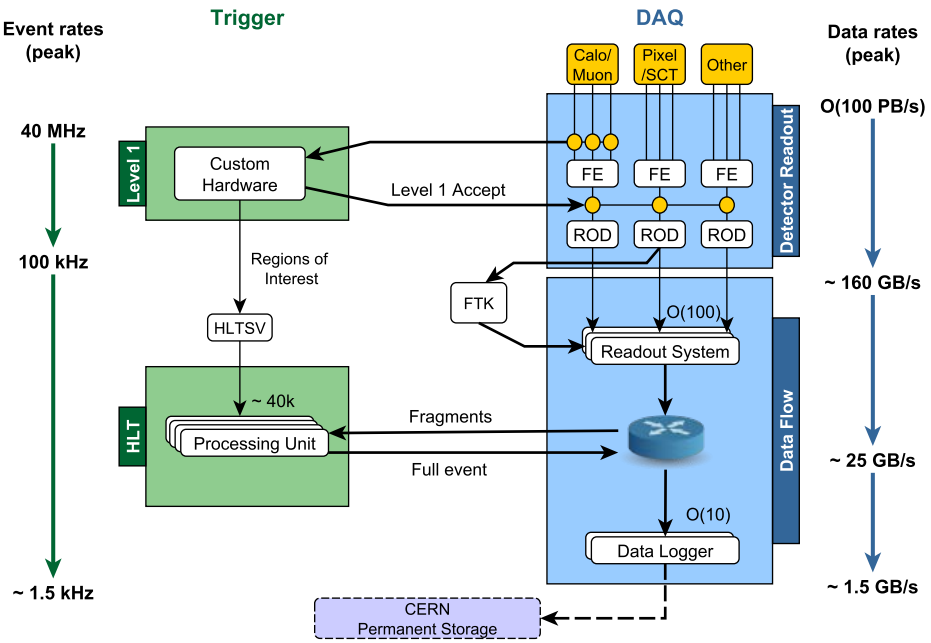

Figure 2.11: Schematic view of the ATLAS trigger system showing output rates in Run 2.

2.2.8 ATLAS operation

The integrated luminosity for each of the two years of Run 2 is reported in figure 2.12. The luminosity delivered by the LHC machine is shown in green while the amount of luminosity collected by the ATLAS detector is reported in yellow. The inefficiency in the data taking arises partly from the so-called "warm start" procedure, which consists in ramping up the voltages for the silicon detector only after the LHC has declared stable beam, or due to transient problems in the trigger and detector data acquisition. The ATLAS data-taking efficiency was above 90% in both years.

The fraction of good data delivered by each subdetector is shown in figure 2.13 for both data-taking years in Run 2 so far. The fraction is $\sim 90\%$ in each year; table 2.2 summarises the integrated luminosity collected by ATLAS and flagged as "good quality data" from all the subdetectors. For the measurements presented in this dissertation, all ATLAS subdetectors are needed, as the physics objects used in the analyses are reconstructed using the information from the full detector. The fraction of data considered was collected in the full 2015 and until July 2016, giving a total integrated luminosity of 13.2 fb^{-1} at $\sqrt{s} = 13$ TeV satisfying data quality requirements.

year	LHC delivered	ATLAS recorded	ATLAS good quality
2015	4.2 fb^{-1}	3.9 fb^{-1}	3.2 fb^{-1}
2016	38.9 fb^{-1}	35.9 fb^{-1}	33.2 fb^{-1}

Table 2.2: Integrated luminosity per year during Run 2. Columns correspond to LHC delivered luminosity, luminosity recorded by ATLAS, and luminosity with good data quality flag from all subdetectors.

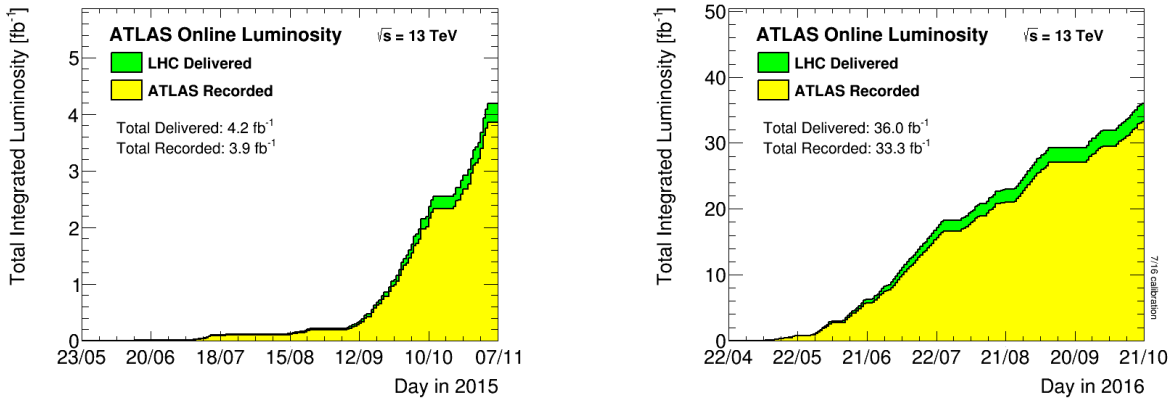

(a) (b)

Figure 2.12: Integrated luminosity delivered by the LHC in the years (a) 2015 and (b) 2016 as a function of time. Also shown is the integrated luminosity recorded by ATLAS.

ATLAS pp 25ns run: August-November 2015

Inner Tracker			Calorimeters		Muon Spectrometer				Magnets	
Pixel	SCT	TRT	LAr	Tile	MDT	RPC	CSC	TGC	Solenoid	Toroid
93.5	99.4	98.3	99.4	100	100	100	100	100	100	97.8

All Good for physics: 87.1% (3.2 fb^{-1})

Luminosity weighted relative detector uptime and good data quality (DQ) efficiencies (in %) during stable beam in pp collisions with 25ns bunch spacing at √s=13 TeV between August-November 2015, corresponding to an integrated luminosity of 3.7 fb^{-1}. The lower DQ efficiency in the Pixel detector is due to the IBL being turned off for two runs, corresponding to 0.2 fb^{-1}. Analyses that don't rely on the IBL can use those runs and thus use 3.4 fb^{-1} with a corresponding DQ efficiency of 93.1%.

ATLAS pp 25ns run: April-July 2016

Inner Tracker			Calorimeters		Muon Spectrometer				Magnets	
Pixel	SCT	TRT	LAr	Tile	MDT	RPC	CSC	TGC	Solenoid	Toroid
98.9	99.9	100	99.8	100	99.6	99.8	99.8	99.8	99.7	93.5

Good for physics: 91-98% (10.1-10.7 fb^{-1})

Luminosity weighted relative detector uptime and good data quality efficiencies (in %) during stable beam in pp collisions with 25ns bunch spacing at √s=13 TeV between 28th April and 10th July 2016, corresponding to an integrated luminosity of 11.0 fb^{-1}. The toroid magnet was off for some runs, leading to a loss of 0.7 fb^{-1}. Analyses that don't require the toroid magnet can use that data.

Figure 2.13: Fraction of good data delivered by each subdetector during the year 2015 (top) and 2016 (bottom).

2.2.9 Future ATLAS upgrades

In the next years, the LHC will undergo a series of upgrades leading ultimately to a five-fold increase of the instantaneous luminosity with leveling according to the High-Luminosity LHC (HL-LHC) project [93]. The goal is to extend the dataset from about 300 fb^{-1}, expected to be collected by the end of the LHC run (in 2022), to 3000 fb^{-1} by 2035. The foreseen higher luminosity at the HL-LHC represents a great challenge for ATLAS.

A second shutdown (LS2), is being planned in 2018 to integrate the Linac4 into the injector complex, to increase the energy of the PS Booster, to reduce the beam emittance, and to upgrade the collider collimation system. When data taking resumes in 2020, the peak luminosity is expected to reach $\sim 2-3\times10^{34}$ $cm^{-2}s^{-1}$, corresponding to 55 to 80 interactions per crossing with 25 ns bunch spacing, well beyond the initial design goals. Therefore, to face the increased event rates, ATLAS will undergo to several upgrades during this long shutdown, referred to as Phase-I upgrade:

- A replacement of the first endcap station of the MS, the New Small Wheel (NSW) [94], is proposed. The NSW must ensure efficient tracking at high particle rate (up to 5×10^{30} $cm^{-2}s^{-1}$) and larger $|\eta|$, with position resolution of < 100 μm. Furthermore, unlike the present layer, the NSW will be integrated into the Level-1 trigger, thus helping in rejecting background by selecting tracks coming from the primary interaction and matched with the most external layers of the muon spectrometer.

- The calorimeter trigger [95] will also have a an upgrade in Phase I, with the goal of providing higher-granularity, higher-resolution and longitudinal shower information from the calorimeter to the Level-1 trigger processors.

- The Fast TracKer (FTK) [96] Trigger will perform the track finding and fitting on-line using dedicated massive parallel processing. FTK will then provide the track parameters with resolution close to that of offline tracks shortly after the start of the Level-2 processing, thus releasing extra resources for more advanced selection algorithms, which ultimately could improve the performance of tracking-based filter algorithms such as b-tagging and τ identification. While the full geometrical coverage for full Phase-I pileup in foreseen after the 2018 shutdown, a progressive coverage and commissioning already started in 2015.

The Phase-I upgrades are designed to be fully forward-compatible with the physics program of the high luminosity HL-LHC (Phase II), when the instantaneous luminosity should reach $\sim 5-7\times10^{34}$ cm^{-2} s^{-1}, giving 200 interactions per crossing and a total integrated luminosity of 3000 fb^{-1}.

A third 36-months long shutdown (LS3) in 2023-25 will be necessary to upgrade the accelerator to this ultimate operation mode. ATLAS is being planning major updates in all its subsystems and trigger architecture. The present ATLAS Inner tracker will have several limitations in Phase II when up to 200 pileup events per bunch crossing are expected. The entire Inner Detector will be replaced with a new, all-silicon Inner Tracker (ITk) [97] with pixel sensors at the inner radii surrounded by microstrip sensors. A new trigger architecture is being developed that is compatible with the constraints imposed by the detector and provides a flexible trigger with the potential to deliver the required performance. As currently envisaged, the baseline design for the Phase-II Trigger foresees a split Level-0/Level-1 hardware trigger with a total L1 accept rate of 200 kHz and total latency of 20 μs.

3
Event simulation

Nature isn't classical, dammit, and if you want
to make a simulation of nature, you'd better make it quantum mechanical,
and by golly it's a wonderful problem, because it doesn't look so easy.
Richard Feynman

Contents

A key point to test the SM or any possible extension of it is to quantify the consistency of the observed data with the theoretical prediction. An accurate simulation, including the state-of-the-art understanding of the pp collision physics and the experimental setup, is necessary to model physics processes and kinematic distributions. Event simulation is a complex procedure divided into two major steps:

- Event generation: Simulation of the physics process of interest including the modelling of the partonic structure of the incoming protons, their collision and the subsequent event development up to the decays into stable particles. As the physics processes occurring in pp collisions are probabilistic in nature, event generation involves pseudo-random numbers, which are generated using Monte Carlo (MC) techniques.

- Detector simulation and digitisation: MC techniques are used to simulate the geometry of the detector, the interaction of particles with the detector materials, and the corresponding detector response, including the digitisation of the detector electronics.

This chapter presents an overview of the simulation of pp collisions, followed by a description of the MC generators used for the analyses in this dissertation, and the ATLAS detector simulation. It also includes a summary of the procedure followed in ATLAS to validate MC samples, which the author has participated in.

3.1 Event generation

The modelling of a pp collision requires a detailed understanding of the dynamics of a deep inelastic interaction at high energy (perturbative QCD), as well as the structure of a relativistic proton and the evolution of partons into stable hadrons at very low energy (non-perturbative QCD). The complication of collisions involving protons is that protons are composite particles, thus a precise understanding of the partonic structure of the proton is needed to calculate the process cross section. A proton is a bound state composed of point-like quarks and gluons interacting among themselves via the constant exchange of soft virtual gluons. According to the uncertainty principle, the time scale of a virtual gluon interaction is inversely proportional to its virtuality q, i.e. t $\sim 1/q$, so that gluons with higher virtuality usually are absorbed by the same quark by which they were radiated. A hard probe interacts within a much shorter timescale $1/Q \ll 1/q$ during which the partonic fluctuations in the struck proton appear almost frozen. The hard probe effectively takes a snapshot of the proton structure, at a characteristic resolution given by $\sim 1/Q$. The independence of long-wavelength (soft) structure on the nature of the hard (short-distance) process, a key aspect in the simulation of pp collision, gives the possibility of factorizing the different processes happening at different energy scales (factorisation theorem). Since the interaction cross section of such collisions decreases as the momentum exchange Q between the colliding particles increases, a pp collision typically consists of one so-called hard scattering/process with a high momentum exchange Q computed at a fixed order (LO or NLO) in perturbation theory, which is sometimes accompanied by further soft collisions, so-called multi-parton interactions that are instead described via phenomenological models.

3.1.1 Factorisation theorem

The event simulation begins with the collision, with large momentum transfer, between two partons within the protons. At high energy, the partons behave as asymptotically free, and a perturbative description is applied. The cross section for a generic process $pp \to X$ is defined in terms of the cross section for the partonic processes, according to the factorisation theorem [99], as

$$\sigma_{pp\to X} = \sum_{a,b} \int dx_a dx_b f_a(x_a, \mu_F^2) f_b(x_b, \mu_F^2) \hat{\sigma}_{ab\to X}(x_a p_a, x_b p_b, \mu_R^2, \mu_F^2), \tag{3.1}$$

where the sum runs over all possible combinations of the partons a and b able to produce X. The parton density function (PDF), $f_i(x_i, \mu_F^2)$, represents the effective density of partons of type/flavor i, as a function of the momentum fraction x_i, when a hadron is probed at a scale μ_F. The factorisation scale μ_F represents the estimated limit between the perturbative and non-perturbative QCD regimes, i.e. the energy at which the running α_s becomes too large for achieving a desired convergence of the perturbation series. In addition, the cross section calculation depends on the choice of the

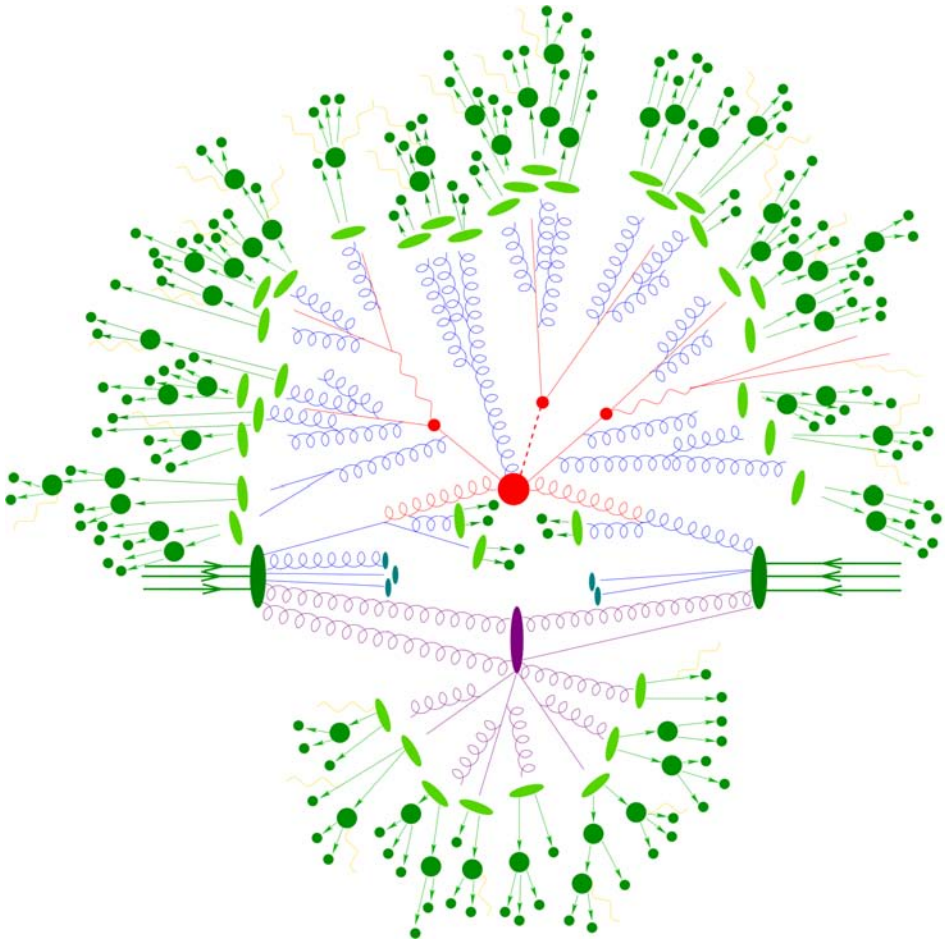

Figure 3.1: Illustration of a pp collision. Two partons from the incoming protons (large green ellipses) undergo initial state radiation and interact in the hard process (big red blob). A parton shower (red) emerges from the products of the hard interaction. The resulting partons hadronise into colourless states (light green blobs) that subsequently decay into stable particles (green circles). A secondary interaction between proton remnants is shown as a purple blob, again creating a parton shower (purple), which hadronises, followed by decays into stable particles. This is part of the underlying event, together with the beam remnants (light blue blobs). Electromagnetic radiation (yellow) can be emitted by charged particles at any stage. From Ref. [98].

renormalisation scale μ_R of QCD, at which α_s is evaluated. As the factorisation and normalisation scales describe the not precisely known boundaries between two physics domains, their values are usually related to some quantities characteristic of the modelled process (e.g. the mass of the particle produced, or the sum of the momenta of outgoing particles). The uncertainties arising from such a convention are typically estimated by comparing the cross section values $\sigma_{pp\to X}$ evaluated varying the nominal scale choice for μ_F or μ_R by a factor of two up and down. The cross section for the partonic process $\hat{\sigma}_{ab\to X}(x_a p_a, x_b p_b, \mu_R^2, \mu_F^2)$ is computed explicitly at a fixed order in perturbation theory. This step is also referred to as Matrix Element (ME) calculation, because it involves the calculation of the scattering matrix relating the initial and final state particles of the process.

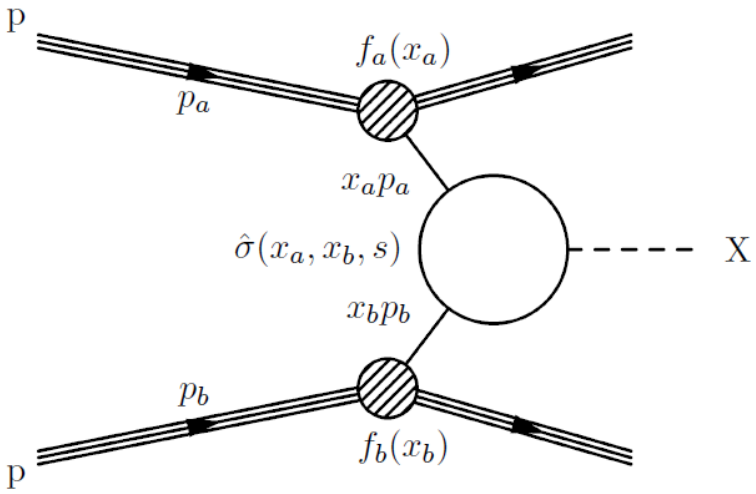

Figure 3.2: Illustration of a hard scattering. A parton with four-momentum $x_a p_a$, originating from a proton with a four-momentum p_a, undergoes a hard collision with a parton carrying a four-momentum $x_b p_b$, coming from a proton with a four-momentum p_b. The spectator partons do not influence the hard interaction and continue their trajectory with slightly distorted directions.

3.1.2 Parton density functions

QCD does not predict the structure of the proton and therefore the PDFs cannot be calculated, but have to be measured from experimental data. Historically, most of the information came from Deep Inelastic Scattering (DIS) in fixed-target lepton-nucleon scattering experiments and from the HERA electron-proton collider at DESY. The energy dependence of the PDFs is given by the DGLAP evolution equations [100–102]:

$$\frac{\partial q_i(x,Q^2)}{\partial \log Q^2} = \frac{\alpha_s}{2\pi}\int_x^1 \frac{dz}{z}\left\{P_{q_i q_y}(z,\alpha_s) q_j(\frac{x}{z},Q^2) + P_{q_i g}(z,\alpha_s) g(\frac{x}{z},Q^2)\right\}, \tag{3.2}$$

$$\frac{\partial g(x,Q^2)}{\partial \log Q^2} = \frac{\alpha_s}{2\pi}\int_x^1 \frac{dz}{z}\left\{P_{g q_j}(z,\alpha_s) q_j(\frac{x}{z},Q^2) + P_{gg}(z,\alpha_s) g(\frac{x}{z},Q^2)\right\}. \tag{3.3}$$

$$\tag{3.4}$$

In the above expressions, $g(x,Q^2)$ is the gluon PDF, $q_i(x,Q2)$ is the quark PDF, and $P_{ab}(z,Q^2)$ are the splitting functions. For the evolution in x, there are no such equations, but it has to be obtained from fits to experimental data. Several collaborations continuously work to improve the PDF fits with the most recent data. PDF sets from the groups CTEQ [103], NNPDF [104] and MSTW [105] are extensively used at the LHC.

3.1.3 Matrix element

The production of an arbitrary final state, $ab \to X$, from a hadron collision can be expressed to all-orders in perturbation theory as:

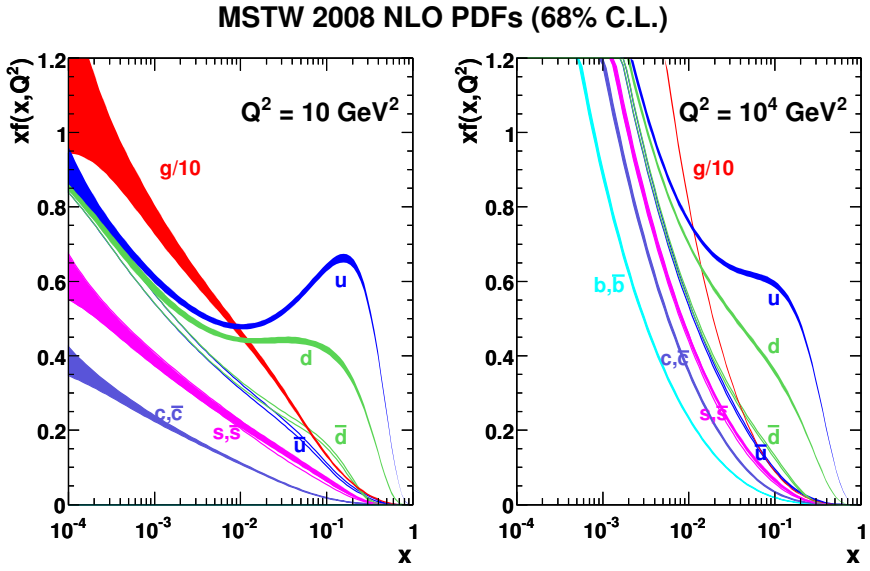

Figure 3.3: Parton luminosities for MSTW 2008 NLO PDF set as function of x with the uncertainty band. On the left (right) panel for $Q^2 = 10$ (10^4) GeV^s. From Ref. [105].

$$\sigma_{ab\hat{\to}X} = \underbrace{\sum_{k=0}^{\infty} \int d\Phi_{X+k}}_{\sum \text{legs}} \underbrace{|\sum_{\ell=0}^{\infty} \mathcal{M}^{(\ell)}_{X+k}|^2}_{\sum \text{loops}}, \tag{3.5}$$

where $\mathcal{M}^{(\ell)}_{X+k}$ is the amplitude for producing X in association with k additional final-state partons (real emission corrections, or "legs") and with ℓ additional virtual correction loops. The phase space of the configuration with k legs is represented by $d\Phi_{X+k}$. Specific values of $k + \ell$ will return the fixed-order calculations of perturbative QCD:

- $k = 0$, $\ell = 0$ $\implies$ Leading Order (usually tree-level) for X production;
- $k = n$, $\ell = 0$ $\implies$ Leading Order for X+n jets;
- $k + \ell \leq$ n $\implies$ N^nLO for$X$ (includes N^{n-1}LO for X+1 jet, N^{n-2}LO for X+2 jets, and so on up to LO for $X + n$ jets).

According to the KLN theorem [106, 107], the infrared (IR) singularities coming from integrating over collinear and soft real-emission configurations should cancel, order by order, with those coming from the IR-divergent loop integrals. However, in a fixed-order calculation, e.g. leading order, in the situation for which $k \geq 1$, $\ell = 0$, the integration over the full momentum phase space will include configurations in which one or more of the k partons become collinear or soft. Such configurations leads to IR singularities in the integration region, which must be regulated cutting away the problematic regions of the phase space. The remaining part of the phase space is then considered by parton shower generators.

3.1.4 Parton shower

Partons involved in a hard-scatter process normally have a very high energy ($Q > 1$ GeV) for which α_s is small ($\ll$1). At such energies, quarks and gluons are likely to radiate off a gluon, carrying a

portion of the energy of its mother particle and a colour connection to it. These gluons can then decay into further gluons or quark-antiquark pairs, leading to the formation of parton showers. This process continues as long as the particles produced have sufficient energy ($Q > 1$ GeV) to reach a distance from the initial particle at which the colour field breaks up into a quark-antiquark pair. Parton Showers (PS) populate regions of the phase space where emissions are collinear or soft (IR divergent) providing an all-orders resummation using an approximation scheme with a leading-log accuracy. The parton shower contribution to the hard process cross section is thus estimated by including only the dominant contribution to each order. Starting from a differential cross section for n particles $d\sigma_n$, a differential cross section for $n+1$ particles is calculated parametrising the probability that the new particle j carries a fraction z of the energy of its mother-particle i emitted at a virtuality scale or invariant mass q^2 using the splitting function $P_{ij}(z, q^2)$:

$$d\sigma_{n+1} \approx d\sigma_n \frac{\alpha_s}{2\pi} \frac{dq^2}{q^2} dz P_{ij}(z, q^2). \tag{3.6}$$

The simulation algorithm develops the shower by applying equation 3.6 iteratively, for each parton involved in the hard interaction. The splitting functions obviously play a crucial role driving the emission probabilities. In MC simulations the formulation of parton shower uses a more convenient expression using the so-called Sudakov form factors:

$$\Delta_i(q_1^2, q_2^2) = \exp\left(- \sum_{j \in q,g} \int_{q_2^2}^{q_1^2} \frac{dq^2}{q^2} \int_{z_{\min}}^{z_{\max}} \frac{\alpha_s}{4\pi} dz P_{ij}(z, q^2) \right), \tag{3.7}$$

which represent the unconditional survival probability for a parton not to undergo a resolvable emission process between the two energy scales q_1^2 and q_2^2. The algorithm implemented in MC simulations goes through the following steps:

- Given the initial scale Q^2, referred to as resummation scale, it produces an emission at scale q_2^2 using equation 3.7.
- If the value of q_2^2 is lower than the hadronisation scale, $q_2^2 \ll Q_0^2 \approx 1$ GeV^2 no further emission occurs, thus the shower developments stops and hadronisation takes place.
- Otherwise, further emissions will occur and the process is repeated for each new parton using q_2^2 as initial scale.

Final-state radiation (FSR), i.e. a gluon radiated off a final-state parton is generated through the above parton shower procedure. For the initial-state radiation (ISR), however, this procedure is not suitable, as the momenta of the partons initiating the hard process need to be precisely adjusted to produce the hard process (e.g. a gluon decaying into a $t\bar{t}$ pair). Thus, the longitudinal momentum fractions x_1 and x_2 of the incoming partons need to be simulated first, and the momentum and angle of the ISR is found by backwards evolution, which involves a PDF-dependent correction to the Sudakov form factors. Due to the existing colour connections, the direction of the ISR tends to be aligned with that of mother parton.

3.1.5 Matrix element and parton shower matching

To improve the leading-log (LL) description given by the parton shower, it is often necessary to go beyond the approximations made in that step. One possibility is to replace the parton shower approximation at given orders in the strong coupling expansion by exact perturbative QCD results.

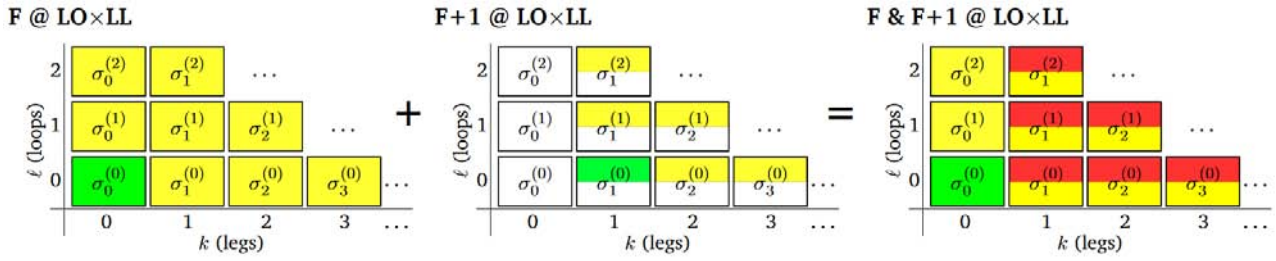

Figure 3.4: The double-counting problem caused by adding cross sections involving matrix elements with different numbers of legs when interfaced to parton showers. From Ref. [108].

The left panel of the figure 3.4 describes the LO cross section computation for some process X and interfacing the parton shower to it. This only gives a LL description of $X+1$ parton. To improve this precision LO matrix element for $X+1$ parton is added with an infrared cut-off to prevent divergences from soft and collinear emissions (see central panel of the figure 3.4). By doing so, final states with one additional emission are generated as both the matrix element term for $X+1$ parton, and in the first radiation of the parton shower starting from the $X+0$ parton. Furthermore, final states with more than one parton are generated twice by the parton shower (see right panel of the figure 3.4). This double-counting problem becomes worse as matrix elements with more legs are added. The double-counting problem can be avoided by separating the phase space to be covered by the parton shower and the matrix element (ME-PS matching). However, such a separation may produce discontinuities in observable spectra because the matrix element includes non-divergent components that are ignored in the parton shower. These procedures are based on the matching of the coefficients calculated by the two parts of the full calculation, parton showers and matrix elements, for each order in perturbation theory, so that the nesting of inclusive and exclusive cross sections is respected without overcounting. The parton-shower expression at fixed order is computed and subtracted from the higher-order calculation to remove double counting. The subtracted result is processed by the parton shower.

These merging schemes typically separate the phase space for emissions into hard and soft/collinear regions by means of a jet criterion, and use the parton shower to fill soft/collinear emissions while using the fixed-order calculation to provide hard/large-angle emissions. Several solutions to this problem have been proposed and implemented in event generators: the CKKW method [109], the MLM prescription [110], and the POWHEG method [111]. Among them, multi-jet (≥ 2 jets) matrix elements can be included by the CKKW method and the MLM prescription only, both based on the suppression method in which multi-jet events coming from matrix elements are suppressed by reinterpreting them in the picture of a parton shower. Generalisations of the CKKW and MLM methods to perform merging of multi-leg NLO matrix elements with parton shower are available at NLO; the MLM prescription is known at NLO as the FxFx method [112].
The CKKW algorithm is as follows:

- Construct a shower history by applying the k_T algorithm to the state from the matrix element.
- Reweight the event with the product of the Sudakov form factors calculated for each branching and the running coupling weight calculated in each branching vertex.
- Set the starting scale of each parton to the scale associated with the node in the shower history where it was produced. Invoke the shower and veto any emission which would give a k_T measure above a certain threshold.

The MLM algorithm proceeds through the following steps:

- Select a merging scale Q_{MS} and a matrix element cutoff Q_{cut} such that $Q_{\mathrm{cut}} < Q_{\mathrm{MS}}$, where the scales are defined using a jet algorithm.
- Cluster the partons from the matrix element using the k_T algorithm and use the clustering scales as in input to α_s and reweight the event.
- Cluster the partons to jets using the algorithm from the first step with a clustering scale set to Q_{MS}. Go through the list of partons, in order of decreasing energy, and match them to the clustered jets. This is done by finding the jet with the smallest distance to the parton defined using some measure based on the jet clustering scheme. If not all partons match or there are extra jets, reject the event.

3.1.6 Hadronisation

The development of the parton shower stops when the partons generated have a virtuality below the hadronisation scale, a regime in which the strong coupling constant α_s becomes large and causes their confinement into colourless hadrons. This process is known as hadronisation. It occurs in the non-perturbative regime of QCD and thus relies on phenomenological models. The most widely used hadronisation models are the Lund String Model [113, 114] and the Cluster Model [115, 116].

The Lund String Model is based on the observation that the quark-antiquark potential rises linearly with the distance between quarks in a meson system. It is translated into a narrow flux tube stretched between the two quarks. Thus, this field is described as a string stretching between the quark and the antiquark. Gluons produced in the parton shower give rise to kinks on the string. When the string energy overcomes the mass threshold of a given quark-antiquark pair, it can break forming an antiquark to match the original quark, and a quark to match the original antiquark, and leaving three shorter strings with lower potential energy. This procedure continues until the energy of the particles drops below the point at which they can no longer escape the confinement. At that point they combine forming the final-state hadrons. This model has some problems describing baryon production. In the simplest scheme for baryon production, diquark pairs are produced instead of quark pairs. A more advanced model is the popcorn approach, where baryons appear from multiple production of quark pairs. The string model of jet fragmentation is infrared and collinear safe, because a soft or collinear gluon induces a vanishingly small kink on the color string.

The Cluster Model is based on the pre-confinement property of QCD. This means that at each point the parton shower forms color-singlet combinations of partons, called clusters, which have an asymptotically universal invariant mass distribution. Thereby, all remaining gluons in the shower are forced to split into quark-antiquark pairs, which participate in the formation of clusters. Once primary clusters are formed, the ones with mass below $3-4$ GeV are transformed into hadrons through a two-body decay according to phase space. Heavier clusters may first undergo non-perturbative splitting processes, and decay into two lighter clusters, or a lighter cluster and a hadron, before the cluster-to-hadron transition is resumed. This process is repeated until all clusters have been transformed into hadrons. However, this model has problems dealing with the decay of very massive clusters, and inadequately suppressing baryon and heavy-quark production.

3.1.7 Underlying event

The processes discussed so far, i.e. the hard process, its higher-order corrections (parton shower) and development (hadronisation), are initiated by one parton from each incoming proton, neglecting any

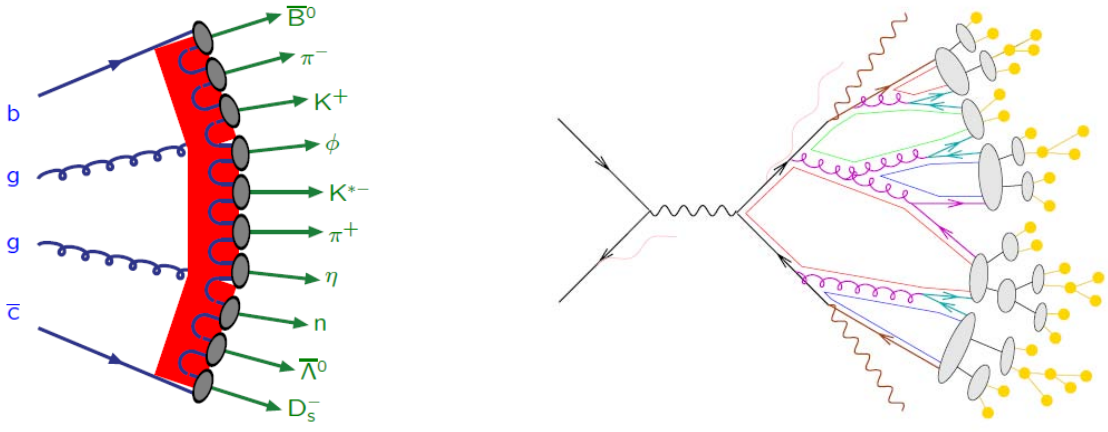

(a) (b)

Figure 3.5: The models of (a) string fragmentation and (b) cluster hadronisation.

effects of rescattering and the exchange of multiple partons between the initial-state protons. However, the event development receives a contribution from additional soft or moderately-hard processes, jointly referred to as "underlying event" (UE). The description of the UE employs phenomenological models, because of the non-perturbative nature of the processes involved. The UE is considered to be composed of thee dominant components: multi-parton interactions, beam remnants and pileup.

Multi-parton interactions (MPI) correspond to moderately-hard interactions of the spectator partons among the incoming protons, i.e. those partons not participating in the hard process. The first detailed MC model for perturbative MPI was proposed in [117]. In this model, the crucial observation is that the t-channel propagators go on shell at low $p_\perp$, causing the differential cross sections to become very large. At the LHC this parton-parton cross section becomes larger than the total hadron-hadron cross section at $p_\perp$ scales of order $4-5$ GeV(see figure 3.6). In the context of MPI models, this is interpreted to mean that each hadron-hadron collision contains several few-GeVparton-parton collisions. MPI interaction typically results in a pair of low-p_T back-to-back jets that are colour connected with the rest of the event.

Incoming beam particles may leave beam remnants that have not undergone any inelastic scattering. These remnants represent the soft QCD activity and need to be put together and colour connected with the rest of the event. What is left in the beam remnant is then a number of partons, with flavours given by the remaining valence content plus the number of sea quarks required for overall flavour conservation. Gluons in the remnant are not explicitly accounted for but are implicit as confinement clouds around the quarks. Beam remnants are modelled by conserving the colour connection and momentum within the event.

Pileup, as discussed in section 2.1.2, refers to the presence of additional inelastic pp collisions in the event originating within the same bunch crossing (in-time) or from an event in a different bunch-crossing (out-of-time). Pileup represents a serious challenge to the reconstruction of the hard process as the products of pileup events largely overlap with those of the hard process (although in the case of in-time pileup typically originating from a vertex displaced with respect to that of the hard scattering). In-time pileup consist of soft QCD interactions and are modelled in a similar way as the UE. Out-of-time pileup is modeled with the same physics process, but considering interactions in past bunch crossings and simulating the time response of the readout electronics. In chapter 4 several techniques to mitigate impact of pileup on reconstructed objects will be discussed.

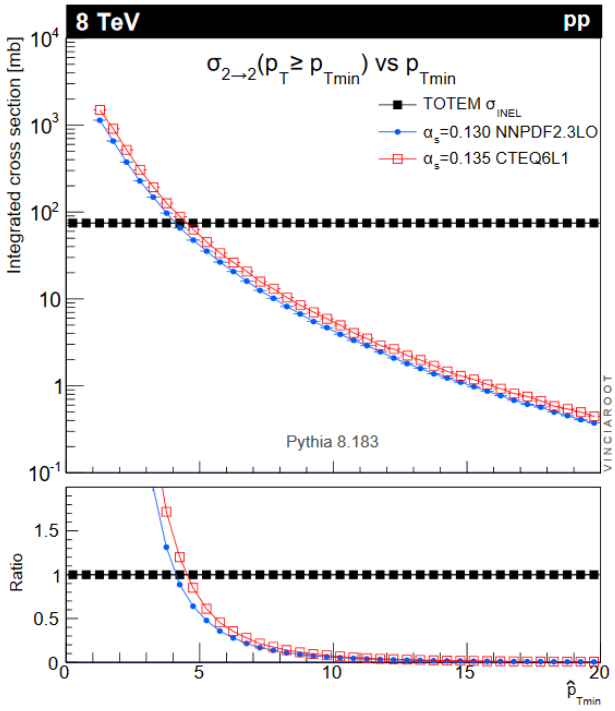

Figure 3.6: Comparison of the total inelastic proton-proton cross section at $\sqrt{s} = 8$ TeV as measured by TOTEM, with the parton-parton cross section at LO in QCD as a function of the minimum parton p_T ($\hat{p}_{T\min}$). The fact that the curves cross at a scale of ~ 5 GeV is interpreted to mean that this is a characteristic scale relevant for MPI. From Ref. [108].

3.1.8 Event generators

Event generators are tools that simulate collision events and their development, using the MC method. Generators can be either general-purpose, performing all steps in the event development, or specialised for a particular step of the event generation. Commonly used generators differ in the approach to various elements of event generation. While some use only a LO matrix-element calculation, others include higher-order corrections, as well as various parton-shower or hadronisation models. In this section, the general features of the generators used in the studies documented in this dissertation are briefly summarised.

3.1.8.1 General-purpose Monte Carlo generators

- PYTHIA [118, 119] is a MC generator using LO calculations for $2 \to n$ ($n \leq 3$) processes, it can simulate collisions at high energies between elementary particles such as e^+, e^-, p and $\bar{p}$ in various combinations. It contains theory and models for a number of physics aspects, including hard and soft interactions, parton distributions, initial- and final-state parton showers (emissions ordered in transverse momentum), multiparton interactions, fragmentation (Lund string model) and decay.

- HERWIG [120] has the same capabilities as PYTHIA with few small differences. It computes $2 \to 2$ processes using LO matrix elements. The parton-shower approach includes colour-coherence effects, with special emphasis on the correct description of radiation from heavy particles, and features emissions ordered in opening angle. The formation of hadrons from the quarks and glu-

ons produced in the parton shower is described using the cluster hadronisation model. HERWIG is typically interfaced with the standalone software JIMMY [121] that simulates the UE.

- SHERPA [122] is a multi-purpose MC generator that can provide multi-leg NLO/LO calculations (ME-PS matching uses CKKW method both at NLO and LO) It can simulate collisions between e^+, e^-, p and $\bar{p}$ in various combinations. It contains theory and models for a number of physics aspects including BSM processes. It contains its own parton shower algorithm based on the Catani-Seymour dipole formalism [123] and its own UE modelling. It can be interfaced with OPENLOOPS [124] to compute loop amplitudes and COMIX [125] to generate matrix element amplitudes.

3.1.8.2 Matrix Element Monte Carlo generators

- POWHEG-BOX [126] is an NLO parton-level generator using the POWHEG method [111]. It generates the hardest radiation in the event using the exact NLO matrix element and is normally interfaced with another parton-shower MC generator (usually PYTHIA or HERWIG) for showering, hadronisation and UE modelling.

- MADGRAPH5_AMC@NLO [127] is an automated MC generator of LO/NLO matrix elements. The NLO calculation implements the MC@NLO method [128]. It is normally interfaced with another parton-shower MC generator (usually PYTHIA or HERWIG) for showering, hadronisation and UE modelling. It can perform ME-PS merging LO using the MLM prescription and at NLO using the FxFx method. It contains theory models and new ones can easily be added using UFO models [129].

- PROTOS [130] is a LO ME generator for some BSM processes involving the top quark. It can be interfaced with PYTHIA for showering and hadronisation.

3.1.8.3 Specialised Monte Carlo generators

- PHOTOS [131] is a MC generator used to model bremsstrahlung in particles decay. It runs after parton shower (PYTHIA or HERWIG) on the HepMC event record.

- TAUOLA [132] is MC event generator that simulates tau decays for both leptonic and hadronic decays modes. It runs after parton shower (PYTHIA or HERWIG) on the HepMC event record.

- EVTGEN [133] is a MC that implements a detailed description of the physics of B-mesons. In particular, it includes detailed models for semileptonic decays, CP-violating decays, and produces accurate results for angular distributions in sequential decays, including all correlations. It runs after parton shower (PYTHIA or HERWIG).

3.2 Detector simulation

MC generators produce a list of four-vectors of all stable particles produced in the event, after hadronisation and decay of the intermediate unstable particles. This is usually referred to as particle level. In order to compare it with the collider data, the MC events have to be processed through the ATLAS detector simulation to model the interactions of the resulting stable particles with the sensitive and dead material of the detector (reconstruction level). The most significant interactions with the detector are simulated with GEANT4 framework [134]. The resulting energy deposits are converted

into simulated electronic signals taking into account the geometry, detector response and readout system of the ATLAS detector. A faster simulation (AF2) [135] was developed to reduce the CPU time necessary to process the event by applying a parameterised description of the particle showers in the calorimeters. Figure 3.7 shows the ATLAS simulation data flow with the different steps for the MC and data processing.

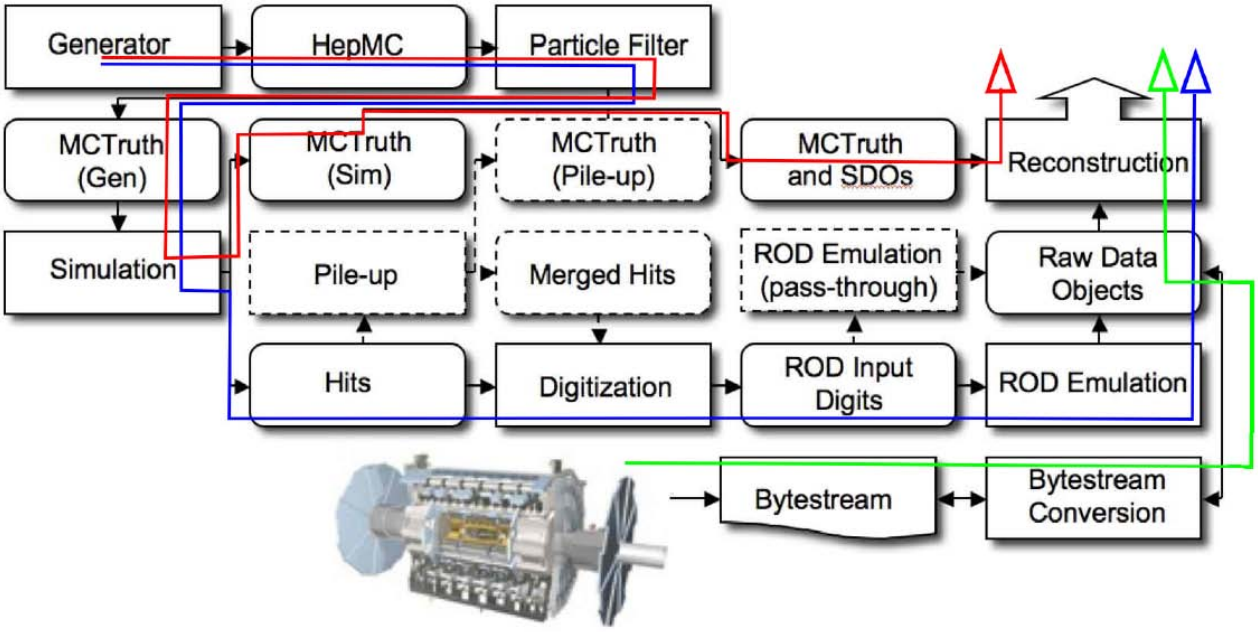

Figure 3.7: The flow of the ATLAS simulation software, from event generators (top left) through reconstruction (top right). The red path leads to particle level physics objects, the blue path to reconstructed level physics objects, while the green path shows the real data flow to physics objects. SDO stands for Simulated Data Object, ROD for Read Out Driver.

3.3 Monte Carlo corrections

The simulated event samples are normalised using the higher-order (typically at NLO in QCD) available cross section calculation for that process. Events are normalised to the integrated luminosity in order to compare the distributions with observed data. In addition, events are reweighted in order to match the expected number of interactions per bunch crossing $\langle\mu\rangle$ in real data-taking conditions. To ensure an accurate modeling of the detector effects, reconstruction and selection effciencies ε are corrected with multiplicative scale factors (SF) defined as

$$\mathrm{SF} = \frac{\varepsilon_{\mathrm{data}}}{\varepsilon_{\mathrm{MC}}}, \tag{3.8}$$

where $\varepsilon_{\mathrm{data}}$ and $\varepsilon_{\mathrm{MC}}$ are measured in dedicated data calibration samples and in the equivalent MC simulation, respectively. Analogously, energy scale and resolution of the different physics objects in the simulation are corrected to match the corresponding measurements in data.

AnalysisGroupName	average priority	#analysis (total / empty)	#tests (ok / total)
/LeptonJet	479.818	141 / 31	14 / 330
/PdfAnalysis	108.905	12 / 0	21 / 36
/PartCont	686.143	49 / 3	8 / 138

AnalysisName	Nr. of tests	OK			WARN			FAIL			unknown			empty histograms
		chi2	KS	bbb	chi2	KS	bbb	chi2	KS	bbb	chi2	KS	bbb	
/LeptonJet	141	3	11	0	15	21	0	92	78	110	0	0	0	31
/PdfAnalysis	12	12	9	0	0	1	0	0	2	12	0	0	0	0
/PartCont	49	1	7	0	0	6	0	45	33	46	0	0	0	3

Figure 3.8: A snapshot of the JEM graphical summary table with the colour-coded statistical tests output. In this example, JEM has highlighted in red the particle content (PartCont) validation as having a large number of histograms failing the regression tests. Roughly 200 histograms produced by the HepMCAnalysis tool are validated per sample.

3.4 Monte Carlo validation procedure

Most MC generators are programs written and maintained by authors external to the ATLAS Collaboration. Moreover, the validation of official ATLAS MC generator configurations in the ATLAS simulation infrastructure and production samples for physics analyses is critically important. To accomplish this task, an automated and central MC event generator validation procedure has been developed in ATLAS. The functionality and performance of the event simulation infrastructure, as well as constant validation of the revisions and updates of the MC generators and/or the ATLAS interface packages are carefully monitored. The validation is designed to be as uniform as possible to reduce the risk of using in physics analyses MC samples affected by problems. Comparisons of the shapes of numerous observables across different MC generators helps in identifying a variety of problems, ranging from simple mistakes in the MC generator user-defined settings to subtle-but-intentional changes in physics modelling. To ensure that the validated quantities are relevant to physical measurements, generator-independent observables defined in a theoretically-safe and unambiguous way are monitored. In some cases, technical MC generator quantities are verified (technical validation), which helps to identify MC generator internal changes. Validation includes also matrix element, particle-level and Rivet [136] validation of the process being tested. The framework used is HepMCAnalysis [137] that contains a collection of generator-independent validation tools based on the HepMC event record [138]. It provides broad information about final-state objects kinematics, particle content and properties), as well as PDF information about the event. The Job Execution Monitor (JEM) [139] is a Web interface used to configure and display the predefined sets of monitored and reference samples. The results of the validation tests are quickly available and presented in a flexible website (see figures 3.8 and 3.9). The agreement between the resulting pairs of histograms is quantified with several statistical tests, which include Kolmogorov-Smirnov, Pearson's χ^2 and a bin-by-bin methods. If no outstanding issues are found, the monitored sample is marked as "validated" and further distributed for large-scale MC production and use in physics analyses.

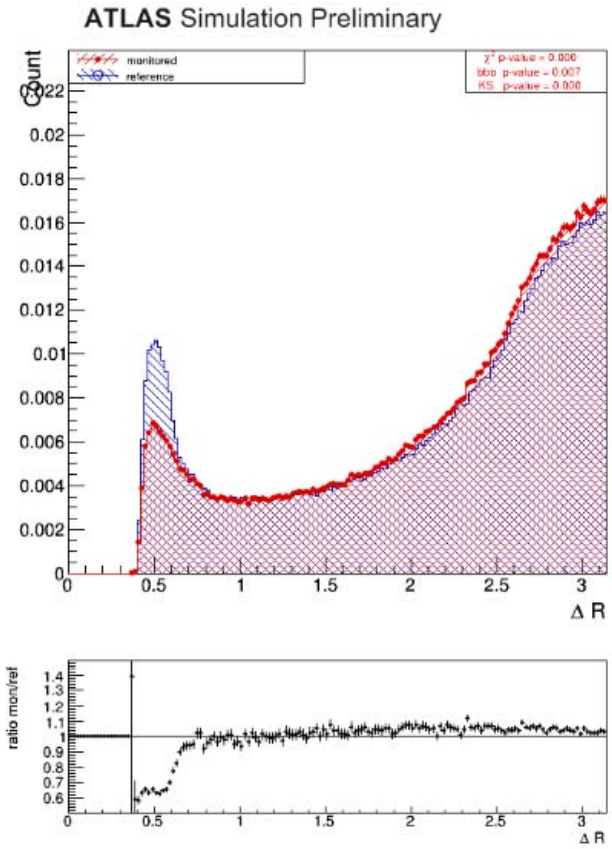

Figure 3.9: Example of a distribution used for MC validation after an upgrade of the ATLAS simulation infrastruture: ΔR between the two leading p_T jet in a dijet MC sample. The reference (monited) sample is displayed as a blue (red) histogram.

4 Event reconstruction

If I could remember the names of all these particles I'd be a botanist.
Enrico Fermi

Contents

The ATLAS detector records events as raw data, which correspond to bits of electric signal collected when particles interact with the detectors. The output information from all subdetectors is combined to form basic quantities such as tracks and calorimeter clusters. Finally, a particle identification step is performed, where the information from the relevant subdetectors is combined to reconstruct as accurately as possible a candidate physics object. In this chapter the techniques used to reconstruct,

identify and calibrate the physics objects used in the analyses presented in this dissertation are described. These objects include: tracks and vertices, electrons, muons, jets, and missing transverse momentum. A brief description of the systematic uncertainties associated with these physics objects is also provided.

4.1 Tracks

The solenoidal magnetic field of the ID bends charged particles in the transverse plane along an helicoidal trajectory with a radius of inversely proportional to its momentum. When charged particles traverse sensitive detector elements of the ID, they deposit energy through ionisation. These energy deposits are read out as hits, which are used to form space points. Each Pixel hit corresponds to one space point, while SCT space points are formed from pairs of SCT hits from each side of a module. Tracks are the reconstruction of these trajectories from the space points. Therefore, tracks enter at multiple levels in the definition of the physics objects used for physics analyses: from the reconstruction of electrons and muons, to the calculation of lepton isolation and the pileup suppression in jets, as well as reconstruction of decays of long-lived particles such as b-hadrons. In a nutshell, track reconstruction can be divided into the procedure of finding track candidates, the pattern recognition, and the estimation of the parameters that describe the particle trajectory, the track fit [140].

The reconstruction of tracks in the ID involves several algorithms. The main sequence is referred to as *inside-out* track finding, which consists of the following steps:

- Track finding starts with the formation of space point triplets (seeds).
- Seeds that pass the initial requirements are then input to a track-finding algorithm that attempts to complete the track candidates within the silicon detector combining space points.
- Ambiguities in track candidates are solved eliminating track candidates from random hit combinations or track duplicates.
- Track candidates passing the previous stage are extended outward to the TRT if they are within the TRT coverage.

For signals in the TRT that are not associated to any track candidate by the inside-out reconstruction, a second algorithm, referred to as *outside-in*, is applied in order to reconstruct tracks from secondary charged particles. The algorithm uses as seeds hits in the TRT and extrapolates to the silicon detector. Several optimisations of the track reconstruction were added for Run 2, from improvements to the seed purity, to an update of the ambiguity-solving method in dense environments [141].

A reconstructed track is characterised by the following set of parameter (see figure 4.1): $\tau = (d_0, z_0, \phi, \theta, q/p)$, where d_0 and z_0 stand for the track impact parameters in the transverse and longitudinal planes respectively, ϕ and θ denote the azimuthal and polar angle respectively, and q/p represents the charge over momentum. The impact parameters are often expressed with respect to the reconstructed hard-scatter primary vertex in the event.

The track reconstruction efficiency ε_{trk}, determined from the simulation, is parametrised in two-dimensional bins of p_{T} and η and is defined as:

$$\varepsilon_{\text{trk}}(p_{\text{T}}, \eta) = \frac{N_{\text{rec}}^{\text{matched}}(p_{\text{T}}, \eta)}{N_{\text{gen}}(p_{\text{T}}, \eta)}, \tag{4.1}$$

where $N_{\text{rec}}^{\text{matched}}(p_{\text{T}}, \eta)$ is the number of reconstructed tracks matched to a generated primary charged particle and $N_{\text{gen}}(p_{\text{T}}, \eta)$ is the number of generated primary charged particles in that bin. A track is

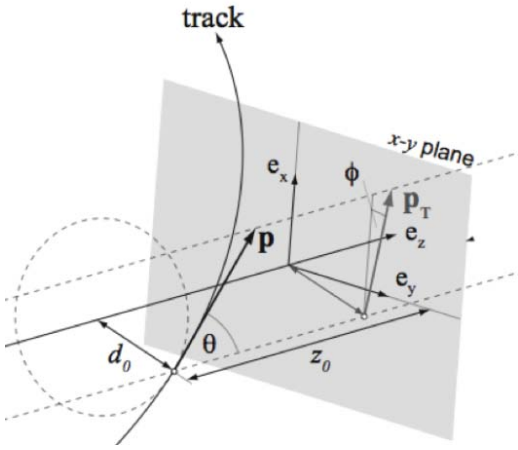

Figure 4.1: Illustration of the geometric definition of the track parameters.

matched to a generated particle if the weighted fraction of hits on the track that originate from that particle exceeds 50%. Figure 4.2 presents the track reconstruction efficiency estimated in simulated events with at least one charged particle with $p_{\mathrm{T}} > 500$ MeV and $|\eta| < 2.5$. The efficiency raises with p_{T} and it flattens out, reaching a value as high as $\approx 90\%$ for tracks with $p_{\mathrm{T}} > 5$ GeV. As a function of η, the efficiency averaged over p_{T} reaches $\approx 90\%$ in the central region and drops below 75% in the forward region.

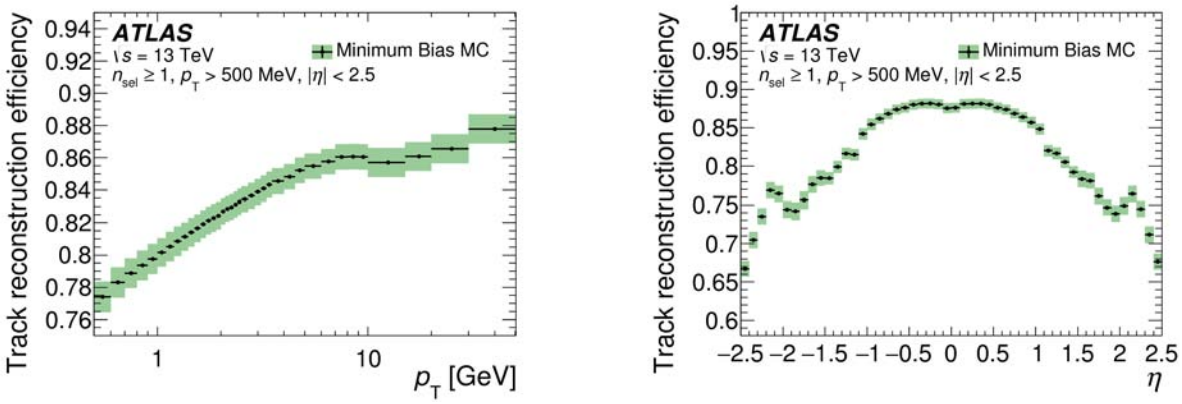

(a) (b)

Figure 4.2: The track reconstruction efficiency as a function of (a) p_{T} and (b) η as estimated in simulated minimum bias events. The statistical uncertainties are shown as black vertical bars, the combination of statistical and systematic uncertainties as green shaded areas. From Ref. [142]

4.2 Primary vertices

The reconstruction of the interaction points, referred to as Primary Vertices (PV), is essential to identify which one corresponds to the hard-scattering process and reconstruct the physics objects accordingly. At the high-luminosity regime in which LHC operates, multiple pp interactions occur per beam crossing, resulting in multiple PV candidates per event. The number of PVs in an event is used to measure the in-time pileup. PVs are reconstructed as points from which fitted tracks originate.

The reconstruction proceeds in two steps: the primary vertex finding, in which reconstructed tracks are associated to the vertex candidates, and the vertex fitting, in which the vertex position and the corresponding uncertainties are estimated. The vertex finding is an iterative procedure that runs over the set of tracks passing certain quality criteria in terms of a p_{T} threshold, the number of hits in the silicon detectors, as well as the longitudinal and transverse impact parameters and their resolutions. An adaptive vertex algorithm [143] fits the vertex position and associates tracks to it. Tracks incompatible with the fitted vertex are returned to the vertex finding for the next iteration. In order to improve the resolution on the vertex spatial position, only vertices that have at least two tracks with $p_{\mathrm{T}} > 400\,\mathrm{MeV}$ associated with them are considered. Among the reconstructed PV candidates consistent with the beam collision region (beamspot), the hard-scatter PV is chosen to be that with the highest sum of the squared transverse momenta of the tracks associated to it. The rest of the PVs are considered pileup interactions. Vertices incompatible with the beamspot are considered secondary vertices, also referred to as displaced vertices. The reconstruction of secondary vertices is useful to identify B- and D-hadrons, as will be described in section 4.4.5.

4.3 Leptons

The reconstruction and identification of electrons and muons is discussed. In this dissertation τ-leptons are not explicitly used, thus τ-lepton reconstruction techniques are not described. Although no attempt is made to identify τ-leptons, they would be identified either as isolated electrons or muons, or as (narrow) jets according to their decay.

4.3.1 Electrons

The reconstruction of electrons in the central region of the ATLAS detector ($|\eta| < 2.47$) starts from energy deposit (clusters) in the EM calorimeter, which are then associated to reconstructed tracks in the ID. A sliding-window algorithm [144] is used to search for electron clusters. Seed clusters are established as longitudinal towers consisting of 3×5 calorimeter segments ($\Delta\eta\times\Delta\phi = 0.025\times0.025$, the granularity of the calorimeter middle layer) with transverse energy $E_{\mathrm{T}} > 2.5\,\mathrm{GeV}$. Electron candidates are formed as seed clusters matched to at least one ID track. The standard pattern recognition for track reconstruction uses the pion hypothesis for energy loss at material surfaces. A modified pattern recognition algorithm for the electron hypothesis allows at most 30% energy loss at each material surface to account for possible bremsstrahlung. Thus, track candidates are fitted either with the pion hypothesis or the electron hypothesis. Tracks, extrapolated in the calorimeter middle layer, are then matched with relaxed criteria to EM clusters. Matched tracks are refitted with stricter conditions to build electron candidates. The track associated with the electron has to be compatible with the hard-scatter PV in order to reduce the background from conversions and secondary particles. The following requirements are made: $|d_0|/\sigma_{d_0} < 5$ and $|z_0 \sin\theta| < 0.5$ mm, where d_0, z_0 and θ are defined in section 4.1. The electron cluster is then rebuilt using 3×7 (5×5) longitudinal towers of cells in the barrel (endcaps) of the EM calorimeter. The energy of the clusters is calibrated to the original electron energy using multivariate techniques [145] based on simulated MC samples. The calibrated cluster energy is determined as a sum of the measured energy deposit in the cluster and the estimated energy deposits in the material in front of the EM calorimeter, in the neighbouring EM segments (lateral leakage) and beyond the EM calorimeter (longitudinal leakage). The momentum of the matched track is also used in the calculation. The η and ϕ directions of an electron are those of the corresponding track, unless the track contains only TRT hits, in which case the η is determined from the cluster pointing (η_{cl}) due to the insufficient resolution of the TRT.

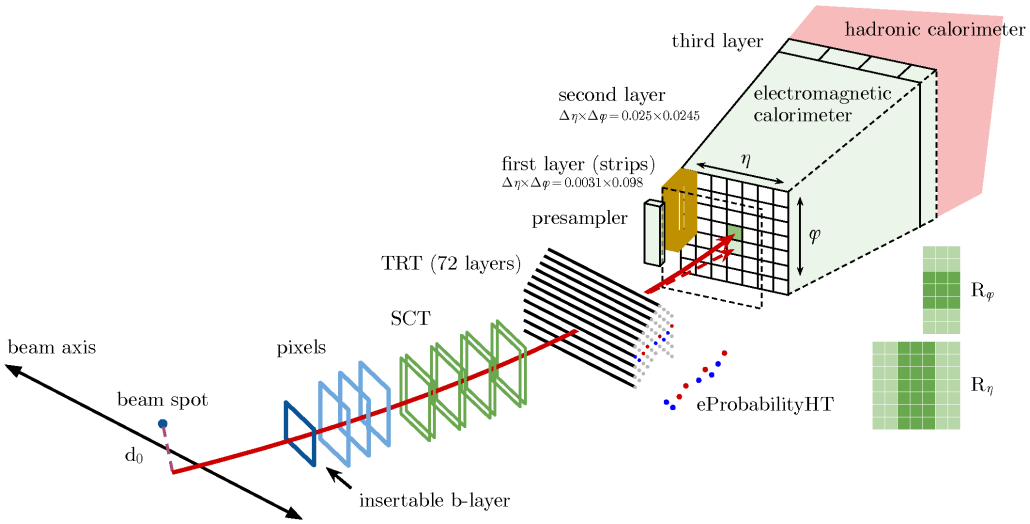

Figure 4.3: Illustration of the electron reconstruction and identification.

Electron identification algorithms [144] use quantities related to the electron cluster and track measurements including calorimeter shower shapes, information from the TRT, track-cluster matching-related quantities, track properties, and variables measuring bremsstrahlung effects used to distinguish electrons from background mimicking them (e.g. hadronic jets or converted photons). The shower development is narrower for electrons than for hadrons, and the hadronic leakage is smaller. Track quality requirements reduce the impact of accidental track association with photons, energetic π^0 or η mesons with electromagnetic decays reconstructed as a single energy cluster. The baseline identification algorithm exploits several properties of the electron candidate, combined using a likelihood-based (LH) method.[1] The list of the discriminating variables used in the electron LH can be found in table 4.1. Several changes to the input variables have been introduced for Run 2. The number of hits in the innermost pixel layer discriminates electrons against converted photons and, with the installation of the IBL, this variable was redefined. Furthermore, a LH based on the TRT high-threshold hits (eProbabilityHT) is introduced to compensate for the lower transition radiation absorption probability, due to the change of the gas (Ar).

Three operating points for electron identification, with increasing background rejection, are defined:: *Loose*, *Medium* and *Tight*. Operating points are defined such that the samples selected by them are subsets of one another (e.g. electrons satisfying the *Medium* criteria also satisfy the *Loose* criteria). Since the distributions of electron shower shapes depend on the amount of material traversed by electrons and on the number of pileup collisions per bunch crossing, the ID operating points were optimised in several bins of $|\eta|$ and E_T and as a function of the number of primary vertices, in order to ensure efficient identification at high pileup. The electron identification efficiency is measured in $Z \to e^+e^-$ events in data and MC using the tag-and-probe method, as illustrated in figure 4.4.

To further disentangle prompt electrons from electrons or photons produced in hadron decays, an additional requirements on the total transverse momentum within a cone around the electron direction are imposed. The selection exploits both track-based and calorimeter-based isolation. The track isolation variable $p_{\mathrm{T}}^{\mathrm{varcone0.2}}$ is the sum of the transverse momenta of all the tracks within a cone of size $\Delta R = \min(0.2, 10\,\mathrm{GeV}/E_T)$ around the electron direction. Only tracks with $p_{\mathrm{T}} > 1\,\mathrm{GeV}$

[1] The LH method uses the signal and background probability density functions (PDFs) of the discriminating variables. Based on these PDFs, an overall probability, defined as the product of the individual PDFs, is calculated for the object to be signal or background.

Type	Name	Description
Hadronic leakage	R_{had1}	Ratio of E_T in the first layer of the hadronic calorimeter to E_T of the EM cluster (used over the range $\|\eta\| < 0.8$ or $\|\eta\| > 1.7$)
	R_{had}	Ratio of E_T in the hadronic calorimeter to E_T of the EM cluster (used over the range $0.8 < \|\eta\| < 1.7$)
Back layer of EM calorimeter	f_3	Ratio of the energy in the back layer to the total energy in the EM accordion calorimeter (used <100 GeV)
Middle layer of EM calorimeter	$w_{\eta 2}$	Lateral shower width, $\sqrt{(\sum E_i \eta_i^2)/(\sum E_i) - ((\sum E_i \eta_i)/(\sum E_i))^2}$, where E_i is the energy and η_i is the pseudorapidity of cell i and the sum is calculated within a windows of 3×5 cells
	R_Φ	Ratio of the energy in 3×3 cells over the energy in 3×7 cells centered at the electron cluster position
	R_η	Ratio of the energy in 3×7 cells over the energy in 7×7 cells centered at the electron cluster position
Strip layer of EM calorimeter	w_{stot}	Shower width, $\sqrt{(\sum E_i (i - i_{\max})^2)/(\sum E_i)}$, where i runs over all strips in a window of $\Delta\eta \times \Delta\phi \approx 0.0625 \times 0.02$, corresponding typically to 20 strips in η, and $i_{\max}$ is the index of the highest-energy strip
	E_{ratio}	Ratio of the energy difference between the largest and second largest energy deposits in the cluster over the sum of these energies
	f_1	Ratio of the energy in the strip layer to the total energy in the EM accordion calorimeter
Track conditions	n_{Blayer}	Number of hits in the innermost pixel layer (IBL)
	n_{Pixel}	Number of hits in the pixel detector
	n_{Si}	Number of total hits in the pixel and SCT detectors
	d_0	Transverse impact parameter with respect to the beam-line
	$d_0/\sigma d_0$	Significance of transverse impact parameter defined as the ratio of d_0 and its uncertainty
	$\Delta p/p$	Momentum lost by the track between the perigee and the last measurement point divided by the original momentum
TRT	eProbabilityHT	Likelihood probability based on transition radiation in the TRT
Track-cluster matching	$\Delta\eta_1$	$\Delta\eta$ between the cluster position in the strip layer and the extrapolated track
	$\Delta\phi_2$	$\Delta\phi$ between the cluster position in the middle layer and the track extrapolated from the perigee
	$\Delta\phi_{\text{res}}$	Defined as $\Delta\phi_2$, but the track momentum is rescaled to the cluster energy before extrapolating the track from the perigee to the middle layer of the calorimeter
	E/p	Ratio of the cluster energy to the track momentum

Table 4.1: Discriminating variables used in the electron LH.

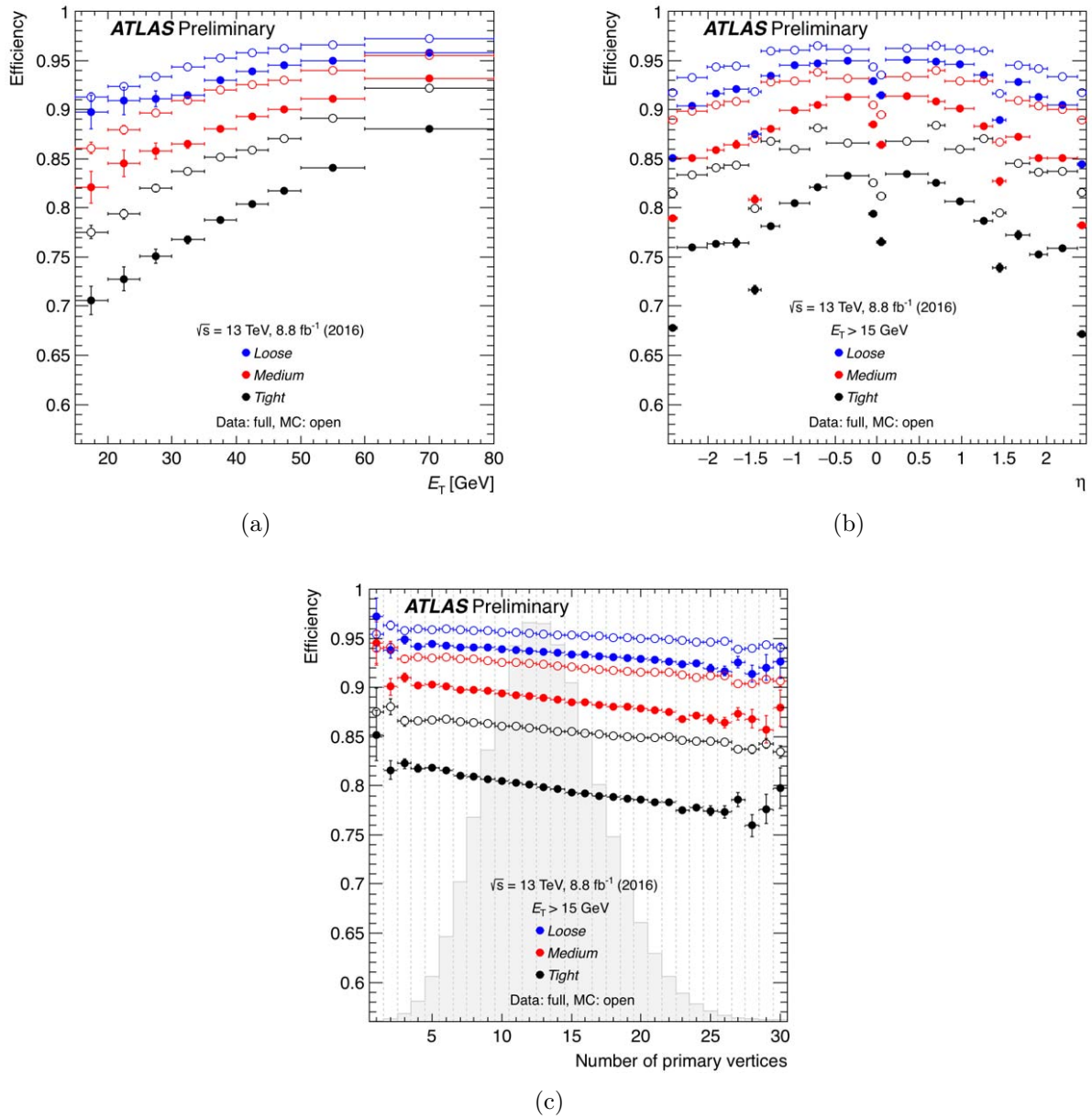

Figure 4.4: Electron identification efficiencies for the different operating points obtained using the tag-and-probe method in $Z \to e^+e^-$ events, as a function of (a) transverse energy E_T, (b) pseudorapidity η and (c) number of reconstructed primary vertices. From Ref. [144].

and compatible with originating from the hard-scatter PV are considered, with the exception of the track used to build the electron candidate. The cone size is chosen to be p_{T}-dependent to improve performance for electrons produced in the decay of particles with large transverse momentum. The calorimetric isolation variable $E_T^{\mathrm{cone0.2}}$ represents the sum of the transverse energy of the calorimetric cells in a cone of size $\Delta R = 0.2$ around the electron, after subtraction of the energy deposits associated with the electron itself and pileup contributions. A variety of operating points are provided with different requirements on $E_T^{\mathrm{cone0.2}}/E_T$ and $p_{\mathrm{T}}^{\mathrm{varcone0.2}}/p_{\mathrm{T}}$. The isolation efficiency corresponding to these operating points can be either constant or a function of E_T. The isolation efficiency for the various operating points estimated for electrons from simulated $Z \to e^+e^-$ events is summarised in

Electron isolation OP	Calorimeter isolation efficiency	Track isolation efficiency	Total efficiency
LooseTrackOnly	-	99%	99%
Loose	99%	99%	$\sim 98\%$
Tight	96%	99%	$\sim 95\%$
Gradient	$0.1143\% \times E_T + 92.14\%$	$0.1143\% \times E_T + 92.14\%$	90/99% at E_{T} =25/60 GeV
GradientLoose	$0.057\% \times E_T + 95.57\%$	$0.057\% \times E_T + 95.57\%$	95/99% at E_{T} =25/60 GeV

Table 4.2: Electron isolation efficiency operating points (OP).

table 4.2.

Reconstruction, identification, isolation, and trigger efficiencies are the different components of the total efficiency $\varepsilon_{\mathrm{total}}$ to find and select an electron in the ATLAS detector:

$$\varepsilon_{\mathrm{total}} = \varepsilon_{\mathrm{reconstruction}} \times \varepsilon_{\mathrm{identification}} \times \varepsilon_{\mathrm{isolation}} \times \varepsilon_{\mathrm{trigger}}, \tag{4.2}$$

with the various components measured relative to the previous requirement. To measure those efficiencies the tag-and-probe method is used. The method employs events containing well-known resonance decays to electrons ($Z \to e^+e^-$ and $J/\Psi \to e^+e^-$) with strict selection criteria on the event selection and on one of the electron (*tag*). The *probe* electron is used for the measurement of the reconstruction, identification, isolation and trigger efficiencies, after accounting for the residual background contamination. The low-E_T range (from 7 to 20 GeV) is covered by $J/\Psi \to e^+e^-$ events, while $Z \to e^+e^-$ events are used for measurements above 15 GeV. The efficiencies are estimated both in data and in simulation and their ratio is used as a scale factor to correct the simulation. These scale factors, derived as a function of electron E_T and η, typically deviate from unity by only a few percent. The combined uncertainties on the reconstruction, identification, isolation and trigger requirement scale factors are at the level of few percent at low E_T and below 1% at high E_T.

The electron energy scale has been measured in data using $Z \to e^+e^-$ event. Correction factors as a function of the electron η are derived to match the known value of the Z-boson mass. The total uncertainty on the electron in-situ calibration is $< 1\%$ in the central region [144]. The main way to probe the electron energy resolution is provided by the study of the Z resonance width. It is found that the resolution in data is slightly worse than that in simulation, and appropriate corrections are derived and applied to the simulation to match the data.

The analyses presented in this dissertation use the *Tight* electron definition since it requires the largest possible rejection of misidentified electrons. Electrons are required to be central ($|\eta| < 2.47$) and to be outside the transition region between the barrel and end-cap EM calorimeter ($1.37 < |\eta| < 1.52$), since this region shows worse reconstruction and energy resolution performances. Finally, electron isolation (*Gradient* OP) is required to reject electrons from semileptonic hadron decays. A different electron definition, with looser selection criteria, is also be used to estimate the contribution of multijet events where a jet is reconstructed as an electron. This looser definition uses *Medium* as identification criteria and no isolation requirement. The use of this looser electron set will be described in detail in section 5.2.6.

4.3.2 Muons

Muons are reconstructed using four different strategies [146], depending on which subdetectors are used in the reconstruction. Muons used in this dissertation are *combined muons*, which exploit measurements from the ID and the MS. A pattern recognition algorithm forms segments in the MS starting from hits in the different subsystems. Muon track candidates in the MS are seeded by segments in the

middle layers of the MS. The fitting procedure uses a combinatorial search to combine segments in the track candidate, taking into account the muon energy loss in the calorimeter. Once track candidates are built, an overlap removal procedure is applied to remove shared segments and the track is refitted with a stricter selection criteria. For combined muons, a global fit of ID and MS tracks is performed. Most muons are reconstructed following an outside-in algorithm, in which the muons are first reconstructed in the MS and then extrapolated inward and matched to an ID track. An inside-out combined reconstruction is used as a complementary approach. In Run 2, muon reconstruction algorithms have been improved providing a better background rejection in the pattern recognition and an improved calculation of the energy loss in the calorimeter [146].

Muon identification is performed by applying quality requirements that suppress background, mainly from pion and kaon decays, while selecting prompt muons with high efficiency and ensuring a robust momentum measurement. The variables used in the muon identification are listed below:

- q/p significance, defined as the absolute value of the difference between the ratio of the charge and momentum of the muons measured in the ID and MS, divided by the sum in quadrature of the corresponding uncertainties;
- ρ', defined as the absolute value of the difference between the transverse momentum measurements in the ID and MS, divided by the p_{T} of the combined track;
- normalised χ^2 of the combined track fit;
- ≥ 1 pixel hit;
- ≥ 5 SCT hits;
- < 3 Pixel or SCT holes;[2]
- at least 10% of the TRT hits originally assigned to the track are included in the final fit (in the $0.1 < |\eta| < 1.9$ range).

Four operating points for muon identification are defined: *Loose*, *Medium*, *Tight* and *High-*p_T. In this dissertation *Medium* muons are used. The *Medium* the identification criteria provides the default selection for muons in ATLAS, minimizing the systematic uncertainties associated with muon reconstruction and calibration. *Medium* identification applies the following additional requirements on the muon:

- ≥ 3 hits in at least two MDT layers except for tracks in the $|\eta| < 0.1$ region, where tracks with at least one MDT layer but no more than one MDT hole layer are allowed;
- q/p significance < 7.

Similarly to electrons, to further disentangle prompt muons from heavy-flavour hadron semileptonic decays, additional requirements on the total transverse energy and momentum within the corresponding cones around the muon direction are imposed. The selection exploits both track-based and calorimeter-based isolation. The track isolation variable $p_{\mathrm{T}}^{\mathrm{varcone30}}$ is the sum of the transverse momenta of the tracks with $p_{\mathrm{T}} > 1\,\mathrm{GeV}$ within a cone of size $\Delta R = \min(0.3, 10\,\mathrm{GeV}/p_{\mathrm{T}}^{\mu})$ around the muon direction, excluding the muon track itself. The cone size is chosen to be p_{T}-dependent for the same reason as for electrons. The calorimeter isolation variable $E_T^{\mathrm{topocone20}}$ represents the sum

[2] A hole is defined as an active sensor traversed by the track but containing no hits.

Muon isolation OP	Discriminating variable	Definition
LooseTrackOnly	$p_{\mathrm{T}}^{\mathrm{varcone30}}/p_{\mathrm{T}}^{\mu}$	99% efficiency constant in η and p_{T}
Loose	$p_{\mathrm{T}}^{\mathrm{varcone30}}/p_{\mathrm{T}}^{\mu}$, $E_T^{\mathrm{topocone20}}/p_{\mathrm{T}}^{\mu}$	99% efficiency constant in η and p_{T}
Tight	$p_{\mathrm{T}}^{\mathrm{varcone30}}/p_{\mathrm{T}}^{\mu}$, $E_T^{\mathrm{topocone20}}/p_{\mathrm{T}}^{\mu}$	96% efficiency constant in η and p_{T}
Gradient	$p_{\mathrm{T}}^{\mathrm{varcone30}}/p_{\mathrm{T}}^{\mu}$, $E_T^{\mathrm{topocone20}}/p_{\mathrm{T}}^{\mu}$	$\geq$90(99)% efficiency at p_{T}=25(60) GeV
GradientLoose	$p_{\mathrm{T}}^{\mathrm{varcone30}}/p_{\mathrm{T}}^{\mu}$, $E_T^{\mathrm{topocone20}}/p_{\mathrm{T}}^{\mu}$	$\geq$95(99)% efficiency at p_{T}=25(60) GeV
FixedCutTightTrackOnly	$p_{\mathrm{T}}^{\mathrm{varcone30}}/p_{\mathrm{T}}^{\mu}$	$p_{\mathrm{T}}^{\mathrm{varcone30}}/p_{\mathrm{T}}^{\mu}<0.06$
FixedCutLoose	$p_{\mathrm{T}}^{\mathrm{varcone30}}/p_{\mathrm{T}}^{\mu}$, $E_T^{\mathrm{topocone20}}/p_{\mathrm{T}}^{\mu}$	$p_{\mathrm{T}}^{\mathrm{varcone30}}/p_{\mathrm{T}}^{\mu}<0.15$, $E_T^{\mathrm{topocone20}}/p_{\mathrm{T}}^{\mu}<0.30$

Table 4.3: Muon isolation efficiency operating points (OP).

of the transverse energy of the topological clusters (see section 4.4.1) in a cone of size $\Delta R = 0.2$ around the muon, after subtraction of the energy deposits associated with the muon itself and pileup contributions. Seven operating points with different requirements on $E_T^{\mathrm{topocone20}}/p_{\mathrm{T}}^{\mu}$ and $p_{\mathrm{T}}^{\mathrm{varcone30}}/p_{\mathrm{T}}^{\mu}$ are defined. The isolation efficiency provided by these operating points can be either constant or a function of p_{T}^{μ}. The isolation efficiency for the various operating points estimated for muons from simulated $Z \to \mu^+\mu^-$ events is summarised in table 4.3.

Like for the electrons, reconstruction/identification and isolation efficiencies are measured in data and simulation with the tag-and-probe method using $Z \to \mu^+\mu^-$ events (for p_{T}^{μ}>15 GeV) and $J/\Psi \to \mu\mu$ events (for 5<p_{T}^{μ}<15 GeV). Muon reconstruction efficiencies are shown in figure 4.5. The total uncertainty on the SFs for medium muons is $< 2\%$ at low p_{T}^{μ} (<15 GeV) and at the per-mille level at higher p_{T}^{μ}.

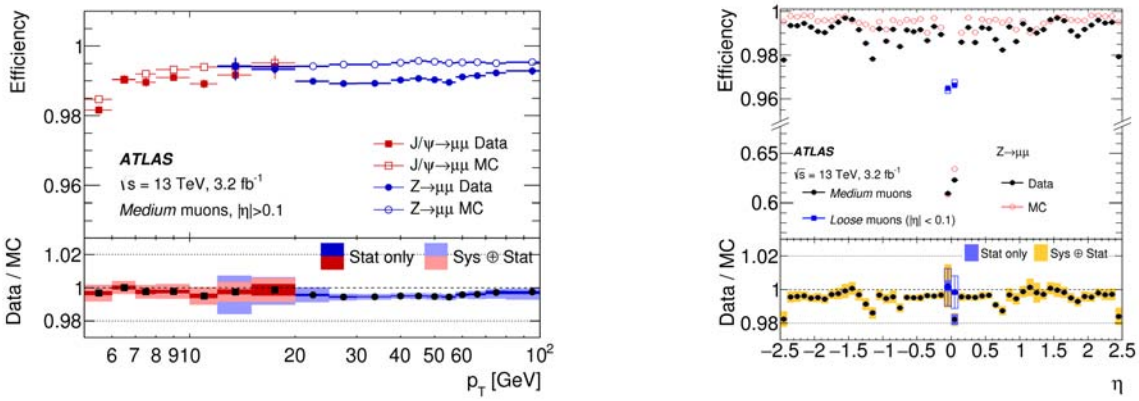

(a) (b)

Figure 4.5: Muon reconstruction efficiencies for the different operating points obtained using the tag-and-probe method in $Z \to \mu^+\mu^-$ and $J/\Psi \to \mu^+\mu-$ events, as a function of (a) transverse momentum p_{T} and (b) pseudorapidity η. From Ref. [146].

The muon momentum scale has been measured in data using $Z \to \mu^+\mu^-$ and $J/\Psi \to \mu\mu$ events. Correction factors as a function of the muon p_{T} in different regions of η are derived to match the known value of the Z-boson mass. The total uncertainty on the muon momentum scale varies from a minimum of $< 0.05\%$ in the barrel region to a maximum of 0.3% for $|\eta| \sim 2.5$ [146]. The main way to probe the muon momentum resolution is provided by the study of the Z and J/Ψ resonance width. It is found that the resolution in data is slightly worse than that in simulation, and appropriate corrections are derived and applied to simulation to match the data.

As briefly discussed above, the analyses presented in this dissertation use the medium combined

muons and *Gradient* muon isolation is required to reject muons from semileptonic hadron decays. A different muon definition, with no isolation requirement, will also be used to estimate the contribution of multijet events as described in section 5.2.6.

4.4 Jets

Color confinement is the reason why quarks and gluons produced in the hard interactions can not be found free. Jets are spray of collimated particles produced by the hadronisation of quarks and gluons. The jet definition aims at grouping this set of particles in order to obtain a physics object whose characteristics are as close as possible to those of the initial parton. Different types of jets can be defined depending on the input objects and algorithms employed to group them into a jet. Jets reconstructed from truth stable particles in MC samples are denoted as particle jets. Jets built from reconstructed tracks in the detector are called track jets. Jets built from energy deposits in the calorimeter are usually referred to as reconstructed jets or simply jets. Jets built from other reconstructed jets are denoted as reclustered jets.

4.4.1 Topoclusters

Calorimeter cells with energy deposits are grouped in three dimensional objects referred to as topoclusters [147]. A topocluster is designed to follow the shower development of a single particle interacting with the calorimeter, taking advantage of the calorimeters' granularity. Topoclusters are formed through an iterative procedure that identifies the most significant energy deposits E_{cell} with respect to their noise (electronic and from pileup) level σ_{noise}, referred to as "seed cells", and then clusters neighbouring cells into a single topocluster. Seed cells are first identified as the calorimeter cells with an energy significantly above a predefined noise threshold, $|E_{\text{cell}}|/\sigma_{\text{noise}} > 4$. The seed cell forms a protocluster and neighbouring cells are iteratively added to it if they satisfy $|E_{\text{cell}}|/\sigma_{\text{noise}} > 2$. Once the iterative process ends and a stable protocluster is formed, all cells adjacent to the protocluster are added, independent of the magnitude of their signal. Through this method a topocluster is formed by a core of cells with significant energy surrounded by an envelope of cells containing any residual or leaked energy (see figure 4.6). Topoclusters are calibrated at the EM scale, which correctly measures the energy in the calorimeter deposited by particles produced in an electromagnetic shower.

4.4.2 Jet finding

Jet-finding algorithms attempt to group inputs into individual jets. To be theoretically well defined at all orders in perturbation theory, jet-finding algorithms need to be infrared-safe[3] and collinear-safe[4] [148]. The anti-k_{T} algorithm [149] is a sequential recombination algorithm that satisfies the above conditions and that has become the most widely-used jet reconstruction algorithm at LHC. This algorithm combines iteratively two inputs into a jet based on the p_{T}-weighted distance between them, as defined in equation 4.3, and between each input and the LHC beam, as defined in equation 4.4. The algorithm defines two distances:

$$d_{ij} = \min\left(k_{Ti}^{2p}, k_{Tj}^{2p}\right)\frac{\Delta R_{ij}^2}{R^2}, \text{ and} \tag{4.3}$$

$$d_{iB} = k_{Ti}^{2p}, \tag{4.4}$$

[3] If the set of inputs is modified by a soft emission, the sets of hard jets found should remain unchanged.
[4] If the set of inputs is modified by a collinear splitting, the sets of hard jets found should remain unchanged.

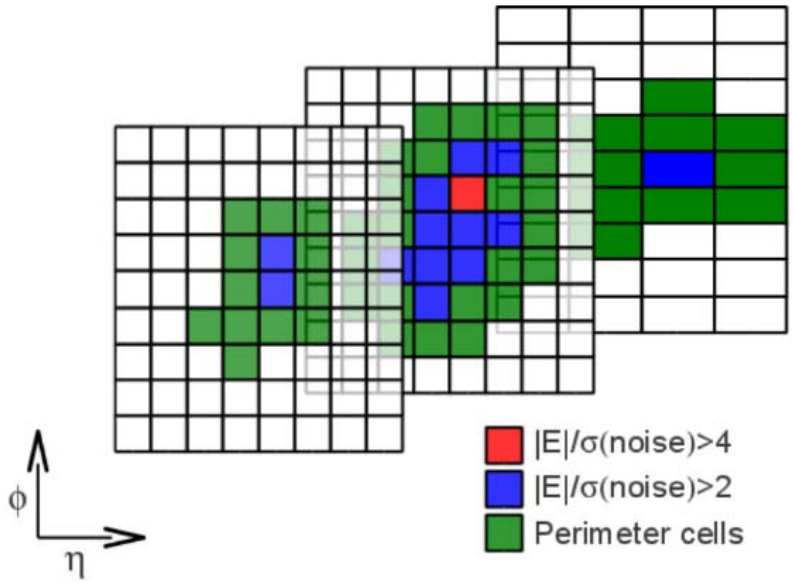

Figure 4.6: Illlustration of the formation of a topocluster in the three hadronic layers in the barrel. The grid represents calorimeter cells.

where k_{Ti} is the p_{T} of input i, $\Delta R_{ij}^2 = (\eta_i - \eta j)^2 + (\phi_i - \phi j)^2$ is the distance squared between inputs i and j, R is a radius parameter that defines the size of the jet, and p is a configurable exponent that is set to $p = -1$ for the anti-k_{T} algorithm. This configuration ensures that clustering is initiated by high transverse momentum objects and that the soft objects preferentially recombine with a high-p_{T} object rather than with each other, which provides rather circular jets. The algorithm starts by identifying the two four-vectors of an event with the smallest distance d_{ij}. If $d_{ij} < d_{iB}$, the two inputs are removed from the event and replaced by a single combined object, simply obtained by adding the four-momenta of the two inputs. The smallest distance d_{ij} between all inputs is then recalculated, and the sequential recombination procedure continues. If d_{iB} is the minimum distance then the input i is designated as a final jet and removed from the event. The procedure continues until all inputs have been classified into jets. Figure 4.7 illustrates the clustering of hard and soft particles into jets when the anti-k_{T} algorithm is applied. The jet radius parameter R defines the size of the jet and its choice is driven by the physics analysis. A larger value of R captures more of the deposited energy, particularly for particles with wide showers, while a jet reconstructed using a smaller value of R is less affected by pileup. Values of R such as 0.2, 0.4 or 1.0 are common in physics analyses. The analyses described in this dissertation use anti-k_{T} jets with $R = 0.4$, referred to as "small-R jets".

4.4.3 Jet calibration

As discussed previously, jets formed from topoclusters are reconstructed at the EM scale. The goal of the jet calibration procedure is to correct the energy of the reconstructed jets to correspond to that of the truth particle jets. This involves a series of corrections derived both from MC simulation and data, with the latter referred to as in-situ corrections [150]. The calibration scheme for calorimeter jets is illustrated in figure 4.8 and described in the following sections.

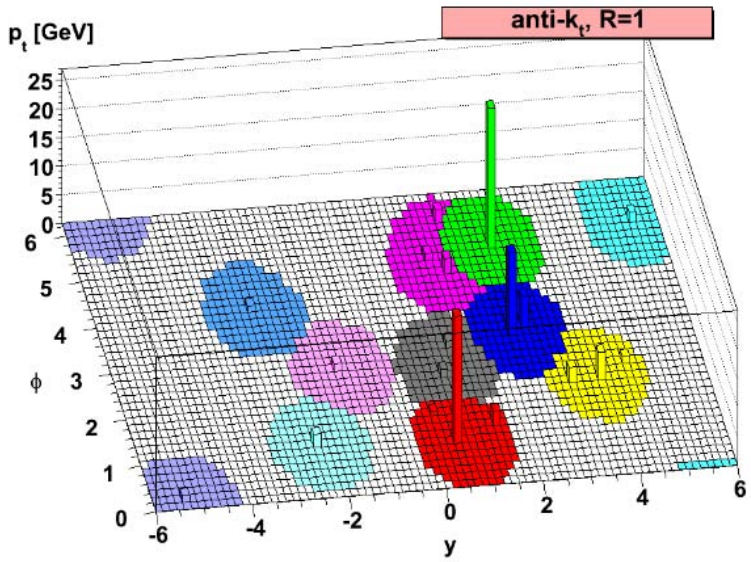

Figure 4.7: Illustration of the clustering of jets with the anti-k_{T} algorithm.

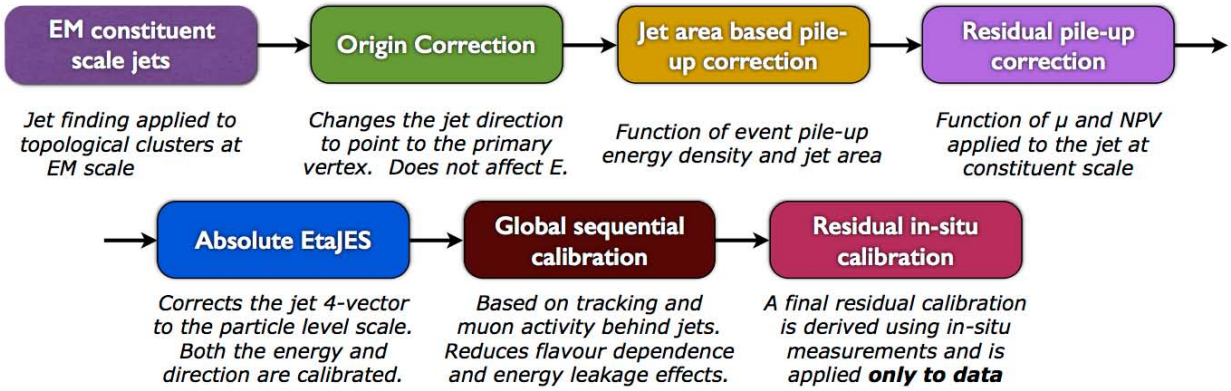

Figure 4.8: Overview of the jet calibration procedure.

4.4.3.1 Origin correction

The origin correction recalculates the four-momentum of jets to point to the hard-scatter PV rather than to the centre of the detector, as done by default in the clustering algorithm. This correction improves significantly the η resolution of jets.

4.4.3.2 Pileup correction

The pileup correction accounts for additional energy deposited within the jet radius from in-time and out-of-time pileup. Pileup is assumed, on average, to deposit energy uniformly in η and ϕ throughout the detector, providing a diffuse background that may be subtracted from individual jets [151]. The correction is performed in three steps according to this equation:

$$p_{\mathrm{T}}^{\mathrm{corr}} = p_{\mathrm{T}} - \rho \cdot A - \alpha \cdot (N_{\mathrm{PV}} - 1) - \beta \cdot \langle \mu \rangle, \tag{4.5}$$

where ρ is the pileup energy density of the event based on the median energy density of jets, N_{PV}

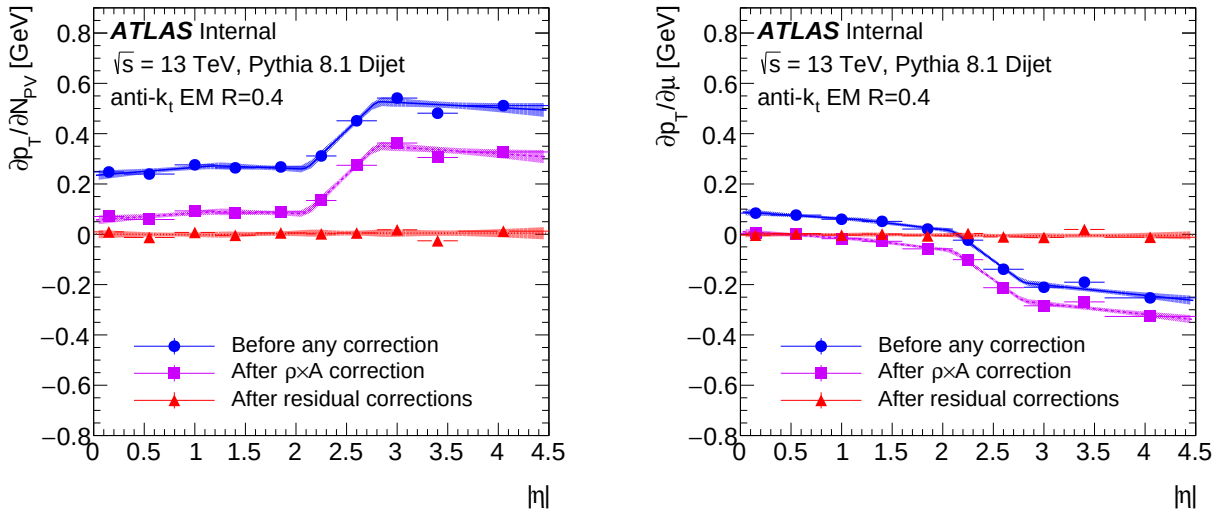

(a) (b)

Figure 4.9: Dependence of the reconstructed jet p_{T} on (a) in-time pileup (N_{PV}) and (b) out-of-time pileup ($\langle\mu\rangle$) as a function of $|\eta|$. The dependence is shown before pileup corrections (circle), after area subtraction (square), and after the residual correction (triangle).

the number of primary vertices, $\langle\mu\rangle$ the average number of interactions per crossing, $\alpha = \frac{\partial p_{\mathrm{T}}}{\partial N_{\mathrm{PV}}}$ and $\beta = \frac{\partial p_{\mathrm{T}}}{\partial \mu}$. The first step represents the jet-area correction which allows a jet-by-jet estimation and subtraction of the energy added to the jet by the pileup. The area A of a jet is calculated using ghost association[5] [152]. The area of a jet is determined by the number of ghost particles associated to a jet after clustering. The additional terms in the formula represent residual corrections that remove the remaining effects for both in-time (α) and out-of-time (β) pileup. Figure 4.9 shows the dependence of jet p_{T} on N_{PV} and $\langle\mu\rangle$ as a function of jet $|\eta|$ at various steps of the correction procedure.

4.4.3.3 Jet energy scale and η correction

The measured jet energy at the EM scale is lower than that at the particle level due to unmeasured energy deposited in inactive detector regions or outside of the jet radius (out-of-cone radiation), the noncompensation[6] of the hadronic calorimeters, or topocluster reconstruction inefficiencies. After pileup correction, the jet energy scale (JES) and η correction restores the reconstructed jet energy to the particle-level jet energy and accounts for detector effects in the jet η reconstruction caused primarily by the transition between different calorimeter technologies and corresponding granularities. The calibration is derived from MC using isolated reconstructed calorimeter jets that are matched geometrically to truth jets within $\Delta R < 0.3$. The ratio of reconstructed jet energy to true jet energy is parametrised as a function of the reconstructed jet's p_{T} and η and its inverse is applied as an energy correction. The average energy response is shown in figure 4.10.

[5] "Ghost" particles of infinitesimal momentum are added uniformly to the event before jet reconstruction.

[6] Noncompensation refers to the different calorimeter response to non-electromagnetic and electromagnetic components of hadron showers.

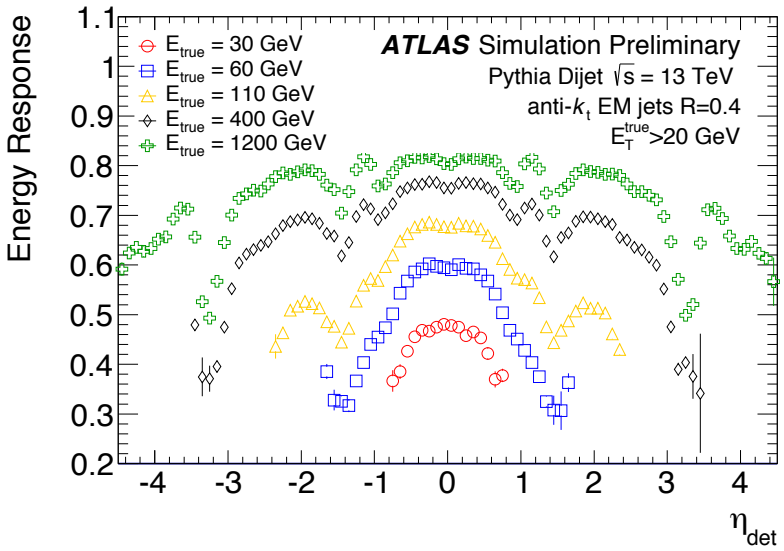

Figure 4.10: Average energy response for jets built from topoclusters at the EM scale. The response is shown separately for various particle-jet energies as function of the jet pseudo-rapidity $|\eta_{\text{det}}|$.

4.4.3.4 Global sequential calibration

The global sequential calibration is a set of independent and sequential corrections designed to remove a residual dependence of jet energy found on longitudinal and transverse features of the jet, primarily due to differences in the shower profiles between jets initiated by quarks and by gluons. Variables used in these corrections are:

- the fraction of energy measured in the first layer of the Tile calorimeter ($|\eta| < 1.7$),
- the fraction of energy measured in the third layer of the EM calorimeter ($|\eta| < 3.5$),
- the number of tracks associated to the jet with $p_{\text{T}} > 1$ GeV ($|\eta| < 2.5$),
- the width of the tracks associated with the jet, defined by the p_{T}-weighted average distance between all constituent tracks and the jet ($|\eta| < 2.5$), and
- the number of muon segments associated with the jet ($|\eta| < 2.7$).

Tracks and muon segments are associated to jets through ghost association. An additional correction, using track segments reconstructed in the muon spectrometer to identify high-p_{T} jets that are not fully contained in the calorimeter (punch-through), is applied to reduce non-Gaussian tails in the jet response distribution.

4.4.3.5 In-situ jet calibration

In the last step of the jet calibration differences in jet response between data and MC are quantified by balancing the p_{T} of individual jets against well-measured physics objects. The ratio between the

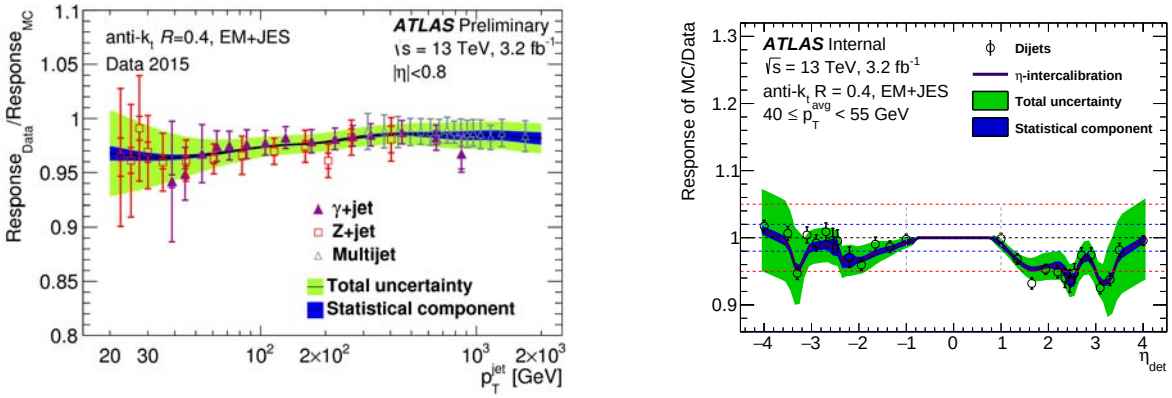

(a) (b)

Figure 4.11: Ratio of the average jet response in data to that measured in MC simulation (a) as a function of jet p_{T} for different in-situ calibration techniques (γ+jet, Z+jet, and multijet balance) and (b) as a function of jet η for jets with $40 < p_{\mathrm{T}} < 55$ GeV using the dijet balance technique.

response in data and MC is derived as function of jet p_{T} and η and applied as a correction to the jets in the simulation. The in-situ techniques [150] used to derive such correction are:

- Dijet balance (η-intercalibration): corrects the p_{T} of forward jets ($0.8 < |\eta| < 4.5$) to that of central jets ($|\eta| < 0.8$) in a dijet system, up to a p_{T} of 1.2 TeV;
- γ/Z+jet balance: corrects the p_{T} of central jets ($|\eta| < 0.8$) to that of a well-measured photon (up to p_{T} of 950 GeV) or Z boson (up to p_{T} of 260 GeV) in γ/Z+jet events.
- Multijet balance: calibrates central high-p_{T} jets ($300 \leq p_{\mathrm{T}} \leq 2000$ GeV) in events with a collection of well calibrated lower-p_{T} jets.

Figure 4.11 shows the ratio of the jet response as function of jet p_{T} and η for the three in-situ calibrations.

4.4.3.6 Jet energy scale uncertainties

The JES calibration [153] used in this dissertation includes a set of 19 uncertainties that takes into account multiple sources of systematic uncertainty:

- Four pileup uncertainties to account for potential mismodelling in the MC simulation of the number of reconstructed primary vertices N_{PV}, the mean number of interactions per bunch crossing $\langle\mu\rangle$, and the pileup density ρ.
- Three jet-flavour-related uncertainties to account for differences in the calorimeter response and simulated jet composition of light-quark, b-quark, and gluon-initiated jets. In-situ techniques mainly measure quark-initiated jets by the nature of the process involved.
- Three uncertainties associated with the η-intercalibration technique.
- Six uncertainties associated with in-situ techniques (γ/Z+jet balance and multijet balance) are divided in different categories (statistical, detector, modeling, mixed) according to their origin.

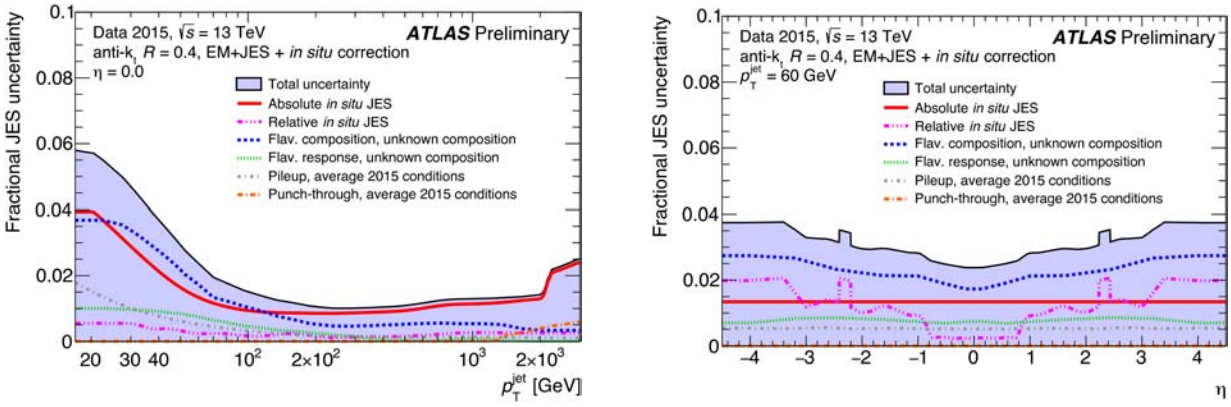

(a) (b)

Figure 4.12: Relative jet energy scale uncertainty (a) as a function of jet p_{T} for central jets (η=0) and (b) as a function of jet η for jets with $p_{\mathrm{T}} = 60$ GeV. The contributions from the leading sources of uncertainty are also displayed.

- One high-p_{T} uncertainty is derived from the single-particle response and applied beyond the reach of in-situ uncertainties.
- One uncertainty associated with the punch-through correction applied in the global sequential calibration.
- One uncertainty associated with the JES correction applied to jets in the MC samples that use parametrised simulation of the calorimeter, to account for non-closure of the jet response.

Figure 4.12 shows the relative JES uncertainty as a function of jet p_{T} and η. The uncertainty is below 6% in the whole jet p_{T} range, reaching a value below 2% for jets with $70 < p_{\mathrm{T}} < 2000$ GeV and $\eta = 0$.

4.4.3.7 Jet energy resolution

The energy of a jet cannot be exactly measured due to electronic noise, stochastic fluctuations in the calorimeter response, and detector calibration effects. The distribution of energy measurements for jets with the same true energy is assumed to have a Gaussian shape, whose width is referred to as the jet energy resolution. The jet energy resolution in data and MC are estimated from in-situ measurements as a function of jet p_{T} and η [154, 155]. Figure 4.13a shows the jet energy resolution as function of the jet p_{T} measured using Run 1 data. Figure 4.13b shows the estimated uncertainty on jet energy resolution as a function of jet p_{T}, applied to Run 2 analyses.

4.4.3.8 Jet cleaning

Quality criteria to reject jets not originating from pp collisions (fake jets) are known as "jet cleaning". Fake jets may be caused by coherent calorimeter noise that passes data quality criteria. Several sources of non-collision background may also create fake jets such as showers induced by cosmic rays or beam-gas interactions. The following quantities are used in jet cleaning:

- A quality factor $\mathcal{Q}_{\mathrm{cell}}$ quantitatively compares the LAr pulse to the expected pulse shape from real jets in a single cell. Jets with a significant deviation from the reference quality factor are rejected.

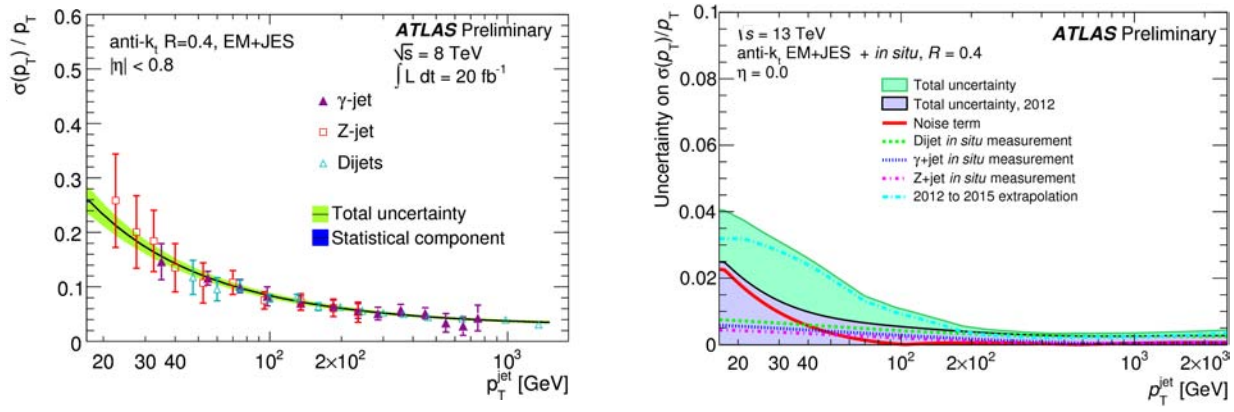

(a) (b)

Figure 4.13: (a) Jet energy resolution measurements using different in-situ techniques using Run 1 data. (b) Jet energy resolution uncertainty applied to Run 2 analyses.

- Noise bursts in the calorimeters may also be reconstructed as negative-energy deposits. Jets with a significant absolute value of energy in all negative-energy cells (>60 GeV) are rejected.

- Energy deposits originating from calorimeter noise or beam-induced backgrounds are often localised in small regions of the calorimeter or the tracker and extend laterally in the detector rather than longitudinally. Requirements on fractions of total energy in layers of the EM calorimeter and relative fraction of jet p_{T} measured by tracks are also used to discriminate against fake jets.

4.4.3.9 Jet vertex tagger

Pileup activity can also produce jets that should not be considered as part of the hard-scatter event. In order to identify and reject in-time pileup, information from the tracks associated to each jet is used. The Jet Vertex Tagger (JVT) [156] combines the information from two variables: corrJVF and $R_{p_{\mathrm{T}}}$.

The corrJVF variable compares the sum p_{T} of all tracks from the hard-scatter primary vertex (PV_0) matched to a jet, to a N_{PV}-dependent average scalar sum p_{T} from pileup tracks associated with a jet. It is defined as:

$$\mathrm{corrJVF} = \frac{\sum_i p_{\mathrm{T}}^{\mathrm{trk_i}}(\mathrm{PV}_0)}{\sum_j p_{\mathrm{T}}^{\mathrm{trk_j}}(\mathrm{PV}_0) + \frac{\sum_{n\geq 1}\sum_j p_{\mathrm{T}}^{\mathrm{trk_j}}(\mathrm{PV}_n)}{(k \cdot n_{\mathrm{trk}}^{\mathrm{PU}})}}, \tag{4.6}$$

where $\sum_i p_{\mathrm{T}}^{\mathrm{trk_i}}(\mathrm{PV}_0)$ is the scalar p_{T} sum of the tracks that are associated with the jet and originate from the hard-scatter vertex. The term $\sum_{n\geq 1}\sum_j p_{\mathrm{T}}^{\mathrm{trk_l}}(\mathrm{PV}_n)$ denotes the scalar p_{T} sum of the associated tracks that originate from any of the pileup interactions. The factor $(k \cdot n_{\mathrm{trk}}^{\mathrm{PU}})$ with k=0.01 corrects for the linear increase of $\langle p_{\mathrm{T}}(\mathrm{PV}_n)\rangle$ with the total number of pileup tracks per event ($n_{\mathrm{trk}}^{\mathrm{PU}}$).

The variable $R_{p_{\mathrm{T}}}$ is defined as the scalar p_{T} sum of the tracks that are associated with the jet and originate from the hard-scatter vertex, divided by the fully-calibrated (i.e. including pileup subtrac-

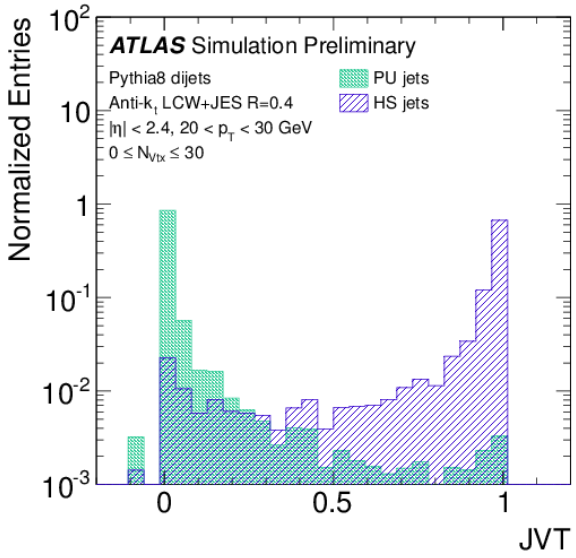

Figure 4.14: JVT distribution for hard-scatter jets (blue shaded histogram) and pileup jets (green histogram) with $20 < p_{\mathrm{T}} < 30$ GeV and $|\eta|<2.4$ in simulated dijet events. From Ref. [156].

tion) jet p_{T}:

$$R_{p_{\mathrm{T}}} = \frac{\sum_i p_{\mathrm{T}}^{\mathrm{trk}_i}(\mathrm{PV}_0)}{p_{\mathrm{T}}^{\mathrm{jet}}}. \tag{4.7}$$

The distribution of the JVT variable for jets originating from the hard-scatter interaction and for pileup originated jets is illustrated in figure 4.14. The JVT variable has a good separation power between hard-scatter jets (peaking at 1) and pileup jets (having substantially lower fraction of tracks from the primary vertex, and thus peaking at 0). A value of -0.1 is assigned to jets with no associated tracks.

The requirement made to suppress pileup jets is JVT > 0.59, which has a 92% selection efficiency for hard-scatter jets. This cut is applied only to jets with $p_{\mathrm{T}} < 60$ GeV with $|\eta| < 2.4$, since the pileup contribution at high p_{T} is negligible. The efficiency of such cut on data and MC, and thus the corresponding SF, are derived using $Z \to \mu^+\mu^-$ events, with a selection that enriches the sample in hard-scatter jets (see figure 4.15). The systematic uncertainty associated to the JVT requirement is estimated by changing the residual contamination from pileup jets and by using different generators for the MC simulation of $Z \to \mu^+\mu^-$ events.

4.4.4 Jet re-clustering

Processes involving the production and decay of W, Z, and Higgs bosons, as well as top quarks, provide benchmarks for testing the SM, as well as probes of physics beyond the SM. During Run 2 the LHC operates at a centre-of-mass energy of 13 TeV, allowing for the first time the production of large samples of W, Z and Higgs bosons and top quarks with a transverse momentum p_{T} that considerably exceeds their rest mass m ($p_{\mathrm{T}} \gg m$). When an unstable heavy particle is produced with such high transverse momentum (referred to as *boosted object*), its decay products will become collimated in

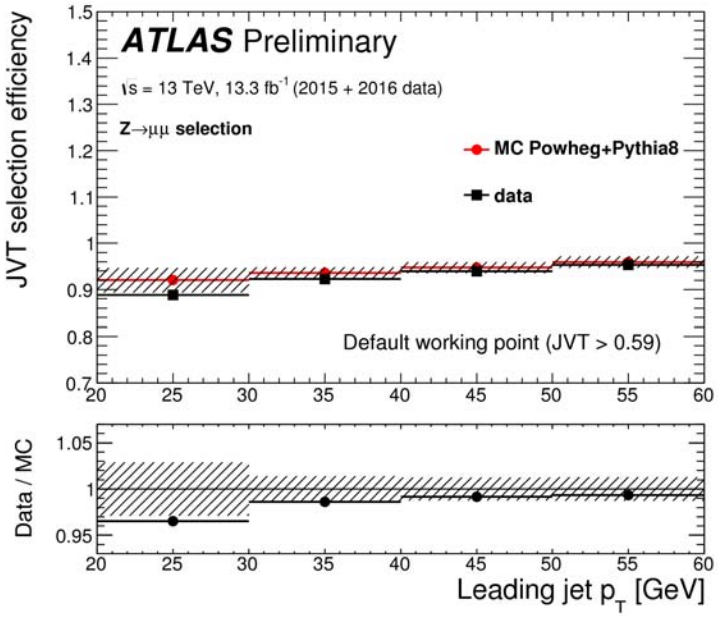

Figure 4.15: JVT selection efficiency for hard-scatter jets as a function of jet p_{T}, estimated in a sample of $Z \to \mu^+\mu^-$ events.

the detector frame: the larger the boost, the closer these particles will be. The angular separation between the decay products (ΔR) is approximately given by:

$$\Delta R \approx \frac{2m}{p_{\mathrm{T}}}, \tag{4.8}$$

where m and p_{T} are respectively the mass and the transverse momentum of the unstable heavy particle. Figure 4.16 illustrates the dependence of ΔR between the decay products of a top quark as a function of top-quark p_{T}.

In the case of hadronic decays of boosted objects, the pairs or triplets of conventional $R = 0.4$ anti-k_{T} jets that would normally be used to reconstruct the heavy particle (resolved regime), may be close enough that it is instead possible to reconstruct the system using a single large-radius (large-R) jet (boosted regime), as shown in figure 4.17.

In the boosted regime, the masses of jets and further details of the jet substructure will be useful in identifying single jets from hadronic decays of boosted objects from those originating from QCD processes (e.g. the jet mass will peak around the resonance mass). A variety of tools are proposed to identify resonances using different substructure observables and algorithms to build large-R jets [157]. The larger radius makes large-R jets more susceptible to pileup effects. Therefore, several techniques (grooming) have been developed to suppress the pileup or underlying-event contaminations affecting large-R jets:

- Trimming [158]: In this approach the constituents of the large-R anti-k_{T} jet are re-clustered into smaller jets with $R_{\mathrm{trim}} = 0.2$, using the anti-k_{T} algorithm again. The resulting subjets are only accepted if their transverse momentum is larger than a fraction f (here $f = 0.03$) of a hard scale, which is chosen to be the p_{T} of the large-R jet. The surviving subjets are recombined into a groomed jet.

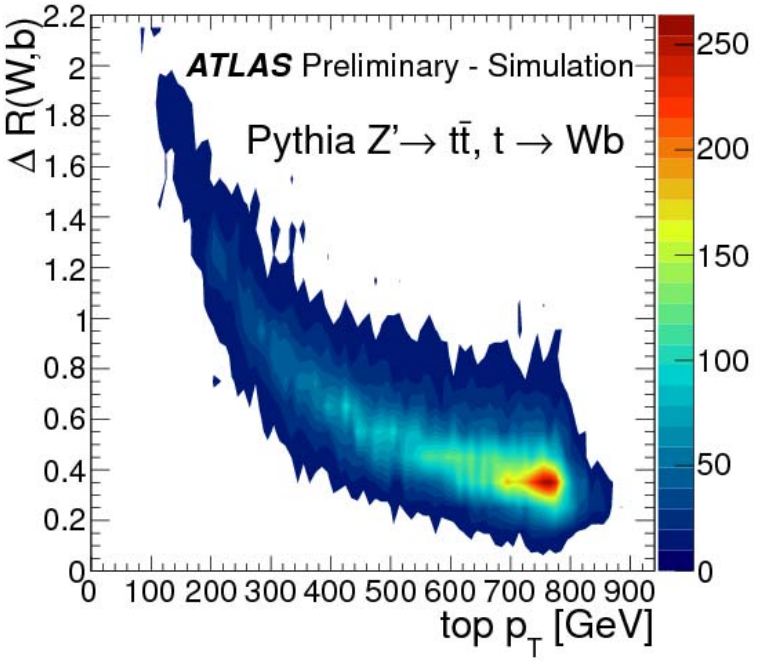

Figure 4.16: Angular separation between the decay products of a boosted top quark from a heavy $Z^{'} \to t\bar{t}$, as a function of top-quark p_{T} .

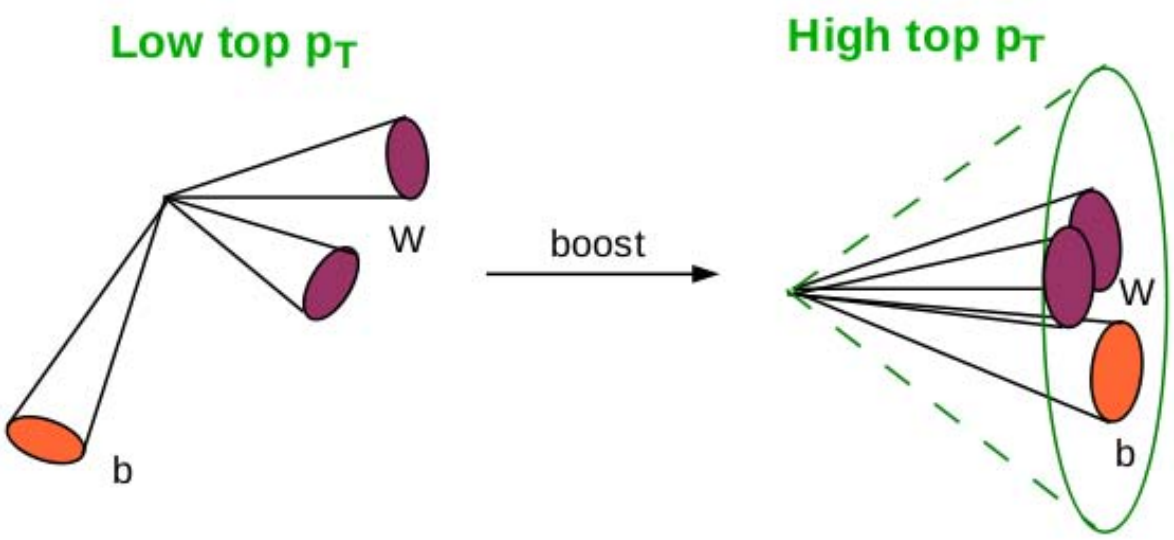

Figure 4.17: Graphical representation of resolved (left) and boosted (right) topologies.

- Filtering [159]: The procedure is similar to trimming, except that in this case the subjets are found with the Cambridge-Aachen algorithm [149] with $R_{\mathrm{filt}} = 0.3$, and only the three highest-p_{T} subjets are retained. The groomed jet is then constructed from these three subjets.

- Pruning [160]: Contrary to trimming and filtering, this procedure is applied during jet finding. It dynamically suppresses soft and large-distance contributions to the jet using two parameters, Z_{cut} for the momentum-based suppression, and D_{cut} for the distance-based suppression. Pruning vetoes recombinations between two objects i and j for which $\Delta R_{ij} > D_{\mathrm{cut}}$ and if the p_{T} of one

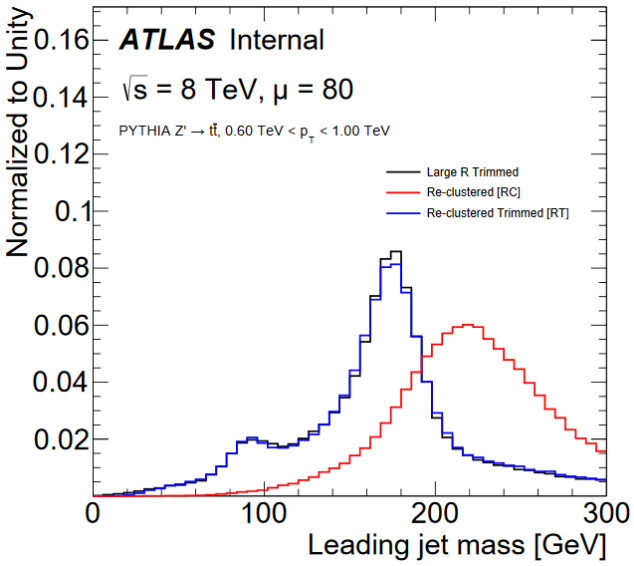

Figure 4.18: Mass distribution for different large-R jets. The jet mass performance for re-clustered large-R jets is comparable to that of standard large-R jets only after trimming. In this figure a value of $\langle\mu\rangle$ much higher than that expected in Run 2 is assumed to check the performance in extreme conditions.

of the objects is less than $Z_{\text{cut}} \times p_{\text{T}}^{ij}$, where p_{T}^{ij} is the combined transverse momentum of i and j. In this case, only the hardest (highest p_{T}) of the two objects is kept. Typical values for these parameters are: $D_{\text{cut}} = 0.5$ and $Z_{\text{cut}} = 0.1$.

In this dissertation only one method to build large-R jets will be discussed, referred to as "jet re-clustering" [161]. Jet re-clustering takes as inputs small-radius ($R \leq 0.4$) jets and clusters them into large-radius ($R \geq 1.0$) jets. The calibrations, corrections, and uncertainties on the re-clustered jets are inherited from the small-R jets, so this method solves difficulties in calibration and uncertainty estimation. By construction, re-clustered jets are already groomed to some extent. Small-R jets can only be calibrated to some low p_{T} value (typically 20 GeV) and thus effectively "subjets" are removed that are below this fixed p_{T} threshold. To improve the performance of the re-clustered jet mass reconstruction, further grooming can be applied. In particular, re-clustered trimmed jets (RT-jets) are subject to the removal of all small-R jets within the re-clustered jet with p_{T} below $f_{\text{cut}} \times p_{\text{T}}^{\text{re-clustered jet}}$, in analogy to standard large-R jet trimming. However, re-clustered trimming differs in an important way: the jet p_{T} of the re-clustered jet and its subjets are calibrated, including pileup correction. In Figure 4.18, the mass distribution of re-clustered jets and RT-jets are compared for simulated $Z' \to t\bar{t}$ events. In the case of the RT-jets, clear peaks are visible around the W boson and top-quark masses with a performance comparable to that of standard large-R trimmed jets.

The usual approach to jet substructure is to build large-R jets and then look inside the jet for structure on finer angular scales (top-down substructure). Re-clustered jets inherit this approach by associating the small-R jet constituents to the large-R jets, and then computing substructure variables as usual. However, an advantage of re-clustered jets is that some substructure variables can be computed using a bottom-up approach, in the sense that they are constructed from the the kinematics of the small-R jets themselves, and thus are a-priori corrected and calibrated. In order to ensure that the mass of the large-R jet originates from the p_{T} and angular separation of the subjets, instead of from the small-R jet mass (that at the time of this writing is not calibrated yet), a requirement of at least two subjets is made. In this way it is possible to evaluate the uncertainty

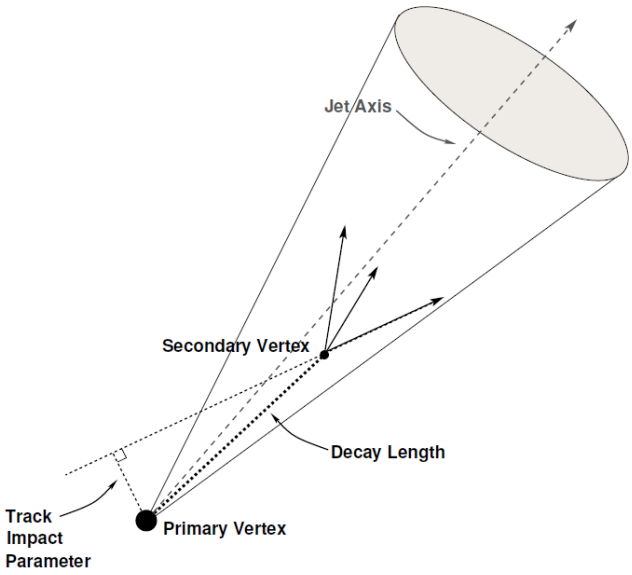

Figure 4.19: Most relevant variables for the identification of b-jets.

on the mass of the large-R jets coming from the calibration of its constituents by varying the energy scale and resolution of small-R jets.

The analyses described in this dissertation use anti-k_{T} RT-jets from small-R jets ($R = 0.4$) with a radius of $R = 1.0$, which are trimmed by removing all small-R jets within a re-clustered jet that have p_{T} below 5% of the p_{T} of the re-clustered jet (i.e. $f_{\mathrm{cut}} = 0.05$). Due to the pileup suppression and $p_{\mathrm{T}} > 25$ GeV requirements made on the small-R jets, the average fraction of small-R jets removed by the trimming requirement is less than 1%.

4.4.5 b-tagging

The identification of jets resulting from the fragmentation of b-quarks (b-jets), usually referred to as b-tagging, is of crucial importance in event topologies involving b-quarksuch as those with top-quark of $H \to b\bar{b}$ decays.

Jets produced in the hadronisation of b-quarks can be distinguished from other types of jets using the characteristic properties of b-hadrons (see figure 4.19). Because of their long lifetime ($\tau \sim 1.5$ ps, $c\tau \sim 450$ μm) b-hadrons can travel several millimetres before decaying producing at least one displaced vertex in the jet, which can be reconstructed. Also, it is possible to measure the impact parameters of the tracks from the b-hadron decay products, which tend to have rather large positive impact parameters and thus can be distinguished from tracks coming from the primary vertex. The sign of the impact parameter is positive if the track extrapolation crosses the jet direction in front of the primary vertex, and negative otherwise. For a jet originating from a b-quark, typically one or more tracks are expected to show a large and positive impact parameter significance, defined as the impact parameter over its error. Negative sign impact parameter typically occurs because of resolution effects. The longitudinal and transverse impact parameters are defined as the minimum distance of the track to the primary vertex respectively in the z direction and in the $x - y$ plane. Finally, the mass of all the particles associated to the displaced vertex can also be exploited, since those vertices tend to have a mass of up to ∼5 GeV (due to neutral decay products not being included).

Several methods exploiting the above features are implemented in ATLAS. The outputs of these b-tagging algorithms are combined in a multivariate discriminant. The most relevant algorithms are:

- IP3D [162]: this algorithm uses both the transverse and the longitudinal impact parameter significances in a two-dimensional likelihood discriminant, to take advantage of their correlation. Input variables are compared to templates for both b-jet and light-jet hypotheses, obtained from MC simulation.

- SV1 [162]: this algorithm explicitly reconstructs a displaced secondary vertex within the jet using tracks fulfilling specific quality criteria. A likelihood discriminant is built using several variables, such as the decay-length significance, the invariant mass of all tracks associated with the vertex, the ratio of the sum of the energies of the tracks in the vertex to the sum of the energies of all tracks in the jet, and the number of two-track vertices.

- JetFitter [163]: this algorithm exploits the topological structure of b- and c-hadron decays inside the jet and attempts to reconstruct the full b-hadron decay chain. It uses a Kalman-filter [164] approach to find a common line on which the primary vertex and the bottom and charm vertices lie, approximating the b-hadron flight path, as well as their positions.

- MV2c10 [165]: this algorithm combines the outputs of the above b-tagging algorithms in a Boosted Decisions Tree (BDT) algorithm to achieve a better discrimination. The MV2c10 algorithm is defined as the output of such a BDT with the training performed using b-jets as signal and a mixture of 90% light-flavour jets and 10% c-jets as background.

The performance of a b-tagging algorithm is characterised in terms of its capability to identify a jet coming from a real b-quark, compared to the probability of mistakenly tagging a jet originating from a c-quark or a light-flavour parton (u, d, s-quark or gluon) as a b-jet. These quantities are commonly referred to as the c-tagging effciency and mistag rate respectively. The b-tagging efficiency compared to the light-jet and c-jet rejection,[7] is summarised in figure 4.20 for the MV2c10 algorithm.

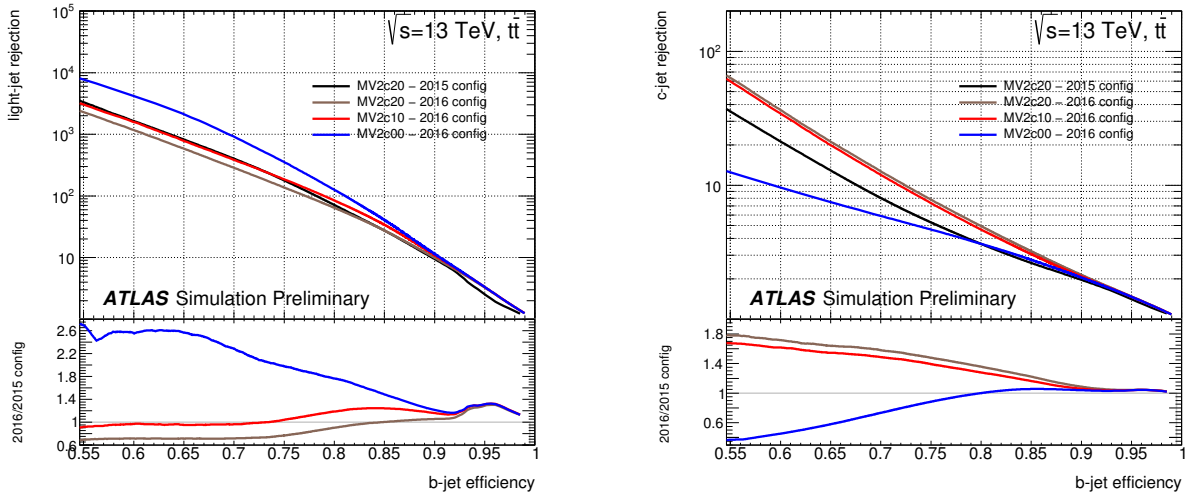

(a) (b)

Figure 4.20: b-tagging efficiency compared to the (a) light-jet and (b) c-jet rejection for the MV2cxx algorithm, where xx represents the fraction of c-jets using in the training.

Several operating points have been defined based on the average b-tagging efficiency of the algorithm on simulated $t\bar{t}$ events (see table 4.4). The 70% and 77% operating points has been chosen for the

[7] The rejection is defined as the reciprocal of the efficiency.

b-jet efficiency [%]	c-jet rejection	light-jet rejection	τ-jet rejection
60	34	1538	184
70	12	381	55
77	6	134	22
85	3.1	33	8.2

Table 4.4: The MV2c10 algorithm operating points and their performance. The b-jet efficiency is the average obtained for b-jets with $p_{\mathrm{T}} > 20$ GeV from simulated $t\bar{t}$ events.

analyses in this dissertation given the compromises in each of them between efficiency and rejection. Figure 4.21 shows the efficiency, obtained from the simulation, of the 70% MV2c10 operating point for b-jet, c-jet and light-jets as a function of the jet p_{T} and $|\eta|$. The b-tagging efficiency increases in the medium p_{T} regime ($50 < p_{\mathrm{T}} < 200$ GeV) where the identification of displaced vertices is more efficient, but at high p_{T} (> 200 GeV) starts dropping since the tracking reconstruction efficiency is worse due to merged-tracks effects. The mistag rate is more important for large $|\eta|$ values due to the worse track resolution.

4.4.5.1 b-tagging calibration

In order to take possible differences between the MC simulation and real data into account, the b-tagging algorithms need to be calibrated in data. Several methods have been developed to measure the b-jet efficiency, the c-jet efficiency and the light-jet rate in data. The result is presented in terms of scale factors, $\mathrm{SF} = \varepsilon_{\mathrm{data}}/\varepsilon_{\mathrm{MC}}$. This allows correcting for mis-modeling by the MC simulation in the input variables used in the b-tagging algorithms.

The b-jet calibration used for the analyses in this dissertation is derived on a high-purity sample of b-jets that can be obtained from $t\bar{t}$ events with two oppositely-charged leptons in the final state [166]. The calibration is based on a likelihood approach which uses correlated information from multiple jets in the event, and it achieves a precision of a few percent for jet p_{T} ranging between 30 and 300 GeV. However a correct use in a physics analysis requires some care in order to avoid a re-use of the same data sample as well as double counting of systematic uncertainties. Since the chosen $t\bar{t}$ -based calibration has been derived using a dileptonic $t\bar{t}$ sample, no overlap of data events exists with analyses considering lower lepton multiplicities, such as the ones discussed in this dissertation.

The tagging calibration for c-quarks has been derived by reconstructing D-mesons within a jet from the decay chain $D^{*+} \to D^0\pi^+$ [167]. The contamination of D^{*+} mesons originating from b-hadron decays is identified fitting the pseudo-proper time distribution of the D^0 meson, and corrected for.

For the mis-tag rate calibration the so-called "negative tag" method is used [168]. Light-flavour jets are tagged as b-jets mainly because of the finite resolution of the inner detector and the presence of tracks from displaced vertices of long-lived particles or material interactions. For prompt tracks the distributions of the lifetime-signed impact parameter and of the signed decay length of vertices reconstructed using these tracks are expected to be symmetric. Therefore, the inclusive tag rate obtained by using negative impact-parameter tracks in the case of impact-parameter-based tagging algorithms, orby using negative decay-length secondary vertices in the case of secondary-vertex-based tagging algorithms, is expected to be a good approximation of the mistag rate due to resolution effects.

Scale factors as a function of jet p_{T} for b-, c- and light jets as extracted from the 2015 dataset are shown in figure 4.22. The scale factors are applied to MC samples as event weight corrections. For each jet tagged by the b-tagging algorithm, a weight equal to the b-tagging SF of the corresponding jet flavour is considered. If a jet fails the b-tagging criterion, a weight corresponding to $(1 - \mathrm{SF} \times$

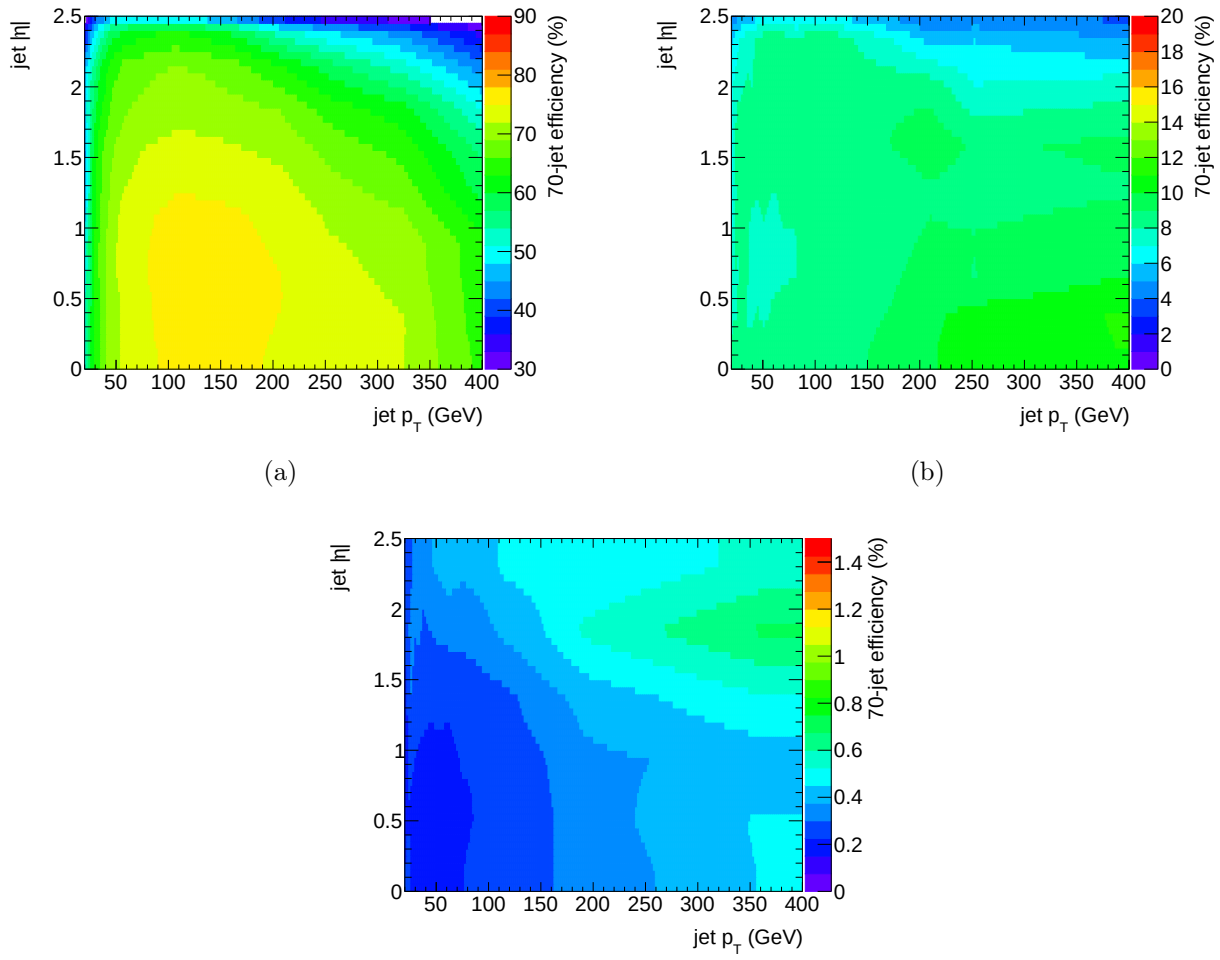

Figure 4.21: b-tagging efficiency for the MV2c10 70% operating point as a function jet p_{T} and $|\eta|$. Efficiencies are shown separately for (a) b-jets, (b) c-jets and (c) light jets from simulated $t\bar{t}$ events.

$\varepsilon_{\mathrm{MC}})/(1-\varepsilon_{\mathrm{MC}})$ is assumed. The individual jet weights for all the selected jets are multiplied in order to obtain an event-level weight. The determination of the b-tagging scale factors is affected by multiple systematic uncertainties. In order to propagate those into the scale factors in a manageable way a reduction in terms of 23 independent nuisance parameters through a diagonalisation method is used. A total of five eigenvectors are considered to describe the systematic uncertainties related to the b-tagging calibration. The same procedure is performed to derive four (fourteen) eigenvectors on the c-tagging (mistag) calibration. An additional uncertainty is included due to the extrapolation of the b-,c-, and light-jet-tagging scale factors for jets with p_{T} beyond the kinematic reach of the data calibration samples used: $p_{\mathrm{T}} > 300\,\mathrm{GeV}$ for b- and c-jets, and $p_{\mathrm{T}} > 750\,\mathrm{GeV}$ for light-jets. Finally, in absence of a direct measurement in data, for τ-jets the c-jet SF is used, and a related extrapolation uncertainty (referred to as $c \to \tau$ extrapolation) is assigned.

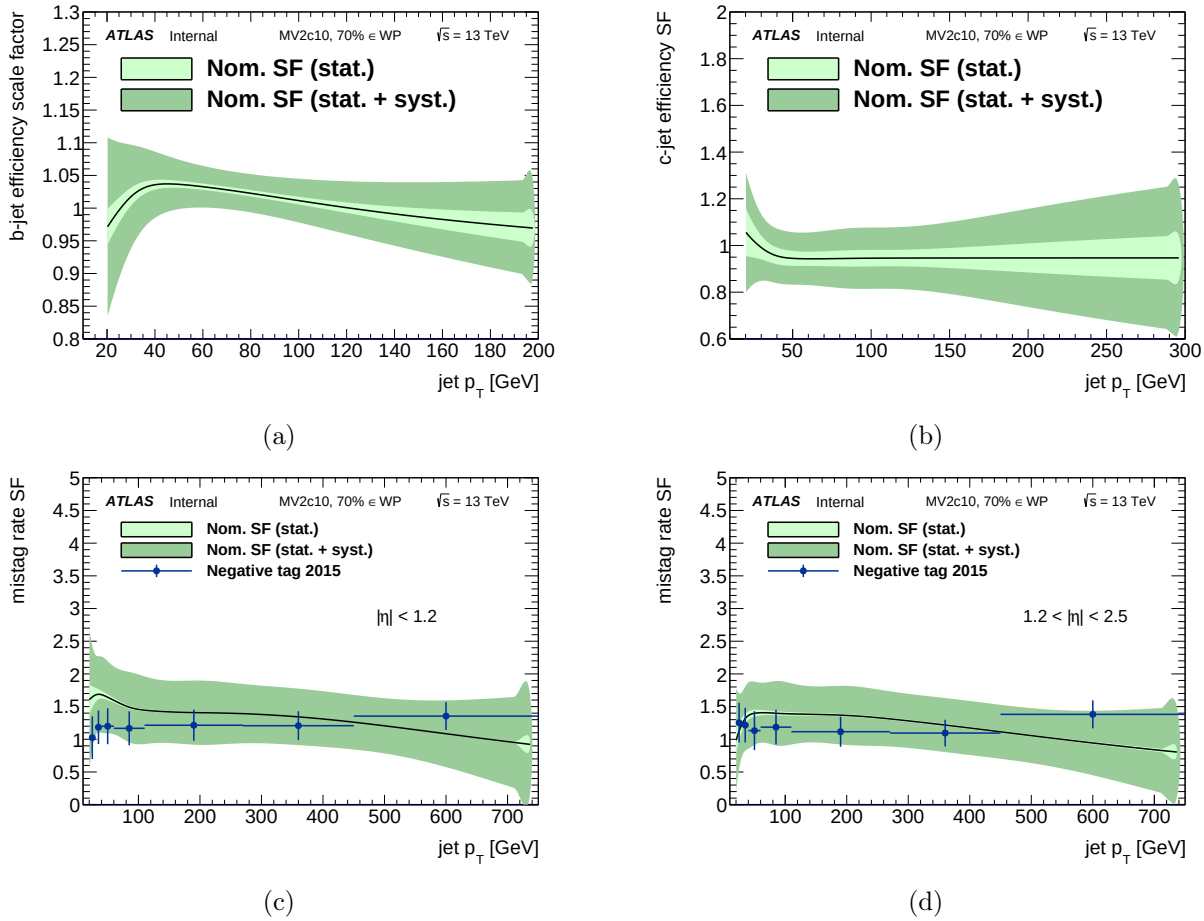

Figure 4.22: Data/MC scale factors for the tagging efficiency of (a) b-jets, (b) c-jets, and (c and d) light jets with the 70% MV2c10 operating point. Total uncertainty are shown as well as the statistics component. Scale factors are measured as a function of jet p_{T} and, in case of mistag rate, the result for two different $|\eta|$ bins are shown.

4.5 Missing transverse energy

The ATLAS subdetectors are not sensitive to neutral weakly-interacting particles like neutrinos or particles predicted in BSM scenarios (e.g. WIMPs, neutralinos). Those particles pass through the ATLAS detector without leaving any electric signals, thus creating an apparent imbalance of the total measured momentum in the transverse plane.

The missing transverse momentum, $\vec{p}_{\mathrm{T}}^{\,\mathrm{miss}}$, is obtained from the negative vector sum of the p_{T} of all particles detected in a pp collision. The magnitude and the direction of this vector are respectively the missing transverse energy, $E_{\mathrm{T}}^{\mathrm{miss}}$, and the missing energy azimuthal angle, ϕ^{miss}. The $E_{\mathrm{T}}^{\mathrm{miss}}$ reconstruction [169] is characterised by two contributions: the hard term from all reconstructed objects (electrons, muons, photons, τ-leptons and jets) and the soft term consisting of reconstructed charged particle tracks not associated with the hard physics objects. To avoid a double-counting of contributions, physics objects are considered in a specific order: electrons, photons, then hadronically decaying τ-leptons, muons and finally jets. The lower priority particle-like objects (γ, τ) are fully rejected if they share their calorimeter signal with an electron that has already entered the $E_{\mathrm{T}}^{\mathrm{miss}}$ reconstruction. Jets can still partially contribute to $E_{\mathrm{T}}^{\mathrm{miss}}$, if not more than 50% of their signal is already used by an overlapping particle with higher priority. After all $E_{\mathrm{T}}^{\mathrm{miss}}$ contributions from hard objects are col-

lected, ID tracks from the hard-scatter PV, but not associated with any of the accepted contributing hard objects, are used to construct the soft term. The reconstruction of $E_{\mathrm{T}}^{\mathrm{miss}}$ should be consistent with the final state selected in a given analysis. Rejecting certain electrons, if the corresponding calorimeter signal is collected with the new assumption, can change the $E_{\mathrm{T}}^{\mathrm{miss}}$. The flexibility needed to re-calculate $E_{\mathrm{T}}^{\mathrm{miss}}$ under changing analysis requirements for the same event is implemented using dedicated variables corresponding to a specific object contribution. In this approach, the full $\vec{p}_{\mathrm{T}}^{\,\mathrm{miss}}$ is the vectorial sum of missing transverse momentum terms:

$$\vec{p}_{\mathrm{T}}^{\,\mathrm{miss}} = \underbrace{-\sum_{\substack{\text{selected}\\\text{electrons}}} \vec{p}_{\mathrm{T}}^{\,e} - \sum_{\substack{\text{accepted}\\\text{photons}}} \vec{p}_{\mathrm{T}}^{\,\gamma} - \sum_{\substack{\text{accepted}\\\tau\text{-leptons}}} \vec{p}_{\mathrm{T}}^{\,\tau} - \sum_{\substack{\text{selected}\\\text{muons}}} \vec{p}_{\mathrm{T}}^{\,\mu} - \sum_{\substack{\text{accepted}\\\text{jets}}} \vec{p}_{\mathrm{T}}^{\,\mathrm{jet}}}_{\text{hard term}} \underbrace{- \sum_{\substack{\text{unused}\\\text{tracks}}} \vec{p}_{\mathrm{T}}^{\,\mathrm{track}}}_{\text{soft term}} \tag{4.9}$$

The sum over electron and muons runs over the selected ones because electrons enter in the calculation first and muons rarely have a calorimetric deposit that overlaps with other objects. The hard term has a little dependence on pileup as the objects used already include pileup corrections. The particular choice of using only tracks from the hard-scatter PV for the soft term strongly suppresses pileup contributions to this term as well.

The performance of $E_{\mathrm{T}}^{\mathrm{miss}}$ reconstruction is evaluated in several topologies:

- $Z \to \ell^+\ell^-$ events are an ideal final state for the evaluation of $E_{\mathrm{T}}^{\mathrm{miss}}$ reconstruction performance (possible both in data and MC) since the events have no intrinsic missing transverse momentum. Scale and resolution measurements in this final state will be indicative of detector limitations affecting the reconstruction quality.
- $W \to \ell\nu$ events provide a good benchmark sample with intrinsic $E_{\mathrm{T}}^{\mathrm{miss}}$ arising from the non-zero neutrino p_{T}. In this sample it is possible (only in MC) to validate scale, resolution and direction of the reconstructed $E_{\mathrm{T}}^{\mathrm{miss}}$.
- $t\bar{t}$ events allow measurements of $E_{\mathrm{T}}^{\mathrm{miss}}$ performance in events with multiple energetic jets in the final state (possible in both data and MC).

Deviation of the observed $E_{\mathrm{T}}^{\mathrm{miss}}$ from the expectation is used to measure the $E_{\mathrm{T}}^{\mathrm{miss}}$ response. If this deviation is independent of the genuine missing transverse momentum, or any other hard p_{T} indicative for the overall hard scatter activity, the $E_{\mathrm{T}}^{\mathrm{miss}}$ response is linear. Detector inefficiencies and limited detector coverage limitation introduce a bias and are expected to translate into a non-linear response. The $E_{\mathrm{T}}^{\mathrm{miss}}$ response and resolution in $W \to \ell\nu$ and $t\bar{t}$ events is shown in figure 4.23.

Systematic uncertainties affecting the $E_{\mathrm{T}}^{\mathrm{miss}}$ computation depend on the composition of the hard term and the magnitude of the resulting soft term. For the former, systematic uncertainties on the physics object calibrations are directly translated into the $E_{\mathrm{T}}^{\mathrm{miss}}$ computation through equation 4.9. Systematics uncertainties affecting the soft term are evaluated in $Z \to e^+e^-$ events. Uncertainties of $\sim 10\%$ and $\sim 20\%$ has been assigned to the resolution and scale respectively.

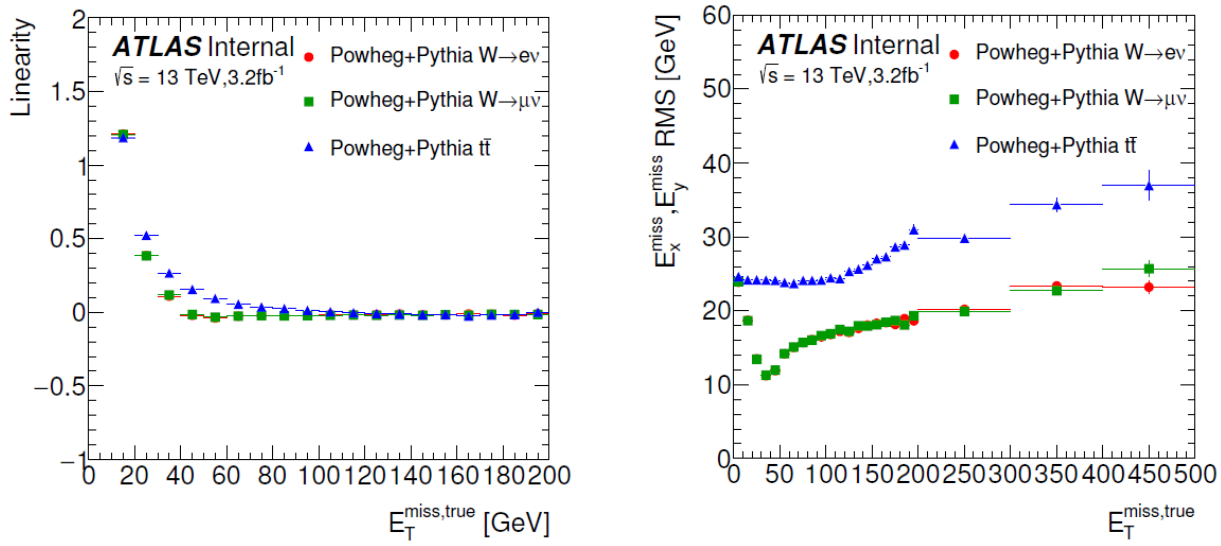

(a) (b)

Figure 4.23: The $E_{\mathrm{T}}^{\mathrm{miss}}$ (a) response and (b) resolution evaluated in $W \to \ell\nu$ and $t\bar{t}$ simulated events. From Ref. [169].

5 Samples and tools

In God we trust;
all others must bring data.
Edward De Ming

Contents

This chapter summarises the characteristics of the data and MC samples used in the analyses presented in this dissertation, giving particular attention to the signal and background modelling. The different signals targeted in this dissertation have as common signature a $t\bar{t}$ pair produced in association with X, where X is a Higgs boson ($H \to b\bar{b}$) in case of $t\bar{t}H$ production, at least one Z boson ($Z \to \nu\bar{\nu}$) or Higgs boson ($H \to b\bar{b}$) in case of $T\bar{T}$ searches, and a $b\bar{b}$ or a $t\bar{t}$ pair in the case of searches for associated production of heavy Higgs bosons or four-top-quark production. Thus a precise modelling of the main background for those searches, $t\bar{t}$+jets production, is crucial for these analyses and will be discussed in detail. Given the large mass of the top quark and that the value of $|V_{tb}|$ is

very close to 1 ($|V_{tb}| = 1.009 \pm 0.031$ [4]), in the SM it decays almost exclusively into an on-shell W boson and a b-quark. A W boson decays in about 1/3 of the cases into a charged lepton and the corresponding neutrino, with all the three lepton flavours being produced with equal probability. In the remaining cases the W boson decays into a quark-antiquark pair and the relative amount of each combination is determined by the corresponding element in the CKM matrix. As $|V_{cb}| \sim 1.7 \cdot 10^{-3}$ [4], production of b-quarks is highly suppressed and the W boson can be considered as a very pure source of light and c-quarks: $W^+ \to u\bar{d}$, $c\bar{s}$. The final-state signature of a $t\bar{t}$ event is thus determined by the decay of the two W bosons present in the event: *dilepton* when both W bosons decay leptonically, *lepton+jets* if one W boson decays leptonically and the other one decays hadronically, and *all-hadronic* if both W bosons decay into quarks. The analyses described in this dissertation target the *lepton+jets* and *all-hadronic*+$E_{\mathrm{T}}^{\mathrm{miss}}$ final states, where in the case of signal events the $E_{\mathrm{T}}^{\mathrm{miss}}$ is likely to come from the presence of high-momentum Z bosons decaying into $\nu\bar{\nu}$ or W bosons decaying leptonically, either to an electron or muon that is not reconstructed, or to a hadronically-decaying τ-lepton that is identified as a jet.

5.1 Data sample

The analyses presented in this dissertation are based on pp collision data at $\sqrt{s} = 13$ TeV collected with the ATLAS detector between August and November 2015, and between April and July 2016. A total integrated luminosity of 13.2 fb^{-1} was recorded under stable beam conditions and requiring all subdetectors to be fully operational during data taking. Events are selected using the lowest unprescaled single-lepton or $E_{\mathrm{T}}^{\mathrm{miss}}$ triggers.

Single-lepton triggers with low p_{T} thresholds and lepton isolation requirements are then combined in a logical OR with higher-threshold triggers without isolation requirements in order to increase the overall efficiency. Different thresholds were used in 2015 and 2016 to keep the output rate ~ 1.5 kHz despite the increase of the instantaneous luminosity. For muon triggers, the lowest-p_{T} threshold is 20 (24) GeV in 2015 (2016), while the higher-p_{T} threshold is 40 (50) GeV. For electrons, isolated triggers with a p_{T} threshold of 24 GeV are used with non-isolated triggers at 60 GeV in both years, along with trigger with a threshold at 120 (140) GeV requiring looser identification criteria. The isolation requirement that is applied offline is tighter than the one included in the trigger; therefore, the analyses are not affected by the isolation requirement applied at the trigger level.

The $E_{\mathrm{T}}^{\mathrm{miss}}$ trigger [170] considered uses an $E_{\mathrm{T}}^{\mathrm{miss}}$ threshold at the HLT level of 70 (100) GeV in 2015 (2016) and becomes fully efficient for on offline $E_{\mathrm{T}}^{\mathrm{miss}} > 200$ GeV.

5.2 Signal and background modelling

The topologies of the signals searched in this dissertation make $t\bar{t}$+jets production the main background for the analyses. In particular, $t\bar{t}+ \geq 1b$ is the main irreducible background in the signal regions. Other background contributions arise from single top-quark production, from the production of a single W or Z boson in association with jets (W/Z+jets), diboson production in association with jets (WW, WZ and ZZ + jets), as well as from the associated production of a vector boson V ($V = W$, Z, γ^*) and a $t\bar{t}$ pair ($t\bar{t}V$). Multijet events contribute to the lepton+jets sample via the misidentification of a jet or a photon as an electron, or the presence of a non-prompt lepton, e.g. from a semileptonic b- or c-hadron decay; instead, they contribute to the all-hadronic+$E_{\mathrm{T}}^{\mathrm{miss}}$ sample via instrumental effects such as jet energy mismeasurements that contribute to $E_{\mathrm{T}}^{\mathrm{miss}}$. All backgrounds are estimated using samples of simulated events and initially normalised to their theoretical cross sections, with the exception of the

multijet background, which is estimated using data-driven methods in the lepton+jets sample.

The top-quark mass and the Higgs boson mass are set to 172.5 GeV and 125 GeV respectively in all simulated samples. Unless stated otherwise, in the following the accuracy of the calculation indicated for all samples corresponds to the order in the strong coupling constant at which the matrix element is computed. All simulated samples use PHOTOS for photon radiation, TAUOLA for τ decays and EVTGEN (except for the samples simulated by SHERPA) for decays of b- and c-hadrons. Simulated samples also include contributions from pileup and UE and are processed through a full simulation of the detector geometry and response using GEANT4, with the exception of the signal samples of associated heavy-Higgs production, for which the AF2 simulation was used. All event generators using HERWIG are also interfaced to JIMMY to simulate the UE. All simulated samples are processed through the same reconstruction software as the data. Simulated events are corrected so that the object identification efficiencies, energy scales and energy resolutions match those determined in data control samples.

5.2.1 $t\bar{t}$+jets production

The large phase space covered by the analyses discussed in this dissertation requires a $t\bar{t}$ simulation that describes correctly the different event topologies, especially the emission of additional jets and the heavy-flavour fraction. Not only the normalisation, but also the kinematics of the full final state have to be correctly modelled since several kinematic variables are used.

The $t\bar{t}$ background is generated using the POWHEG-BOX v2 NLO generator with the CT10 PDF set, which has been chosen as the baseline generator for the modelling of $t\bar{t}$ production based on measurements at $\sqrt{s} = 7$ and 8 TeV [171–173]. The *hdamp* parameter, which controls the p_{T} of the first additional emission beyond the Born configuration, is set equal to the top quark mass. The parton shower and hadronisation are modelled by PYTHIA 6.428 with the CTEQ6L1 PDF set [174] and the Perugia2012 [175] settings for the tunable parameters of the underlying event (UE tune). The sample is normalised to the TOP++ 2.0 [176] theoretical cross section of 832^{+46}_{-51} pb, calculated at next-to-next-to-leading order (NNLO) in QCD and including resummation of next-to-next-to-leading logarithmic (NNLL) soft-gluons terms [177–180].

The $t\bar{t}$+jets sample is generated inclusively and events are categorised according to the flavour of additional jets in the event, using the following procedure. Particle jets are reconstructed from stable particles (excluding muons and neutrinos) using the anti-k_T algorithm with a radius parameter $R = 0.4$, and are required to have $p_{\mathrm{T}} > 15$ GeV and $|\eta| < 2.5$. The p_{T} threshold for particle jets (15 GeV) is chosen to be 10 GeV below the reconstructed-jet threshold, in order to allow for resolution effects. The flavour of the jets is determined by matching them within $\Delta R < 0.4$ to b- or c-hadrons. Jets matched to exactly one b-hadron with p_{T} above 5 GeV, are labelled b-jets, while those matched to two or more b-hadrons are labelled B-jets (with no p_{T} requirement on the second hadron); c- and C- jets are defined analogously, considering only jets not already defined as b- or B- jets. Events that have at least one b- or B-jet, not counting heavy-flavour jets from top-quark or W boson decays, are labelled $t\bar{t}+ \geq 1b$, those with no b- or B-jet but at least one c- or C-jet are labelled $t\bar{t}+ \geq 1c$, while those with no heavy flavour jets are labelled $t\bar{t}$+light-jets. The $t\bar{t}+ \geq 1b$ and $t\bar{t}+ \geq 1c$ contributions are together referred to as $t\bar{t}$+HF, with HF denoting heavy flavour. In order to perform more detailed studies of the $t\bar{t}$+HF modelling and the related systematic uncertainties, a more detailed categorisation is also used: events with at least three b- or B-jets are labeled $t\bar{t}+ \geq 3b$, those with exactly two b-jets are labelled $t\bar{t} + b\bar{b}$, those with only one B-jet are labelled $t\bar{t} + B$, and those with only one b-jet are labelled $t\bar{t} + b$; $t\bar{t}+ \geq 1c$ events are divided analogously.

In the following sections some corrections applied to this simulation in order to improve its predic-

tion are described.

5.2.1.1 $t\bar{t}$+light-jets

The high $t\bar{t}$ production cross section and high-luminosity pp collisions make the LHC a top-quark factory that allows precision measurements of the kinematics of the top quark compared to the Tevatron [180]. Detailed studies of a number of differential distributions of the top quarks in $t\bar{t}$ events using the $\sqrt{s}$ = 7, 8 and 13 TeV datasets by the ATLAS detector [171–173, 181, 182] revealed significant differences between the unfolded data distributions and the predictions from POWHEG-BOX+PYTHIA. The most significant discrepancy with data is observed in the top-quark p_{T} spectrum where MC predictions tend to be harder than data, as shown in figures 5.1 and 5.2.

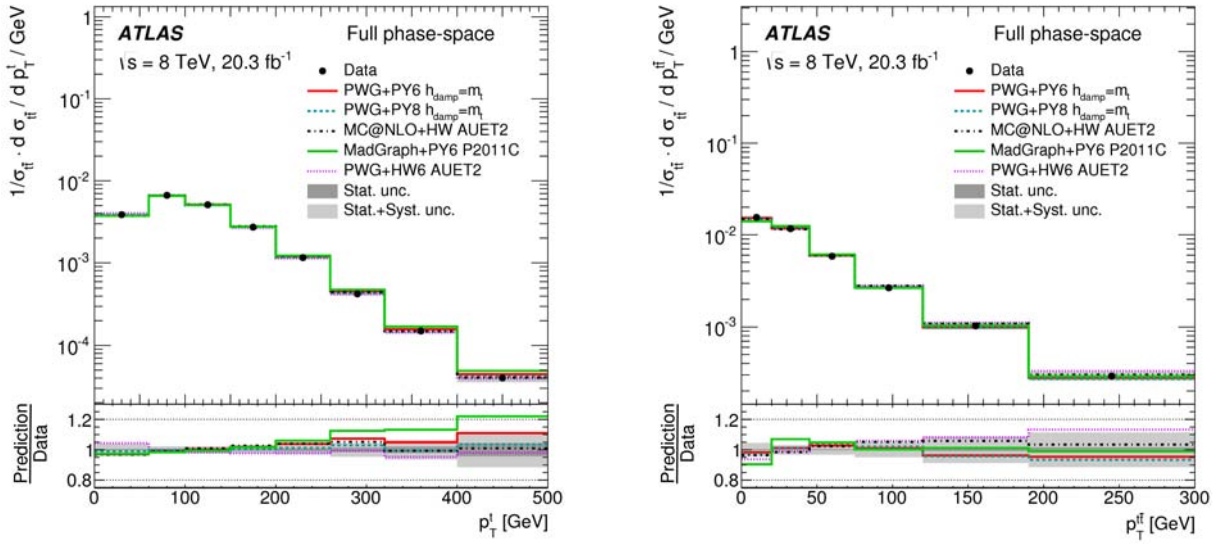

(a) (b)

Figure 5.1: Normalised differential cross sections at 8 TeV for (a) the transverse momentum of the hadronically-decaying top quark, $p_{\mathrm{T}}^{\mathrm{top}}$, and (b) the transverse momentum of the $t\bar{t}$ system, $p_{\mathrm{T}}^{t\bar{t}}$. The POWHEG-BOX+PYTHIA prediction is shown in red. The gray bands indicate the total uncertainty on the data in each bin. From Ref. [173].

A recent study [183, 184] showed that missing higher-order QCD corrections to $t\bar{t}$ production can at least partly explain the "top-quark p_{T} discrepancy". The NNLO QCD correction to the top-quark p_{T} softens the spectrum and brings it closer to the $\sqrt{s}$ = 8 TeV data, as shown in figure 5.3. To correct for this effect, two reweighting factors are derived from the NNLO calculation at $\sqrt{s}$ = 13 TeV and their product is applied as a multiplicative factor to each event based on the value of top-quark p_{T} and $t\bar{t}$ system p_{T}. First a reweighting factor based on $p_{\mathrm{T}}^{t\bar{t}}$ is derived, in order to bring the $p_{\mathrm{T}}^{t\bar{t}}$ distribution in POWHEG-BOX+PYTHIA in agreement with the NNLO calculation. After applying this first reweighting factor, a second factor is derived to correct the $p_{\mathrm{T}}^{\mathrm{top}}$ distribution. This two-step sequential procedure is needed in order to take into account the non-negligible correlation between both variables. Table 5.1 summarises the correction factors. An alternative procedure, where only the $p_{\mathrm{T}}^{\mathrm{top}}$ distribution is corrected, is available. This reweighting procedure, which will be referred to as $t\bar{t}$ and top-quark p_{T} reweighting, is applied inclusively to two subsamples: $t\bar{t}$+light-jets and $t\bar{t}+ \geq 1c$. This correction is not applied to $t\bar{t}+ \geq 1b$ events, which instead have a dedicated reweighting described in the next section.

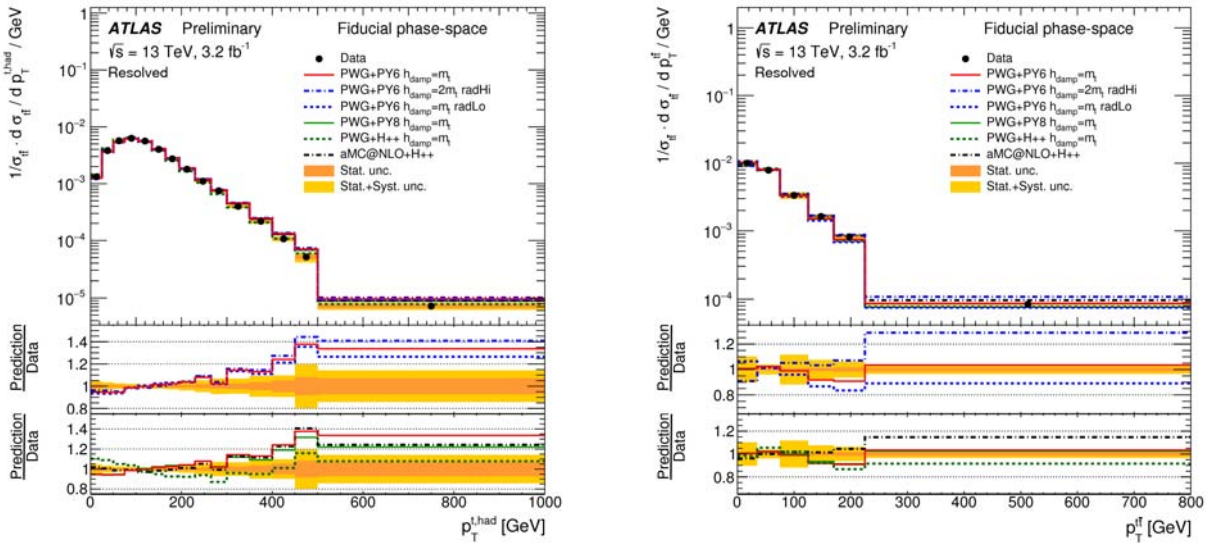

(a) (b)

Figure 5.2: Normalised differential cross sections in the fiducial phase space at 13 TeV for (a) the transverse momentum of the hadronically-decaying top quark, $p_{\mathrm{T}}^{\mathrm{top}}$, and (b) the transverse momentum of the $t\bar{t}$ system, $p_{\mathrm{T}}^{t\bar{t}}$. The POWHEG-BOX+PYTHIA prediction is shown in red. The yellow bands indicate the total uncertainty on the data in each bin. From Ref. [182].

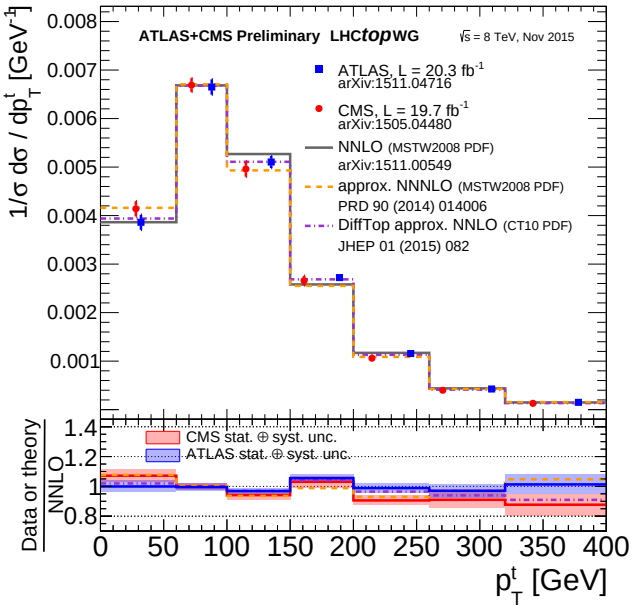

Figure 5.3: Normalised differential cross section at 8 TeV for the transverse momentum of the hadronically-decaying top quark, $p_{\mathrm{T}}^{\mathrm{top}}$. The measurements from the ATLAS and CMS collaborations are compared to different theoretical predictions.

5.2.1.2 $t\bar{t}+ \geq 1b$

The modelling of $t\bar{t}+ \geq 1b$ production is crucial for the analyses in this dissertation since it constitutes the main irreducible background in the signal regions. In the POWHEG-BOX generator, $t\bar{t}+ \geq 1b$ production is described at LO for diagrams of the type $gg \to t\bar{t}b$ and at leading-logarithmic (LL)

p_{T}^{tt}					
Bins [GeV]	[0, 35]	[35, 80]	[80, 140]	[140, 200]	[200,500)
Rew. factor	0.96	1.03	1.01	1.06	1.05

$p_{\mathrm{T}}^{\mathrm{top}}$									
Bins [GeV]	[0, 45]	[45, 90]	[90, 135]	[135, 180]	[180, 225]	[225, 270]	[270, 315]	[315,400]	[400,800)
Rew. factor	1.07	1.03	1.00	0.97	0.95	0.94	0.92	0.90	0.84

Table 5.1: Reweighting factors for the PowHeg+Pythia sample as a function of the $t\bar{t}$ system p_{T} (top) and the top-quark p_{T} (bottom). The two factors are multiplied to obtain the event weight correction.

accuracy through the parton shower for processes involving a $b\bar{b}$ pair. A reliable theoretical description of production in association with two b-jets requires matrix elements at NLO since the inclusion of such effects can reduce perturbative uncertainties from the 70−80% level at LO to about 20−30% [185–187]. NLO predictions with massive b-quarks in the four-flavour number scheme, or 4FNS, matched to a parton shower [188] are available in the Sherpa and MadGraph5_aMC@NLO (referred to in the following as MG5_aMC) frameworks. The finite b-quark mass allows to extend the $t\bar{t}+b\bar{b}$ matrix elements to the full phase space, including regions where b-quark pairs become collinear and matrix elements with $m_b = 0$ would be divergent. Therefore, in the 4FNS it is possible to simulate $t\bar{t}+b$-jets production in a fully inclusive way, including also signatures where a b-quark remains unresolved and a single b-jet is observed [188].

Three sets of $t\bar{t}+b\bar{b}$ samples were tested and compared to Powheg-Box+Pythia in order to improve the $t\bar{t}+\geq 1b$ modelling and/or estimate the associated systematic uncertainties:

- A $t\bar{t}+b\bar{b}$ sample is generated with Sherpa 2.1.1 version interfaced with OpenLoops (referred to as SherpaOL in the following) using the CT10 PDF set. The renormalisation scale for this sample is set to the CMMPS [188] value, $\mu_{\mathrm{CMMPS}} = \prod_{i=t,\bar{t},b,\bar{b}} E_{T,i}^{1/4}$ while the factorisation scale and resummation scale are set to $\mu_{\mathrm{F}} = \mu_{\mathrm{Q}} = H_{\mathrm{T}}/2$, where H_{T} is defined as the scalar sum of the transverse masses of all final state particles. The ME is then interfaced to the Sherpa parton shower with a dedicated tune developed for Sherpa;

- Two $t\bar{t}+b\bar{b}$ samples simulated with MG5_aMC for the hard-process use NNPDF3.0NLO [189] as PDF set and are interfaced to either Pythia8 (v8.210) or Herwig++ v2.7.1 for the showering and hadronisation, configured respectively with the A14 [190] and UE-EE-5 [191] tunes for the UE model. The same renormalisation and factorisation scales used in the Sherpa sample were employed in the generation of the two MG5_aMC sample; instead, the resummation scale was set to $\mu_R = f\sqrt{\hat{s}}$ with $f \in [0.1,0.25]$.

For the sake of completeness, it should be noted that there is a small contribution of $t\bar{t}+b\bar{b}$-like diagrams not included in the 4FNS samples: first, $b\bar{b}$ pairs arising from multiple parton interaction (MPI) overlaying $t\bar{t}$+jets events; and second, the production of a $b\bar{b}$ pair from a gluon radiated off the top decay products, which will be labeled as final-state radiation (FSR). Example Feynman diagrams for these contributions are shown in figure 5.4. These two contributions, MPI and FSR, have to be identified and excluded from the comparison between the above 4FNS NLO predictions and the 5FNS predictions (e.g. from Powheg-Box+Pythia).

The contribution of the various $t\bar{t}+\geq 1b$ particle-jet topologies to the cross section is shown in figure 5.5. The $t\bar{t}+b$ and $t\bar{t}+b\bar{b}$ are the two sub-categories that dominates the cross section; in those sub-categories the MG5_aMC samples and the Powheg-Box+Pythia sample predict higher

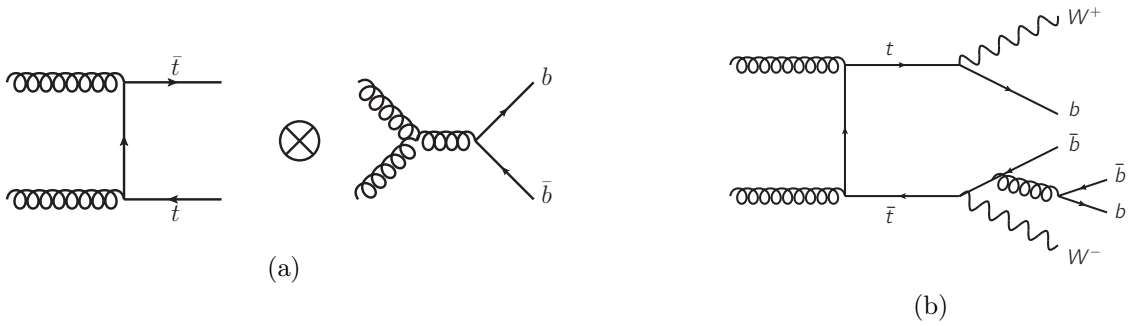

Figure 5.4: (a) $b\bar{b}$ production from multiple parton interaction overlayed with a $t\bar{t}$ event from the hard scatter and (b) $g \to b\bar{b}$ from final state radiation in a $t\bar{t}$ event.

cross sections than SherpaOL, with discrepancies that go up to 30%. Some examples of normalised distributions of different relevant variables the two main sub-categories are shown in figure 5.6. The MG5_aMC samples and the Powheg-Box+Pythia sample predicts a softer spectrum for the leading extra b-jet in the $t\bar{t}+b$ sub-category compared to SherpaOL, with differences up to 20%, as shown in figure 5.6a. For the ΔR between the two leading b-jets in $t\bar{t}+b\bar{b}$ sub-category, shown in figure 5.6b, the disagreements are smaller, reaching only 10%.

To improve the $t\bar{t}+\geq 1b$ modelling in Powheg-Box+Pythia, a reweighting procedure is applied to match the prediction from SherpaOL. The correction is performed by applying a kinematic reweighting separately in each of the $t\bar{t}+\geq 1b$ sub-categories, such that the relative normalisation of the sub-categories and the kinematic distributions match the SherpaOL prediction. In each sub-category, a two-dimensional reweighting based on the p_{T} of the top quark and the p_{T} of the $t\bar{t}$ system is performed. This is followed in the $t\bar{t}+b\bar{b}$ and $t\bar{t}+\geq 3b$ sub-categories by a two-dimensional reweighting of the ΔR between the two leading b-jets and the p_{T} of the system of the two leading b-jets; in the $t\bar{t}+B$ and $t\bar{t}+b$ sub-categories, the B or b-jet p_{T} and η are used instead. This reweighting improves

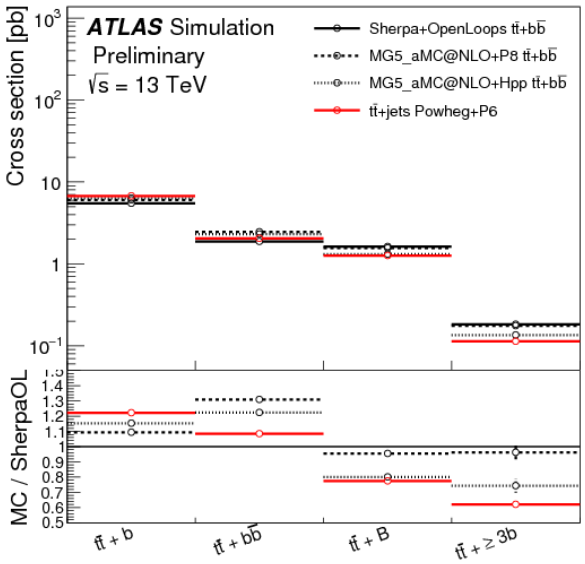

Figure 5.5: Cross section for different categories of $t\bar{t}+\geq 1b$ events. The three 4FNS NLO samples are compared to the Powheg-Box+Pythia $t\bar{t}$+jets sample.

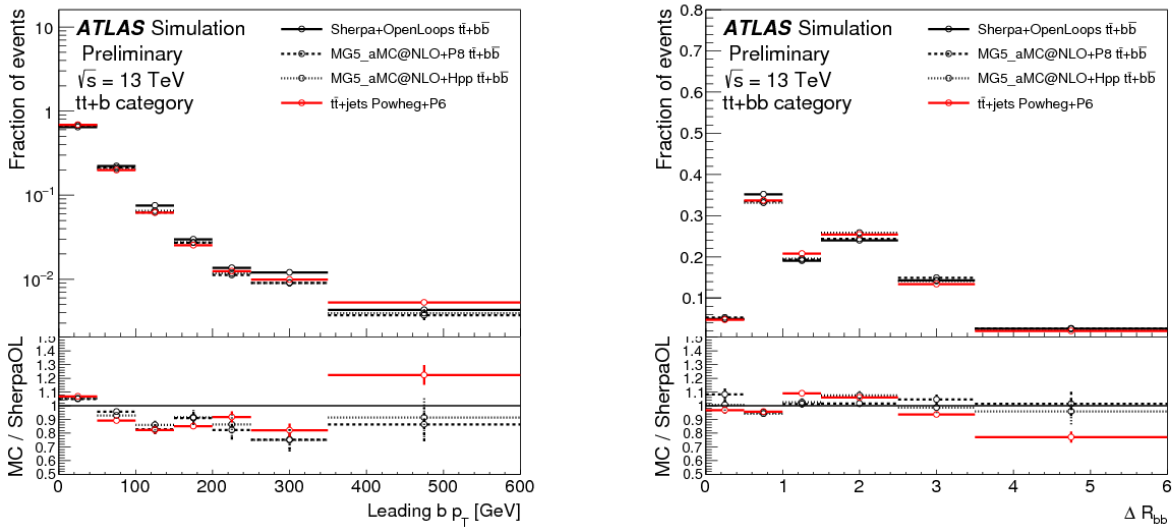

(a) (b)

Figure 5.6: (a) Transverse momentum of the leading extra b-jet in the $t\bar{t}+b$ sub-category and (b) ΔR between the two leading b-jets in the $t\bar{t}+b\bar{b}$ sub-category.

the modelling of the rest of the variables, though some minor differences remain. The effect of the reweighting both on shape and normalisation is $< 10\%$ (e.g. see figure 5.7). As discussed in section 6.5.1, the 4FNS NLO prediction from MG5_aMC will be used to assess systematic uncertainties.

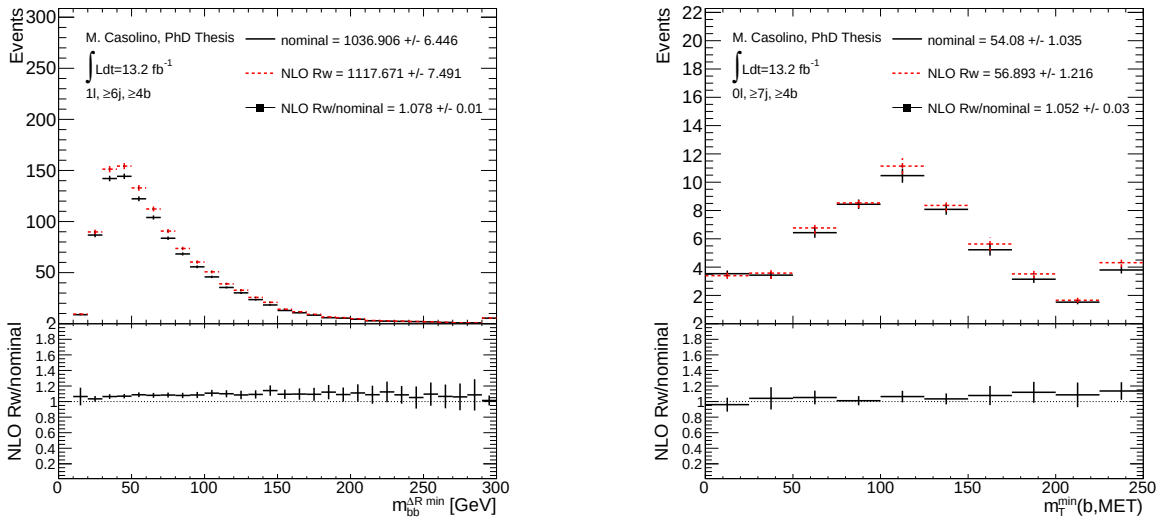

(a) (b)

Figure 5.7: (a) The mass of the $b\bar{b}$ pair with smallest ΔR distance, $m_{b\bar{b}}^{\min\Delta R}$ for events with 1 lepton at least six jets and at least four b-tags, and (b) the minimum transverse mass between $E_{\mathrm{T}}^{\mathrm{miss}}$ and any of the three leading b-tagged jets in the event, $m_{\mathrm{T,min}}^{b}$, for events with 0 lepton at least seven jets and at least four b-tags. In red the prediction obtained with the reweighting to SherpaOL and in black the nominal prediction.

5.2.1.3 $t\bar{t}+\geq 1c$

In case of $t\bar{t}+\geq 1c$ production, there is little guidance from theory or experiment on whether the parton shower provides a sufficiently accurate modelling of this process or whether a prediction with $t\bar{t}+c\bar{c}$ calculated in the matrix element is needed. Therefore, Powheg-Box+Pythia is used for the $t\bar{t}+\geq 1c$ prediction, with the possibility of applying as correction the $t\bar{t}$ and top p_{T} NNLO reweighting or only the top p_{T} NNLO reweighting. A novel simulation [192] using MG5_aMC interfaced with Herwig++ to generate $t\bar{t}+c\bar{c}$ at NLO in 3FNS using the CT103f PDF set is used to assess systematic uncertainties for analyses particularly sensitive to this background as described in section 7.4.1.

5.2.2 W/Z+jets production

The production of a single W or Z boson associated with additional jets is simulated using Sherpa 2.2 for all analyses presented in this dissertation, except for the $t\bar{t}H$ search where a slightly older version, 2.1.1 was used. The matrix element calculation is performed using up to two partons at NLO and up to four parton at LO using Comix and OpenLoops and then merged with the Sherpa parton shower using the ME+PS@NLO prescription [193]. The PDF set used in the calculation is CT10 with a dedicated parton shower tuning developed for Sherpa. Samples are generated separately for W/Z+light-jets, $W/Z+\geq 1b$ and $W/Z+\geq 1c$ using filters and then combined into the inclusive sample. Both W+jets and Z+jets processes are normalised to their respective NNLO theoretical cross sections calculated with Fewz [194].

5.2.3 Single top-quark production

Samples of single top-quark production in t-channel are generated using the Powheg-Box-Box 2.0 generator that uses the 4FNS for the NLO matrix element calculations and the fixed four-flavour CT10f4 PDF set. Samples corresponding to the s-channel and Wt production mechanisms are generated with Powheg-Box-Box 2.0 at NLO using the CT10 PDF set. For the Wt samples, the "diagram removal" scheme [195] is used to remove the overlap with $t\bar{t}$ production. The parton shower, hadronisation and the underlying event are modelled using Pythia 6.425 with the CTEQ6L1 PDF set in combination with the P2012 UE tune. The single-top-quark samples are normalised to the approximate NNLO theoretical cross sections [196–198].

Higgs boson production in association with a single top quark is also considered. The $tHbj$ process is generated with MG5_aMC interfaced to Herwig++ with the UE-EE5 tune. The CT10 PDF set is used, and the renormalisation and factorisation scales are fixed to 75 GeV. The tWH process is produced with the same generators and settings, but the renormalisation and factorisation scales are set to $H_{\mathrm{T}}/2$. The cross sections are calculated at NLO [199].

5.2.4 Diboson production

Samples of $WW/WZ/ZZ$+jets events are generated with Sherpa 2.1.1 using the CT10 PDF set and include processes containing up to four electroweak vertices. The matrix-element includes zero additional partons at NLO and up to three partons at LO using the same matching procedure between matrix element and parton shower as for the W/Z+jets samples. A requirement of a leptonic decay of at least one boson is applied at generation level. All diboson samples are normalised to their NLO theoretical cross sections provided by Sherpa.

5.2.5 $t\bar{t}V$ production

Samples of $t\bar{t}V$ events are generated with MG5_aMC 2.3.2, using LO matrix elements including up to one parton for $t\bar{t}\gamma^*/Z, \gamma^*/Z \to \ell^+\ell^-$ with $\ell = e$, μ, τ and two partons for $t\bar{t}W$ and $t\bar{t}Z, Z \to \nu\bar{\nu}$. For all samples showering is performed using Pythia 8.210 and the A14 UE tune, using the NNPDF2.3LO PDF set. The $t\bar{t}V$ samples are normalised to their NLO cross sections [200, 201].

5.2.6 Multijet production

Multijet events can enter the selected data sample through several production and misreconstruction mechanisms. In the case of non-prompt or fake electrons, these include contributions from semileptonic decays of b- and c-quarks, photon conversions and jets with large electromagnetic energy (from hadronisation to giving an energetic π^0 or from early showering in the calorimeter). Non-prompt or fake muons can originate from semileptonic decays of b- and c-hadrons, from charged hadron decays in the tracking volume or in hadronic showers, or from punch-through particles emerging from high-energy hadronic showers. While the probability of reconstructing a lepton from a "fake" source in a multijet event is very low, multijet events are characterised by a cross section several orders of magnitude larger than typical sources of prompt leptons (W and Z bosons).

Since this background is very difficult to model accurately with a MC simulation, a data-driven method, referred to as Matrix Method [202] (MM), is used to estimate the expected number of multijet events in the final selection sample. The MM relies on the difference in the lepton identification efficiency between real and "fake" leptons. It uses two samples: a "tight" sample, which corresponds to the final event selection, and a "loose" sample, which is obtained from the tight sample by relaxing some of the identification and isolation requirements (see sections 4.3.1 and 4.3.2). Due to the relaxation of the selection criteria, the loose sample contains a higher fraction of fake leptons. The number of selected events in each sample (N_{loose} and N_{tight}) are given by the sum of events containing real and fake leptons:

$$N_{\text{loose}} = N_{\text{loose}}^{\text{real}} + N_{\text{loose}}^{\text{fake}}, \tag{5.1}$$

$$N_{\text{tight}} = \varepsilon^{\text{real}} \cdot N_{\text{loose}}^{\text{real}} + \varepsilon^{\text{fake}} \cdot N_{\text{tight}}^{\text{fake}}, \tag{5.2}$$

where $\varepsilon^{\text{real}}$ ($\varepsilon^{\text{fake}}$) represents the probability for a real (fake) lepton satisfying the loose criteria to also satisfy the tight criteria, and both are measured in data control samples. An estimate for the number of events with fake leptons in the tight sample is obtained by solving the above system of equations:

$$N_{\text{tight}}^{\text{fake}} = \frac{\varepsilon^{\text{fake}}}{\varepsilon^{\text{real}} - \varepsilon^{\text{fake}}} \cdot (\varepsilon^{\text{real}} \cdot N_{\text{loose}} - N_{\text{tight}}). \tag{5.3}$$

As shown in equation 5.3, the power of the method resides in having sufficiently different efficiencies for the real and fake leptons. The efficiencies $\varepsilon^{\text{real}}$ and $\varepsilon^{\text{fake}}$ depend on lepton kinematics and event characteristics, such as the number of jets or b-jets. To correctly account for this, an event weight is computed from the efficiencies, which are parametrised as a function of the various object kinematics:

$$w_i = \frac{\varepsilon^{\text{fake}}}{\varepsilon^{\text{real}} - \varepsilon^{\text{fake}}} \cdot (\varepsilon^{\text{real}} - \delta_i) \tag{5.4}$$

where δ_i equals unity if the loose event i passes the tight event selection and 0 otherwise. The background estimate in a given bin of the final observable is given by the sum of w_i over all events in that bin.

The efficiencies $\varepsilon^{\text{real}}$ and $\varepsilon^{\text{fake}}$ are extracted from data in specific control regions designed to increase the fraction of real and fake leptons. For $\varepsilon^{\text{real}}$ the tag and probe method is employed to extract a very pure sample of prompt isolated leptons from $Z \to \ell^+\ell^-$ decays. The average $\varepsilon^{\text{real}}$ is ~ 0.89 (~ 0.93) for electrons (muons). To measure $\varepsilon^{\text{fake}}$, samples enriched in multijet background are selected by requiring 1 loose lepton, 1 b-jet, low $E_{\text{T}}^{\text{miss}}$, low transverse mass between the lepton and the $E_{\text{T}}^{\text{miss}}$,[1] and high impact parameter significance for the track (required only for muons). The average $\varepsilon^{\text{fake}}$ value is 0.17 (0.43) for electrons (muons).

5.2.7 Signal modelling

5.2.7.1 $t\bar{t}H$ production

The $t\bar{t}H$ signal process is modelled at NLO using MG5_aMC 2.3.2, interfaced to the Pythia 8.210 parton shower using the A14 UE tune. The NNPDF3.0NLO PDF set is used, and the factorisation and renormalisation scales are set to $\mu_F = \mu_R = H_{\text{T}}/2$, where H_{T} is defined as the scalar sum of the transverse energies of all final state particles. The top quarks are decayed using MadSpin [203], preserving all spin correlations. The sample is normalised to the NLO cross section [204–208]. All decay modes are considered and the branching fractions are calculated using Hdecay [209].

5.2.7.2 Vector-like quark pair production

Samples of simulated $T\bar{T}$ events are generated with the LO generator Protos 2.2 using the NNPDF2.3 LO PDF set and processed through Pythia 8.186 for parton showering and fragmentation using the A14 UE tune. The vector-like quarks are forced to decay with a branching ratio of 1/3 to each of the three modes (W, Z, H). Events are reweighted using generator-level information to obtain any arbitrary sets of branching ratios consistent with the three decay modes summing to unity. Samples are generated assuming singlet couplings and for heavy-quark masses between 350 GeV and 1500 GeV in steps of 50 GeV. Additional samples are produced for a few mass points assuming doublet couplings, in order to confirm that kinematic differences arising from the different chirality of singlet and doublet couplings, after reweighting the singlet and doublet samples to the same branching ratios, have negligible impact on this analysis. The $T\bar{T}$ samples are normalised using the theoretical cross section computed using Top++ 2.0 at NNLO including resummation of NNLL soft-gluon terms, and using the MSTW 2008 NNLO PDF set.

5.2.7.3 Four-top-quark production

Samples of simulated four-top-quark events for the three production mechanisms discussed in section 1.2.5 are generated at LO with the MG5_aMC generator (the versions used are 2.2.2, 2.2.3 and 1.5.14 for SM, EFT and 2UED/RPP, respectively) and the NNPDF2.3 LO PDF set, interfaced to Pythia 8 (the versions used are 8.186, 8.205 and 8.186 for SM, EFT and 2UED/RPP, respectively) and the A14 tune. The SM $t\bar{t}t\bar{t}$ sample is normalised to a cross section of 9.2 fb (computed at NLO with MG5_aMC), while the EFT $t\bar{t}t\bar{t}$ sample is normalised assuming $|C_{4t}/\Lambda^2| = 4\pi\text{TeV}^{-2}$, which yields a cross section of 928 fb. In the case of the 2UED/RPP model, samples are generated for four different values of m_{KK} (1000 to 1800 GeVin steps of 200 GeV) and the Bridge [210] generator is used to decay the pair-produced excitations from tier (1,1) generated by MG5_aMC.

[1] See equation 6.1for the definition.

5.2.7.4 Associated production of heavy Higgs bosons

Samples of simulated $b\bar{b}H(\to t\bar{t})$ and $t\bar{t}H(\to t\bar{t})$ events are generated assuming a Type-II 2HDM model using the MG5_aMC 2.3.3 generator, interfaced to Pythia 8.210 and the A14 tune. The matrix element calculation is performed at LO in 4FNS and the corresponding 4FNS CTEQ6L1 PDF set is used. Spin correlations are taken into account in the decays of top quarks and W bosons. Samples are generated for heavy Higgs-boson masses between 400 GeV and 1000 GeV in steps of 100 GeV. These samples can also be used to model $b\bar{b}A(\to t\bar{t})$ and $t\bar{t}A(\to t\bar{t})$ production, as generator level studies showed no significant differences in the kinematics of the decay products for processes involving the production of a CP-even or CP-odd Higgs boson of the same mass. The $tbH^{\pm}(\to tb)$ samples are generated at NLO using MG5_aMC 2.2.2 with the NNPDF2.3 PDF set, interfaced to Pythia 8.212 with the A14 tune. A Type-II 2HDM model is assumed. The width of the charged Higgs boson has been set to zero. Samples are generated for charged Higgs boson masses between 200 GeVand 2000 GeV.

All samples are normalised to a reference cross section times branching ratio of 1 pb. For the interpretation of results, cross sections and branching ratios are computed separately for Type-I and Type-II 2HDMs, as a function of heavy Higgs boson mass, $\tan\beta$ and $\cos(\beta-\alpha)$. In the case of $b\bar{b}H(\to t\bar{t})$ and $t\bar{t}H(\to t\bar{t})$ production, the predictions are obtained using the codes SusHi 1.5.0 [211], which implements calculations from Refs. [212–216], and 2HDMC 1.7.0 [50]. The $t\bar{t}H(\to t\bar{t})$ cross sections are computed at NLO, whereas the $b\bar{b}H(\to t\bar{t})$ cross sections are obtained from the so-called "Santander matching" of NLO cross sections in 4FNS and NNLO cross sections in 5FNS [217]. Similarly, the $tbH^{\pm}(\to tb)$ cross sections are obtained using the "Santander matching" of 4FNS NLO and 5FNS NNLO cross sections [218–221]. The charged Higgs boson branching ratios are also obtained using 2HDMC.

5.3 Tag rate function method

The estimation of backgrounds at high b-tag multiplicity can be challenging if MC statistics is fairly low, especially for those samples that are selected because of light-jet mistags (mistag rate $< 1\%$). Analyses that use the shape information to extract the signal can be negatively affected by the large statistical uncertainties on the templates and unreliable systematic uncertainties due to shape fluctuations. The tag rate function (TRF) method [222, 223] helps increase the effective statistics of the MC samples by using all the events prior to the b-tag selection and weighting, rather than rejecting, those events not containing the specific number of b-tagged jets in simulation. The weight is computed by combining the tagging probabilities of each jet in the event. For events with a large number of b-jets, the method effectively compensates for the statistics losses due to b-tagging efficiencies. To achieve this, the tagging efficiency is parametrised as function of p_{T}, η and truth jet flavour,[2] $\varepsilon(\eta, p_T, f)$ and is used to calculate the event weight based on the kinematics of the selected jets in each event. The efficiency maps used are shown in figure 4.21.

When requiring a given number of b-tagged jets in the event (n_b), all permutations are built considering n_b jets labelled as tagged among N jets in the event; in total $C(N, n_b) = \binom{N}{n_b}$ permutations are possible. The probability of each permutation is computed from the multiplication of the per-jet weights: the jet weight is equal to the tagging efficiency if the jet is labelled as tagged, one minus the efficiency in the opposite case. Summing the probabilities of all permutations gives the per-event TRF

[2] The true jet flavour is defined by looking at hadrons with $p_{\mathrm{T}} > 5$ GeVwithin a $\Delta R < 0.3$ cone around the jet direction. If a b-hadron is found, the jet is labelled as a b-quark jet. If no b-hadrons are found, c-hadrons are considered and, if found, the jet is labelled as a c-quark jet. If no c-hadrons are found either, the jet is labelled as a light-jet.

weight. As an example, the probability of having exactly one b-tagged jet in the event with N jets is given by:

$$P_{=1} = \sum_{i=1}^{N} \left(\varepsilon_i \prod_{i \neq j} (1 - \varepsilon_j) \right) \tag{5.5}$$

and in general the probability for inclusive b-tagging selections can be computed as:

$$P_{\geq 1} = 1 - P_{=0}, \tag{5.6}$$

where $P_{=0}$ is the probability that the event contains exactly zero b-tags. To compute the shape of the distributions built using b-tagged jet information, not only the probability for a given event is required, but also the knowledge of which jets are considered as tagged when a given number of tags is assumed. This is achieved by randomly choosing one of the possible permutations based on their relative probabilities. When comparing to data, the tagging efficiencies in the formulas above are multiplied by the corresponding SFs. To propagate the effect of systematic uncertainties, the efficiencies are modified due to the change in the SFs leading to a different event probability.

Closure tests on MC have been performed to validate the good performance of the parametrisation, Figure 5.8 shows the comparison between the prediction obtained with the TRF method and the direct application of the cut on the b-tagging algorithm output for the $t\bar{t}$+light-jets background. In a region with exactly two b-tags (see figure 5.8a) the TRF method improves the statistical error on the yields, while in a region with at least four b-tags (see figure 5.8b) it improves not only the statistical error but as well the description of the shape. Within the available statistics, the TRF method provides a good description of yields and shapes with respect to the direct application of the b-tagging algorithm in the analysis regions. Whenever there is a statistically-significant ($\geq 2\sigma$) discrepancy in yields between the two methods, the yields from the TRF prediction are corrected to match those of direct b-tagging, in order to ensure that no bias is introduced.

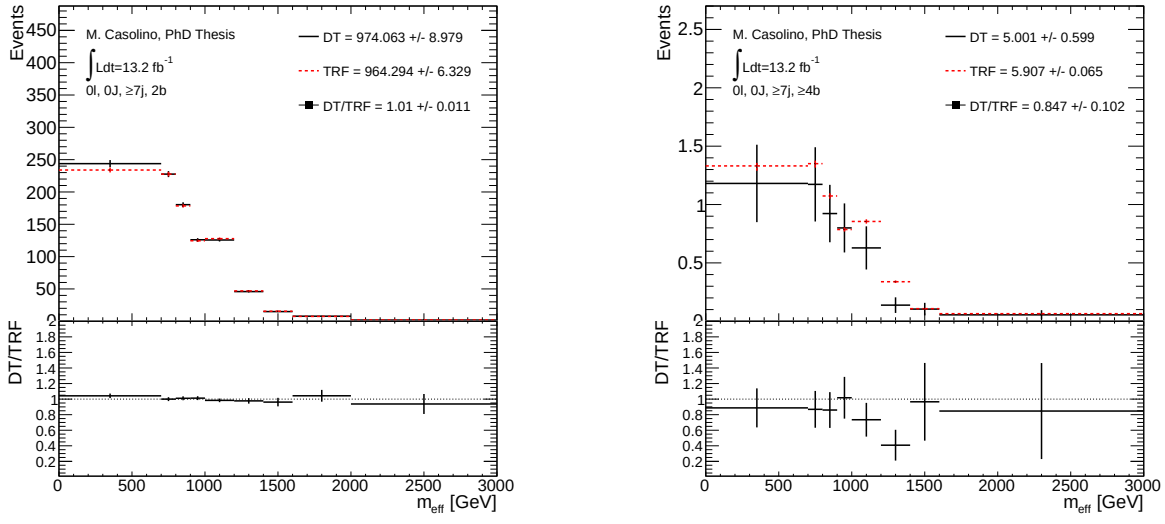

(a) (b)

Figure 5.8: The m_{eff} distribution, defined as the scalar sum of lepton p_{T}, jets p_{T} and $E_{\text{T}}^{\text{miss}}$, for a region (a) with exactly two b-tags and (b) with at least four b-tags. Shown in red is the prediction obtained with the TRF method and in black from the direct application of the cut on the b-tagging algorithm output.

5.4 Statistical tools

The primary goal of data analysis in particle physics is to test our understanding of particle interactions and to search for new phenomena not accounted by the SM. Statistical concepts help in quantifying the correspondence between theoretical predictions and experimental observations. The use of a statistical test in a physics analysis, involving different event types, comes up in different ways: sometimes to carry out measurements and sometimes to make a statement about the existence of a new signal process. Hypothesis testing addresses the question whether some observed data sample is more compatible with a given theory model or with an alternative one. Discovery is formulated in terms of a hypothesis test where the background-only hypothesis plays the role of the null hypothesis, H_0, and the signal-plus-background hypothesis plays the role of the alternative test hypothesis, H_1. The two hypotheses can be generalised by introducing a signal strength modifier, μ, which acts as a multiplicative factor to the signal cross section. The null (test) hypothesis is recovered for $\mu = 0$ (1). In the search for the $t\bar{t}H$ process, the SM without the Higgs boson is considered the background-only hypothesis, while the signal-plus-background hypothesis includes the Higgs boson as signal. Searches for BSM signatures include the SM Higgs boson in the background model.

The claim of discovery is a statement that the data are incompatible with the background-only hypothesis. Testing an hypothesis means to quantify the agreement between the outcome of a measurement and the predictions coming from that hypothesis using a test statistic. From the test statistic a p-value, p_μ, is the probability to obtain a value of the test statistic as large or larger than the one observed, assuming a model with signal strength μ. If this p-value is less than some specified value α, usually referred to as the power of the test, the model is rejected. The p-value is often translated into an equivalent quantity called the Gaussian significance, Z, defined as the number of standard deviations that correspond to an upper-tail probability of p-value for a Gaussian-distributed variable. The definition of significance and p-value are shown in figure 5.9. The convention to exclude a new process ($\mu = 1$) is that p-value should be less than 5% but to claim a discovery (excluding $\mu = 0$ hypothesis), instead, it is common to set the p-value to a very low value of 2.9×10^{-7} that corresponds to a significance Z=5. Setting the p-value to the value of the power of the test ($p_\mu = \alpha$) and solving for μ provides the highest and the lowest μ that are not excluded (upper and lower limits respectively) at a confidence level equal to $1 - \alpha$.

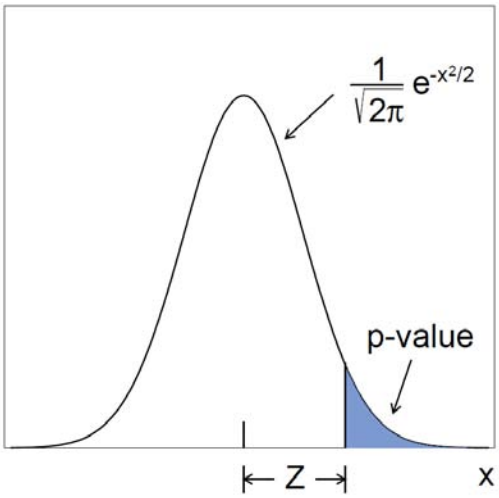

Figure 5.9: Illustration of the definition of p-value and significance Z.

5.4.1 CL_s method

In case the distributions of a test statistic, q_μ, for signal and background are very close ("low sensitivity"), the p-value can reject a model even if there is no enough sensitivity due to downwards fluctuations in the observed data. With α set to 5% a model every twenty will be excluded even if there is no sensitivity. A solution to this problem is the CL_s method [224], which in case of low sensitivity alters the threshold to reject a model by defining:

$$CL_s = \frac{p_\mu}{1 - p_0}, \tag{5.7}$$

where p_0 is the p-value for the background-only hypothesis. In case of low sensitivity if $p_\mu < \alpha$ the quantity $1 - p_0$ will be small as well leading to CL_s value greater than p_μ such that the model will not be rejected (see figure 5.10). For searches at the LHC, the CL_s value is used instead of p_μ to set upper limits. If $CL_s < 0.05$, the signal-plus-background hypothesis with a signal strength μ is excluded at 95% confidence level.

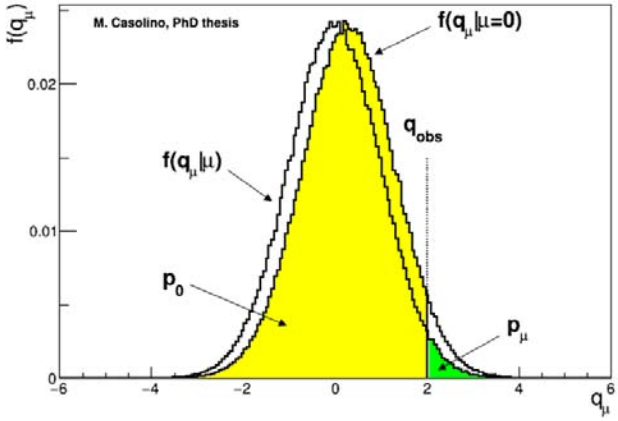

Figure 5.10: Illustration of the ingredients for the CL_s limit in case of low sensitivity.

5.4.2 Profile likelihood ratio

The data in each bin of each distribution are expected to follow a Poisson probability distribution around the expected mean of $\mu s + b$, where s and b correspond to the number of expected signal and background events, and μ is the signal strength modifier. A likelihood function is obtained from the probability of data given a certain hypothesis. Therefore, the likelihood for the observed data produced by this model is:

$$L(\mu) = \prod_{i=1}^{\text{bins}} \frac{\mu s_i + b_i}{n_i!} e^{-\mu s_i + b_i}. \tag{5.8}$$

To establish the existence of the signal process tests of different hypothetical values of μ should be performed. To maximise the probability of a discovery the test of the background-only ($\mu = 0$) hypothesis should have as high power as possible. According to the Neyman-Pearson lemma, the maximum power is achieved by basing the test on the likelihood ratio $L(\mu)/L(\mu = 0)$, or equivalently on the statistic:

$$q_\mu = -2 \ln \frac{L(\mu)}{L(\mu = 0)}. \tag{5.9}$$

Thus the best estimate for μ is obtained minimizing this statistic, which means to maximise the likelihood for the signal-plus-background hypothesis.

The number of background in events is usually affected by uncertainties in the form of systematic and statistical errors. A more realistic approach consists in including the systematic uncertainties directly in the definition of the likelihood through a suitable set of continuous parameters θ, referred to as nuisance parameters (NPs), that parametrise the effect of each uncertainty on the signal and background predictions. As a net effect, the various terms in the likelihood acquire a dependence on θ; varying the values of the NPs allows to modify both the shape and normalisation of the signal and background predictions. The maximisation of the likelihood leads to adjustments in the NPs in order to improve the agreement of the expectation with the observed data. The NPs are characterised by a probability distribution function (pdf) $\rho(\theta)$, encoding the information about its best estimate and width, which is related to the size of the uncertainty. The pdfs for each systematic uncertainty are determined beforehand by auxiliary measurements. The pdf is also included in the likelihood and is usually referred to as penalty term or prior on θ. The prior distribution for NPs is commonly assumed to be a Gaussian but other distributions (log-normal, gamma) could be more suitable in specific cases. This description of the priors is based on the absolute values of the NP and their uncertainties, and understanding the fit result becomes very difficult since it requires the knowledge of the pre-fit values for each NP. In order to simplify the analysis, all NPs are redefined in order to be centred at zero and with a width of one. The nuisance parameters are unknown parameters that need to be determined by the fit. This approach allows the data under study to potentially improve the initial knowledge of systematic uncertainties obtained from external inputs to the analysis. In case the data are not particularly sensitive to a given source of systematics, the constraint term in the likelihood ensures that the nuisance parameter stays at 0 and its error is dominated by the input uncertainties. On the other hand, the fit procedure could shift (pull) a nuisance parameter to achieve a better data/MC description or, at the same time, produce a reduction (constraint) of the error of the nuisance parameter with respect to its initial value. This usually happens when the large effects of a particular systematic uncertainties are not supported by the available data statistics. Furthermore, during the likelihood maximisation process, correlations can be established among nuisance parameters that have similar effects in the regions considered by the fit, which further aids in the reduction of the final effect of the total systematic uncertainties.

Using the pdf for the NPs we can write the likelihood as:

$$L(\mu,\theta) = \prod_{i=1}^{bins} \frac{\mu s_i + b_i}{n_i!} e^{-\mu s_i + b_i} \prod_{k=1}^{NPs} \rho(\theta_k). \tag{5.10}$$

The profile likelihood is defined as:

$$L_p(\mu) = L(\mu, \hat{\hat{\theta}}(\mu)), \tag{5.11}$$

where $\hat{\hat{\theta}}(\mu)$, known as profile values of the NPs θ, are the values that maximise $L(\mu,\theta)$ for the fixed value of μ.

The test static used at the LHC and in this dissertation is based on a likelihood ratio to maximise the power of the test. Specifically, it is a profile likelihood ratio [225] defined as:

$$q_\mu = -2\ln\lambda(\mu) = -2\ln\frac{L_p(\mu)}{L(\hat{\mu})}, \tag{5.12}$$

where $\hat{\mu}$ is the value that globally maximises the likelihood. The profile likelihood ratio $\lambda(\mu)$ lies between 0 and 1, with values of λ close to 1 implying good agreement between the data and the

hypothesised value of μ.

From the test statistic a p-value can be computed, giving the probability that the observed data originates from the considered hypothesis:

$$p_\mu = \int_{q_{\mu,\text{obs}}}^{\infty} f(q_\mu|\mu,\theta)dq_\mu, \tag{5.13}$$

where $q_{\mu,\text{obs}}$ is the observed value of the test statistic in data and $f(q_\mu|\mu,\theta)$ denotes the pdf of q_μ assuming the hypothesis μ. The computation of background-only quantities such as p_0 are just special cases with $\mu = 0$.

For sufficiently large data samples the Wilk and Wald theorems [226] demonstrate that the distribution of the pdf for the test static q_μ approaches an asymptotic form related to the chi-square distribution with one degree of freedom. The test statistic in this approximation has a form:

$$q_\mu = -2\ln\lambda(\mu) = \frac{(\mu-\hat{\mu})^2}{\sigma^2} + \mathcal{O}(1/\sqrt{N}), \tag{5.14}$$

where the fitted strength parameter $\hat{\mu}$ follows a Gaussian distribution with a mean μ and standard deviation σ, and N accounts for the data sample size. This formula require knowing the variance of the maximum likelihood estimate of μ , which can be estimated from an artificial dataset referred to as the Asimov dataset [225]. The Asimov data set is defined as the one where the pseudo-data is equal to the expectation value, i.e. to the sum of background predictions. An important advantage of using the profile likelihood ratio is that its asymptotic distribution is independent of the nuisance parameters. For the searches described in this dissertation the asymptotic approximation [225] is used in order to compute the relevant p-values.

6

Search for new phenomena in $t\bar{t}$ final states with additional heavy-flavour jets

If we knew what it was we were doing,
it would not be called research, would it?
Albert Einstein

Contents

This chapter presents a broad search for new phenomena involving top quarks and Higgs bosons, probing several physics processes predicted by BSM models. The search targets a variety of signals:

- pair production of a vector-like top quark (T) (see section 1.2.4) with a significant branching ratio to a top quark and either a SMl Higgs boson or a Z boson,

- four-top-quark production within the SM and in several BSM scenarios (see section 1.2.5), and
- heavy Higgs bosons (neutral and charged) produced in association with, and decaying into, third generation quarks (see section 1.2.1.1).

This search uses the data and simulated samples described in chapter 5. In this chapter the event selection, analysis strategy, event categorisation, and the discriminating variable are discussed, and the details of the profile likelihood fit are explained. Results and interpretations of this search are presented at the end of the chapter along with a comparison with other existing searches. Finally, prospects for future improvements are discussed.

6.1 Event preselection

Events satisfying the trigger selection described in section 5.1 are further classified into the "1-lepton" or "0-lepton" channels depending on the multiplicity of the selected leptons. Events in the 1-lepton channel are required to have exactly one reconstructed electron or muon satisfying the quality and kinematic criteria discussed in sections 4.3.1 and 4.3.2. The selected lepton is required to match the lepton reconstructed by the single-lepton trigger with $\Delta R < 0.15$. The lepton is required to have $p_{\mathrm{T}} > 25$ GeV in order to be in the region where the trigger is fully efficient. Events satisfying either the electron or muon selections are combined and treated coherently, regardless of the lepton flavour. Events in the 0-lepton channel are required to satisfy the $E_{\mathrm{T}}^{\mathrm{miss}}$ trigger and to have $E_{\mathrm{T}}^{\mathrm{miss}}$ >200 GeV in order to be in the region where the trigger is fully efficient. Events are required to have ≥5 (≥6) jets with $p_{\mathrm{T}} > 25$ GeV and $|\eta| < 2.5$ in the 1-lepton (0-lepton) channel. Given the high number of b-quarks in the final state for signal events, a requirement of at least two b-tagged jets (77% operating point) is included for both channels to remove backgrounds not including b-quark jets. Additional requirements are related to the quality of the event reconstruction or the detector status and are usually referred to as "event cleaning":

- Data quality: the "Good Runs List" is the collection of lumiblocks[1] with no subdetector problems; thus only events present in this list are retained.
- Corrupted data removal: detector problems happening for periods shorter than a lumiblock are rejected with event-level flags without losing the entire lumiblock. Events are removed if integrity problems or noise bursts are found in the calorimeters or if they are affected by the recovery procedure for single-event upsets in the SCT.
- Bad jets removal: events are rejected if a "bad jet", as defined in section 4.4.3.8, with $p_{\mathrm{T}} > 20$ GeV and $|\eta| < 2.5$ is found. This condition is particularly important to minimise the contribution from mismeasured jets to the $E_{\mathrm{T}}^{\mathrm{miss}}$ computation.

In the 1-lepton channel the presence of a leptonically-decaying W boson in the final state can also be exploited to suppress background from multijet events, which are characterised by a fake lepton. The transverse mass of the leptonic W boson, m_{T}^{W}, can be reconstructed from the lepton and the $E_{\mathrm{T}}^{\mathrm{miss}}$:

$$m_{\mathrm{T}}^{W} = \sqrt{2p_{T}^{\ell}E_{\mathrm{T}}^{\mathrm{miss}}(1-\cos\Delta\phi(\ell, E_{\mathrm{T}}^{\mathrm{miss}}))}, \tag{6.1}$$

[1] A luminosity block (lumiblock) is the smallest unit of time in the ATLAS data-taking defined as the minimal period where all the data-taking configurations are constant. In general the duration of a luminosity block is of the order of 1 minute.

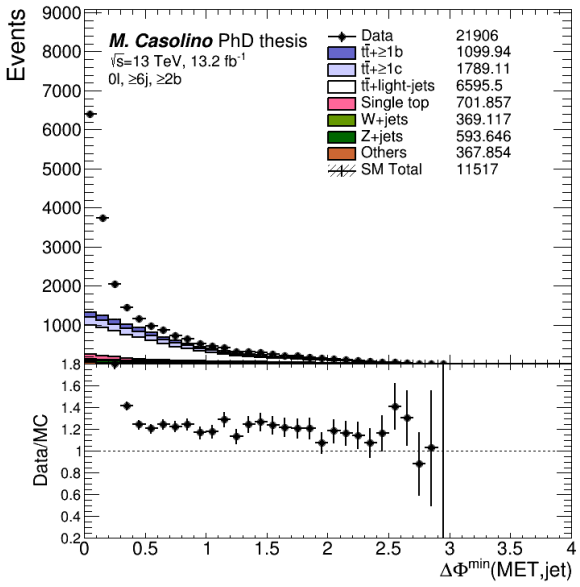

Figure 6.1: Distribution of $\Delta\phi_{min}^{4j}$ at preselection level prior to cutting on this variable.

Preselection requirements		
Requirement	1-lepton channel	0-lepton channel
Event cleaning	✓	✓
Trigger	Single-lepton trigger	$E_{\mathrm{T}}^{\mathrm{miss}}$ trigger
Leptons	=1 isolated e or μ	=0 isolated e or μ
Jets	≥5 jets	≥6 jets
b-tagging	≥2 b-tagged jets	≥2 b-tagged jets
$E_{\mathrm{T}}^{\mathrm{miss}}$	$E_{\mathrm{T}}^{\mathrm{miss}} > 20$ GeV	$E_{\mathrm{T}}^{\mathrm{miss}} > 200$ GeV
Other $E_{\mathrm{T}}^{\mathrm{miss}}$-related	$E_{\mathrm{T}}^{\mathrm{miss}} + m_{\mathrm{T}}^{W} > 60$ GeV	$\Delta\phi_{\mathrm{min}}^{4j} > 0.4$

Table 6.1: Summary of preselection requirements for the 1-lepton and 0-lepton channels. Here m_{T}^{W} is the transverse mass of the lepton and the $E_{\mathrm{T}}^{\mathrm{miss}}$ vector, and $\Delta\phi_{\mathrm{min}}^{4j}$ is the minimum azimuthal separation between the $E_{\mathrm{T}}^{\mathrm{miss}}$ vector and the four highest-p_{T} jets.

where p_{T}^{ℓ} is the transverse momentum (energy) of the muon (electron) and $\Delta\phi$ is the azimuthal separation between the lepton and the direction of the missing transverse momentum. Thus, additional requirements are made on $E_{\mathrm{T}}^{\mathrm{miss}}$ and m_T^W: $E_{\mathrm{T}}^{\mathrm{miss}}$ >20 GeV and $E_{\mathrm{T}}^{\mathrm{miss}} + m_T^W > 60$ GeV.

Multijet events in the 0-lepton originate from mismeasured high-p_{T} jets resulting in large $E_{\mathrm{T}}^{\mathrm{miss}}$ that tends to be aligned with the jet direction. A requirement of $\Delta\phi_{\mathrm{min}}^{4j} > 0.4$ is made to suppress it (see figure 6.1), where $\Delta\phi_{\mathrm{min}}^{4j}$ is the minimum azimuthal separation between the $E_{\mathrm{T}}^{\mathrm{miss}}$ vector and the four highest-p_{T} jets. This requirement is very effective to suppress multijet events at negligible level. Figure 6.2 show the m_{eff}[2] distribution before and after the $\Delta\phi_{\mathrm{min}}^{4j}$ cut, which suppresses the multijet background and improves data-to-MC agreement.

Table 6.1 summarises the requirements described above and referred to as the "preselection".

[2]Defined in section 6.4.

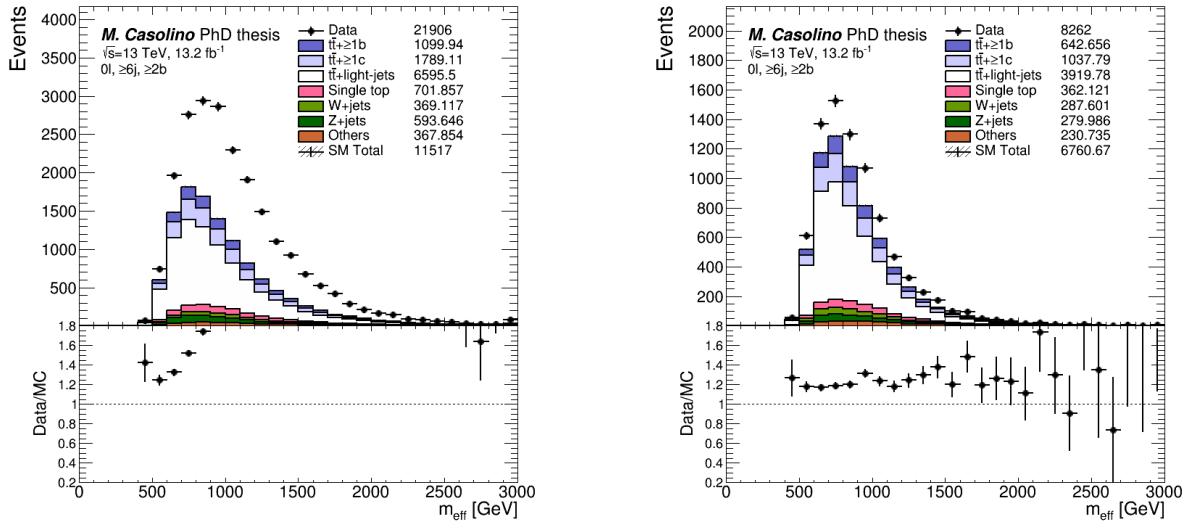

(a) (b)

Figure 6.2: m_{eff} distribution (b) before and (c) after the $\Delta\phi^{4j}_{min} > 0.4$ cut.

6.2 Comparison between data and prediction

The requirement of at least two b-tagged jets selects a sample dominated by $t\bar{t}$+jets. Thus data-to-MC comparisons at preselection level give the possibility to validate the modelling of the main backgrounds. Figures 6.3 and 6.4 show basic kinematic variables at preselection level in both 1-lepton and 0-lepton channels.

Most of the observed discrepancies are covered by systematic uncertainties, which at the preselection level are $\sim$ 25%, dominated by jet energy scale, JVT SFs and b-tagging SFs. Additional contributions from the $t\bar{t}$ cross section and modelling cover the discrepancy in the jet multiplicity (see figure 6.5a). A significant mismodelling in the b-jet multiplicity related to an underestimate of the $t\bar{t}+ \geq 1b$ cross section in Powheg+Pythia, is not covered by systematic uncertainties since no uncertainty is assigned to it (see figure 6.5b) as this background will be directly fitted from data. The treatment of systematics uncertainties is described in section 6.5.1.

6.3 Analysis strategy and event categorisation

The search is optimised for discovery of $T\bar{T}$ production where at least one of the T quarks decays into a Higgs boson and a top quark: $T\bar{T} \to HtHt, HtZt, HtWb$.[3] For the dominant $H \to b\bar{b}$ decay mode, the final state signature involves high jet[4] and b-tag multiplicities characteristic of $t\bar{t}$ with additional heavy-flavour jets. The 0-lepton channel exploits, with the addition of high $E_{\text{T}}^{\text{miss}}$ in the final state, the presence of high-momentum Z bosons decaying into $\nu\bar{\nu}$ or W bosons decaying leptonically, either to an electron or muon that is not reconstructed, or to a hadronically-decaying τ-lepton that is identified as a jet. To a lesser extent, this search is also sensitive to $T\bar{T} \to ZtZt, ZtWb$ with $Z \to b\bar{b}$.

Four-top-quark production, both within the SM and in BSM extensions are also characterised by

[3] In the following $HtZt$ will be used to denote both $HtZ\bar{t}$ and its charge conjugate, $H\bar{t}Zt$. Similar notation will be used for other processes, as appropriate.

[4] In the following, the term "jet" is used to refer to a small-R jet, while the term "mass-tagged jet" denotes a large-R jet satisfying several kinematic criteria described in this section

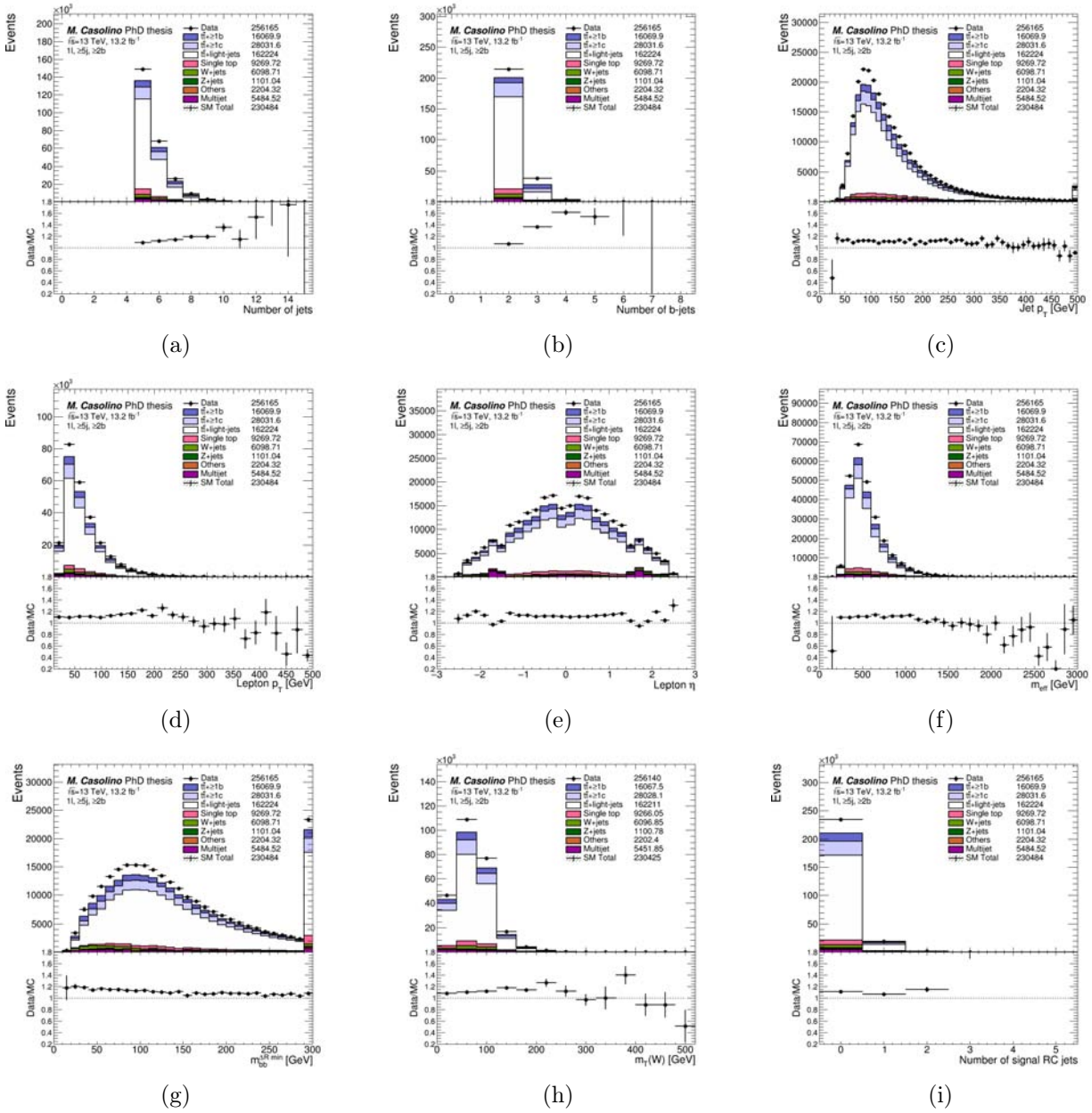

(a) (b) (c)

(d) (e) (f)

(g) (h) (i)

Figure 6.3: Comparison between data and prediction in 1-lepton channel for (a) jet multiplicity, (b) b-tag multiplicity, (c) leading jet p_{T}, (d) lepton p_{T}, (e) lepton η, (f) m_{eff}, (g) invariant mass of the closest b-jets pair ($m_{bb}^{\mathrm{min}\Delta R}$) , (h) transverse mass of the W boson m_{T}^{W}, and (j) RT-jet multiplicity.

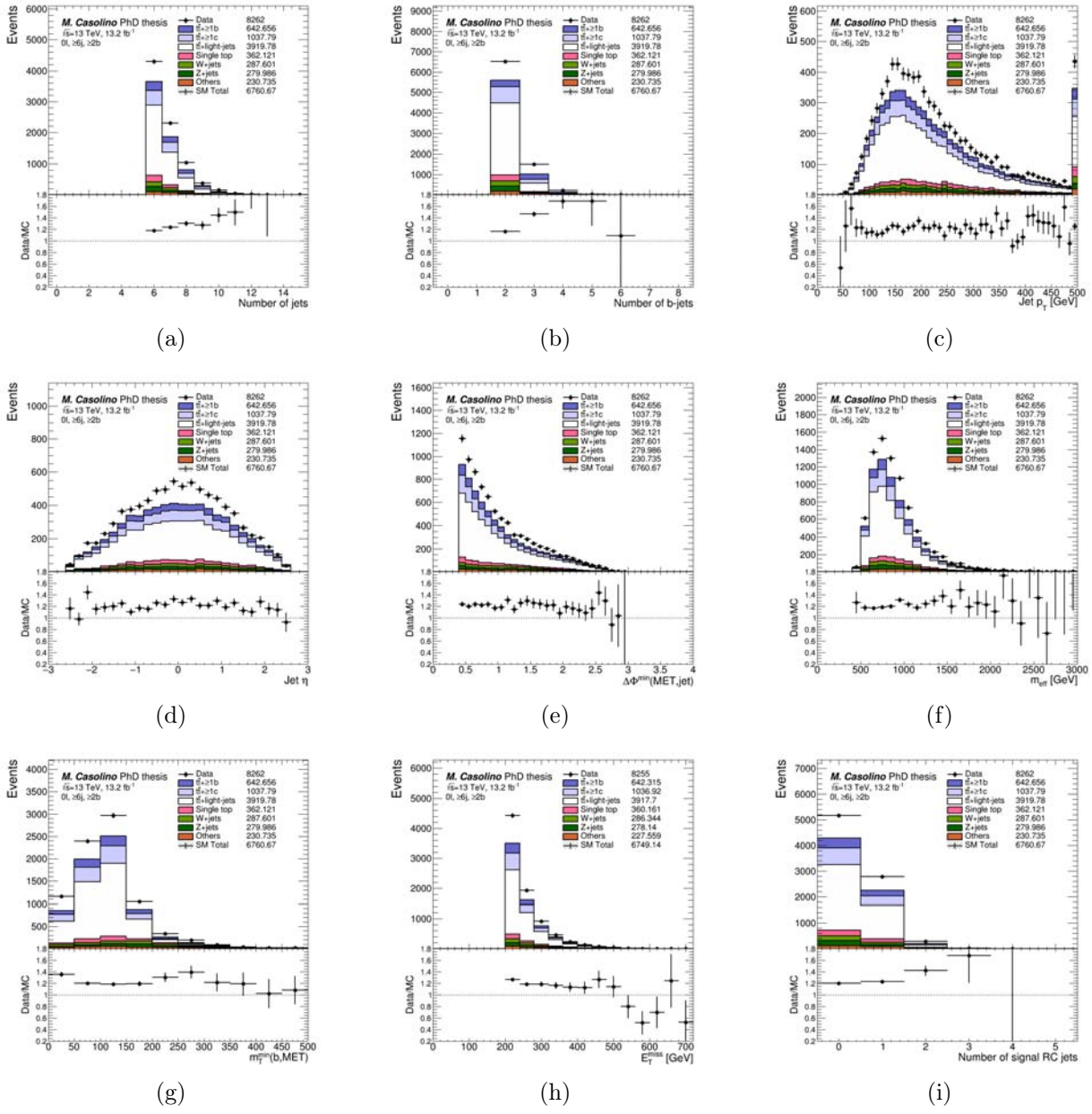

(a) (b) (c)

(d) (e) (f)

(g) (h) (i)

Figure 6.4: Comparison between data and prediction in 0-lepton channel for (a) jet multiplicity, (b) b-tag multiplicity, (c) leading jet p_{T} and (d) leading jet η, (e) $\Delta\phi^{4j}_{\mathrm{min}}$, (f) m_{eff}, (g) minimum transverse mass of the leading four b-jets and $E_{\mathrm{T}}^{\mathrm{miss}}$ ($m^{b}_{T,\mathrm{min}}$) , (h) $E_{\mathrm{T}}^{\mathrm{miss}}$ and (j) RT-jet multiplicity.

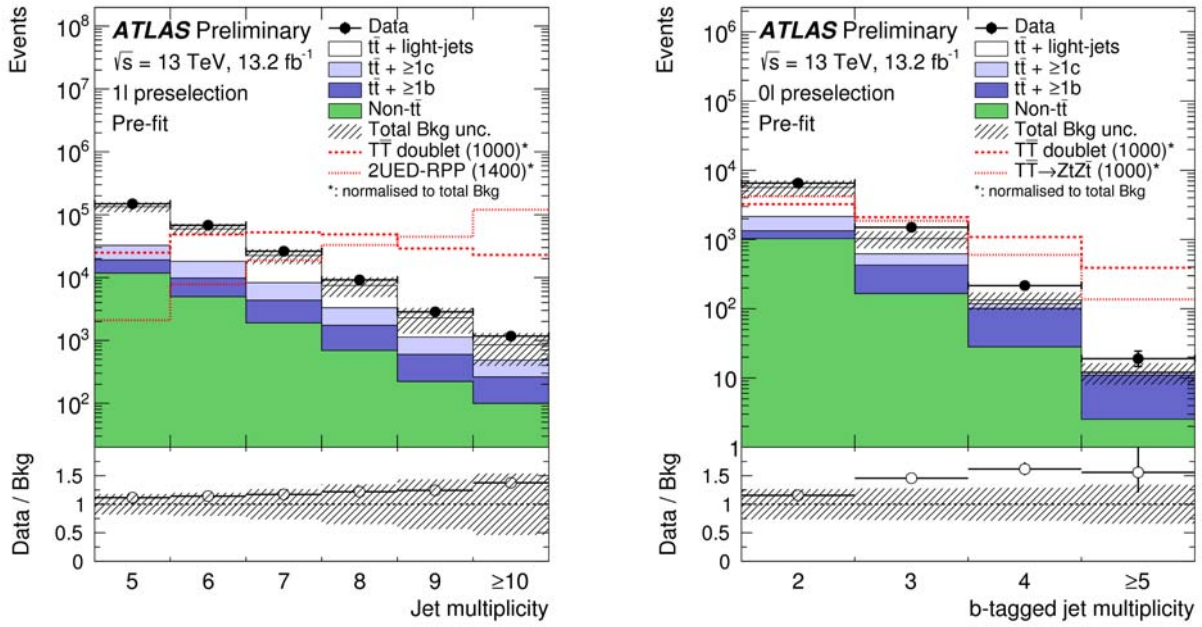

(a) (b)

Figure 6.5: Comparison between data and prediction before performing the fit to data for (a) the jet multiplicity in 1-lepton channel and (b) the b-tag multiplicity in 0-lepton channel. The small contributions from $t\bar{t}V$, $t\bar{t}H$, single top, W/Z+jets, diboson, and multijet backgrounds are combined into a single background source referred to as "Non-$t\bar{t}$". The expected signal distributions are shown, normalised to the total background prediction, for three scenarios considered in this search: $T\bar{T}$ production in the weak-isospin doublet scenario and for BR($T \to Zt$) = 1 assuming m_T=1000 GeV (red dashed and continuous histogram respectively), and $t\bar{t}t\bar{t}$ within the 2UED/RPP model assuming m_{KK}=1400 GeV (red dotted histogram). The last bin in all figures contains the overflow. The normalisation uncertainty on the $t\bar{t}+ \geq 1b$ background is not included in the background uncertainty band.

high jet and b-tag multiplicities, making this search also sensitive to those final states. Processes like $b\bar{b}H(\to t\bar{t})$ $t\bar{t}H(\to t\bar{t})$ and $tbH^{\pm}(\to tb)$ can be targeted as well by this analysis since they share the same final-state signature. Since most of these signal scenarios do not lead to large $E_{\mathrm{T}}^{\mathrm{miss}}$, only the 1-lepton search is used to probe them, without a dedicated re-optimisation.

Figure 6.6a compares the jet multiplicity distribution in the 1-lepton channel after preselection between the total background and several signal scenarios. Signal events have, on average, higher jet multiplicity than the background in both 1-lepton and 0-lepton channels. The higher b-quark content of signal events results in a higher b-tag multiplicity than for the background, as illustrated in Figure 6.6b for events in the 0-lepton channel after preselection plus the requirement of $\geq$7 jets. The increase of centre-of-mass energy in Run 2 gives the possibility to explore higher-mass signals compared to the ones accessible during Run 1. High-mass T quarks may decay into boosted SM particles (W, Z, Higgs bosons and top quarks) potentially giving rise to high multiplicity of large-R jets capturing their products, which can be used to further discriminate signal from background. Large-R jets used in this search are RT-jets with $p_{\mathrm{T}} > 300$GeV, $|\eta| < 2.0$ and mass above 100 GeV. The latter requirement is used to identify boosted top-quark and Higgs-boson candidates. Background $t\bar{t}$+jets events are expected, both in 1-lepton and 0-lepton channels, to contain up to one mass-tagged jet from a boosted, hadronically-decaying top quark, while signal events are characterised by higher

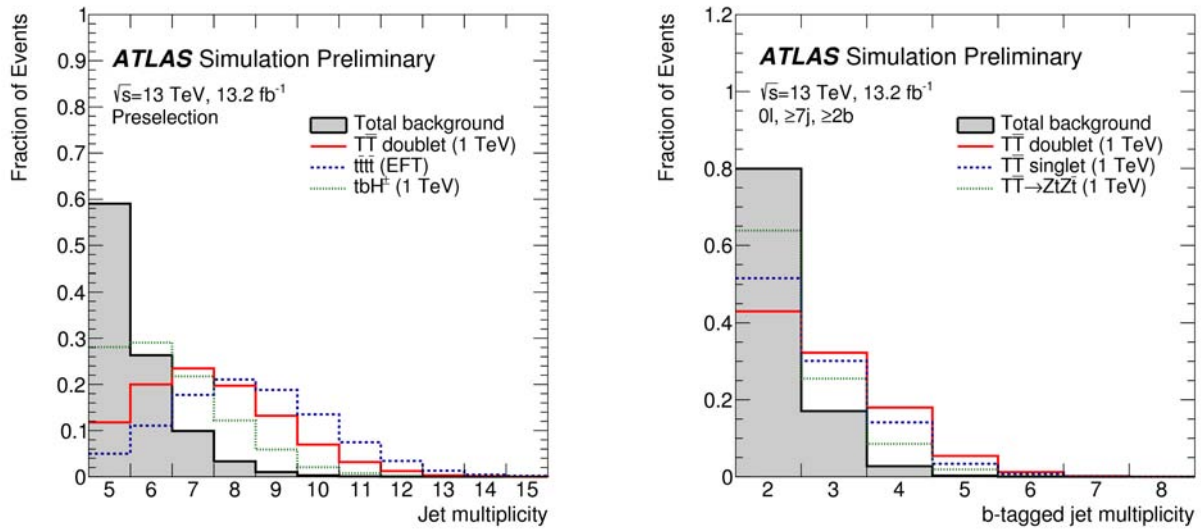

(a) (b)

Figure 6.6: Comparison of the shape of (a) the jet multiplicity distribution in the 1-lepton channel after preselection, and (b) the b-tag multiplicity distribution in the 0-lepton channel after preselection plus the requirement of ≥7 jets, between the total background (shaded histogram) and several signal scenarios considered in this search. The signals shown are: $T\bar{T}$ production in the weak-isospin doublet and singlet scenarios, and for BR($T \to Zt$) = 1, assuming $m_T = 1$ TeV; $t\bar{t}t\bar{t}$ production within an EFT model; and $tbH^{\pm}(\to tb)$ production assuming $m_{H^{\pm}} = 1$ TeV. The last bin contains the overflow.

mass-tagged jet multiplicity as shown in figure 6.7.

In order to optimise the sensitivity of the searches, the selected events are categorised into different regions depending on the jet multiplicity (5 and ≥6 jets in the 1-lepton channel; 6 and ≥7 jets in the 0-lepton channel), b-tag multiplicity (2, 3 and ≥4) and mass-tagged jet multiplicity (0, 1 and ≥2). In the following, channels with N mass-tagged jets, n jets, and m b-tagged jets are denoted as (NJ, nj, mb). In addition, events in particular regions are further categorised by exploiting the kinematic features of the signal and the background. In the case of the $T\bar{T} \to Ht + X$ signal, the presence of a partially-boosted Higgs boson is exploited using the property that the $b\bar{b}$ pair from the Higgs boson decay has smaller angular separation than pairs resulting from combinatorial background. In this regime, the two b-jets are separated enough as to be reconstructed in two individual jets but are very close in ΔR. The mass of the $b\bar{b}$ pair with smallest ΔR distance, $m_{b\bar{b}}^{\min\Delta R}$, provides a good approximation to the reconstructed $H \to b\bar{b}$ invariant mass, as shown in figure 6.8a for events in the (1J, ≥6j, ≥4b) region of the 1-lepton channel. This distribution, which for signal shows a clear peak near 125 GeV, allows the classification of events into two regions depleted or enriched in $T \to Ht, H \to b\bar{b}$ decays, by requiring $m_{b\bar{b}}^{\min\Delta R} < 100$ GeV (referred to as "LM", standing for "low mass") or $m_{b\bar{b}}^{\min\Delta R} > 100$ GeV (referred to as "HM", standing for "high mass"). The minimum transverse mass between $E_{\mathrm{T}}^{\mathrm{miss}}$ and any of the three leading b-tagged jets in the event, $m_{\mathrm{T,min}}^{b}$, is used instead in the 0-lepton channel. This variable exhibits excellent separation between signal and background, which shows a Jacobian peak around the top quark mass, as shown in Figure 6.8b for events in the (≥2J, ≥7j, ≥3b) region of the 0-lepton channel. Therefore, two regions are defined: $m_{\mathrm{T,min}}^{b} > 160$ GeV (referred to as "LM", standing for "low mass") and $m_{\mathrm{T,min}}^{b} < 160$ GeV (referred to as "HM", standing for "high mass"), the latter having a higher signal-to-background ratio than the former.

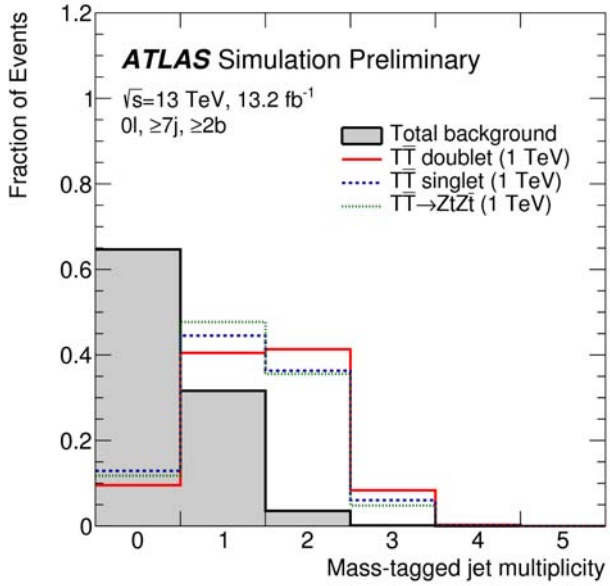

Figure 6.7: Comparison of the shape of the mass-tagged jet multiplicity distribution in the 0-lepton channel after preselection plus the requirement of ≥7 jets, between the total background (shaded histogram) and several signal scenarios considered in this search. The signals shown are: $T\bar{T}$ production in the weak-isospin doublet and singlet scenarios, and for BR($T \to Zt$) = 1, assuming $m_T = 1$ TeV. The last bin contains the overflow.

6.4 Discriminant variable: m_{eff}

The separation between the signal and background can be further increased exploiting the distinct kinematic features of the signal. In the case of $T\bar{T}$ signal, the large T quark mass results in leptons and jets with large energy in the final state. A powerful discriminating variable between signal and background can be build as the scalar sum of the transverse momenta of the lepton, the selected jets and the missing transverse momentum: the effective mass (m_{eff}). In this case, the m_{eff} distribution peaks at approximately $2m_T$ for signal events and at lower values for the $t\bar{t}$+jets background. The different $t\bar{t}t\bar{t}$ signals, particularly those from BSM scenarios, also populate high values of m_{eff}, whereas signals from associated heavy Higgs boson production are typically softer in this variable. In the 1-lepton channel, an additional selection requirement of $m_{\text{eff}} > 400$ GeV ($m_{\text{eff}} > 700$ GeV) is made for regions with exactly zero (one) mass-tagged jets, in order to minimise the effect of a possible mis-modelling of the m_{eff} distribution at low values originating from small backgrounds with large systematic uncertainties, such as multijet production. This additional requirement on m_{eff} has no impact on the search sensitivity because the $T\bar{T}$ signal is characterised by having at least one mass-tagged jet and large values of m_{eff}. Figure 6.9 compares the m_{eff} distribution between signal and background for events in two signal-rich regions of the 0-lepton and 1-lepton channels. The discrimination between signal and background becomes better with increasing T-quark masses.

6.5 The fit model

Fits to data, as part of the statistical analysis, are performed under the background-only and signal-plus-background hypotheses. The fit model is completely specified by the discriminating variable used to build template distributions for signal and backgrounds in each fitted region, and by the list of

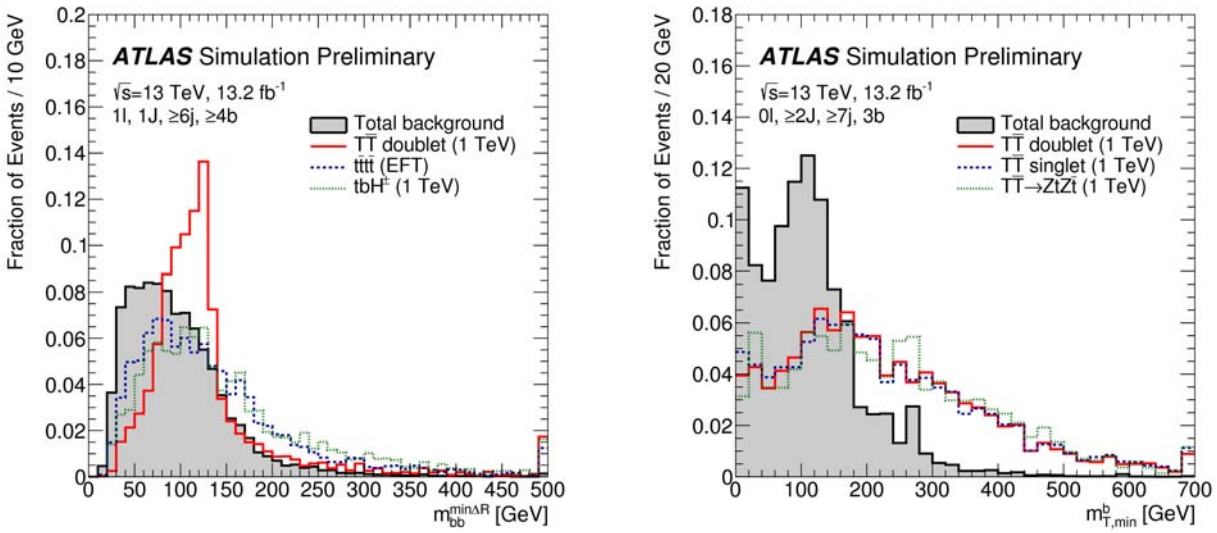

(a) (b)

Figure 6.8: Comparison of the shape of (a) the invariant mass distribution of the two b-tagged jets with lowest ΔR separation ($m_{b\bar{b}}^{\min\Delta R}$), and (b) the distribution of the minimum transverse mass between $E_{\mathrm{T}}^{\mathrm{miss}}$ and any of the three leading b-tagged jets in the event ($m_{\mathrm{T,min}}^{b}$), between the total background (shaded histogram) and several signal scenarios considered in this search. The signals shown are: $T\bar{T}$ production in the weak-isospin doublet and singlet scenarios, and for BR($T \to Zt$) = 1, assuming m_T = 1 TeV; $t\bar{t}t\bar{t}$ production within an EFT model; and $tbH^{\pm}(\to tb)$ production assuming $m_{H^{\pm}}$ = 1 TeV. The selection used in (a) corresponds to events in the (1J, ≥6j, ≥4b) region of the 1-lepton channel, whereas the selection used in (b) corresponds to events in the (≥2J, ≥7j, 3b) region of the 0-lepton channel. The last bin contains the overflow.

systematic uncertainties considered and their assumed correlations across regions and for the various templates. The m_{eff} distribution is used in all regions considered in this search. The regions with ≥6 jets (≥7 jets) are used to perform the actual search in the 1-lepton (0-lepton) channel, whereas the regions with exactly 5 jets (6 jets) are used to validate the background modelling in different regimes of event kinematics and heavy-flavour content. A total of eight search regions and six validation regions are considered in the 1-lepton channel, whereas twelve search regions and nine validation regions are considered in the 0-lepton channel, defined in tables 6.2 and 6.3 respectively.

Figures 6.10 and 6.11 show the expected S/B and $S/\sqrt{B}$ (where S and B are the expected signal and background yields respectively) for 1-lepton regions and 0-lepton regions respectively assuming as signal $T\bar{T}$ production in the weak-isospin doublet and $m_T = 0.8$ TeV.

The signal strength is considered as a free-floating parameter in the fit. The normalisation of background can be controlled through:

- specific nuisance parameters that implement the theoretical knowledge of the respective cross section or the uncertainty on the data-driven estimates, or
- free-floating normalisation parameters, whenever data is used directly to normalise a background without assuming prior knowledge.

Additional nuisance parameters associated with the rest of systematic uncertainties can impact the acceptance for each sample, the distribution of events among the analysis regions, and the shape

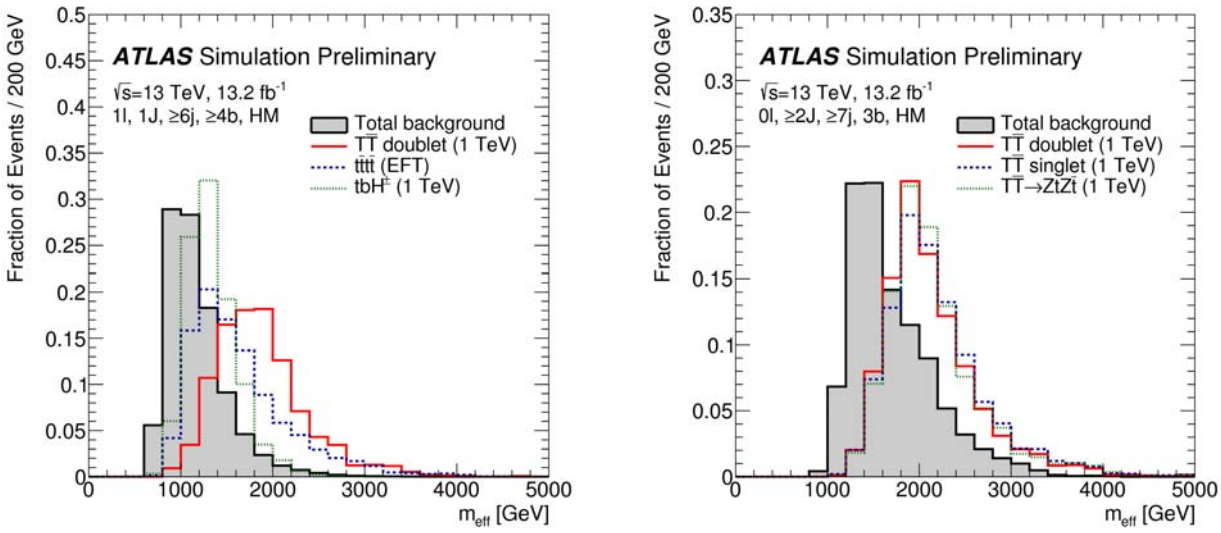

(a) (b)

Figure 6.9: Comparison of the shape of the distribution of the scalar sum of the transverse momenta of the lepton, the selected jets and the missing transverse momentum (m_{eff}) between the total background (shaded histogram) and several signal scenarios considered in this search. The signals shown are: $T\bar{T}$ production in the weak-isospin doublet and singlet scenarios, and for BR($T \to Zt$) = 1, assuming m_T = 1 TeV; $t\bar{t}t\bar{t}$ production within an EFT model; and $tbH^{\pm}(\to tb)$ production assuming $m_{H^{\pm}}$ = 1 TeV. The selection used in (a) corresponds to events in the (1J, ≥6j, ≥4b, HM) region of the 1-lepton channel, whereas the selection used in (b) corresponds to events in the (≥2J, ≥7j, 3b, HM) region of the 0-lepton channel. The last bin in both figures contains the overflow.

of the discriminant distributions. Sources of systematic uncertainties include the finite precision of the calibration of the reconstructed objects, uncertainties affecting the modelling of signal and backgrounds, and the inaccuracies in the description of the experimental conditions, e.g. luminosity or pileup. Additional nuisance associated with the finite MC statistics used to build the templates is considered only for bins for which the relative statistical uncertainty is larger than 5%. Individual sources of systematic uncertainty are considered uncorrelated. Table 6.4 presents a summary of the systematic uncertainties considered in the analysis, indicating if they affect the normalisation ("N") and shape ("S") of the templates. The table also indicates the number of specific components for systematic uncertainty. The breakdown into components is particularly desirable in the implementation of the profile likelihood fit since it results in a more flexible model, it allows to decouple the effect of each uncertainty better and to treat them as initially uncorrelated. It also helps preventing false over-constraints in some of largest systematic uncertainties due to an over-simplified treatment.

The composition of the $t\bar{t}$+jets background strongly depends on the jet and b-tag multiplicities, as illustrated in Figure 6.12 and 6.13. The $t\bar{t}$+light-jets background is dominant in events with exactly two or three b-tagged jets. The former typically consists of events with the two b-quarks from the top quark decays being tagged, while the latter is dominated by events where in addition a charm quark from the hadronic W boson decay is tagged. Contributions from $t\bar{t}$+≥1c and $t\bar{t}$+≥1b become significant as the b-tag multiplicity increases, with the $t\bar{t}$+≥1b background being dominant for events with ≥ 4 b-tagged jets. The regions with different mass-tagged jet multiplicities allow probing different kinematic regimes, both soft (e.g. low-mass T quark or SM $t\bar{t}t\bar{t}$) and hard (e.g. high-mass T quark or BSM $t\bar{t}t\bar{t}$). The aim of the profiled likelihood procedure is to use the background dominated

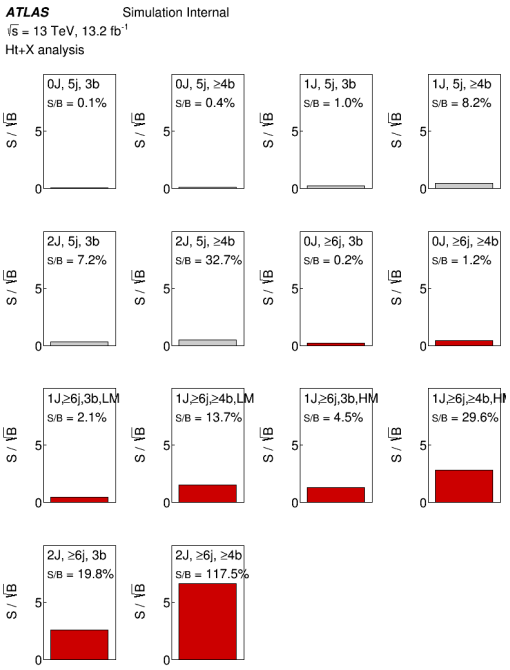

Figure 6.10: S/B and $S/\sqrt{B}$ in the 1-lepton regions. The search (validation) regions are highlighted in red (grey). The signal assumed is $T\bar{T}$ production in the weak-isospin doublet and $m_T = 0.8$ TeV.

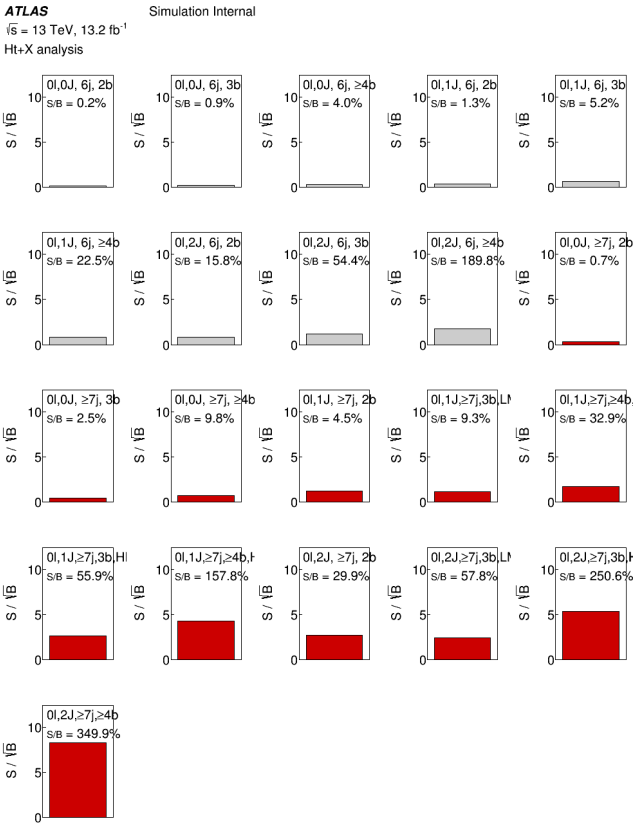

Figure 6.11: S/B and $S/\sqrt{B}$ in the 0-lepton regions. The search (validation) regions are highlighted in red (grey). The signal assumed is $T\bar{T}$ production in the weak-isospin doublet and $m_T = 0.8$ TeV.

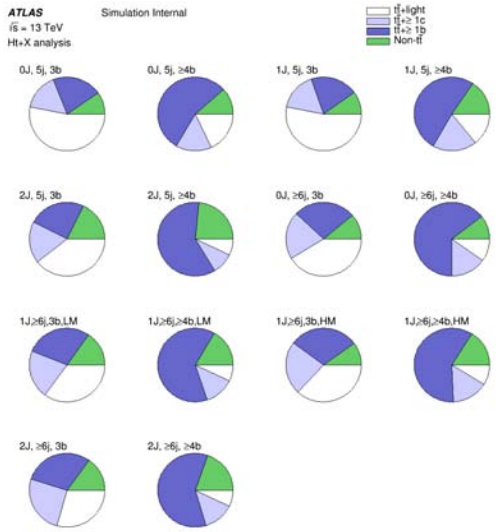

Figure 6.12: Fractional contribution of the various backgrounds to the total background prediction in the different 1-lepton regions. The small contributions from $t\bar{t}V$, $t\bar{t}H$, single top, W/Z+jets, diboson, and multijet backgrounds are combined into a single background source referred to as "Non-$t\bar{t}$".

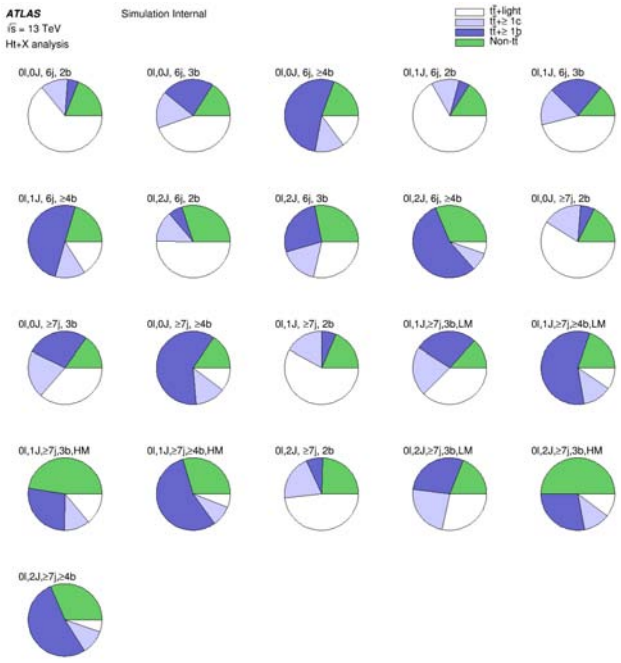

Figure 6.13: Fractional contribution of the various backgrounds to the total background prediction in the different 0-lepton regions. The small contributions from $t\bar{t}V$, $t\bar{t}H$, single top, W/Z+jets, diboson, and multijet backgrounds are combined into a single background source referred to as "Non-$t\bar{t}$".

Search regions (≥6 jets)				
Mass-tagged jet multiplicity	b-jet multiplicity	$m_{bb}^{min\Delta R}$	m_{eff}	Channel name
0	3	-	> 400 GeV	0J, ≥6j, 3b
0	≥4	-	> 400 GeV	0J, ≥6j, ≥4b
1	3	< 100 GeV	> 700 GeV	1J, ≥6j, 3b, LM
1	3	> 100 GeV	> 700 GeV	1J, ≥6j, 3b, HM
1	≥4	< 100 GeV	> 700 GeV	1J, ≥6j, ≥4b, LM
1	≥4	> 100 GeV	> 700 GeV	1J, ≥6j, ≥4b, HM
≥2	3	-	-	≥2J, ≥6j, 3b
≥2	≥4	-	-	≥2J, ≥6j, ≥4b
Validation regions (5 jets)				
Mass-tagged jet multiplicity	b-jet multiplicity	$m_{bb}^{min\Delta R}$	m_{eff}	Channel name
0	3	-	> 400 GeV	0J, 5j, 3b
0	≥4	-	> 400 GeV	0J, 5j, ≥4b
1	3	-	> 700 GeV	1J, 5j, 3b
1	≥4	-	> 700 GeV	1J, 5j, ≥4b
≥2	3	-	-	≥2J, 5j, 3b
≥2	≥4	-	-	≥2J, 5j, ≥4b

Table 6.2: Definition of the search and validation regions in the 1-lepton channel.

regions to improve the knowledge of the background (through constraints of nuisance parameters or creation of correlations) and extrapolate this knowledge into signal-enriched regions where a smaller uncertainty on the background predictions can lead to an improvement in sensitivity. The search regions, with the higher multiplicities of mass-tagged jets and b-tagged jets, typically have the largest signal-to-background ratio, and therefore drive the sensitivity of the search. The rest of search regions have significantly lower signal-to-background ratios, but they are useful for checking and correcting the $t\bar{t}$+jets background prediction and constraining the related systematic uncertainties through the likelihood fit to data. This is particularly important in the context of the $t\bar{t}+ \geq 1b$ normalisation, which is underestimated by the simulation, leading to a deficit in the prediction relative to the data that is most apparent in the channels with ≥4 b-tagged jets. The distribution of expected and observed yields across the multiple search regions before the fit to data ("pre-fit") is shown in figure 6.14. A summary of the observed and expected yields pre-fit in four of the most sensitive search regions in the 1-lepton and 0-lepton channels can be found in tables 6.5 and 6.6 respectively. The search regions shown in table 6.5 for the 1-lepton channel, all requiring ≥4 b-tagged jets but with different requirements on mass-tagged multiplicity, are a selection of some of the regions with the highest S/B ratio across several signal benchmark scenarios considered ($T\bar{T}$ in the T doublet scenario, $t\bar{t}t\bar{t}$ within SM and BSM, associated heavy Higgs boson production). Similarly, the search regions shown in table 6.6 for the 0-lepton channel are a superset of the regions with the highest S/B ratio for different $T\bar{T}$ signal benchmark scenarios (T doublet, T singlet and $\text{BR}(T \to Zt) = 1$).

In the following sections, a brief description of the sources of systematic uncertainties is provided, with particular emphasis on the $t\bar{t}$+jets uncertainties. The expected fit performance and the actual fit results are also discussed.

Search regions (≥7 jets)			
Mass-tagged jet multiplicity	b-jet multiplicity	m_T^{bmin}	Channel name
0	2	-	0J, ≥7j, 2b
0	3	-	0J, ≥7j, 3b
0	≥4	-	0J, ≥7j, ≥4b
1	2	-	1J, ≥7j, 2b
1	3	< 160 GeV	1J, ≥7j, 3b, LM
1	3	> 160 GeV	1J, ≥7j, 3b, HM
1	≥4	< 160 GeV	1J, ≥7j, ≥4b, LM
1	≥4	> 160 GeV	1J, ≥7j, ≥4b, HM
≥2	2	-	≥2J, ≥7j, 2b
≥2	3	< 160 GeV	≥2J, ≥7j, 3b, LM
≥2	3	> 160 GeV	≥2J, ≥7j, 3b, HM
≥2	≥4	-	≥2J, ≥7j, ≥4b
Validation regions (6 jets)			
Mass-tagged jet multiplicity	b-jet multiplicity	$m_{T,\mathrm{min}}^{b}$	Channel name
0	2	-	0J, 6j, 2b
0	3	-	0J, 6j, 3b
0	≥4	-	0J, 6j, ≥4b
1	2	-	1J, 6j, 2b
1	3	-	1J, 6j, 3b
1	≥4	-	1J, 6j, ≥4b
≥2	2	-	≥2J, 6j, 2b
≥2	3	-	≥2J, 6j, 3b
≥2	≥4	-	≥2J, 6j, ≥4b

Table 6.3: Definition of the search and validation regions in the 0-lepton channel.

6.5.1 Systematic uncertainties

6.5.1.1 Luminosity

The uncertainty on the integrated luminosity is estimated to be of 2.9% at $\sqrt{s} = 13$ TeV. This systematic uncertainty affects all processes for which the event yield from simulation is used. The multijet background is not affected by this uncertainty since it is derived from a data-driven method.

6.5.1.2 Pileup

The uncertainty is evaluated changing the rescaling of μ in the pileup reweighting procedure.

6.5.1.3 Reconstructed objects

The object reconstruction and calibration introduces uncertainties associated with the definition of leptons, jets and $E_{\mathrm{T}}^{\mathrm{miss}}$. The corresponding systematic uncertainties were described in chapter 4 . The largest individual uncertainties affecting the background in the most-sensitive search regions are the first eigenvalues of the flavour tagging uncertainty (b, c and mistag efficiency), jet energy scale and jet vertex tagger uncertainties.

Systematic uncertainty	Type	Components
Luminosity	N	1
Reconstructed Objects		
Electron trigger+reco+ID+isolation	SN	5
Electron energy scale+resolution	SN	2
Muon trigger+reco+ID+isolation	SN	6
Muon momentum scale+resolution	SN	3
Pileup reweighting	SN	1
Jet vertex tagger	SN	1
Jet energy scale	SN	18
Jet energy resolution	SN	1
Missing transverse momentum	SN	3
b-tagging efficiency	SN	5
c-tagging efficiency	SN	4
Light-jet tagging efficiency	SN	14
b-tagging extrapolation	SN	2
Background Model		
$t\bar{t}$ cross section	N	1
$t\bar{t}$+HF: normalisation	N	2
$t\bar{t}+\geq 1b$: NLO Shape	SN	10
$t\bar{t}$ modelling: Radiation	SN	3
$t\bar{t}$ modelling: Generator	SN	3
$t\bar{t}$ modelling: Parton shower+hadronisation	SN	3
$t\bar{t}$ NNLO reweighting	SN	2
V+jets normalisation	N	18
Single top normalisation	N	6
Diboson normalisation	N	6
$t\bar{t}V$ cross section	N	2
$t\bar{t}H$ cross section	N	2
SM $t\bar{t}t\bar{t}$ cross section	N	2
Multijet normalisation	N	1

Table 6.4: List of systematic uncertainties considered. An "N" means that the uncertainty is taken as normalisation-only for all processes and channels affected, whereas "SN" means that the uncertainty is taken on both shape and normalisation. Some of the systematic uncertainties are split into several components for a more accurate treatment.

6.5.1.4 $t\bar{t}$ modelling

The $t\bar{t}$ inclusive cross section is computed at NNLO+NNLL in QCD with a total uncertainty of $+5.5\%/-6.1\%$ [176], including effects from varying the factorisation and renormalisation scales, the PDF, α_S, and the top-quark mass. In the regions where $t\bar{t}+\geq 1b$ dominates, the background prediction underestimates the data, although the excess is compatible with the prediction given the large uncertainties associated with $t\bar{t}+\geq 1b$ production. Therefore, the $t\bar{t}+\geq 1b$ normalisation, assumed

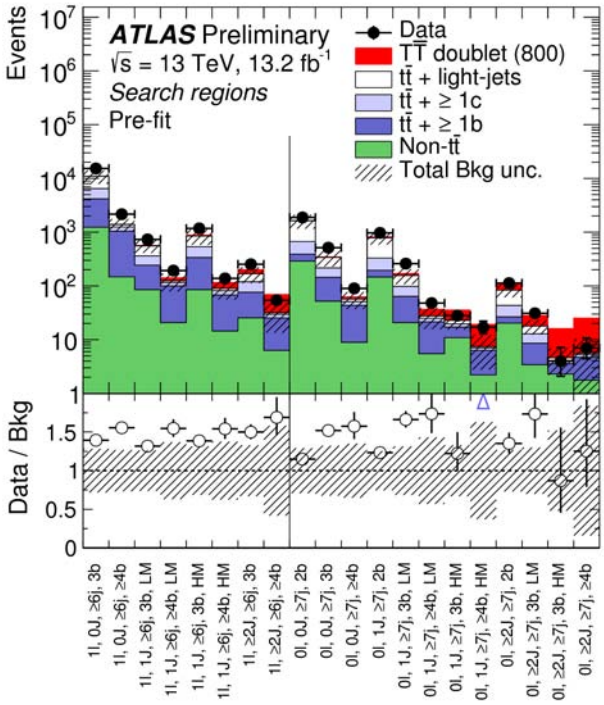

Figure 6.14: Comparison between the data and the background prediction for the yields in the search regions considered in the 1-lepton and 0-lepton channels, before the fit to data ("Pre-fit"). The small contributions from $t\bar{t}V$, $t\bar{t}H$, single top, W/Z+jets, diboson, and multijet backgrounds are combined into a single background source referred to as "Non-$t\bar{t}$". The expected $T\bar{T}$ signal (solid red) corresponding to $m_T = 800$ GeV in the T doublet scenario is also shown, added on top of the background prediction. The bottom panel displays the ratio of data to the SM background ("Bkg") prediction. The blue triangles indicate points that are outside the vertical range of the figure. The hashed area represents the total uncertainty on the background, excluding the normalisation uncertainty on the $t\bar{t}+ \geq 1b$ background.

without any prior uncertainty, will be determined from data using a free floating parameter in the fit to avoid any bias. The analysis regions have little sensitivity for the $t\bar{t}+ \geq 1c$ normalisation, and thus the fit is unable to measure it from data. As a result, the analysis has very limited sensitivity to this uncertainty, for which a normalisation uncertainty of 50% is assumed.

The effects of initial and final-state radiation (ISR/FSR) are explored using two alternative Powheg-Box+Pythia samples, one with `hdamp` parameter set to $2m_t$, the renormalisation and factorisation scales set to half the nominal value and using the P2012 radHi UE tune, giving more radiation (referred to as "radHi"), and one with the P2012 radLo UE tune, `hdamp` set to m_t and the renormalisation and factorisation scales set to twice the nominal value, giving less radiation (referred to as "radLow"). The uncertainties associated with the modelling of ISR/FSR are obtained from the comparison of the two alternative samples, "radHi" and "radLow", with the nominal Powheg-Box+Pythia sample.

An uncertainty associated with the choice of NLO generator is derived by comparing two $t\bar{t}$ samples, one generated with Powheg-Box+Herwig++ and another generated with MG5_aMC+Herwig++, and propagating the resulting fractional difference to the nominal Powheg-Box+Pythia prediction. An uncertainty due to the choice of parton shower and hadronisation model is derived by comparing events produced by Powheg- Box interfaced to Pythia or Herwig++. Finally, the uncertainty on the modelling of the top-quark p_{T} is evaluated by taking the

1-lepton channel	0J, ≥6j, ≥4b	1J, ≥6j, ≥4b LM	1J, ≥6j, ≥4b HM	≥2J, ≥6j, ≥4b
$T\bar{T}$ ($m_T = 1$ TeV)				
BR($T \to Ht$) = 1	3.13 ± 0.67	4.0 ± 1.0	8.7 ± 1.6	19.2 ± 3.1
(T, B) or (X, T) doublet	2.38 ± 0.47	2.98 ± 0.56	5.04 ± 0.94	9.6 ± 1.7
T Singlet	1.24 ± 0.25	1.27 ± 0.25	2.46 ± 0.51	3.83 ± 0.73
$t\bar{t}t\bar{t}$				
EFT ($\lvert C_{4t}\rvert/\Lambda^2 = 4\pi$ TeV^{-2})	205 ± 34	105 ± 18	155 ± 29	181 ± 34
2UED/RPP ($m_{\mathrm{KK}} = 1.4$ TeV)	0.31 ± 0.09	0.48 ± 0.11	2.08 ± 0.52	9.7 ± 1.9
Heavy Higgs bosons ($m_{H^\pm,H} = 1$ TeV, $\sigma = 1$ pb)				
$b\bar{b}H$	42.0 ± 7.5	23.2 ± 4.2	31.2 ± 6.0	5.3 ± 1.3
$t\bar{t}H$	210 ± 34	162 ± 27	205 ± 35	220 ± 38
$tbH^\pm$	90 ± 16	29.6 ± 5.7	56 ± 11	19.7 ± 4.5
$t\bar{t}$+light-jets	136 ± 82	9.0 ± 5.3	7.8 ± 5.1	2.3 ± 1.6
$t\bar{t}$+≥1c	210 ± 130	16 ± 10	14 ± 10	4.2 ± 3.2
$t\bar{t}$+≥1b	890 ± 210	79 ± 38	53 ± 24	19 ± 14
$t\bar{t}V$	25.4 ± 9.0	4.2 ± 1.5	2.19 ± 0.80	1.21 ± 0.44
$t\bar{t}H$	51 ± 18	5.7 ± 2.0	5.7 ± 2.0	2.27 ± 0.83
W+jets	19 ± 10	3.7 ± 2.0	1.08 ± 0.56	0.56 ± 0.32
Z+jets	4.0 ± 2.2	0.41 ± 0.38	0.11 ± 0.07	0.08 ± 0.06
Single top	42 ± 15	5.0 ± 1.7	4.3 ± 1.6	1.04 ± 0.57
Diboson	3.9 ± 2.2	0.62 ± 0.47	0.06 ± 0.19	0.09 ± 0.06
$t\bar{t}t\bar{t}$ (SM)	2.88 ± 0.47	1.04 ± 0.18	1.03 ± 0.18	1.08 ± 0.19
Total background	1390 ± 370	125 ± 45	89 ± 31	32 ± 16
Data	2160	193	138	54

Table 6.5: Predicted and observed yields in the 1-lepton channel in four of the most-sensitive search regions (depending on the signal scenario) considered. The multijet background is estimated to be negligible in these regions and thus not shown. The background prediction is shown before the fit to data. Also shown are the signal predictions for different benchmark scenarios considered. The quoted uncertainties are the sum in quadrature of statistical and systematic uncertainties on the yields, excluding the normalisation uncertainty on the $t\bar{t}+ \geq 1b$ background.

full difference between applying and not applying the reweighting to match the NNLO prediction.[5]

The above uncertainties are taken as uncorrelated between the $t\bar{t}$+light-jets, $t\bar{t}+ \geq 1c$ and $t\bar{t}+ \geq 1b$ processes, except for the uncertainty on the inclusive $t\bar{t}$ cross section. This treatment prevents an undue reduction of these systematic uncertainties on $t\bar{t}+ \geq 1c$ and $t\bar{t}+ \geq 1b$ by constraining them for $t\bar{t}$+light-jets via the fit to data in the high-statistics channels with two b-tagged jets. In the case of $t\bar{t}+ \geq 1b$, in all instances the various HF categories and the corresponding partonic kinematics for the alternative MC samples are reweighted to match the NLO prediction of SherpaOL, so that only

[5] This uncertainty only affects the $t\bar{t}$+light-jets and $t\bar{t}+ \geq 1c$ processes.

0-lepton channel	1J, ≥7j, ≥4b HM	2J, ≥7j, ≥2b	≥2J, ≥7j, 3b HM	≥2J, ≥7j, ≥4b
$T\bar{T}$ ($m_T = 1$ TeV)				
BR($T \to Zt$) = 1	1.58 ± 0.42	10.2 ± 1.4	2.92 ± 0.58	1.96 ± 0.61
(T, B) or (X, T) doublet	2.44 ± 0.50	7.56 ± 0.78	3.94 ± 0.48	6.0 ± 1.1
T Singlet	0.94 ± 0.29	3.98 ± 0.41	1.62 ± 0.21	2.17 ± 0.41
$t\bar{t}$+light-jets	0.44 ± 0.26	40 ± 12	0.48 ± 0.19	0.30 ± 0.18
$t\bar{t}$+≥1c	0.70 ± 0.46	17 ± 10	0.54 ± 0.33	0.60 ± 0.40
$t\bar{t}$+≥1b	4.1 ± 3.0	6.3 ± 2.6	1.28 ± 0.45	2.93 ± 0.90
$t\bar{t}V$	0.40 ± 0.11	3.80 ± 0.80	0.40 ± 0.10	0.28 ± 0.08
$t\bar{t}H$	0.46 ± 0.11	0.66 ± 0.14	0.11 ± 0.03	0.29 ± 0.09
W+jets	0.37 ± 0.20	5.2 ± 2.4	0.32 ± 0.16	0.21 ± 0.14
Z+jets	0.32 ± 0.22	3.5 ± 1.7	0.29 ± 0.15	0.08 ± 0.11
Single top	0.37 ± 0.27	4.9 ± 3.2	0.62 ± 0.47	0.21 ± 0.19
Diboson	0.19 ± 0.21	2.1 ± 1.7	0.50 ± 0.76	0.48 ± 0.49
$t\bar{t}t\bar{t}$ (SM)	0.10 ± 0.04	0.22 ± 0.08	0.05 ± 0.02	0.20 ± 0.07
Total background	7.5 ± 3.5	84 ± 21	4.6 ± 1.5	5.6 ± 1.6
Data	17	113	4	7

Table 6.6: Predicted and observed yields in the 0-lepton channel in four of the most-sensitive search regions (depending on the signal scenario) considered. The multijet background is assumed to be negligible in these regions and thus not shown. The background prediction is shown before the fit to data. Also shown are the signal predictions for different benchmark scenarios considered. The quoted uncertainties are the sum in quadrature of statistical and systematic uncertainties on the yields, excluding the normalisation uncertainty on the $t\bar{t}+ \geq 1b$ background.

effects other than distortions to the inter-normalisation of the various $t\bar{t}+ \geq 1b$ topologies and their parton-level kinematics are propagated. In the case of $t\bar{t}$+light-jets and $t\bar{t}+ \geq 1c$, the full effect of these uncertainties is propagated. Similarly to the treatment of the NLO corrections and uncertainties on $t\bar{t}+ \geq 1b$ discussed above, in the case of the additional uncertainties derived by comparing alternative $t\bar{t}$ samples, the overall normalisation of the $t\bar{t}+ \geq 1b$ and $t\bar{t}+ \geq 1c$ background at the particle level is fixed to the nominal prediction. In this way, only migrations across categories and distortions to the shape of the kinematic distributions are considered. In order to maintain the inclusive $t\bar{t}$ cross section, the $t\bar{t}$+light-jets background is adjusted accordingly. These uncertainties are referred to as "$t\bar{t}+\geq 1b$ residual uncertainties". This approach gives to the $t\bar{t}+ \geq 1b$ and $t\bar{t}+ \geq 1c$ normalisation NPs the meaning of scale factors to the cross section at particle level for these two processes.

Finally, uncertainties on the SherpaOL NLO prediction, which is used for reweighting the nominal Powheg-Box+Pythia $t\bar{t}+ \geq 1b$ prediction, are considered. They are evaluated by varying the renormalisation scale up and down by a factor of two and as well as using two different scale variations (see table 6.7), a different shower-recoil model scheme, and two alternative PDF sets (MSTW and NNPDF), and they affect both shape and intercategory migration effects in $t\bar{t}+ \geq 1b$ production. An uncertainty associated on the choice of NLO generator is derived by comparing the $t\bar{t}+ \geq 1b$ predictions obtained after reweighting Powheg-Box+Pythia to the NLO calculation from SherpaOL and to

Scale	default	glosoft	Q-CMMPS
μ_{R}	μ_{CMMPS}	μ_{CMMPS}	μ_{CMMPS}
μ_{F}	$H_{\mathrm{T},t}/2$	μ_{CMMPS}	$H_{\mathrm{T},t}/2$
μ_{Q}	$H_{\mathrm{T},t}/2$	μ_{CMMPS}	μ_{CMMPS}

Table 6.7: Different scale variations (default, as well as two alternative choices) considered in the NLO prediction for $t\bar{t}+\geq 1b$ from SherpaOL. The renormalisation, factorisation and resummation scales are denoted by μ_{R}, μ_{F}, and μ_{Q}, respectively.

an equivalent NLO calculation from MG5_aMC+Pythia8. The uncertainty from the parton shower and hadronisation model is taken from the difference between the MG5_aMC calculation showered with either Pythia8 or Herwig++. These uncertainties are referred to as "$t\bar{t}+\geq 1b$ reweighting uncertainties". Additional uncertainties are assessed for the contributions to the $t\bar{t}+\geq 1b$ background originating from MPI or FSR from top-quark decay products, which are not part of the NLO prediction. The MPI uncertainty is assumed to be 50% based on studies of different underlying event tunes while the FSR uncertainty is assessed via the alternative "radHi" and "radLow" samples.

6.5.1.5 V+jets modelling

Uncertainties affecting the normalisation of the V+jets background are estimated for the sum of W+jets and Z+jets, and separately for V+light-jets, $V+\geq 1c$+jets, and $V+\geq 1b$+jets subprocesses. The uncertainty on V+light-jets is estimated from analysis regions at preselection level but with the additional requirement of 0 or 1 b-tagged jets, in which this background dominates. The agreement between data and total background prediction is found to be within $\sim 30\%$, which is taken to be the total normalisation uncertainty correlated across all V+jets subprocesses. Additional 30% normalisation uncertainties are assumed for $V+\geq 1c$+jets and $V+\geq 1b$+jets subprocesses, and taken to be uncorrelated between them. These uncertainties are treated as uncorrelated across mass-tagged multiplicity bins and between the 1-lepton and 0-lepton channels. Therefore, a total of nine independent nuisance parameters per channel are considered.

6.5.1.6 Single-top-quark modelling

The total cross section uncertainty for single-top-quark production is $+5\%/-4\%$, estimated as a weighted average of the theoretical uncertainties on t-, Wt- and s-channel production [196–198]. Additional uncertainties associated with the modelling of ISR/FSR are assessed by comparing the nominal samples with alternative samples where generator parameters have been varied (i.e. "radHi" and "radLow"). For the t- and Wt-channel processes, an uncertainty due to the choice of parton shower and hadronisation model is derived by comparing events produced by Powheg-Box interfaced to Pythia or Herwig++. Since alternative samples were generated using fast simulation the comparisons are done with the Powheg-Pythia sample using fast simulation, and then applied to the nominal sample, which was instead generated with full simulation. These uncertainties are treated as fully correlated among single-top-quark production processes, but uncorrelated with the corresponding uncertainty on the $t\bar{t}$+jets background. An additional systematic uncertainty on the interference of the Wt-channel with $t\bar{t}$ at NLO [227] is assessed by comparing the nominal sample, which uses the so-called "diagram removal" scheme, with an alternative sample using the "diagram subtraction" scheme. The above uncertainties cannot be estimated in each analysis region due to the small size, and hence limited statistical precision, of the simulated samples. Thus, they are estimated at preselection level. The

sum in quadrature of the above uncertainties on the single-top-quark normalisation amounts to 24% and 52% for the 1-lepton and 0-lepton channels, respectively. They are treated as uncorrelated across mass-tagged multiplicity bins, resulting in a total of three independent nuisance parameters considered.

6.5.1.7 Diboson modelling

The theoretical uncertainty on the inclusive NLO cross sections for the diboson background is 5% [228], which is expected to apply to events with ≥2 jets resulting from either $WV \to \ell\nu jj$ or $ZV \to \nu\bar{\nu}jj$. To estimate the uncertainty at higher jet multiplicities, an extrapolation based on a comparison among different algorithms for merging LO matrix elements and parton showers was used [229]. Therefore, an additional 24% normalisation uncertainty is added in quadrature for each additional inclusive jet-multiplicity bin beyond ≥2 jets resulting in a total normalisation uncertainty of 48% for events with ≥ 6 jets. This uncertainty is taken to be uncorrelated across mass-tagged multiplicity bins and between the 1-lepton and 0-lepton channels. A total of three independent nuisance parameters per channel are considered.

6.5.1.8 $t\bar{t}+X$, $X = V, H, t\bar{t}$ modelling

The uncertainties on $t\bar{t}V$ and $t\bar{t}H$ NLO theoretical cross sections [19, 230, 231] are respectively 15% and $+9\%/-13\%$. An uncertainty of 30% is estimated for the NLO prediction of the SM $t\bar{t}t\bar{t}$ cross section [127]. Since no additional modelling uncertainties are taken into account for these backgrounds, and the 1-lepton and 0-lepton channels cover different kinematic phase space, the above uncertainties on the $t\bar{t}V$, $t\bar{t}H$, and SM $t\bar{t}t\bar{t}$ cross sections are taken to be uncorrelated between both channels.

6.5.1.9 Multijet modelling

Uncertainties on the data-driven multijet background estimate receive contributions from the limited sample size in data, particularly at high jet and b-tag multiplicities, as well as from the uncertainty on the misidentified-lepton rate, measured in different control regions (e.g. selected with a requirement on either the maximum $E_{\mathrm{T}}^{\mathrm{miss}}$ or m_{T}^{W}). The uncertainty on the misidentified-lepton rate is estimated in a multijet enriched region which is obtained at preselection level but with additional requirements of 0 b-tagged jets and without $E_{\mathrm{T}}^{\mathrm{miss}}$ related cuts. The agreement between data and total background prediction is found to be within approximately 50%, which is taken to be the total normalisation uncertainty correlated across jet and b-tag multiplicity bins. No explicit shape uncertainty is assigned since the large statistical uncertainties associated with the multijet background prediction, which are uncorrelated between bins in the final discriminant distribution, effectively cover possible shape uncertainties.

6.5.2 Expected fit performance

The performance of the fit has been evaluated using an Asimov dataset generated assuming background-only hypothesis using a total of 20 search regions: 8 regions for the 1-lepton channel and 12 regions for the 0-lepton channel. In this combined fit all common systematic uncertainties are considered fully correlated between the 1-lepton and 0-lepton channels, with the exception of those affecting non-$t\bar{t}$ backgrounds. The reason is that both channels cover a different kinematic phase space and non-$t\bar{t}$ backgrounds have a more simplified description of their modelling uncertainties. To obtain the results in the individual channels, separate fits are performed. In general, good consistency is found among the fitted nuisance parameters in the individual and combined fits. Figure

6.15 illustrates the constraints on the nuisance parameters which are expected with the described fit model; it shows three fits using 1-lepton search regions only, 0-lepton search regions only, and both together (referred to as "combined fit"). All the nuisance parameters are fitted to a value of 0 since no shift is needed to improve the agreement. The error on the nuisance parameters obtained from the fit is reported in units of the "pre-fit"' (prior) uncertainty, so they are expected to be close to unity if these data do not provide any further improvement on that uncertainty. Since the constraining power of systematic uncertainties is dominated by the higher-statistics 1-lepton channel, the expected constrains in the combined fit are similar as for the 1-lepton-only fit. The expected uncertainty on the $t\bar{t}+ \geq 1b$ normalisation parameter is 0.21 from the combined fit to the Asimov dataset.

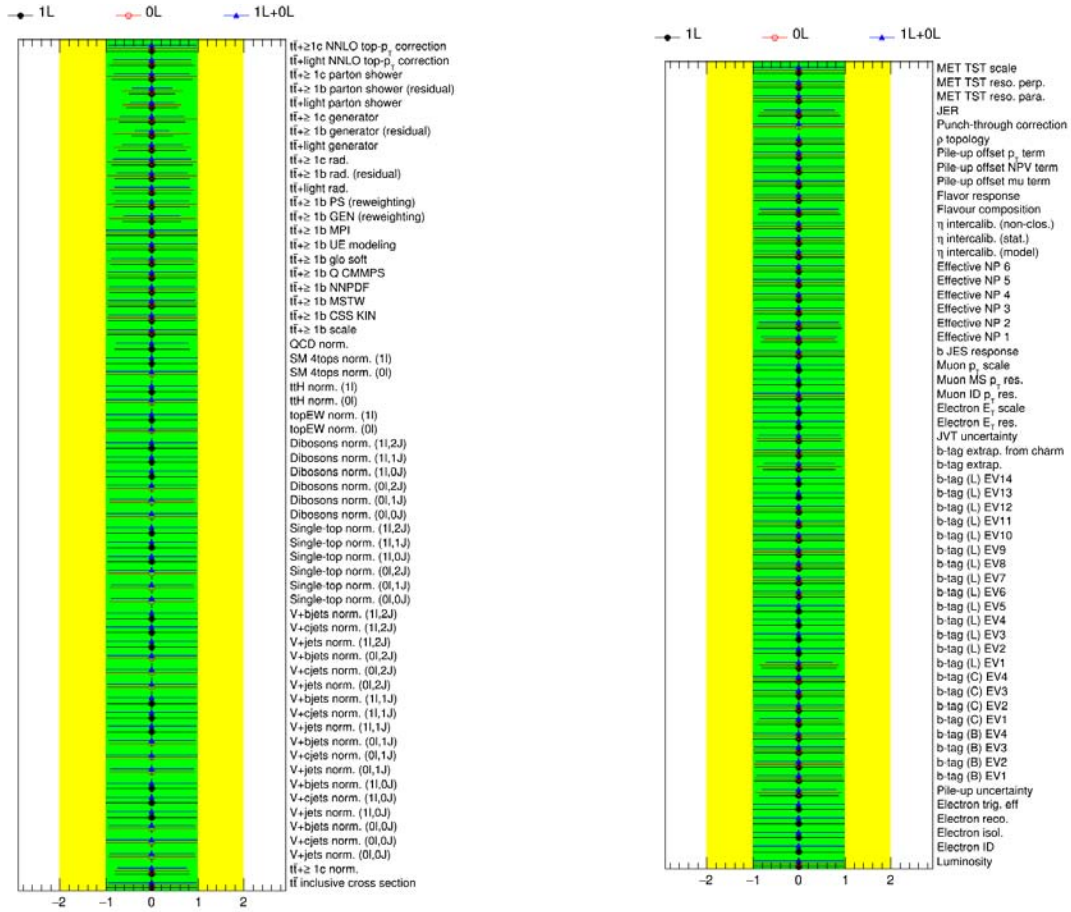

(a) (b)

Figure 6.15: Fitted NPs from a fit to the Asimov dataset under the background-only hypothesis. Shown are the fits using the 1-lepton channel only (black), 0-lepton channel only (red), and the combination of both channels (blue). A detailed description of the naming of the NPs can be found in appendix B.

For what concerns the detector-related systematic uncertainties, no major constraints are observed with the exception of the pileup uncertainty, jet energy resolution, two components of the jet energy scale uncertainty, the largest component of the c-jet and light-jet tagging efficiency uncertainties, and the uncertainty on extrapolation of tagging SFs above the kinematics reach of data used for calibration. The first four uncertainties give a larger contribution at low jet p_{T} (and hence low m_{eff}) where large data statistics is available, especially in the 2 and 3 b-tagged jets and 0 mass-tagged jets regions.

For the largest component of the c-jet and light-jet tagging efficiency uncertainties, these are large uncertainties affecting $t\bar{t}$+light-jets with ≥ 4 b-tagged jets, where two of the b-tagged jets originate from charm and light-jet mistags. In the regions with one mass-tagged jet, which requires the presence of energetic objects, there is enough statistics to improve as well the extrapolation at high p_{T}.

The analysis is specifically designed to improve background-related systematic uncertainties, particularly those that are potentially overestimated through the comparison of extreme theoretical models, rather than being based on previous data measurements. The fit constraints mostly $t\bar{t}$-related uncertainties since the analysis is dominated by this background. A notable example is the determination of the $t\bar{t}+\geq 1b$ normalisation factor, which is determined by the fit, with a precision of about 20%. This is due to the large amount of data collected at 13 TeV combined with the event categorisation in multiple jet, b-tagged jet and mass-tagged jets multiplicity regions. After the fit, the uncertainty on the $t\bar{t}+\geq 1c$ normalisation is reduced from the initial 50% down to 40%, showing the limited sensitivity of this analysis to this background process, mostly coming from the interplay of regions with 2 and 3 b-tagged jets and 0 mass-tagged jets. The other important aspect is related to the modelling of $t\bar{t}$+light-jets events; the nuisance parameters that are constrained are the ones that correspond to large variations not compatible with the available data precision. This is the case for the radiation, generator and parton-shower uncertainties, which produce effects of up to 30% as a function of the number of jets, while the statistical uncertainty of data in the 3 b-tagged jets regions is of the order of few percent.

6.5.3 Fit results

A fit to the data in the 20 analysis regions is performed under the background-only hypothesis, and the fitted NPs are shown in figure 6.16. The corresponding correlation matrix for the fitted NPs can be found in figure 6.17.

Figure 6.18 shows the distribution of observed and expected yields in the search regions in the 1-lepton and 0-lepton channels after the combined fit. The post-fit yields in four of the most sensitive search regions in the 1-lepton and 0-lepton channels can be found in tables 6.8 and 6.9 respectively.

Figures 6.19 and 6.20 show the comparison of data and prediction for the m_{eff} distributions in the most-sensitive search regions in the 1-lepton and 0-lepton channels respectively, before and after the fit to data.

The large number of events in the signal-depleted regions, together with their different background compositions, and the assumptions of the fit model, allows to constrain the combined effect of several sources of systematic uncertainty. Compared to the pre-fit distributions, the total background uncertainty is significantly reduced after the fit, not only in the background-dominated channels, but also in the signal-rich channels, resulting in an increase in the search sensitivity.

The reduced uncertainty results from the significant constraints on some systematic uncertainties, as well as the anti-correlations among sources of systematic uncertainty resulting from the fit to the data. A good agreement is found between data and prediction in all channels. The good performance of the fit can further be validated through comparison between data and total prediction in the validation regions. Pre-fit and post-fit distributions for validation regions can be found in figure 6.21. The agreement for those regions not used in the fit is also improved after the fit, giving confidence in the overall procedure.

The observed constraints on the systematic uncertainties (i.e. the post-fit error on the NPs) are compatible with the expected values from the Asimov fit (see figure 6.15). In general, good consistency is found among the fitted nuisance parameters in the individual and combined fits. As for the Asimov fit, the higher statistical power of the 1-lepton channel drives the combined fit. Pulls present in the

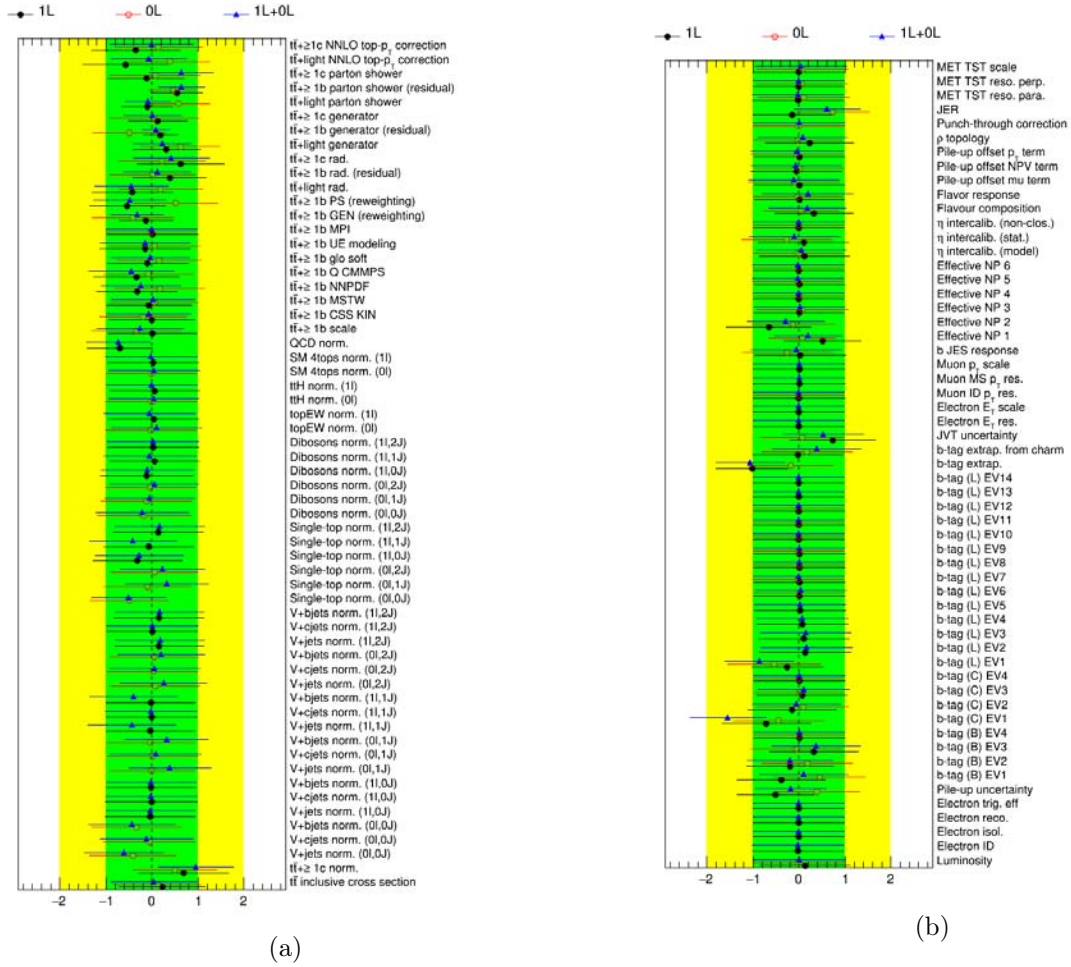

(a) (b)

Figure 6.16: Fitted NPs from a fit under the background-only hypothesis. Shown are the fits using the 1-lepton channel only (black), 0-lepton channel only (red), and the combination of both channels (blue). A detailed description of the naming of the NPs can be found in appendix B.

1-lepton fit are in most cases translated into the combined fit as well; few exceptions are due to an increase of the statistical power in the combination that allows to pull a NP in the combined fit that was not pulled in the individual fits, or a NP being pulled driven by a high-statistics region in the 0-lepton channel. The most relevant pulls are discussed in the following:

- The fitted value for the $t\bar{t}+ \geq 1b$ normalisation parameter is 1.2 ± 0.3, leading to an increase of this background. In addition, the nuisance parameter controlling the $t\bar{t}+ \geq 1c$ normalisation is adjusted to scale this background by a factor of 1.5 ± 0.4 relative to its nominal prediction. Those two pulls correct the underestimation of $t\bar{t}$+HF where those processes dominates. The former is mostly pulled in the 1-lepton 0J, $\geq$ 6j, $\geq$ 4b region, where there is enough statistics to measure this background in a region that is depleted in signal. The latter is pulled from the interplay of regions with 3 and $\geq$4 b-tagged jets and 0 mass-tagged jets in the combined fit.

- b, c- and light-jet tagging: the fitted values of these NP lead to an increased SF for c-tag, mistag and at high p_{T}. The NP corresponding to the largest c-tagging uncertainty is pulled. The calibration used the SF from Run 1 (based on a different tagger), which might not be suitable for the new MV2c10 tagger, and the large statistics in the 0 mass-tagged jets regions, play a role

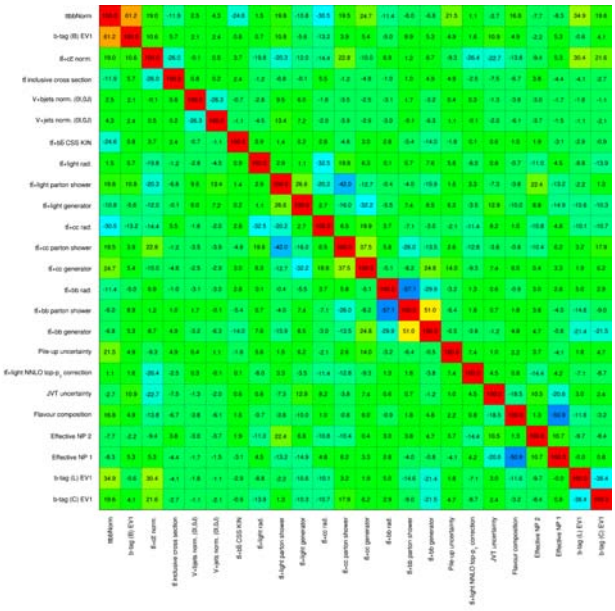

Figure 6.17: Correlation matrix between NPs corresponding to the fit to data under the background-only hypothesis. Only NPs with a correlation coefficient of at least 20% with any other parameter are displayed.

1-lepton channel	0J, ≥6j, ≥4b	1J, ≥6j, ≥4b LM	1J, ≥6j, ≥4b HM	≥2J, ≥6j, ≥4b
$t\bar{t}$+light-jets	250 ± 100	15.7 ± 6.6	13.0 ± 6.2	3.3 ± 1.7
$t\bar{t}$+≥1c	450 ± 150	37 ± 12	28 ± 10	8.5 ± 3.3
$t\bar{t}$+≥1b	1260 ± 130	128 ± 17	79 ± 10	36.9 ± 7.7
$t\bar{t}V$	30 ± 10	4.7 ± 1.5	2.54 ± 0.85	1.33 ± 0.44
$t\bar{t}H$	57 ± 18	6.3 ± 2.1	5.9 ± 2.0	2.28 ± 0.76
W+jets	26 ± 11	3.6 ± 1.6	1.05 ± 0.45	0.85 ± 0.41
Z+jets	5.3 ± 2.3	0.49 ± 0.37	0.12 ± 0.06	0.16 ± 0.09
Single top	52 ± 14	5.4 ± 1.5	4.4 ± 1.3	1.61 ± 0.70
Diboson	4.6 ± 2.4	0.76 ± 0.51	0.09 ± 0.20	0.10 ± 0.06
$t\bar{t}t\bar{t}$ (SM)	3.2 ± 1.0	1.17 ± 0.38	1.09 ± 0.36	1.11 ± 0.36
Total background	2135 ± 79	203 ± 15	134.3 ± 8.7	56.2 ± 8.3
Data	2160	193	138	54

Table 6.8: Predicted and observed yields in the 1-lepton channel in four of the most-sensitive search regions considered. The multijet background is considered negligible in these regions and thus not shown. The background prediction is shown after the combined fit to data in the 0-lepton and 1-lepton channels under the background-only hypothesis. The quoted uncertainties are the sum in quadrature of statistical and systematic uncertainties on the yields, computed taking into account correlations among nuisance parameters and among processes.

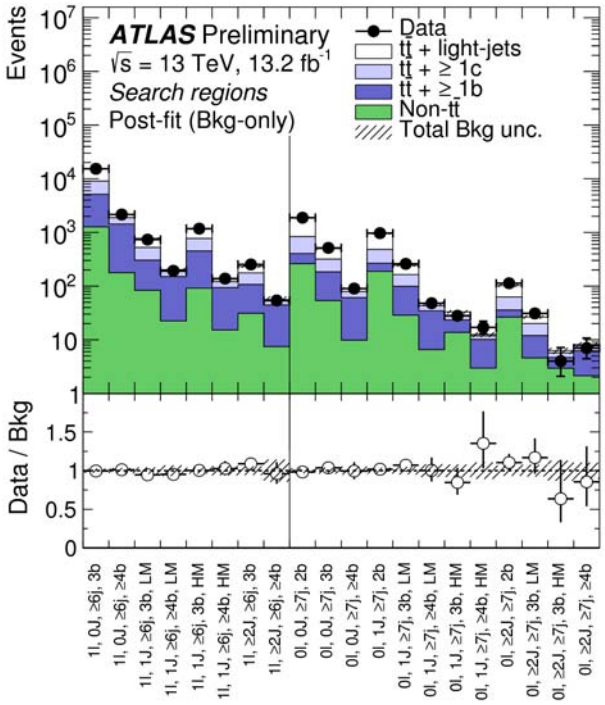

Figure 6.18: Comparison between the data and the background prediction for the yields in the search regions considered in the 1-lepton and 0-lepton channels, after the combined fit to data ("Post-fit") under the background-only hypothesis. The small contributions from $t\bar{t}V$, $t\bar{t}H$, single top, W/Z+jets, diboson, and multijet backgrounds are combined into a single background source referred to as "Non-$t\bar{t}$". The bottom panel displays the ratio of data to the SM background ("Bkg") prediction. The hashed area represents the total uncertainty on the background.

in the fit's ability to pull this NP. In particular, the interplay of regions with 2 and 3 b-tagged jets in $t\bar{t}$+light-jets events is mainly controlled by the tagging of a c-jet from hadronic W boson decay. This feature brings a good potential for a better derivation of the c-jets scale factor.[6] The light-tagging eigenvector is pulled by the interplay of regions with different b-tag multiplicity. With high statistics of b-jets at high p_{T} is possible as well to improve the NP that controls the extrapolation at high p_{T}.

- Jet energy resolution: the pull of this uncertainty comes from the region 0J, $\geq$ 7j, $\geq$ 2b in the 0-lepton channel, where the jet energy resolution uncertainty can significantly affect the shape of m_{eff} distribution at low p_{T}. Given that this uncertainty has no impact on the signal or background predictions in the search regions, this pull is not considered problematic.

- $t\bar{t}$ modelling: those uncertainties are strongly constrained, as expected from the Asimov fit, specially those with large variations not compatible with data. The constraints on those NPs come from high-statistics regions with 0 mass-tagged jets. Their pulls corrects the slope observed in the m_{eff} distribution, particularly in the signal-depleted regions where the $t\bar{t}$+light-jets background is dominant.

- QCD normalisation: this pull arises from bins in the very low tail of the m_{eff} distributions

[6] The determination of the c-jet SF in $t\bar{t}$ events has not been exploited yet by the ATLAS b-tagging calibration effort.

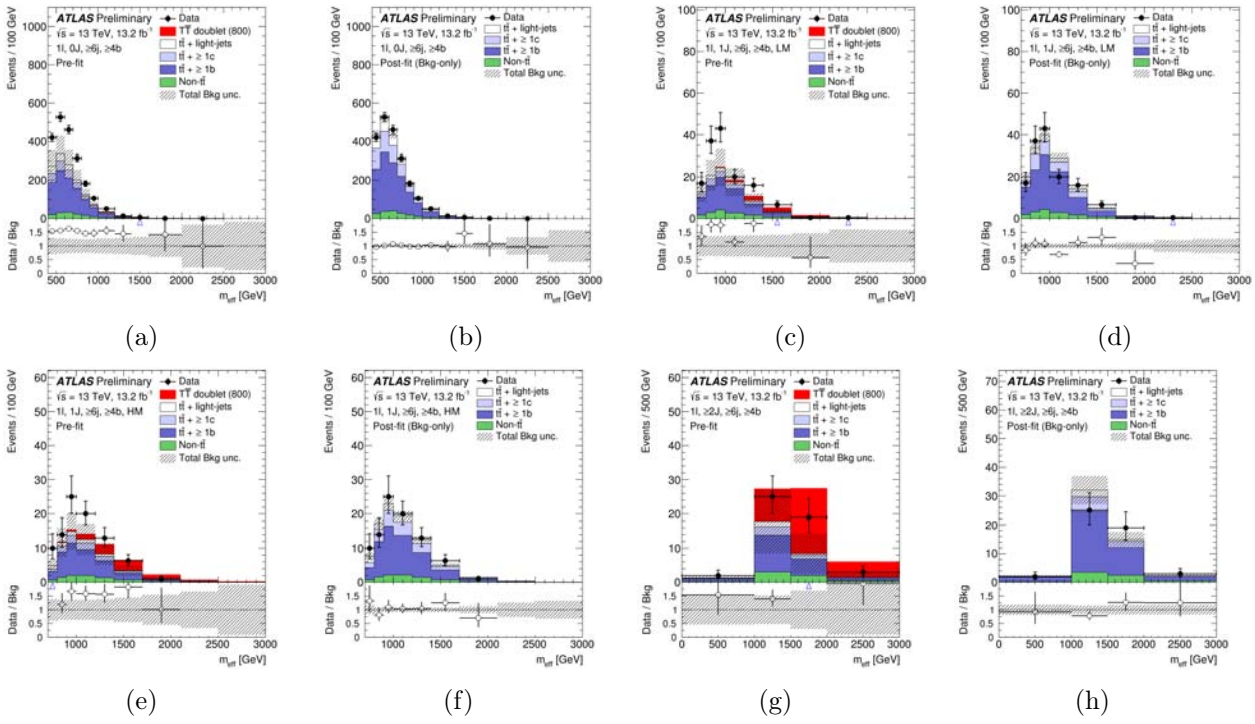

Figure 6.19: Comparison between the data and prediction for the m_{eff} distribution in some of the most-sensitive search regions in the 1-lepton channel, before and after performing the combined fit to data in the 0-lepton and 1-lepton channels ("Pre-fit" and "Post-fit", respectively) under the background-only hypothesis. Shown are the (0J, ≥6j, ≥4b) region (a) pre-fit and (b) post-fit, and the (1J, ≥6j, ≥4b, LM) region (c) pre-fit and (d) post-fit, (1J, ≥6j, ≥4b, HM) region (e) pre-fit and (f) post-fit, and the (≥2J, ≥6j, ≥4b) region (g) pre-fit and (h) post-fit. In the pre-fit figures the expected $T\bar{T}$ signal (solid red) corresponding to $m_T = 800$ GeV in the T doublet scenario is also shown, added on top of the background prediction. The small contributions from $t\bar{t}V$, $t\bar{t}H$, single top, W/Z+jets, diboson, and multijet backgrounds are combined into a single background source referred to as "Non-$t\bar{t}$". The last bin in all figures contains the overflow. The bottom panels display the ratios of data to the total background prediction ("Bkg"). The blue triangles indicate points that are outside the vertical range of the figure. The hashed area represents the total uncertainty on the background. In the case of the pre-fit background uncertainty, the normalisation uncertainty on the $t\bar{t}+ \geq 1b$ background is not included.

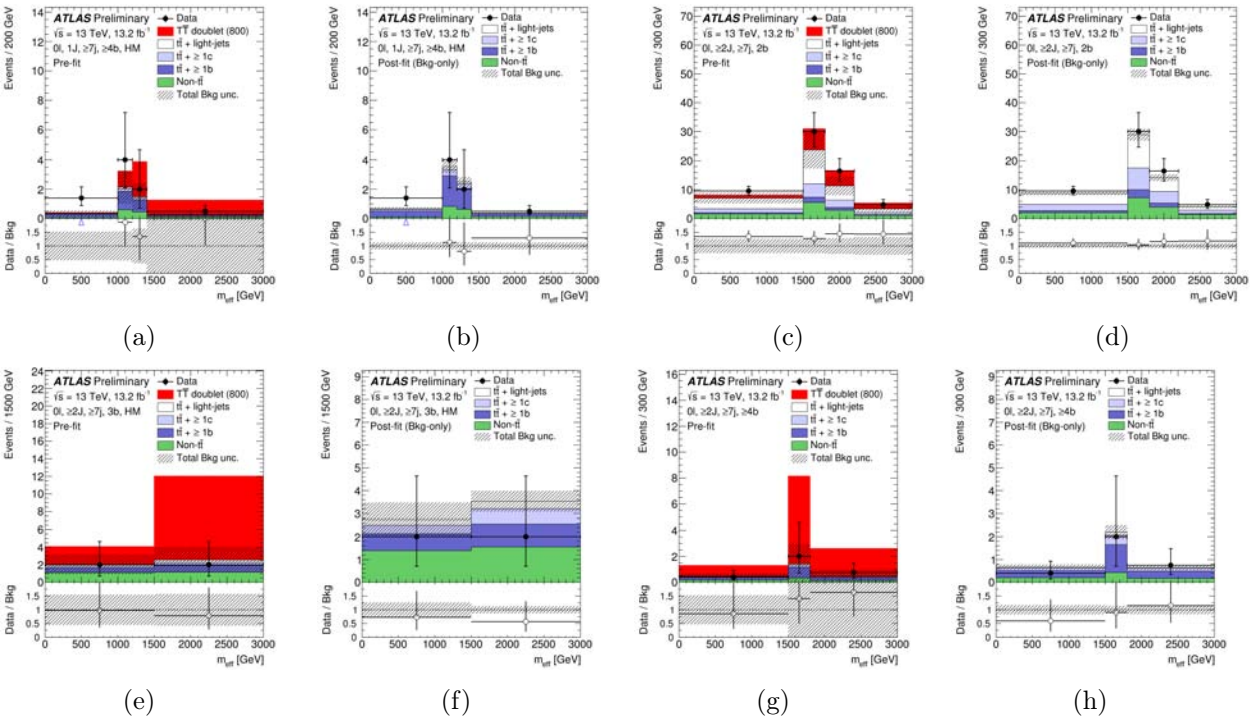

Figure 6.20: Comparison between the data and prediction for the m_{eff} distribution in some of the most-sensitive search regions in the 1-lepton channel, before and after performing the combined fit to data in the 0-lepton and 1-lepton channels ("Pre-fit" and "Post-fit", respectively) under the background-only hypothesis. Shown are the (1J, ≥7j, ≥4b, HM) region (a) pre-fit and (b) post-fit, the (≥2J, ≥7j, ≥2b) region (c) pre-fit and (d) post-fit, (≥2J, ≥7j, ≥3b, HM) region (e) pre-fit and (f) post-fit, and the (≥2J, ≥7j, ≥4b) region (g) pre-fit and (h) post-fit. In the pre-fit figures the expected $T\bar{T}$ signal (solid red) corresponding to $m_T = 800$ GeV in the T doublet scenario is also shown, added on top of the background prediction. The small contributions from $t\bar{t}V$, $t\bar{t}H$, single top, W/Z+jets, diboson, and multijet backgrounds are combined into a single background source referred to as "Non-$t\bar{t}$". The last bin in all figures contains the overflow. The bottom panels display the ratios of data to the total background prediction ("Bkg"). The blue triangles indicate points that are outside the vertical range of the figure. The hashed area represents the total uncertainty on the background. In the case of the pre-fit background uncertainty, the normalisation uncertainty on the $t\bar{t}+ \geq 1b$ background is not included.

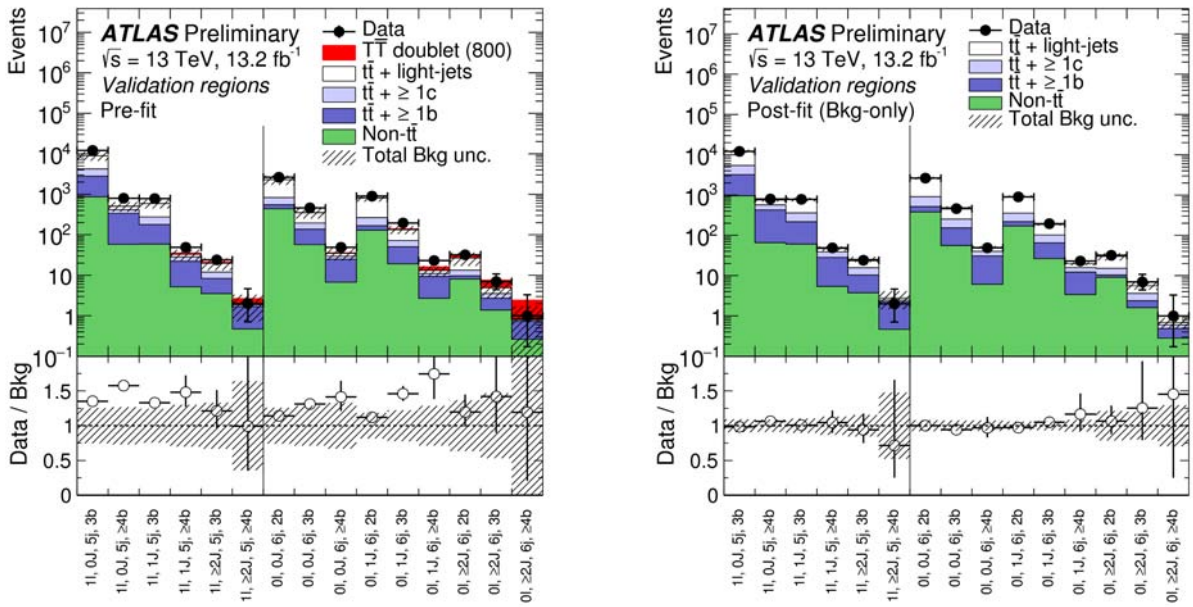

(a) (b)

Figure 6.21: Comparison between the data and background prediction for the yields in each of the validation regions considered in the 1-lepton and 0-lepton channels (a) before the fit ("Pre-fit") and (b) after the fit ("Post-fit"). The fit is performed on the data in 1-lepton and 0-lepton channels under the background-only hypothesis considering only the search regions. In the pre-fit figure the expected $T\bar{T}$ signal (solid red) corresponding to $m_T = 800$ GeV in the T doublet scenario is also shown, added on top of the background prediction. The small contributions from $t\bar{t}V$, $t\bar{t}H$, single top, W/Z+jets, diboson, and multijet backgrounds are combined into a single background source referred to as "Non-$t\bar{t}$". The last bin in all figures contains the overflow. The bottom panels display the ratios of data to the total background prediction ("Bkg"). The blue triangles indicate points that are outside the vertical range of the figure. The hashed area represents the total uncertainty on the background. In the case of the pre-fit background uncertainty, the normalisation uncertainty on the $t\bar{t}+ \geq 1b$ background is not included.

0-lepton channel	1J, ≥7j, ≥4b HM	2J, ≥7j, ≥2b	≥2J, ≥7j, 3b HM	≥2J, ≥7j, ≥4b
$t\bar{t}$+light-jets	0.76 ± 0.31	39.7 ± 6.7	0.58 ± 0.16	0.50 ± 0.21
$t\bar{t}$+≥1c	1.66 ± 0.55	27 ± 10	1.02 ± 0.36	1.47 ± 0.52
$t\bar{t}$+≥1b	7.2 ± 1.5	9.3 ± 2.8	1.75 ± 0.47	4.08 ± 0.83
$t\bar{t}V$	0.52 ± 0.11	3.86 ± 0.63	0.48 ± 0.09	0.33 ± 0.07
$t\bar{t}H$	0.50 ± 0.09	0.71 ± 0.10	0.12 ± 0.02	0.33 ± 0.07
W+jets	0.58 ± 0.25	7.0 ± 2.6	0.44 ± 0.18	0.30 ± 0.16
Z+jets	0.56 ± 0.25	4.9 ± 1.9	0.40 ± 0.17	0.10 ± 0.12
Single top	0.55 ± 0.31	6.6 ± 3.4	0.90 ± 0.54	0.36 ± 0.24
Diboson	0.13 ± 0.15	3.2 ± 2.0	0.55 ± 0.63	0.49 ± 0.47
$t\bar{t}t\bar{t}$ (SM)	0.11 ± 0.04	0.23 ± 0.08	0.05 ± 0.02	0.22 ± 0.07
Total background	12.6 ± 1.4	102.3 ± 7.0	6.3 ± 1.0	8.2 ± 1.0
Data	17	113	4	7

Table 6.9: Predicted and observed yields in the 0-lepton channel in four of the most-sensitive search regions considered. The multijet background is considered negligible in these regions and thus not shown. The background prediction is shown after the combined fit to data in the 0-lepton and 1-lepton channels under the background-only hypothesis. The quoted uncertainties are the sum in quadrature of statistical and systematic uncertainties on the yields, computed taking into account correlations among nuisance parameters and among processes.

in the 1-lepton regions due to an overestimation of the multijet background. Given the negligible contributionof this background in the signal-enriched regions, this pull is not considered problematic.

Other systematic uncertainties are not discussed since their pulls and constrains are less significant, and/or they do not affect appreciably the sensitivity of the analysis.

6.6 Limits on $T\bar{T}$ production

Given that no significant excess is observed in the signal regions, upper limits at 95% CL on the $T\bar{T}$ production cross section are set in several benchmark scenarios as a function of m_T and are compared to the theoretical prediction. The resulting lower limits on m_T correspond to the central value of the theoretical cross section. The scenarios considered involve different assumptions on the decay branching ratios. The search in the 1-lepton channel is particularly sensitive to the benchmark scenario of $\mathrm{BR}(T \to Ht) = 1$, while the 0-lepton channel instead is particularly sensitive to $\mathrm{BR}(T \to Zt) = 1$, as shown in figure 6.22. Both the 1-lepton and the 0-lepton searches have comparable sensitivity to the weak-isospin doublet and singlet scenarios. Therefore, their combination represents an improvement of $50 - 70$ GeV on the expected T-quark mass exclusion over the individual searches. The corresponding limits obtained for the combination are shown in figure 6.23.

For a vector-like singlet T-quark, an observed (expected) 95% CL limit of $m_T > 1020$ (960) GeV is obtained. For a vector-like doublet T-quark the observed (expected) 95% CL lower limit is $m_T > 1160$ (1110) GeV. This is the most sensitive search to date for a vector-like top partner in the singlet and

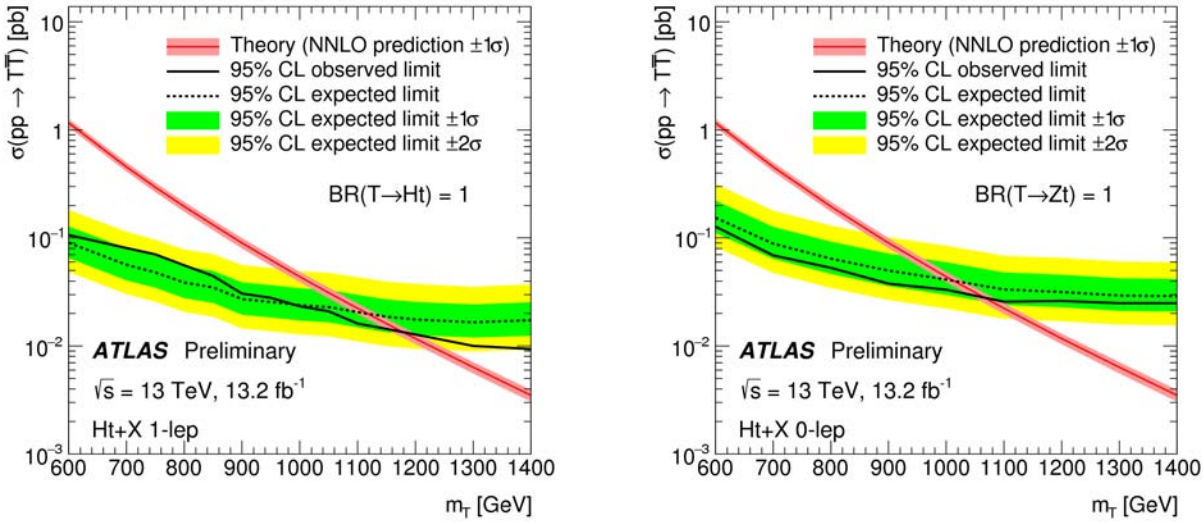

(a) (b)

Figure 6.22: Observed (solid line) and expected (dashed line) 95% CL upper limits on the $T\bar{T}$ cross section as a function of the T-quark mass for (a) the 1-lepton search under the assumption $\mathrm{BR}(T \to Ht) = 1$, and (b) the 0-lepton search under the assumption $\mathrm{BR}(T \to Zt) = 1$. The surrounding shaded bands correspond to ± 1 and ± 2 standard deviations around the expected limit. The thin red line and band show the theoretical prediction and its ± 1 standard deviation uncertainty.

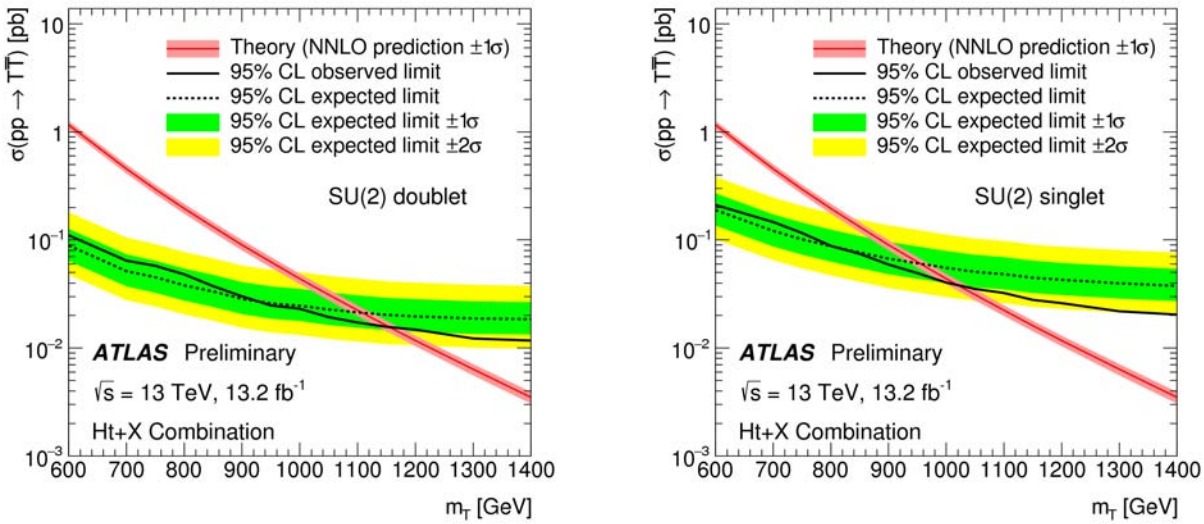

(a) (b)

Figure 6.23: Observed (solid line) and expected (dashed line) 95% CL upper limits on the $T\bar{T}$ cross section as a function of the T-quark mass for the combination of the 1-lepton and 0-lepton searches (a) for a T-quark doublet, and (b) for a T-quark singlet. The surrounding shaded bands correspond to ± 1 and ± 2 standard deviations around the expected limit. The thin red line and band show the theoretical prediction and its ± 1 standard deviation uncertainty.

doublet scenarios. A summary of the observed and expected upper limits on the T-quark mass in the different benchmark scenarios is given in table 6.10, including a comparison to the limits obtained by previous $T\bar{T} \to Ht + X$ searches in the 1-lepton channel. As can be appreciated, the current results extend the sensitivity of previous searches by $\sim 200 - 300$ GeV, depending on the assumed benchmark scenario.

95% CL lower limits on T-quark mass [GeV]				
Search	BR($T \to Ht$) = 1	BR($T \to Zt$) = 1	Doublet	Singlet
1-lepton channel	1180 (1120)	740 (820)	1060 (1000)	900 (880)
0-lepton channel	1090 (1070)	1060 (1010)	1090 (1060)	950 (890)
Combination	**1200 (1160)**	**1100 (1040)**	**1160 (1110)**	**1020 (960)**

Previous ATLAS $T\bar{T} \to Ht$+X searches (1-lepton)					Ref.
Run 2 (3.2 fb^{-1})	900 (980)	700 (740)	800 (900)	750 (780)	[232]
Run 1	950 (880)	750 (690)	860 (820)	760 (720)	[233]

Table 6.10: Summary of observed (expected) 95% CL lower limits on T-quark mass (in GeV) for the 1-lepton and 0-lepton channels, as well as their combination, under different assumptions on the decay branching ratios. Also shown are the corresponding limits obtained by previous ATLAS $T\bar{T} \to Ht$+X searches in the 1-lepton channel [232, 233].

Relaxing the assumption of a fixed branching ratio, exclusion limits can be set on vector-like T-quark production for different values of m_T and as a function of the two branching ratios BR($T \to Wb$) and BR($T \to Ht$).[7] The resulting 95% CL exclusion limits are shown in figure 6.24, for different values of m_T for the combination and the individual 1-lepton and 0-lepton channels. It can be noticed the complementarity between the 1-lepton and 0-lepton channels in terms of the coverage of the branching ratio plane. Therefore, the combination represents a significant improvement over the individual results. Figure 6.25 presents the corresponding observed and expected T-quark mass limits in the plane of BR($T \to Ht$) versus BR($T \to Wb$) for the combination obtained by linear interpolation of the calculated CLs versus m_T. The result is an observed lower limit on the T-quark mass ranging between 810 GeV and 1200 GeV for all possible values of the branching ratios into the three decay modes. This implies that a T-quark with mass below 810 GeV is excluded at 95% CL for any branching ratio configuration. The corresponding range of expected lower limits is between 730 GeV and 1160 GeV.

6.6.1 Comparison with other Run 2 searches

In addition to the $T\bar{T} \to Ht + X$ search, the ATLAS Collaboration has performed searches for $T\bar{T}$ production using the $\sqrt{s} = 13$ TeV dataset in several final states: lepton+jets final state with low jet multiplicity with low and high $E_{\mathrm{T}}^{\mathrm{miss}}$ (referred to as $Wb + X$ [234] and $Zt + X$ [235] searches respectively) and same-charge dileptons/trileptons with b-jets [236] (referred to as $Zb/t + X$ search). These searches have overlapping selections and thus a combination of all analyses in ATLAS has not been attempted yet. Figures 6.26–6.28 summarise the observed and expected T-quark mass limits in

[7] The branching ratio $T \to Zt$ is determined as: BR($T \to Zt$) = 1 − BR($T \to Wb$) − BR($T \to Ht$).

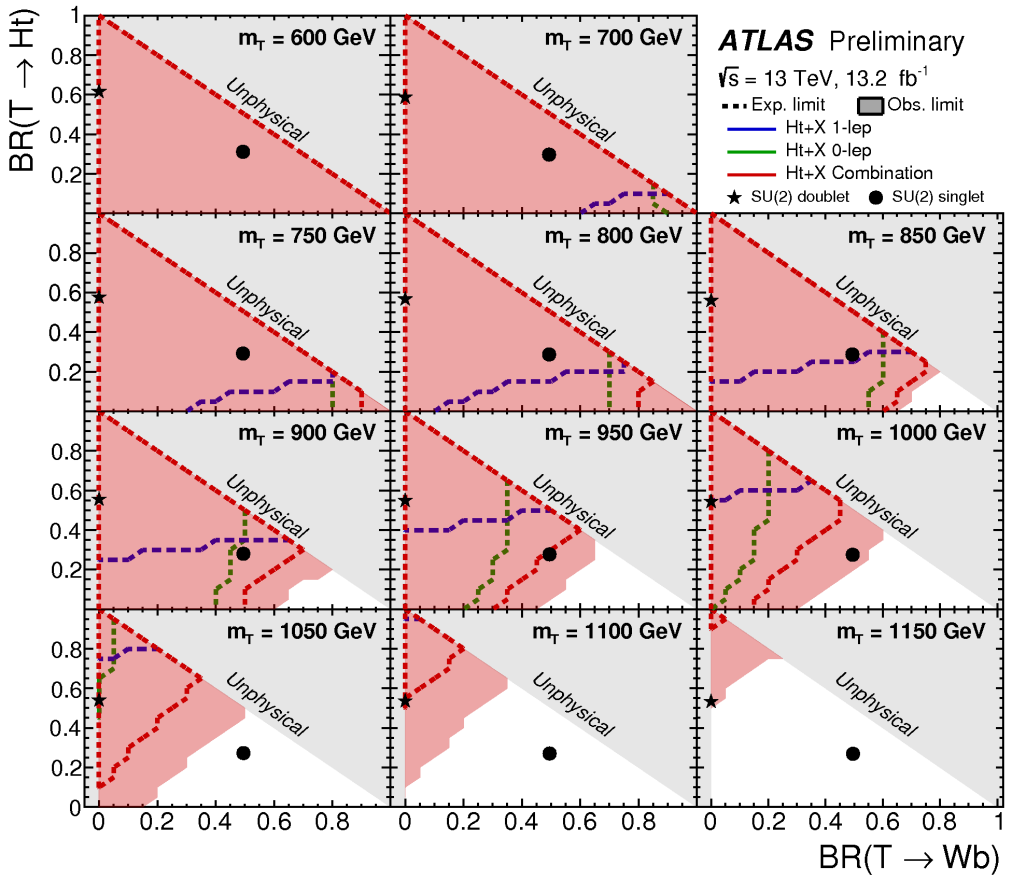

Figure 6.24: Observed (red filled area) and expected (red dashed line) 95% CL exclusion in the plane of BR($T \to Wb$) versus BR($T \to Ht$), for different values of the vector-like T-quark mass for the combination of the 1-lepton and 0-lepton searches. Also shown are the expected exclusions by the individual searches, which can be compared to that obtained through their combination. The grey (light shaded) area corresponds to the unphysical region where the sum of branching ratios exceeds unity, or is smaller than zero. The default branching ratio values from the PROTOS event generator for the weak-isospin singlet and doublet cases are shown as plain circle and star symbols respectively.

the plane of BR($T \to Ht$) versus BR($T \to Wb$), set by these searches. The $Wb + X$ and $Zt + X$ searches target respectively the Wb and Zt corner in the branching ratio plane and complement the coverage of the $Ht + X$ search. For example the $Ht + X$ search alone is not able to exclude at 95% CL a T quark with mass below 900 GeV for any branching ratio configuration, but considering the $Wb + X$ and $Zt + X$ searches it can be excluded. The $Zb/t + X$ search has a similar exclusion shape in the branching ratio plane to the $Ht + X$ 0-lepton channel, but with a limited sensitivity. Therefore, to date the $Zb/t + X$ search does not add new information to the branching ratio exclusion plane. The CMS Collaboration in Run 2 has performed a $Wb + X$ search [237] with observed (expected) lower limits on the T-quark mass ranging between $\sim$ 700 GeV and 850 GeV ($\sim$ 700 GeV and 870 GeV) and a $Ht + X$ search [238] with corresponding observed (expected) limits ranging between $\sim$ 700 GeV and 860 GeV ($\sim$ 700 GeV and 870 GeV).

In summary, the $Ht + X$ search presented in this dissertation is to date the most sensitive search for the well-motivated singlet and doublet benchmarks, and the search with the widest coverage in the branching ratio plane.

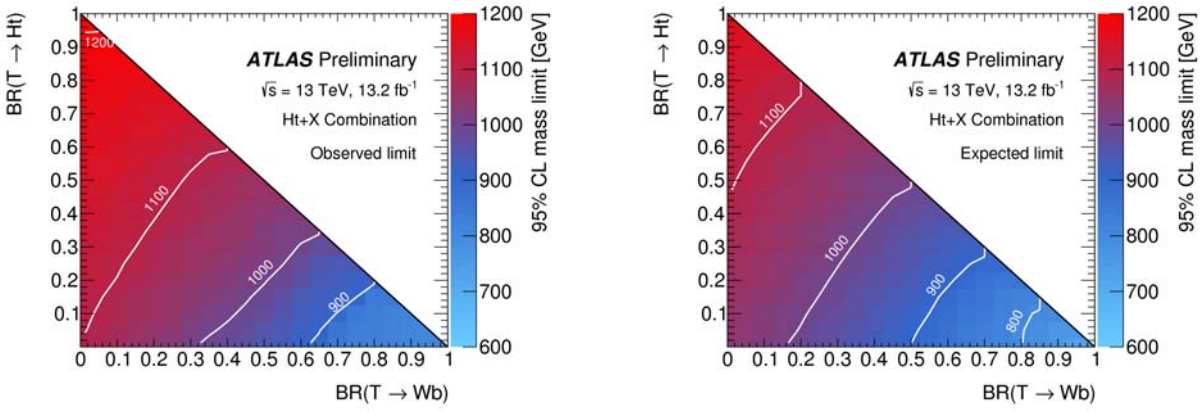

(a) (b)

Figure 6.25: (a) Observed and (b) expected limit (95% CL) on the mass of the T quark in the plane of BR($T \to Ht$) versus BR($T \to Wb$) for the combination of the 1-lepton and 0-lepton searches. Contour lines are provided to guide the eye.

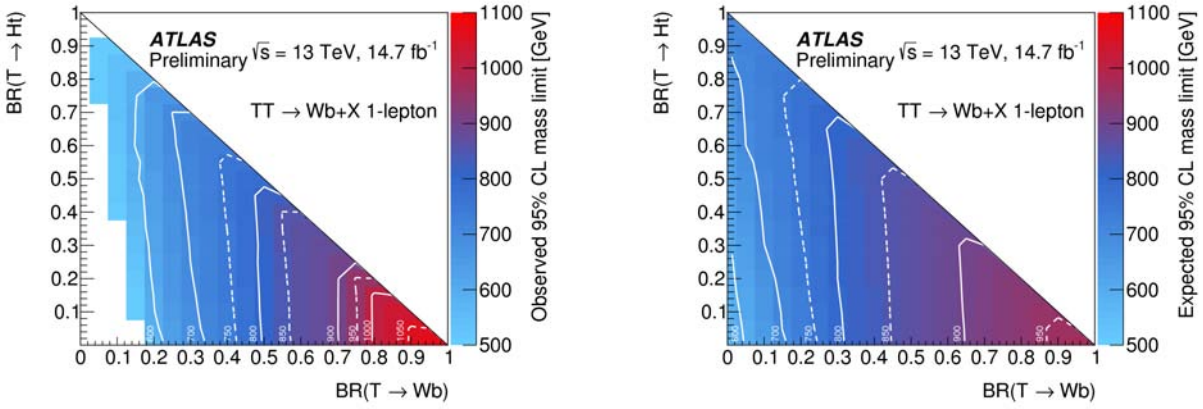

(a) (b)

Figure 6.26: (a) Observed and (a) expected limit (95% CL) on the mass of the T quark in the plane of BR($T \to Ht$) versus BR($T \to Wb$) for the $Wb+X$ search. Contour lines are provided to guide the eye.

6.7 Limits on $t\bar{t}t\bar{t}$ production

As discussed previously, the 1-lepton search is also used to set limits on four-top-quark production considering different signal benchmark scenarios: SM $t\bar{t}t\bar{t}$ production, $t\bar{t}t\bar{t}$ production via an EFT model with a four-top contact interaction, and $t\bar{t}t\bar{t}$ production in a Universal Extra Dimension (UED) model with two extra dimensions compactified under the Real Projective Plane (RPP) geometry.

In the case of $t\bar{t}t\bar{t}$ production within the SM, the observed (expected) 95% CL upper limit on the production cross section is 130 fb (110 fb), or 15 (12) times the SM prediction. In this scenario the expected sensitivity of this analysis is improved compared to that of previous ATLAS searches [232, 239]. The CMS Collaboration has performed as well a search in this scenario reporting an observed (expected) 95% CL upper limit on the production cross section of 10.2 (10.8) times the SM prediction [240].

In the case of $t\bar{t}t\bar{t}$ production via an EFT model with a four-top contact interaction, the observed

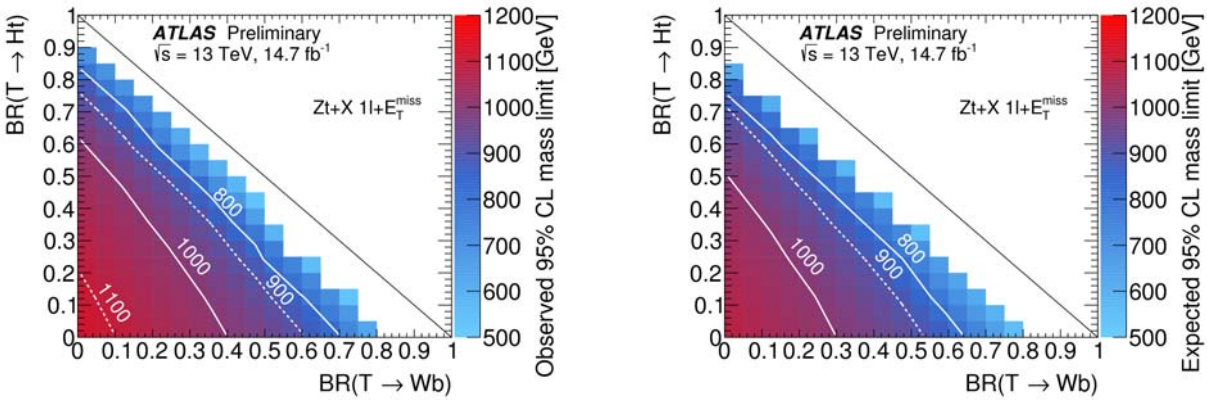

(a) (b)

Figure 6.27: (a) Observed and (a) expected limit (95% CL) on the mass of the T quark in the plane of BR($T \to Ht$) versus BR($T \to Wb$) for the $Zt + X$ search. Contour lines are provided to guide the eye.

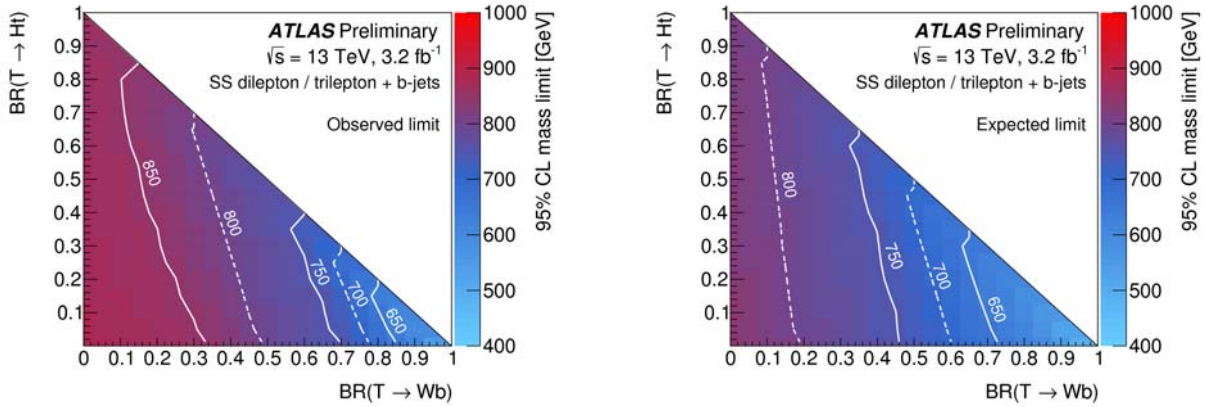

(a) (b)

Figure 6.28: (a) Observed and (a) expected limit (95% CL) on the mass of the T quark in the plane of BR($T \to Ht$) versus BR($T \to Wb$) for the same-charge dileptons/trileptons search. Contour lines are provided to guide the eye.

(expected) 95% CL upper limit on the production cross section is 51 fb (54 fb). The improved sensitivity in the case of the EFT model results from the harder m_{eff} spectrum compared to that of SM $t\bar{t}t\bar{t}$ production. The upper limit on the production cross section can be translated into an observed (expected) limit on the free parameter of the model: $|C_{4t}|/\Lambda^2 < 2.9$ TeV^{-2} (3.0 TeV^{-2}).

Finally, the observed and expected upper limits on the production cross section times branching ratio for the UED model are shown in figure 6.29 as a function of m_{KK} for the symmetric case ($\xi = R_4/R_5 = 1$), assuming production by tier (1,1) alone. The comparison to the LO theoretical cross section sets an observed (expected) 95% CL lower limit on m_{KK} of 1.6 TeV (1.5 TeV).

In summary, the search presented here obtains the most restrictive limits to date for BSM $t\bar{t}t\bar{t}$ production in the various new physics scenarios considered.

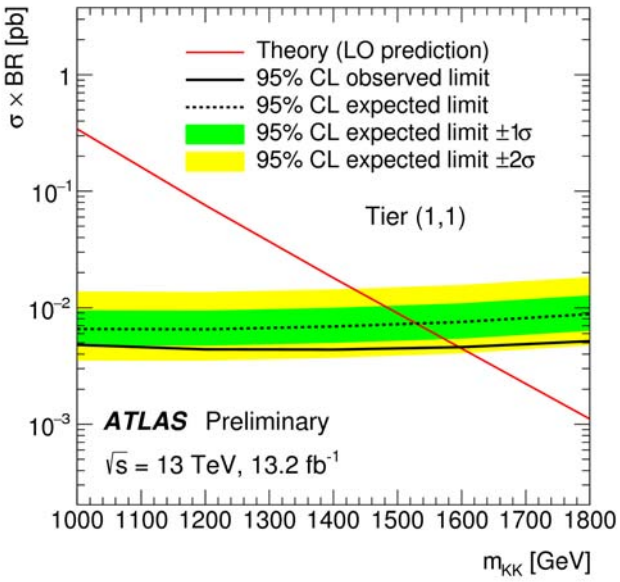

Figure 6.29: Observed (solid line) and expected (dashed line) 95% CL upper limits on the production cross section times branching ratio of four-top-quark events as a function of the Kaluza–Klein mass (m_{KK}) from tier (1,1) in the symmetric case ($\xi = R_4/R_5 = 1$). The surrounding shaded bands correspond to ± 1 and ± 2 standard deviations around the expected limit. The thin red line shows the theoretical prediction, computed at LO in QCD, for the production cross section of four-top-quark events by tier (1,1) assuming $BR(A^{(1,1)} \to t\bar{t}) = 1$, where the heavy photon $A^{(1,1)}$ is the lightest particle of this tier.

6.8 Limits on associated heavy Higgs-boson production

Using the 1-lepton search, 95% CL upper limits on the associated heavy Higgs boson production cross sections times branching ratios are derived for the three signal processes studied: $b\bar{b}H$, $t\bar{t}H$, and tbH^+. The upper limits on $b\bar{b}H$ and $t\bar{t}H$ production can be applied to $b\bar{b}A$ and $t\bar{t}A$ production respectively, since there are no significant differences in the kinematic distributions at the reconstructed level. The limits are derived under the assumption that only a single signal process at a time contributes in the signal regions, which makes these limits conservative. Stronger limits would be obtained if simultaneous contributions from four mass-degenerate states (H, A, and $H^{\pm}$) had been considered.

Figure 6.30 shows the observed and expected upper limits on $\sigma(pp \to b\bar{b}H) \times \mathrm{BR}(H \to t\bar{t})$ as a function of the heavy Higgs-boson mass m_H, compared to benchmark theoretical predictions within a Type-I and Type-II 2HDM. In both cases, the obtained limits are more than one order of magnitude above the largest predictions in the alignment limit ($\cos(\beta - \alpha) = 0$), which correspond to $\tan\beta$ values of about 0.1 and 5 respectively. The limited sensitivity of this search is due to the small signal acceptance, since often at least one of the associated b-quarks is not reconstructed and/or b-tagged.

Much better sensitivity is achieved in the $t\bar{t}H$ search, characterised by a large multiplicity of b-tagged jets and mass-tagged jets. The resulting observed and expected upper limits on $\sigma(pp \to t\bar{t}H) \times \mathrm{BR}(H \to t\bar{t})$ as a function of m_H are shown in figure 6.31. The comparison to the predictions for a Type-I or Type-II 2HDM[8] in the alignment limit allows the exclusion at the 95% CL of $\tan\beta$ values below 0.17 (0.11) for $m_H = 400$ GeV(1 TeV). The corresponding expected lower limit is 0.23 (0.15).

[8]The ttH couplings have the same value in a Type-I and a Type-II 2HDM.

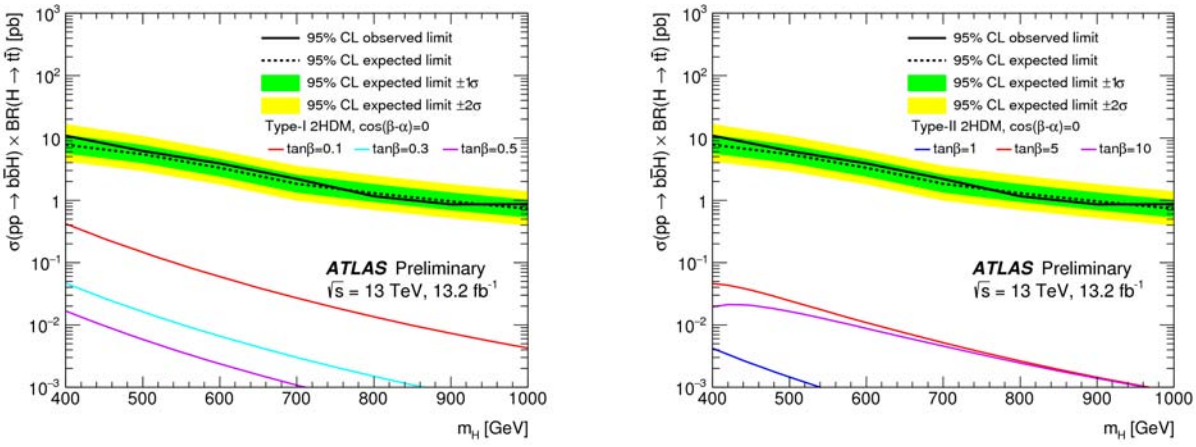

(a) (b)

Figure 6.30: Observed (solid line) and expected (dashed line) 95% CL upper limits on $\sigma(pp \to b\bar{b}H) \times \mathrm{BR}(H \to t\bar{t})$ as a function of the heavy Higgs-boson mass m_H, compared to the theoretical predictions assuming (a) a Type-I 2HDM, and (b) a Type-II 2HDM. The surrounding shaded bands correspond to ± 1 and ± 2 standard deviations around the expected limit. The coloured thin lines show the theoretical predictions corresponding to different values of $\tan\beta$, assuming $\cos(\beta - \alpha) = 0$.

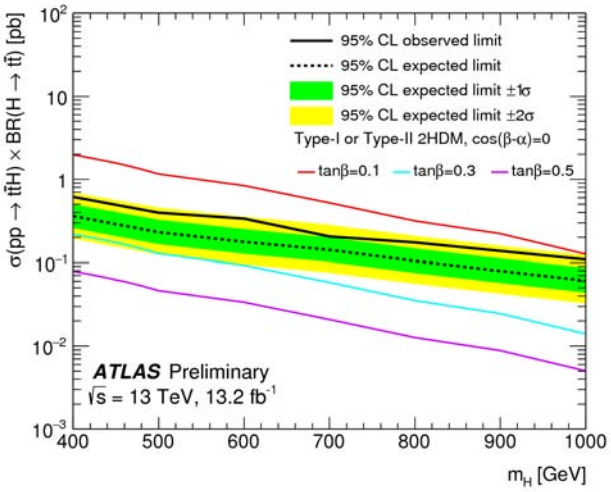

Figure 6.31: Observed (solid line) and expected (dashed line) 95% CL upper limits on $\sigma(pp \to t\bar{t}H) \times \mathrm{BR}(H \to t\bar{t})$ as a function of the heavy Higgs-boson mass m_H, compared to the theoretical predictions assuming a Type-I or Type-II 2HDM. The surrounding shaded bands correspond to ± 1 and ± 2 standard deviations around the expected limit. The coloured thin lines show the theoretical predictions corresponding to different values of $\tan\beta$, assuming $\cos(\beta - \alpha) = 0$.

Finally, figure 6.32 shows the observed and expected upper limits on $\sigma(pp \to \bar{t}bH^+) \times \mathrm{BR}(H^+ \to t\bar{b})$ as a function of the heavy Higgs boson mass m_{H^+}. The larger signal production cross section, compared to the neutral Higgs boson case, allows to set more restrictive limits on $\tan\beta$. In this case the 95% CL observed lower limit on $\tan\beta$ for a Type-II 2HDM is 0.65 (0.15) for $m_{H^\pm} = 200$ GeV(1 TeV). The corresponding expected lower limit is 0.55 (0.25).

The ATLAS Collaboration [241] has published a dedicated analysis targeting $tbH^+(\to tb)$ process

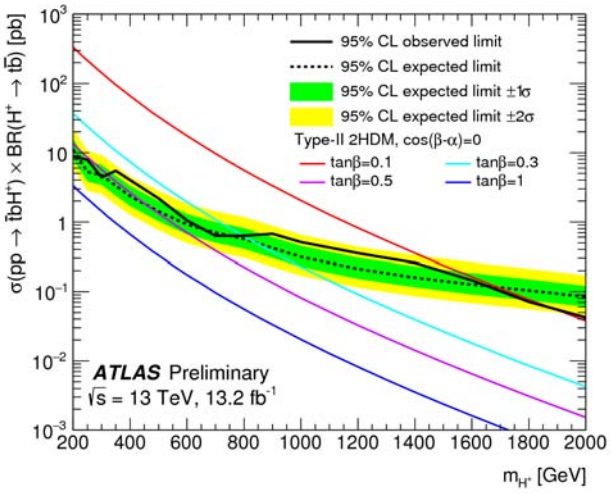

Figure 6.32: Observed (solid line) and expected (dashed line) 95% CL upper limits on $\sigma(pp \to \bar{t}bH^+) \times \mathrm{BR}(H^+ \to t\bar{b})$ as a function of the heavy Higgs-boson mass m_{H^+}, compared to the theoretical predictions assuming a Type-II 2HDM. For the values of $\tan\beta$ displayed, the predictions from a Type-I 2HDM are very close to those from a Type-II 2HDM. The surrounding shaded bands correspond to ± 1 and ± 2 standard deviations around the expected limit. The coloured thin lines show the theoretical predictions corresponding to different values of $\tan\beta$, assuming $\cos(\beta - \alpha) = 0$

with higher sensitivity compared to the analysis presented in this dissertation. It set upper limits on the cross section of 1.09-0.18 pb for $m_{H^\pm} = 300 - 1000$ GeV. The interests of the analysis presented in this dissertation is that can set simultaneously limits on the three processes $b\bar{b}H$, $t\bar{t}H$, and tbH^+ and it can push the limit up to 2 TeV for tbH^+ targeting boosted scenarios. The CMS Collaboration has not yet published results at $\sqrt{s} = 13$ TeV for $b\bar{b}H$, $t\bar{t}H$ and tbH^+ searches.

6.9 Future improvements

Although this search has shown excellent sensitivity over a wide range of BSM signals sharing the same signature, further improvements are still possible. They can be divided in different categories:

- Event categorisation: currently events are categorised using the multiplicity of mass-tagged jets, which efficiently tag boosted hadronic Higgs bosons and top quarks but without any further identification. An improved categorization using the multiplicity of boosted hadronic top-quarks and the multiplicity of boosted Higgs bosons present in the event can improve the discrimination between $T\bar{T}$ production and $t\bar{t}$+jets background using the presence of multiple boosted particles in the T-quark decay. A simple implementation of this event categorisation can be done using a mass window on the RT-jets mass instead of a lower cut as present in this analysis. Preliminary studies using this refined categorization lead to an improvement on the mass reach of $\sim 50\ GeV$.

- Extension of the 0-lepton analysis: the design of the current 0-lepton analysis leads to high sensitivity for the $T\bar{T} \to HtZt$ decay, covering a wide range of possible branching ratios, provided the $\mathrm{BR}(T \to Wb)$ is not too high. A possible improvement would be to extend the sensitivity to higher $\mathrm{BR}(T \to Wb)$ at high mass, targeting the $T\bar{T} \to ZtWb$ decay. This can be explored allowing for lower jet and b-tag multiplicities and targeting the decay of boosted hadronically-decaying W bosons whose decay products would be collimated in a small-R jet for high m_T

masses (>1 TeV). A splitting of the event categories using number of jets can improve the sensitivity to four-top-quark scenarios since those signals live at very high jet multiplicity (≥ 8 jets).

- Extension of the 1-lepton analysis: the current 1-lepton analysis is very powerful for high values of BR($T \to Ht$). It is possible to extend the reach making this analysis more sensitive to high BR($T \to Zt$) exploiting the presence of a $Z \to \nu\bar{\nu}$ decay. This can be achieved by adding a 1-lepton high-$E_{\mathrm{T}}^{\mathrm{miss}}$ channel selected via the $E_{\mathrm{T}}^{\mathrm{miss}}$ trigger, and splitting the analysis in low-$E_{\mathrm{T}}^{\mathrm{miss}}$ and high-$E_{\mathrm{T}}^{\mathrm{miss}}$ regions. In the case of the high-$E_{\mathrm{T}}^{\mathrm{miss}}$ channel, further splittings of regions according to powerful variables such as $m_{T,\mathrm{min}}^{b}$ (used in the 0-lepton channel) should lead to improved sensitivity.

- Discriminating variable: the current discriminant m_{eff} has good discrimination for hard signals (T quark, $t\bar{t}t\bar{t}$ in EFT and UEDRPP model) but it's not optimal for softer signals (SM $t\bar{t}t\bar{t}$ and $b\bar{b}H/t\bar{t}H/H^{+}tb$ production). The use of multivariate techniques for those signals benchmarks would lead to an improved sensitivity.

- $t\bar{t}$ modelling: ultimately this search is limited by large uncertainties that affect the main background. Further refinements on the background prediction through NLO MC simulations matched to parton shower (MEPS@NLO) will be important to obtain the most accurate possible modelling.

7

Search for $t\bar{t}H$ production

Physics is becoming too difficult for the physicists
David Hilbert

Contents

After the discovery by the ATLAS and CMS Collaborations of a Higgs boson with mass of approximately of 125 GeV, the focus has shifted towards measurements of its properties in order to determine whether it is the SM Higgs boson or whether it has a completely different (e.g. composite) nature. Of particular importance is the top-Higgs Yukawa coupling which is close to unity, due to the large measured top-quark mass. Any deviation from its SM value might give insight on the scale of BSM physics. Indirect constraints are extracted through measurements of the Higgs-boson production rates at the LHC, since the top-Higgs Yukawa coupling yields the dominant contribution to the main production mode ($gg \to H$, or gluon fusion) and it also contributes to Higgs-boson decay to a photon pair ($H \to \gamma\gamma$). However, its contribution to these processes only enters through loop effects, which cannot be disentangled from other possible BSM contributions. The observation of the production of the Higgs boson in association with a pair of top quarks ($t\bar{t}H$) can measure directly the magnitude of the top-Higgs Yukawa coupling, since at LO the cross section is proportional to the squared top-quark Yukawa coupling. Searches for $t\bar{t}H$ are performed in several final states according to the Higgs boson

decay mode. This chapter presents a search for $t\bar{t}H$ production with the Higgs boson decaying to a $b\bar{b}$ pair, which for a Higgs boson with $M_H = 125$ GeV is the dominant decay mode with a branching ratio of 58%.

7.1 Event preselection

Events used in the $t\bar{t}H$ search share part of the preselection described in section 6.1. Events are required to pass the same "event cleaning" and to satisfy the single-lepton requirements, both at the trigger and offline-selection levels. Events are further required to have at least four jets[1] and at least two b-tagged jets (70% operating point). No selection is applied on the $E_{\mathrm{T}}^{\mathrm{miss}}$ and the W-boson transverse mass; the signal-to-background ratio of the analysis is not altered by the relaxation of the selection since $t\bar{t}H$ and the main background ($t\bar{t}$) are affected in the same way. Nevertheless, it brings an increase in signal acceptance that helps to improve the statistical precision of the analysis. Table 7.1 summarises the requirements described above and referred to as the "preselection".

Preselection requirements		
Requirement	$t\bar{t}H$ search	$T\bar{T}/t\bar{t}t\bar{t}$ search
Event cleaning	✓	✓
Trigger	Single-lepton trigger	Single-lepton trigger
Leptons	=1 isolated e or μ	=1 isolated e or μ
Jets	≥4 jets	≥5 jets
b-tagging	≥2 b-tagged jets @70% OP	≥2 b-tagged jets @77% OP
$E_{\mathrm{T}}^{\mathrm{miss}}$	-	$E_{\mathrm{T}}^{\mathrm{miss}} > 20$ GeV
Other $E_{\mathrm{T}}^{\mathrm{miss}}$-related	-	$E_{\mathrm{T}}^{\mathrm{miss}} + m_T^W > 60$ GeV

Table 7.1: Summary of preselection requirements for the $t\bar{t}H$ search. For comparison, a summary of preselection requirements made in the 1-lepton channel for the search described in section 6.1 is reported as well. Here m_{T}^W is the transverse mass of the lepton and the $E_{\mathrm{T}}^{\mathrm{miss}}$ vector.

7.1.1 Comparison between data and prediction

Figure 7.1 presents basic kinematic variables at preselection level, showing reasonable agreement between data and the background prediction. As indicated for the search described in chapter 6, in this case the observed discrepancies are covered by systematic uncertainties, shown by the hashed area. Differences in the systematic uncertainties treatment compared to that discussed in section 6.5.1 are summarised in section 7.4.1.

7.2 Analysis strategy and event categorisation

After the preselection, the data sample is dominated by the background from $t\bar{t}$ events. Following a strategy similar to the one described in section 6.3, preselected events are categorised into exclusive "regions" based on the number of jets and the number of b-tagged jets in order to take advantage of the higher jet and b-jet multiplicity of the $t\bar{t}H$ signal process. A region with m jets and n b-tagged jets is denoted as (mj, nb). Events are categorised into four, five, or six or more jets, and two, three, or four or more b-tagged jets, as illustrated in figure 7.2. The "signal regions" are (5j, ≥4b), (≥6j, 3b),

[1] In the following, the term "jet" is used to refer to a small-R jet since no large-R jets are used in this search.

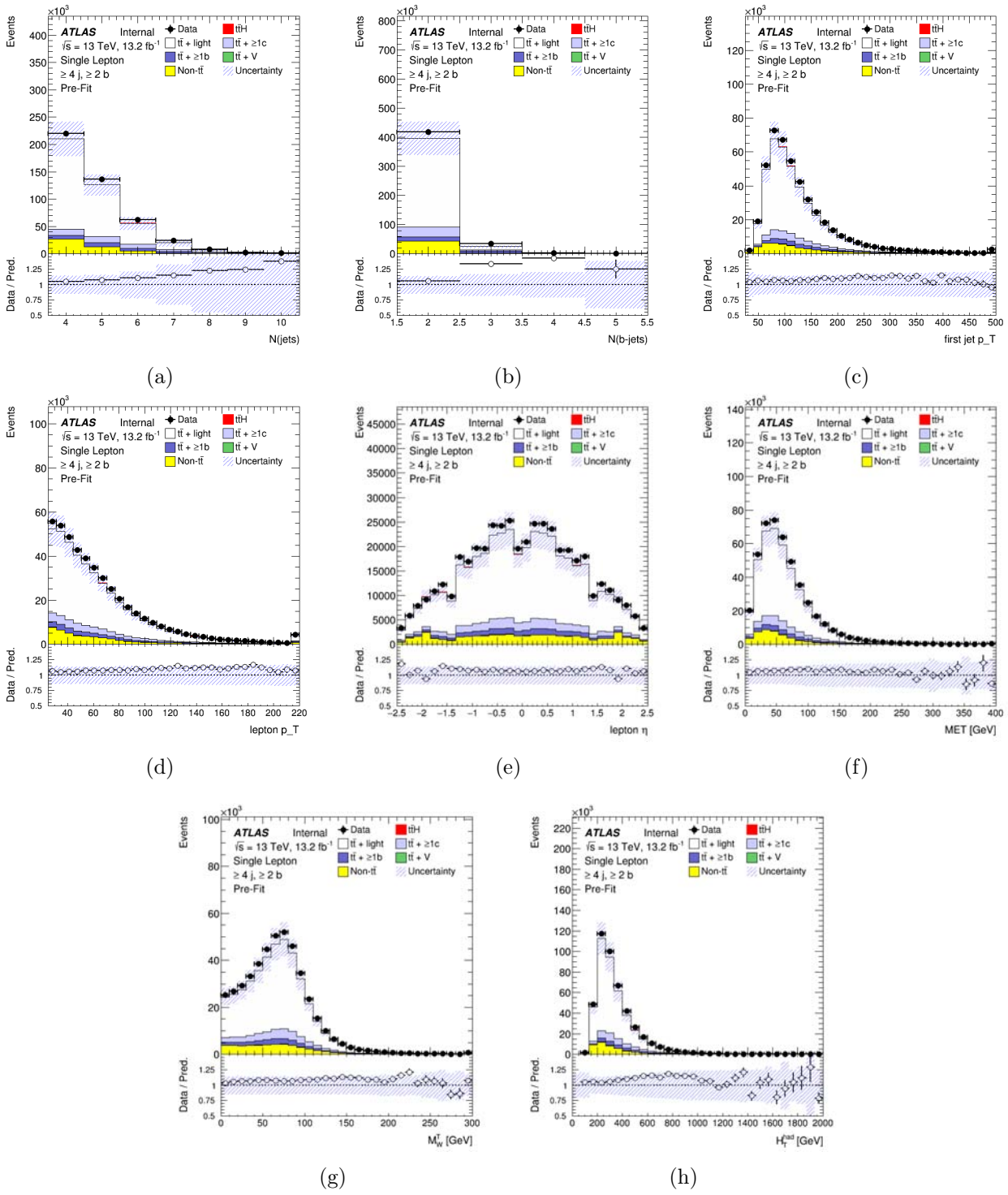

Figure 7.1: Comparison between data and prediction in at the preselection level in the $t\bar{t}H$ search for (a) jet multiplicity, (b) b-tag multiplicity, (c) leading jet p_{T}, (d) lepton p_{T}, (e) lepton η, (f) $E_{\mathrm{T}}^{\mathrm{miss}}$, (g) transwerse mass of the W boson (m_{T}^{W}), and (h) scalar sum of jet p_{T} (H_T^{had}). The hashed area represents the total uncertainty on the background.

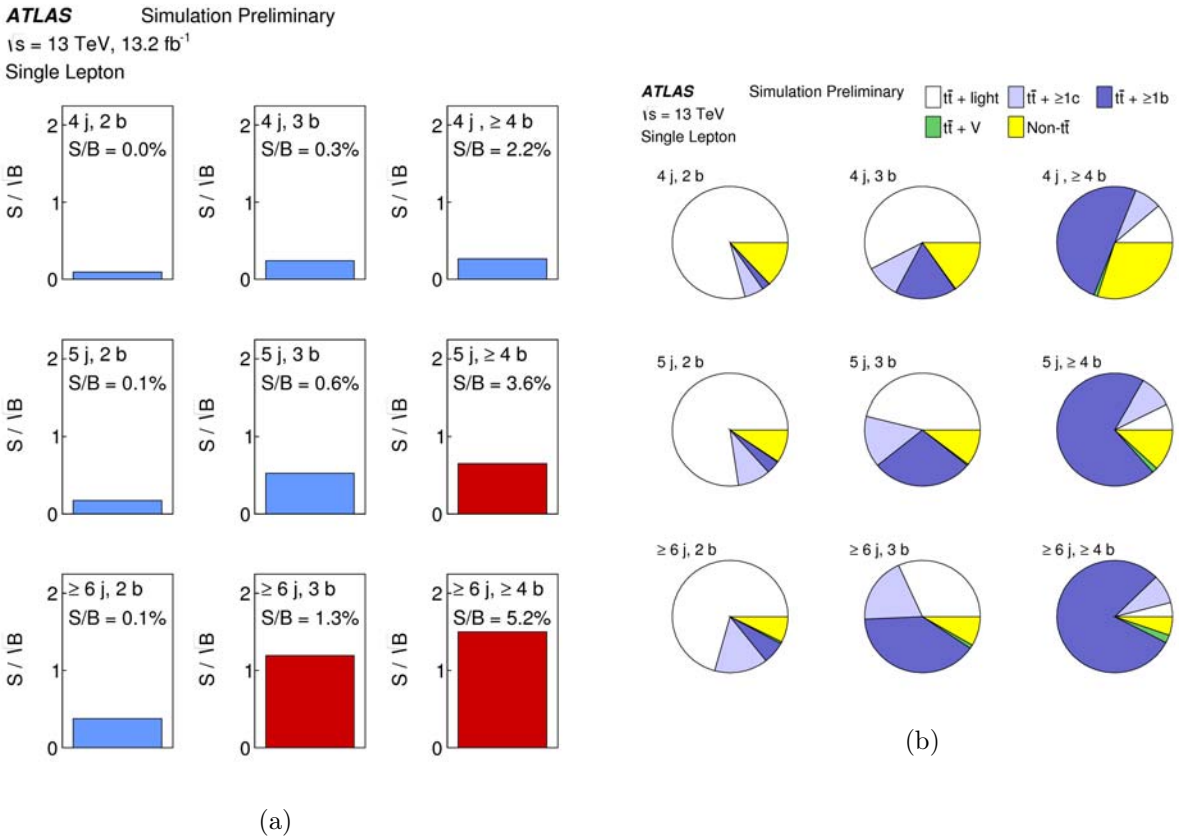

(a) (b)

Figure 7.2: (a) S/B and $S/\sqrt{B}$ for the analysis regions. Signal regions are shaded in red and control regions in blue. (b) Fractional contribution of the various backgrounds to the total background prediction. The small contributions from single top, W/Z+jets, diboson and multijet backgrounds are combined into a single background source referred to as "Non-$t\bar{t}$". Each row corresponds to a different jet multiplicity, while each column corresponds to a different b-tag multiplicity.

and ($\geq$6j, $\geq$4b), where the $t\bar{t}H$ signal is enhanced relative to the backgrounds; the remaining regions are referred to as "control regions". The background is dominated by $t\bar{t}$ events in all regions, while $t\bar{t}$ events with additional heavy-flavour jets are especially important in the signal regions.

7.3 Reconstruction and discriminating variable

After event categorisation it is quite difficult to further suppress the irreducible $t\bar{t}+\geq 1b$ background in the signal regions. For this purpose, the presence of the $H \to b\bar{b}$ resonance can be exploited but the identification of the correct $b\bar{b}$ pair is dominated by a combinatorial background; in an event with four b-tagged jets there are six combinations to assign a $b\bar{b}$ pair to the Higgs boson. In this search, the kinematic reconstruction of the $t\bar{t}H$ system in the signal regions relies on a multivariate analysis (MVA) technique. An MVA technique allows combining the information from several input variables into one output discriminant that can exploit the correlation among the variables and can reproduce a quasi-optimal selection in the "variables" phase space. Boosted decision trees (BDT), as implemented in the TMVA package [242], are used to discriminate the correct jet-parton assignments from the combinatorial background. A decision tree is a binary-tree-structured classifier where repeated yes/no decisions are taken on one single variable at a time until a stop criterion is fulfilled. In this way, the

phase space is split into many regions that are eventually classified as signal or background. While a cut-based analysis is able to select only one hypercube as region of phase space, the decision tree is able to split the phase space into a large number of hypercubes, each of which is identified as either "signal-like" or "background-like". Input variables to this BDT, referred to as "reconstruction" BDT, are natural discriminating variables between the correct jet-parton assignments and combinatorial background; examples of these variables are the reconstructed Higgs-boson invariant mass, but as well angular distances between reconstructed objects. All possible jet combinations are constructed, the trained BDT is evaluated for each jet combination, and the jet combination with the largest BDT output is selected. The best possible reconstruction efficiency is obtained by including information related to the Higgs boson, such as the candidate Higgs boson invariant mass. However, this biases the $t\bar{t}+ \geq 1b$ background distribution for these Higgs-related variables to be closer to the signal expectation, reducing their discriminating power. For this reason, two versions of the reconstruction BDT are used, with and without the Higgs boson information respectively, and information from both versions is used in the definition of the final discriminating variable between $t\bar{t}H$ signal and $t\bar{t}+\geq 1b$ background. The maximum reconstruction efficiency achieved is 12% in the (≥6j, ≥4b) region using the Higgs-boson information, and 8% without, compared to a theoretical maximum of 38%. This efficiency is defined as the fraction of events in which each of the partons from top-quark or Higgs-boson decays is matched within $\Delta R < 0.3$ to the correctly-assigned reconstructed jet. The low efficiency is partly due to the jets from the hadronically decaying W-boson, which are not always reconstructed because of being too soft ($\sim$ 50% of the times in case of the jet associated to the down-type quark). The jets from the Higgs boson are correctly matched around 30% of the time, without using Higgs-boson information, and the corresponding reconstructed Higgs-boson invariant mass is shown in figure 7.3.

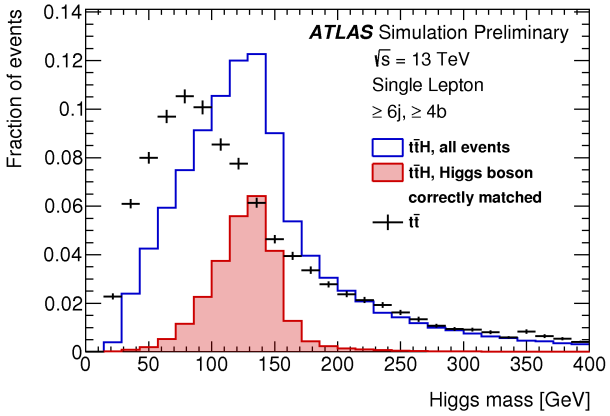

Figure 7.3: The reconstructed Higgs-boson invariant mass in the (≥6j, ≥4b) region, from the reconstruction BDT that does not use Higgs-related input variables. All signal events are shown in blue, while those with the correct jets assigned to the Higgs boson are shown in red. The $t\bar{t}$ background, consisting primarily of $t\bar{t}+ \geq 1b$, is shown in black.

Given the difficulty to increase the purity of the signal-rich regions just using kinematic reconstruction of the $t\bar{t}H$ system, the sensitivity can only to be optimised by introducing a more powerful discriminating variable. An additional BDT, referred to as "classification" BDT, is trained in each signal region (5j, ≥4b), (≥6j, 3b) and (≥6j, ≥4b) to discriminate the $t\bar{t}H$ signal from the background. Different types of variables are considered, from simple object kinematics such as jet p_{T} or di-jet properties, to complex event variables that make use of the full final state. As an example of the latter, the eigenvalues of the linear momentum tensor [243] are used to construct discriminant variables such

as the aplanarity of the event. Fox-Wolfram moments are used to describe the geometrical correlation among objects in the event in terms of spherical harmonics [244]. In general, event shape variables have the advantage that they can be constructed in all topologies and are less sensitive to the loss of jets through acceptance effects. The information coming from the two reconstruction BDTs is included as well in the classification BDT. All variables used for the BDT training and their pairwise correlations are required to be described well by the simulation in all regions. The following approach is used to find an optimal set of variables in each signal-rich region: the candidate input variables are ranked by their signal-to-background separation power defined as:

$$\mathcal{D} = \frac{1}{2}\sum_{i}^{\text{bins}} \frac{(N_i^S - N_i^B)^2}{N_i^S + N_i^B}, \tag{7.1}$$

where N_i^S and N_i^B are the entries in each bin of the normalised signal and background distributions, respectively. An iterative process then removes variables with no significant improvement of discrimination between signal and background and it stops when the best 15 variables are selected in each signal region. The complete list of variables used in the classification BDTs and their definition can be found in table 7.2. Figure 7.4 shows the distribution of the resulting classification BDT defined in each of the signal-rich regions.

7.4 The fit model

The search described in chapter 6 and the one described in this chapter share a similar fit model; the few existing differences are highlighted in this section. A total of nine search regions are used in the fit, summarised in table 7.3 along with the corresponding final discriminating variable used: the classification BDT in signal regions and $H_{\text{T}}^{\text{had}}$, defined as the scalar sum of jet p_{T}, in the control regions.

Control regions have a very low sensitivity to signal, and so $H_{\text{T}}^{\text{had}}$ is chosen due to its sensitivity to the background modelling and to systematic uncertainties such as jet energy scale or b-tagging, which have a p_{T} dependence. No explicit validation regions are considered, but the agreement for other kinematic distributions not used in the fit is used to gain confidence in the overall procedure. The control regions have high data statistics and the fit of $H_{\text{T}}^{\text{had}}$ allows controlling the impact of systematic uncertainties primarily affecting the $t\bar{t}$+light-jets background; it also provides more sensitivity to systematic uncertainties affecting the $t\bar{t}+ \geq 1c$ background compared to the search described in chapter 6. The following sections provide a summary of the differences in the treatment of systematic uncertainties compared to that in section 6.5.1, as well as a discussion of the results obtained from the fit to data.

7.4.1 Systematic uncertainties

7.4.1.1 $t\bar{t}$ modelling

Due to the presence of high-statistics regions with different jet multiplicity in the fit, the uncertainty on the modelling of the p_{T} of $t\bar{t}$ system is included. The p_{T} of $t\bar{t}$ system is directly linked to the emission of additional jets. The uncertainty is evaluated by taking the full difference between applying and not applying the reweighting to match the NNLO prediction on the p_{T} of $t\bar{t}$ system.

The increased sensitivity to $t\bar{t}+ \geq 1c$ events gives the possibility to measure the normalisation of this background directly from data. Therefore a free-floating parameter is used in the fit instead of the 50% normalisation uncertainty. The increased sensitivity to the $t\bar{t}+ \geq 1c$ background also calls for a

Variable	Definition	Region		
		$\geq$ 6j, $\geq$ 4b	$\geq$ 6j, 3b	5j, $\geq$ 4b
General kinematic variables				
$\Delta R_{bb}^{\text{avg}}$	Average ΔR for all b-tagged jet pairs	✓	✓	✓
$\Delta R_{bb}^{\text{max } p_T}$	ΔR between the two b-tagged jets with the largest vector sum p_{T}	✓	–	–
$\Delta\eta_{\text{jj}}^{\text{max}}$	Maximum $\Delta\eta$ between any two jets	✓	✓	✓
$m_{bb}^{\text{min}\Delta R}$	Mass of the combination of the two b-tagged jets with the smallest ΔR	✓	✓	–
$m_{jj}^{\text{min}\Delta R}$	Mass of the combination of any two jets with the smallest ΔR	–	–	✓
$m_{bj}^{\text{max } p_{\text{T}}}$	Mass of the combination of a b-tagged jet and any jet with the largest vector sum p_{T}	–	✓	–
$p_{\text{T}}^{\text{jet5}}$	p_{T} of the fifth leading jet	✓	✓	✓
N_{bb}^{Higgs30}	Number of b-jet pairs with invariant mass within 30 GeV of the Higgs boson mass	✓	–	✓
N_{40}^{jet}	Number of jets with $p_{\text{T}} \geq 40$GeV	–	✓	–
H_T^{had}	Scalar sum of jet p_{T}	–	✓	✓
$\Delta_{\text{lep}-bb}^{\text{min}\Delta R}$	ΔR between the lepton and the combination of the two b-tagged jets with the smallest ΔR	–	–	✓
Aplanarity	$1.5\lambda_2$, where λ_2 is the second eigenvalue of the momentum tensor [243] built with all jets	✓	✓	✓
Centrality	Scalar sum of the p_{T} divided by sum of the E for all jets and the lepton	✓	✓	✓
$H1$	Second Fox–Wolfram moment computed using all jets and the lepton	✓	✓	✓
Variables from reconstruction BDT output				
BDT output		✓*	✓*	✓*
m_H	Higgs boson mass	✓	✓	✓
$m_{H,b_{\text{lep top}}}$	Mass of Higgs boson and b-jet from leptonic top	✓	–	–
$\Delta R_{\text{Higgs bb}}$	ΔR between b-jets from the Higgs boson	✓	✓	✓
$\Delta R_{H,t\bar{t}}$	ΔR between Higgs boson and $t\bar{t}$ system	✓*	✓*	✓*
$\Delta R_{H,\text{lep top}}$	ΔR between Higgs boson and leptonic top	✓	–	–
$\Delta R_{H,b_{\text{had top}}}$	ΔR between Higgs boson and b-jet from hadronic top	–	✓*	✓*

Table 7.2: Definition of the variables used in the classification BDT for the signal regions. For the variables from the reconstruction BDT, those with a * are from the BDT using Higgs boson information, while those with no * are from the BDT without Higgs boson information.

	4 jets	5 jets	$\geq$6jets
2 b-tagged jets	$H_{\text{T}}^{\text{had}}$	$H_{\text{T}}^{\text{had}}$	$H_{\text{T}}^{\text{had}}$
3 b-tagged jets	$H_{\text{T}}^{\text{had}}$	$H_{\text{T}}^{\text{had}}$	BDT_{6j3b}
$\geq$4 b-tagged jets	$H_{\text{T}}^{\text{had}}$	BDT_{5j4b}	BDT_{6j4b}

Table 7.3: Summary of regions included in the fit and variable used in each region. The sub-script in the BDT output variables indicates that a specific BDT is trained in each region.

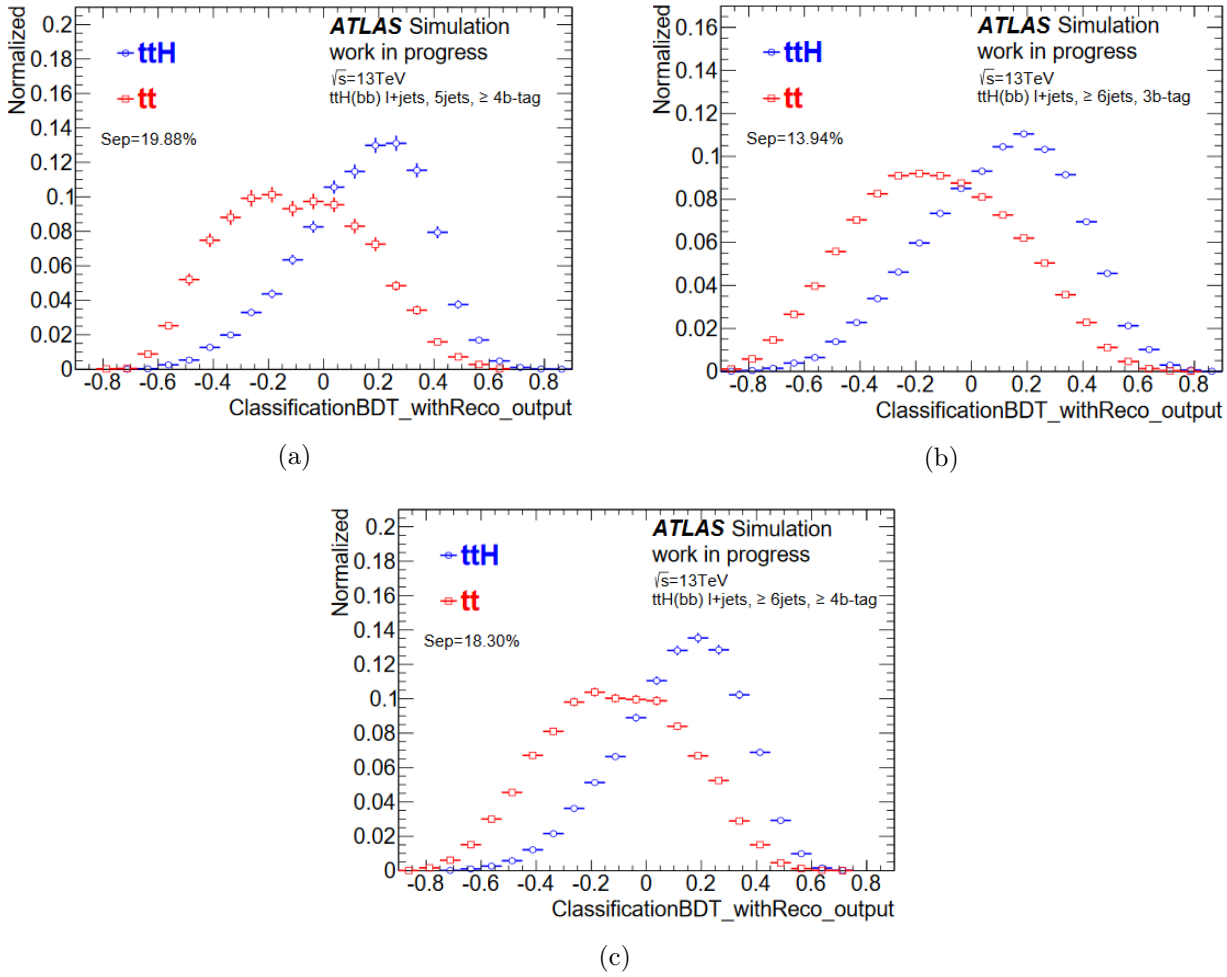

Figure 7.4: Comparison of the shape of the classification BDT output distribution between $t\bar{t}H(H \to b\bar{b})$ signal and $t\bar{t}$+jets background in the (a) (5j, $\geq$ 4b) , (b) ($\geq$6j, 3b) and (c) ($\geq$6j, $\geq$4b) regions.

more complete treatment of systematic uncertainties for this background component. Therefore, the difference between the NLO sample described in section 5.2.1.3, and an inclusive $t\bar{t}$ sample produced with MG5_aMC is taken as an uncertainty on the $t\bar{t}+ \geq 1c$ prediction.

7.4.1.2 W/Z+jets modelling

The uncertainties affecting the normalisation of the V+jets background are estimated separately for W+jets and Z+jets. For W+jets a normalisation uncertainty of 30% is assumed, taken to be uncorrelated across jet multiplicity. An additional 30% normalisation uncertainty is assumed for W+HF-jets correlated between $W+ \geq 1c$ and $W+ \geq 1b$ processes but uncorrelated across b-tag multiplicity. Therefore, a total of six independent nuisance parameters are considered. For Z+jets, which has a smaller contribution to the total background, a normalisation uncertainty of 30% is assumed, considered as one nuisance parameter. No additional uncertainty on Z+HF-jets is assumed.

7.4.1.3 Single top modelling

Since in the search regions the event kinematics is not as extreme as for the $T\bar{T}/t\bar{t}t\bar{t}$ search, there is enough MC statistics to evaluate the uncertainties for Wt production described in section 6.5.1.6 in each region, without summing in quadrature with those for the t-channel and s-channel processes. Therefore, a total of five independent nuisance parameters are considered in the fit.

7.4.1.4 $t\bar{t}+V$ modelling

The uncertainty on the $t\bar{t}Z$ and $t\bar{t}W$ normalisations is 15%, from the uncertainties on their respective NLO theoretical cross sections. This uncertainty is treated as uncorrelated between $t\bar{t}Z$ and $t\bar{t}W$ and is split into scale and PDF uncertainties, also treated as uncorrelated. Therefore, a total of four independent nuisance parameters are considered.

7.4.1.5 Multijet modelling

A 50% normalisation uncertainty is taken as correlated across jet multiplicity but uncorrelated across lepton flavours (electron or muon) and b-tag multiplicity. Thus, a total of six independent nuisance parameters are considered.

7.4.1.6 Signal modelling

The uncertainty on the $t\bar{t}H$ signal cross-section is $+10\%/-13\%$, including contributions from scale and PDF uncertainties, which are treated as uncorrelated [204, 207, 245]. Uncertainties on the Higgs-boson branching ratios are also considered; these amount to 2.2% for the $b\bar{b}$ decay mode [209]. An additional uncertainty on the choice of parton shower and hadronisation model is derived by comparing the default prediction from MG5_aMC+Pythia8 to that from MG5_aMC+Herwig++. Finally, the effect of the QCD scale choice is evaluated by varying the renormalisation and factorisation scales up and down by a factor of two. Therefore, a total of seven independent nuisance parameters are considered.

7.4.2 Fit results

A fit to the data is performed in the nine analysis channels under the signal-plus-background hypothesis. The resulting fitted NPs and the corresponding correlation matrix can be found in figures 7.5 and 7.6 respectively.

The fitted values for the $t\bar{t}+\geq 1b$ and $t\bar{t}+\geq 1b$ normalisation parameters are 1.2 ± 0.2 and $1.4^{+0.7}_{-0.6}$ respectively. As discussed in section 6.5.3, given the regions considered in the fit, only few NPs are expected to be pulled and somewhat constrained by the data. Such discussion is also valid for this fit since the dataset and categorisation is very similar. The introduction of the 4-jet and 5-jet channels improves the statistical power of the fit, and some of the pulls and constraints such as the ones that were present in $t\bar{t}$+light-jets modelling or multijet modelling are accentuated. The fit results between the two searches are quite consistent, taking into account the existing differences of fitted regions and uncertainties modelling.

A complementary search for $t\bar{t}H(H\rightarrow b\bar{b})$ in the dileptonic channel has also been performed in ATLAS [246]. The analysis procedure in the dileptonic channel is completely equivalent, and given that the datasets are orthogonal, the combination of both analyses can be performed. A combined fit is performed to the nine regions of the single-lepton search and six regions of the dilepton search. The results of the fit are in good agreement between the individual and the combined analyses.

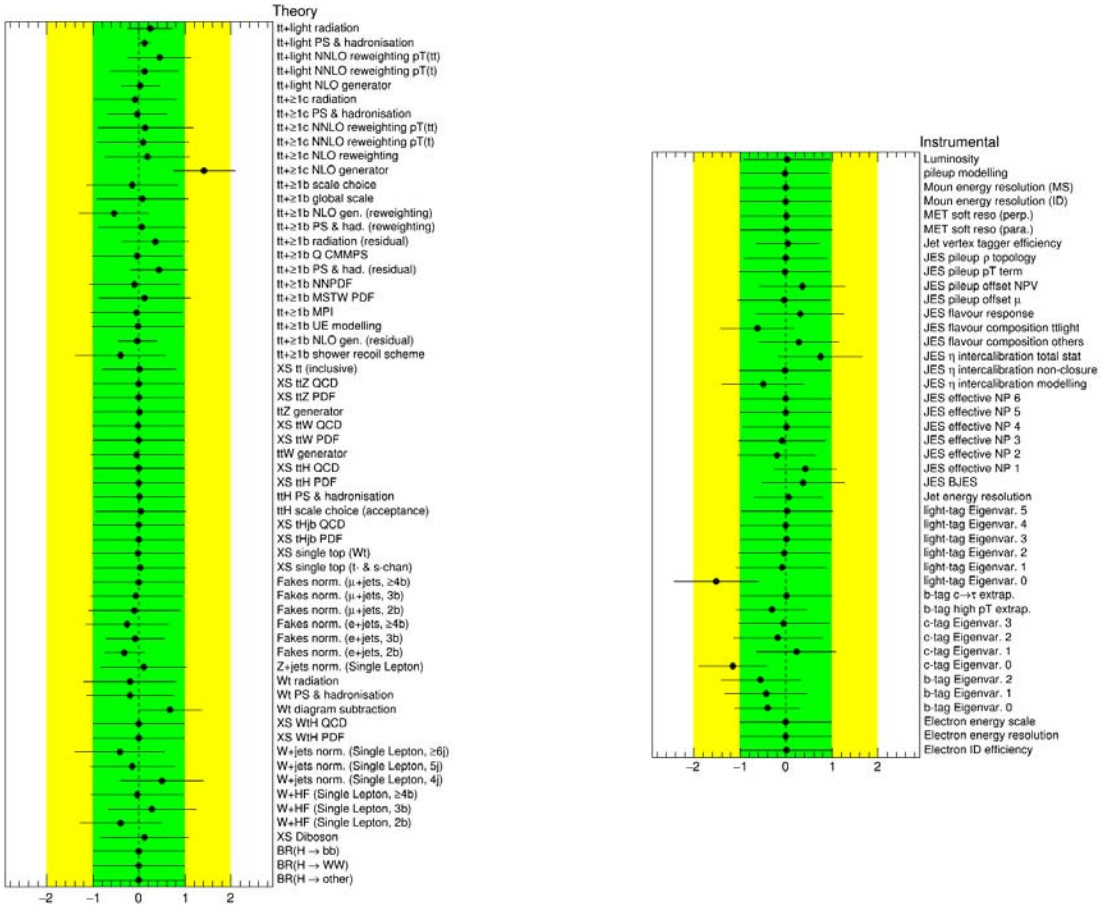

Figure 7.5: Nuisance parameters from the fit to data in the single-lepton channel under the signal-plus-background hypothesis. A detailed description of the naming of the NPs can be found in appendix B.

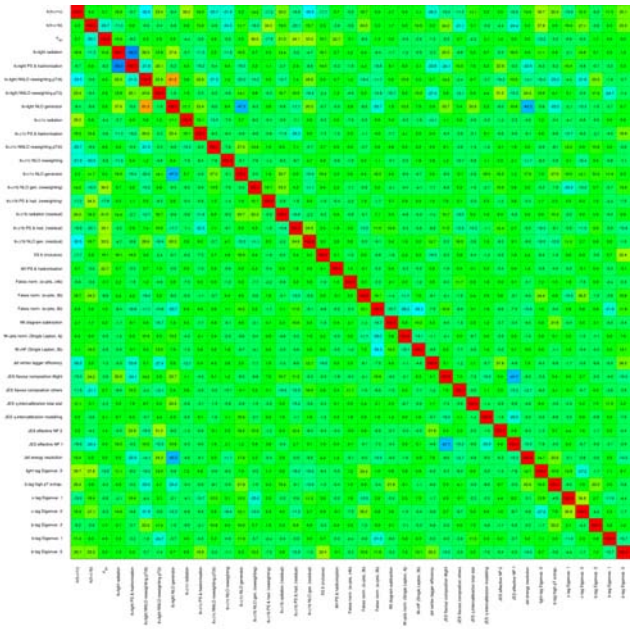

Figure 7.6: Correlation matrix between NPs corresponding to the fit to data in the single-lepton channel under the signal-plus-background hypothesis. Only NPs with a correlation coefficient of at least 20% with any other parameter are displayed.

Figure 7.7 demonstrates the effect of various systematic uncertainties on the fitted value of μ and the constraints provided by the data. The largest effects arises from the modelling of the $t\bar{t}+\geq 1b$ background, with six of them being among the ten highest-ranked systematic uncertainties.

Figures 7.8 and 7.9 show the comparison of data and prediction for the $H_{\mathrm{T}}^{\mathrm{had}}$ and BDT distributions in each of the analysis channels considered before and after the combined fit. The corresponding predicted and observed yields per channel can be found in table 7.4, and also displayed in figure 7.10, before and after the combined fit. Compared to the pre-fit distributions, the total background uncertainty is significantly reduced after the fit, not only in the background-dominated channels, but also in the signal-rich channels, resulting in an increase in the search sensitivity. The reduced uncertainty results from the significant constraints provided by the data on some systematic uncertainties, as well as the anti-correlations among sources of systematic uncertainty resulting from the fit to the data.

7.5 Limits on $t\bar{t}H$ production

For the single-lepton search the best-fit signal strength is $\mu = 1.6 \pm 1.1$. Since no significant excess of events above the background expectation is found for the SM Higgs boson with mass of 125 GeV, a 95% CL upper limit on the signal strength modifier is set. A signal cross section larger than 3.6 times the SM prediction is excluded at 95% CL. The expected exclusion is 2.2 times the SM prediction in the absence of the $t\bar{t}H$ process.

Combining those results with the dilepton search, the expected sensitivity improves by 15% with respect to the single-lepton-only search. The best-fit μ values for the single-lepton and dilepton searches, and their combination, are shown in figure 7.11. The fitted signal strength for the combined analysis is $\mu = 2.1^{+1.0}_{-0.9}$. The observed (expected) significance of the signal is 2.4 (1.2) standard deviations. The observed and expected limits for both searches and their combination are shown in figure 7.12. A signal cross section 4.0 times larger than predicted by the SM is excluded at 95% CL.

	4j, 2b		4j, 3b		4j, ≥4b	
	Pre-fit	Post-fit	Pre-fit	Post-fit	Pre-fit	Post-fit
$t\bar{t}$ + light-jets	160000 ± 30000	158800 ± 4800	5300 ± 1500	6300 ± 440	17 ± 11	36 ± 14
$t\bar{t}+\geq 1c$	10800 ± 2400	16800 ± 4100	880 ± 300	1680 ± 350	11.7 ± 5.4	24.4 ± 6.3
$t\bar{t}+\geq 1b$	4580 ± 930	5760 ± 980	1570 ± 470	1930 ± 320	76 ± 24	94 ± 13
$t\bar{t}$+V	212 ± 27	218 ± 24	18.4 ± 3.8	20.4 ± 3.6	1.60 ± 0.42	1.73 ± 0.33
Single top	10300 ± 1700	10400 ± 1300	390 ± 87	476 ± 80	9.6 ± 3.5	12.9 ± 3.2
W/Z+jets	6500 ± 2400	7800 ± 2200	220 ± 100	410 ± 150	2.1 ± 1.2	2.6 ± 1.2
Diboson	420 ± 220	390 ± 190	15 ± 10	19 ± 11	3.9 ± 3.3	3.5 ± 3.0
Multijet	9200 ± 4200	7800 ± 1500	770 ± 360	770 ± 240	29 ± 27	23 ± 23
tH	9.3 ± 1.3	9.3 ± 1.2	4.41 ± 0.66	4.55 ± 0.57	0.62 ± 0.13	0.64 ± 0.10
Total background	202000 ± 32000	208000 ± 1900	9200 ± 1900	11610 ± 300	152 ± 44	199 ± 28
$t\bar{t}H$	63.8 ± 6.2	134 ± 42	24.6 ± 4.1	54 ± 21	3.32 ± 0.87	7.7 ± 2.9
Total	202000 ± 32000	208200 ± 1900	9200 ± 1900	11660 ± 300	155 ± 45	207 ± 28
Data	208239		11686		218	

	5j, 2b		5j, 3b		5j, ≥4b	
	Pre-fit	Post-fit	Pre-fit	Post-fit	Pre-fit	Post-fit
$t\bar{t}$ + light-jets	91000 ± 17000	91500 ± 3900	3640 ± 880	4580 ± 450	24 ± 15	45 ± 19
$t\bar{t}+\geq 1c$	10800 ± 2100	16600 ± 3800	1170 ± 330	2150 ± 410	30 ± 12	64 ± 11
$t\bar{t}+\geq 1b$	4440 ± 530	5760 ± 840	2230 ± 460	2830 ± 370	224 ± 62	278 ± 29
$t\bar{t}$+V	277 ± 33	287 ± 30	35.3 ± 6.1	39.6 ± 5.9	4.9 ± 1.5	5.4 ± 1.4
Single top	4900 ± 1200	4790 ± 690	305 ± 87	338 ± 67	14.3 ± 5.6	16.1 ± 3.9
W/Z+jets	2700 ± 1100	2720 ± 780	200 ± 100	300 ± 120	3.0 ± 3.0	3.3 ± 2.3
Diboson	200 ± 110	210 ± 110	15.7 ± 9.7	16.0 ± 8.7	0.39 ± 0.28	0.43 ± 0.29
Multijet	3300 ± 1500	2800 ± 670	300 ± 150	300 ± 110	20 ± 17	16 ± 16
tH	7.4 ± 1.3	7.5 ± 1.3	3.88 ± 0.72	4.14 ± 0.69	0.82 ± 0.16	0.91 ± 0.14
Total background	117000 ± 20000	124600 ± 1400	7900 ± 1400	10560 ± 280	322 ± 78	429 ± 28
$t\bar{t}H$	96.5 ± 7.7	206 ± 61	49.7 ± 6.9	110 ± 42	11.8 ± 2.6	27 ± 10
Total	118000 ± 20000	124900 ± 1400	7900 ± 1400	10670 ± 280	333 ± 79	457 ± 27
Data	124688		10755		418	

	≥6j, 2b		≥6j, 3b		≥6j, ≥4b	
	Pre-fit	Post-fit	Pre-fit	Post-fit	Pre-fit	Post-fit
$t\bar{t}$ + light-jets	54000 ± 24000	58600 ± 4000	2600 ± 1100	3610 ± 500	34 ± 22	74 ± 32
$t\bar{t}+\geq 1c$	11500 ± 3700	12500 ± 5200	1550 ± 560	1960 ± 660	71 ± 37	91 ± 36
$t\bar{t}+\geq 1b$	4800 ± 1200	7180 ± 920	3240 ± 800	4830 ± 470	670 ± 190	955 ± 70
$t\bar{t}$+V	470 ± 61	498 ± 49	86 ± 13	98 ± 10	19.1 ± 4.2	22.3 ± 3.5
Single top	2690 ± 840	2430 ± 400	278 ± 100	286 ± 65	29 ± 14	32 ± 12
W/Z+jets	1610 ± 660	1720 ± 520	121 ± 55	169 ± 65	11.9 ± 6.7	12.9 ± 6.4
Diboson	164 ± 88	166 ± 83	14.4 ± 8.3	15.8 ± 8.4	2.0 ± 1.3	2.1 ± 1.3
Multijet	1220 ± 560	1050 ± 310	270 ± 150	270 ± 120	1.2 ± 1.2	1.2 ± 1.2
tH	9.6 ± 2.4	9.9 ± 2.3	5.7 ± 1.5	6.2 ± 1.5	1.86 ± 0.53	2.10 ± 0.50
Total background	77000 ± 26000	84200 ± 1400	8200 ± 1900	11250 ± 240	840 ± 230	1191 ± 55
$t\bar{t}H$	198 ± 18	430 ± 120	119 ± 16	261 ± 99	44.9 ± 9.4	107 ± 39
Total	77000 ± 26000	84600 ± 1400	8300 ± 1900	11520 ± 220	890 ± 230	1298 ± 41
Data	84556		11561		1285	

Table 7.4: Expected and observed event yields in the single lepton channel. Post-fit yields are after the combined fit to data in the single-lepton and dilepton channels under the signal-plus-background hypothesis. The quoted uncertainties are the sum in quadrature of statistical and systematic uncertainties on the yields. In the pre-fit case, they do not include the uncertainties on the $t\bar{t}+\geq 1b$ or $t\bar{t}+\geq 1c$ normalisations. In the post-fit case, these uncertainties are computed taking into account correlations among nuisance parameters and among processes, including the uncertainties on the determination of the $t\bar{t}+\geq 1b$ and $t\bar{t}+\geq 1c$ normalisations. For the $t\bar{t}H$ signal, the pre-fit yield values correspond to the theoretical prediction and corresponding uncertainties, whilst the post-fit yield and uncertainties correspond to those on the signal strength measurement.

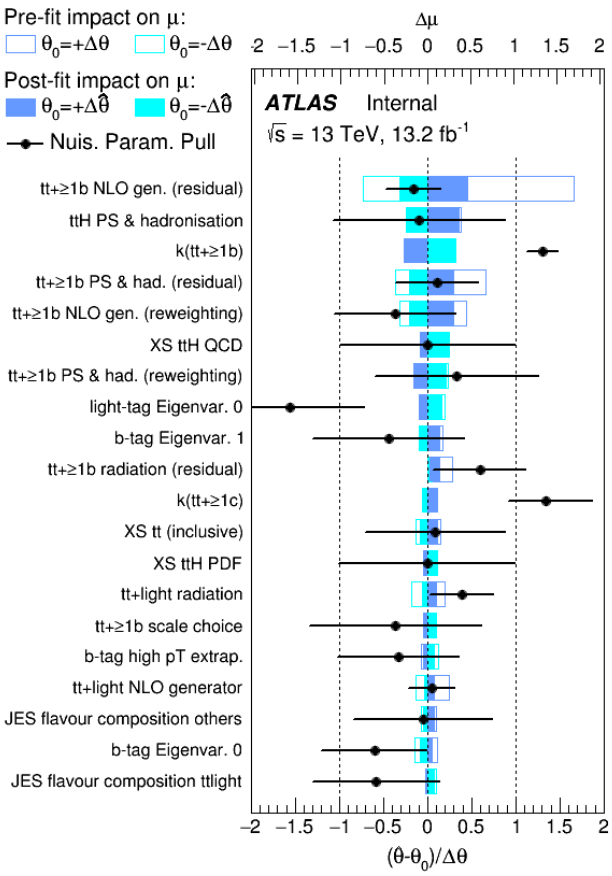

Figure 7.7: The fitted values of the NPs with the largest impact on the measured signal strength. The points, which are drawn conforming to the scale of the bottom axis, show the deviation of each of the fitted NPs, $\hat{\theta}$, from θ_0, which is the nominal value of that NP, in units of the pre-fit standard deviation $\Delta\theta$. The error bars show the post-fit uncertainties, σ_θ, which are close to 1 if the data do not provide any further constraint on that uncertainty. Conversely, a value of σ_θ much smaller than 1 indicates a significant reduction with respect to the original uncertainty. The NPs are sorted according to the post-fit effect of each on μ (plain area) conforming to the scale of the top axis, with those with the largest impact at the top.

The expected exclusion is 1.9 times the SM prediction in the absence of the $t\bar{t}H$ process, and 2.7 times the SM prediction if the $t\bar{t}H$ process is present with the SM predicted rate.

Finally, figure 7.13 summarises the post-fit event yields as a function of $\log_{10}(S/B)$, for all bins of the distributions used in the combined fit of the single-lepton and dilepton channels. The signal is normalised to the fitted value of the signal strength ($\mu = 2.1$) and a signal 4.0 times larger than predicted by the SM, which is excluded at 95% CL, is also shown.

7.5.1 Comparison with other analyses

Searches for the $t\bar{t}H$ process have also been performed in ATLAS in the diphoton [247] and multilepton [248] final states. The expected exclusion limits are 2.7 and 2.3 times the SM prediction, respectively. The combination [249] of the three analyses: $b\bar{b}$, diphoton and multilepton, has been performed in order to achieve the most sensitive result. The best-fit value of the signal strength is $\mu = 1.8 \pm 0.7$. A signal 1.2 times larger than the SM Higgs boson is expected to be excluded in the case of no SM Higgs boson, while a signal 3.0 times larger than predicted by the SM is excluded at 95% CL. The sensitivity

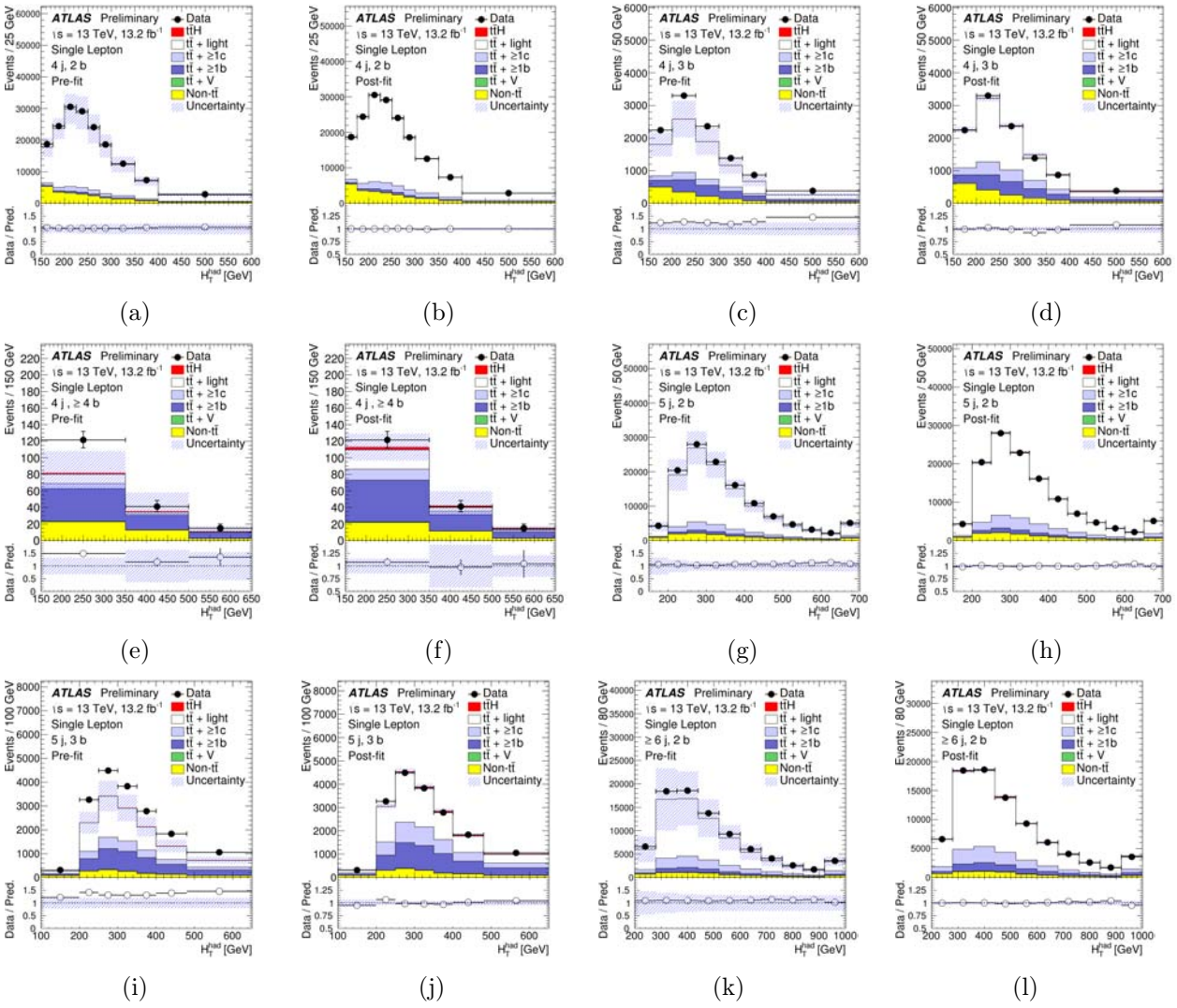

Figure 7.8: Comparison between the data and prediction for the $H_{\mathrm{T}}^{\mathrm{had}}$ distributions before and after performing the combined fit to data in the single-lepton and dilepton channels ("Pre-fit" and "Post-fit", respectively) under the signal-plus-background hypothesis. Shown are the (4j, 2b) region (a) pre-fit and (b) post-fit, the (4j, 3b) region (c) pre-fit and (d) post-fit, the (4j, ≥4b) region (e) pre-fit and (f) post-fit, the (5j, 2b) region (g) pre-fit and (h) post-fit, the (5j, 3b) region (i) pre-fit and (j) post-fit, and the (≥6j, 2b) region (k) pre-fit and (l) post-fit. The small contributions from single top, W/Z+jets, diboson, and multijet backgrounds are combined into a single background source referred to as "Non-$t\bar{t}$". The last bin in all figures contains the overflow. The bottom panels display the ratios of data to the total background prediction ("Bkg"). The blue triangles indicate points that are outside the vertical range of the figure. The hashed area represents the total uncertainty on the background. In the case of the pre-fit background uncertainty, the normalisation uncertainties on the $t\bar{t}+ \geq 1b$ and $t\bar{t}+ \geq 1c$ backgrounds are not included.

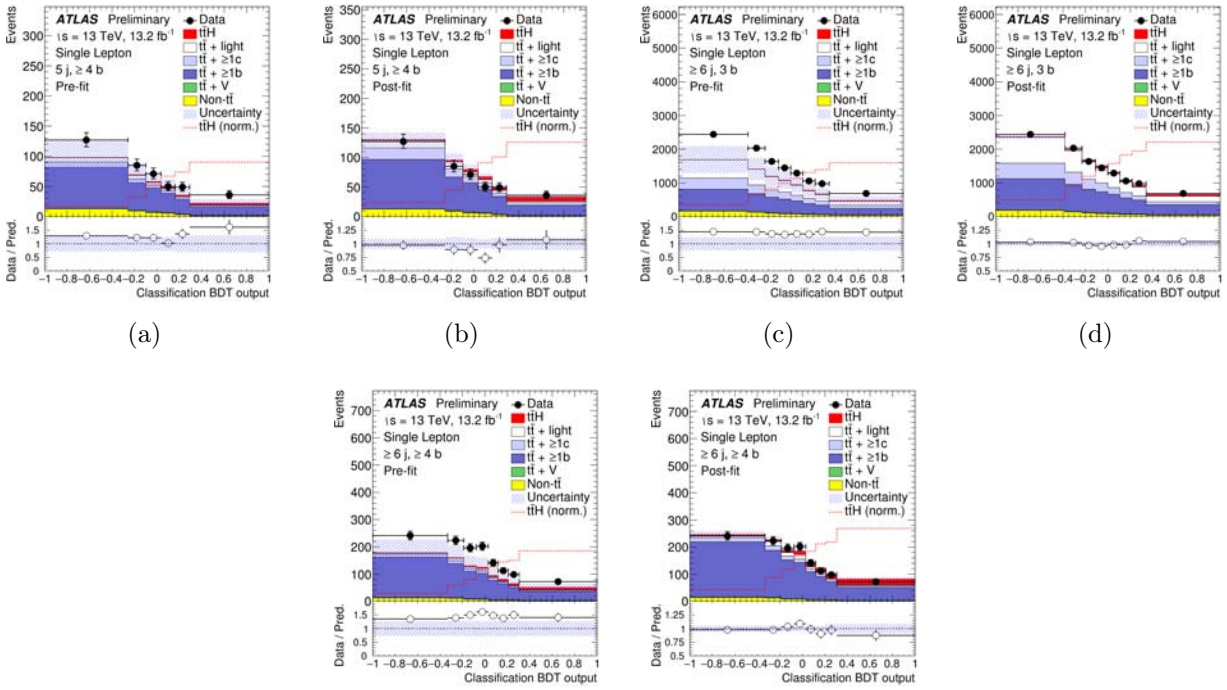

Figure 7.9: Comparison between the data and prediction for the classification BDT output distributions before and after performing the combined fit to data in the single-lepton and dilepton channels ("Pre-fit" and "Post-fit", respectively) under the signal-plus-background hypothesis. Shown are the (5j,≥4b) region (a) pre-fit and (b) post-fit, the (≥6j, 3b) region (c) pre-fit and (d) post-fit, and the (6j, ≥4b) region (e) pre-fit and (f) post-fit. The small contributions from single top, W/Z+jets, diboson, and multijet backgrounds are combined into a single background source referred to as "Non-$t\bar{t}$". The last bin in all figures contains the overflow. The bottom panels display the ratios of data to the total background prediction ("Bkg"). The blue triangles indicate points that are outside the vertical range of the figure. The hashed area represents the total uncertainty on the background. In the case of the pre-fit background uncertainty, the normalisation uncertainties on the $t\bar{t}+ \geq 1b$ and $t\bar{t}+ \geq 1c$ backgrounds are not included.

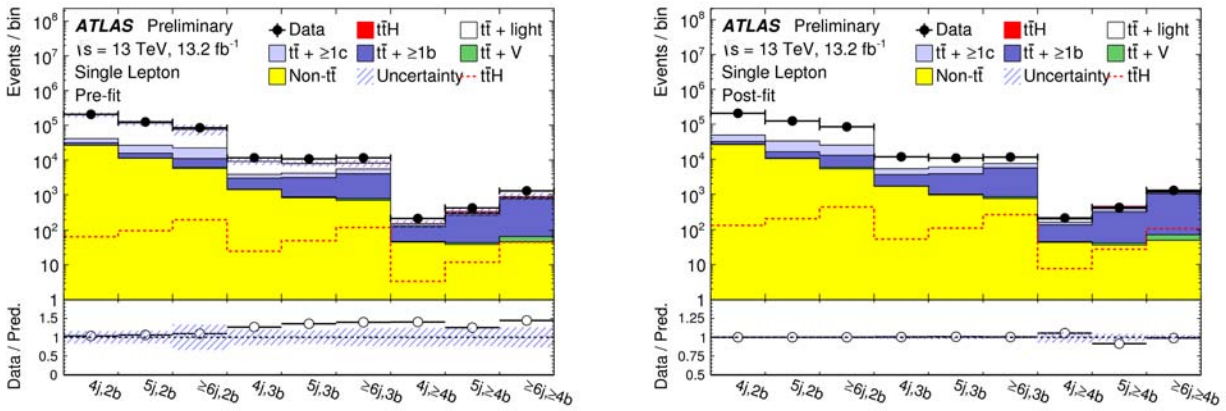

(a) (b)

Figure 7.10: Comparison between the data and background prediction for the yields in each of the search regions considered (a) before the fit ("Pre-fit") and (b) after the fit ("Post-fit"). The fit is performed on the data in single-lepton and dilepton channels under the signal-plus-background hypothesis. The small contributions from single top, W/Z+jets, diboson, and multijet backgrounds are combined into a single background source referred to as "Non-$t\bar{t}$". The last bin in all figures contains the overflow. The bottom panels display the ratios of data to the total background prediction ("Bkg"). The blue triangles indicate points that are outside the vertical range of the figure. The hashed area represents the total uncertainty on the background. In the case of the pre-fit background uncertainty, the normalisation uncertainties on the $t\bar{t}+\geq 1b$ and $t\bar{t}+\geq 1c$ backgrounds are not included.

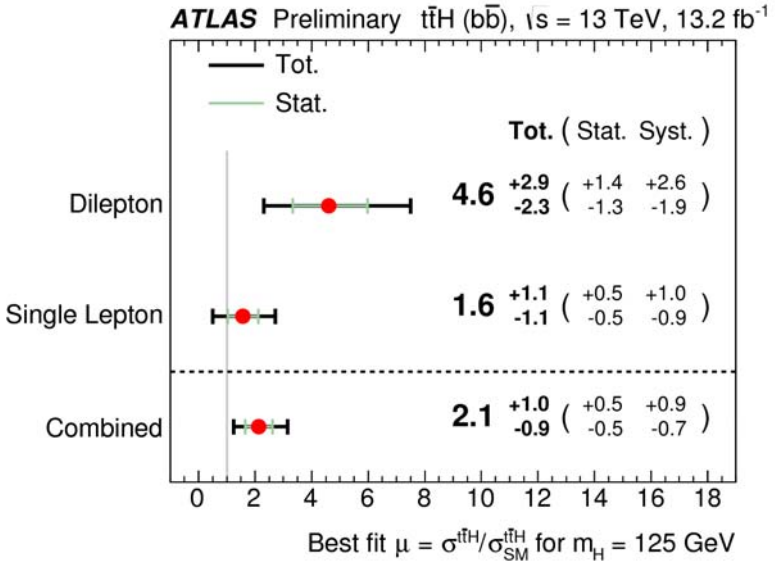

Figure 7.11: Signal-strength measurements for the individual channels, as well as their combination.

of this combination already exceeds the Run 1 ATLAS combination [250]. The fitted signal strengths and 95% CL upper limits are summarised in figures 7.14 and 7.15 respectively, for the individual searches and their combination. The observed (expected) significance is 2.8 (1.8) standard deviations, which represents an improvement of 50% relative to the most-sensitive individual analysis.

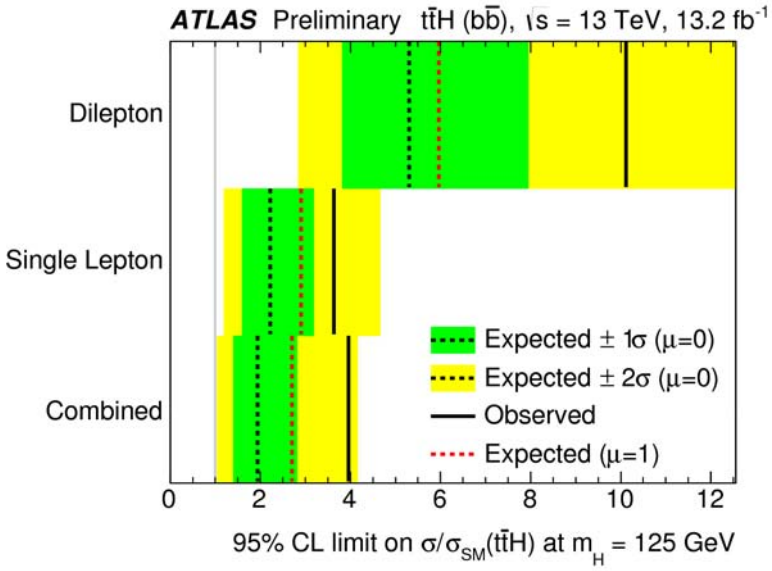

Figure 7.12: Summary of the 95% CL upper limits on $\sigma(t\bar{t}H)$ relative to the SM prediction for the individual channels, as well as their combination.

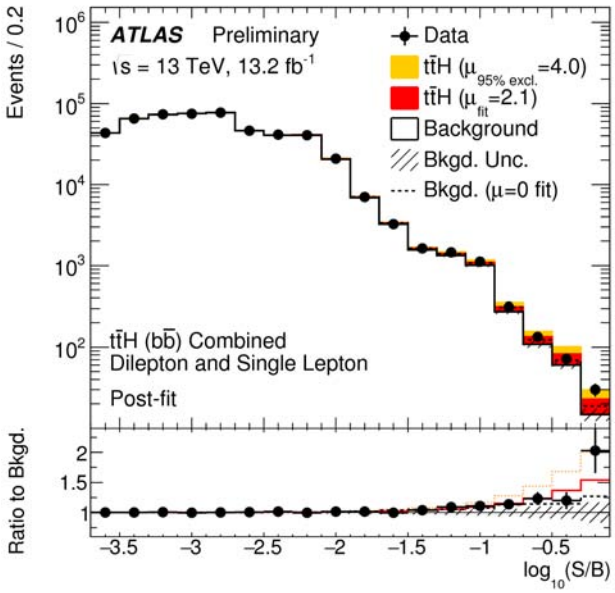

Figure 7.13: Post-fit event yields, as a function of $\log_{10}(S/B)$, where S (B) denotes the signal (background) yield, for all bins used in the combined fit of the single-lepton and dilepton channels. The signal is shown normalised to the best-fit value and to the excluded value. The background is also shown after the fit to data assuming zero signal contribution.

Searches for $t\bar{t}H$ production at $\sqrt{s} = 13$ TeV considering several Higgs-boson decay modes (including $H \to b\bar{b}$) have been published by the CMS Collaboration [251–253]. The search in the $H \to b\bar{b}$ channel uses 12.9 fb^{-1} of data, and as final discriminating variable it uses the matrix element method in conjunction with a classification BDT. The observed (expected) 95% CL upper limit on $\sigma(t\bar{t}H)$ is 1.5 (1.7) times the SM prediction. The fitted signal strength, combining single-lepton and dilepton channels, is $\mu = -0.2 \pm 0.8$. The error on μ is reduced compared to the ATLAS result due to the

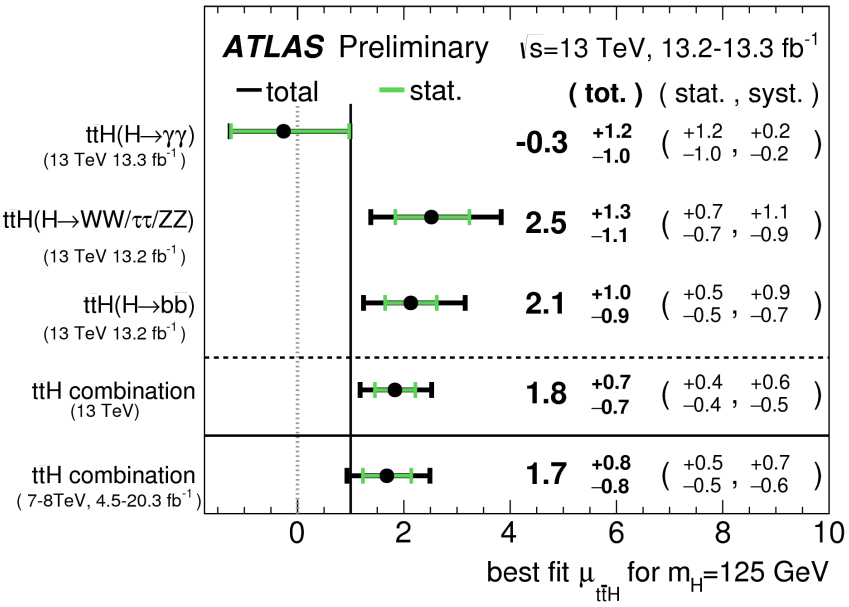

Figure 7.14: Signal strength measurements in the individual channels and for the combination.

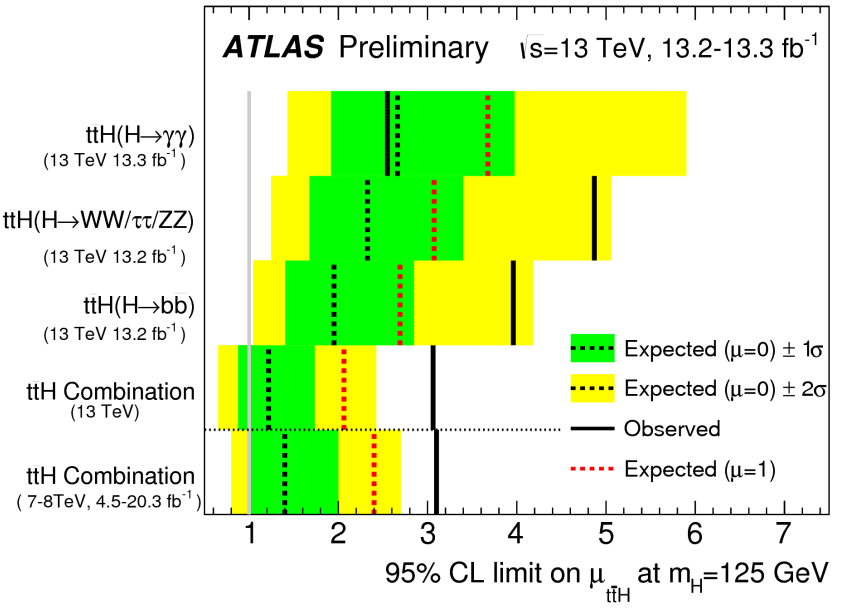

Figure 7.15: Summary of the of 95% CL upper limits on $\sigma(t\bar{t}H)$ relative to the SM prediction.

simplified systematic model used by CMS.

In summary, the analysis for the $t\bar{t}H$ process described in this dissertation is the most sensitive search to date in ATLAS and quite competitive with CMS.

7.6 Future improvements

As shown in this chapter, despite the use of MVA techniques, the kinematic reconstruction of the $t\bar{t}H$ system remains challenging due to the high combinatorial background. With higher luminosities since only a small fraction of $t\bar{t}H$ events have the top and Higgs bosons with sufficiently high momentum, the boosted regime can improve significantly the signal-to-background ratio and give the possibility to reconstruct the Higgs-boson candidate. In the boosted regime, the two b-quarks from the Higgs-boson decay will have small angular separation and would be reconstructed as a single jet (see figure 7.16), whose mass would peak at the correct Higgs-boson mass.

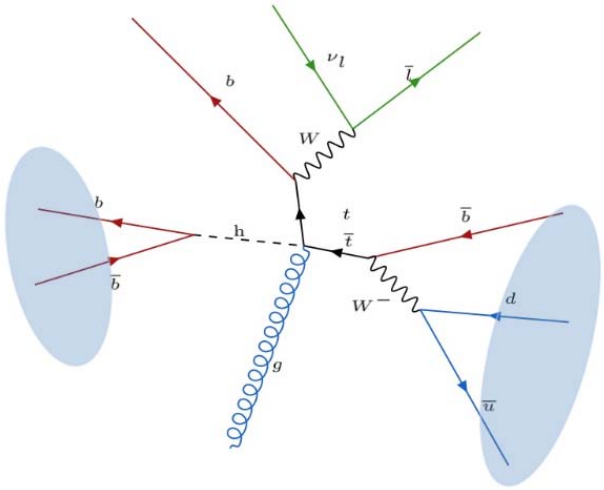

Figure 7.16: Sketch of boosted $t\bar{t}H$ event in which the Higgs and the hadronic top are reconstructed as large-R jets. From Ref. [254].

In recent publications [254] it is highlighted that the application of these techniques to the $t\bar{t}H$ search will represent a major improvement in sensitivity, allowing the observation of the Higgs boson in this production mode, as well as the most precise measurement of the top-Higgs Yukawa coupling. The boosted scenario can help as well in measuring the Higgs-boson p_{T} distribution in $t\bar{t}H$ production, which is one of the main probes for a CP-odd component in the top-Higgs interaction [255]. Boosted techniques in the associated $t\bar{t}$ production mode can be exploited as well to perform searches of light scalars ($<$100 GeV) decaying to $b\bar{b}$ at the LHC (see Appendix A).

In the context of the inclusive search, the use of jet-flavour information by exploiting the shape of the MV2c10 variable (referred to as "continuous b-tagging"), as well as adding kinematic information via sophisticated techniques such as the Matrix Element method, will further improve the discriminating power of the classification BDT. Finally, as already discussed in section 6.9, a reduced modelling uncertainties of the $t\bar{t}$+jets background through higher-order calculations (MEPS@NLO) and validated with data measurements will allow a reduction in the systematic uncertainties for the main background, further boosting the sensitivity of this search.

Conclusions

In this dissertation searches for new phenomena involving top quarks and Higgs bosons, with $H \to b\bar{b}$, were presented using 13.2 fb^{-1} of pp collision data at $\sqrt{s} = 13$ TeV, recorded with the ATLAS detector at the LHC. The top quark, together with the Higgs boson, via their special relationship through the large Yukawa coupling ($y_t \sim 1$), is a perfect tool to probe several BSM scenarios addressing some of the shortcomings of the SM. One of the main challenges for the analyses presented is the precise modelling of the main background, $t\bar{t}+ \geq 1b$ processes, for which no suitable differential measurements are available yet. These analyses required the developments of an improved description of the $t\bar{t}+ \geq 1b$ process through the implementation of state-of-art MC predictions and a sophisticated model of systematic uncertainties, although this still constitutes the main source of sensitivity degradation. Both analyses presented used a profile likelihood fit exploiting high-statistics control regions to improve the background modelling and reduce the impact of the leading sources of systematic uncertainty.

The first analysis presented searched for a variety of signals, including the pair production of a vector-like top quark (T) with a significant branching ratio to a top quark and either a SM Higgs boson or a Z boson; four-top-quark production, both within the SM and in several new physics scenarios; and heavy Higgs bosons (neutral and charged) produced in association with, and decaying into, third generation quarks. The data was analysed in the lepton-plus-jets final state (1-lepton channel) as well as, for the first time, in the jets+$E_{\mathrm{T}}^{\mathrm{miss}}$ final state (0-lepton chennel), characterised by multiple jets and large missing transverse momentum providing a very sensitive and complementary channel. This search profited from the increase in centre-of-mass energy exploiting the high scalar sum of transverse momenta of all final state objects, and the presence of boosted, hadronically-decaying resonances reconstructed as large-radius jets. No excess over the background expectation was found and 95% CL upper limits were derived for the different signal benchmark scenarios considered, which are summarised below.

For a vector-like singlet (doublet) T-quark, a mass below 1020 (1160) GeV is excluded. More generally, a vector-like top partner with a mass below 810 GeV is excluded for any value of the branching ratios into the three decay modes considered. The 1-lepton channel is also used to set limits on four-top-quark production in different signal benchmark scenarios and on heavy Higgs-boson associated production. In the case of four-top-quark production, a cross section of 15 times the SM prediction is excluded. In the scenario of $t\bar{t}t\bar{t}$ production via an EFT model, a cross section of 51 fb is excluded, which translates into $|C_{4t}|/\Lambda^2 < 2.9$ TeV^{-2}. Finally, within the 2UED/RPP model m_{KK} masses below 1.6 TeV are excluded. In the context of a 2HDM within the alignment limit, the $t\bar{t}H(H \to t\bar{t})$ search excludes $\tan\beta$ values below 0.17 (0.11) for $m_H = 400$ GeV (1 TeV), the $b\bar{b}H(H \to t\bar{t})$ search has insufficient sensitivity to exclude any region of $\tan\beta$, and the $\bar{t}bH^+(H^+ \to t\bar{b})$ search excludes $\tan\beta$ values below 0.65 (0.15) for $m_H = 200$ GeV (1 TeV). In summary, this represents the most sensitive search to date for the well-motivated singlet and doublet vector-like top quark scenarios, providing also the widest coverage in the branching ratio plane, and also the most restrictive bounds on BSM $t\bar{t}t\bar{t}$ production.

The second analysis presented aims to measure the cross-section for production of the SM Higgs boson in association with a pair of top quarks, from which the top-quark Yukawa coupling can be extracted. Boosted decision trees are employed to reconstruct the event and to discriminate the $t\bar{t}H$ signal from the background. No evidence for the $t\bar{t}H$ process was found, and 95% CL upper limits on the production cross section are set at 3.6 times the SM prediction. Performing a signal-plus-background fit the signal strength is measured to be $\mu = 1.6 \pm 1.1$. The combination with the dileptonic channel excludes a signal cross section 4.0 times larger than the SM prediction and yields a best-fit value of $\mu = 2.1^{+1.0}_{-0.9}$. This search is one of the most sensitive to date and has already exceeded the Run 1 sensitivity.

For all analyses presented in this dissertation a number of future improvements have been identified that should help extend the reach of the BSM searches and aid towards the eventual observation of the $t\bar{t}H$ production mode. At the time of the writing of this dissertation the ATLAS detector has already collected 36 fb^{-1} at $\sqrt{s} = 13$ TeV and in the next two years the LHC will deliver pp collisions at the design luminosity providing roughly ten times more data than analysed in this dissertation. Building on the analysis strategies developed in this dissertation, searches involving top quarks and Higgs boson at the energy frontier will continue to play an important role in providing new insights that may reveal the secrets of the Universe.

The effort to understand the universe
is one of the very few things that lifts
human life a little above the level of farce,
and gives it some of the grace of tragedy.
S. Weinberg

Appendices

A

Light CP-odd scalar search in top-quark pair associated production at the LHC

Contents

This chapter presents the feasibility of a search at the LHC for a light ($m_A \leq 100$ GeV) CP-odd scalar produced with a top-quark pair and subsequent decay into $b\bar{b}$ pair. CP-odd scalars are introduced in several SM extensions, e.g. Supersymmetry or a general N Higgs Doublet Model, and they are natural candidates for dark matter. For example, in the context of Coy Dark Matter models [256–258], CP-odd scalars are used as mediators between dark matter and SM particles to explain the diffuse gamma-ray excess from the Galactic Centre [259–262]. Their elusive nature because of the absence of direct coupling to gauge bosons, reflects in weak constraints from direct searches [263–265] on the mass of CP-odd scalars, so that light scalars with $m_A \geq 5$ GeV are still allowed. This search targets the lepton+jets $t\bar{t}$ final state. A brief description of the simplified-model approach used to generate the signal samples is presented, as well as the simulated and the event reconstruction. A novel analysis strategy to target this final state, the results obtained and their interpretation in the context of 2HDM and NMSSM models is also discussed. This study was published in [266].

A.1 Signal and background modelling

All samples, assuming pp collisions at $\sqrt{s} = 14$ TeV, are generated at LO in QCD using MADGRAPH5 2.1.1 with the CTEQ6L1 PDF set, and interfaced with the PYTHIA v6.427 parton shower and the Perugia2011C UE tune. The top-quark mass is set to 172 GeV and top-quark decay is performed by PYTHIA, as for W/Z-boson and Higgs-boson decays.

A.1.1 Signal modelling

In this search the coupling of the CP-odd scalar (referred to as "A boson") with the bottom and top quarks are added in the SM Lagrangian using a simplified-model approach:

$$\mathcal{L} = \mathcal{L}_{\text{SM}} + \mathcal{L}_{\text{CP-odd}}, \tag{A.1}$$

where

$$\mathcal{L}_{CP-odd} = i\frac{g_t y_t}{\sqrt{2}}\bar{t}\gamma_5 tA + i\frac{g_b y_b}{\sqrt{2}}\bar{b}\gamma_5 bA, \tag{A.2}$$

and g_i $(i = t, b)$ represents the deviation from the SM Yukawa coupling $y_i = m_i/v$. In this simplified approach, for $m_b < m_A < m_t$ the A boson decays exclusively into bottom quarks with BR$(A \to b\bar{b}) = 1$. The decay width, Γ_A, is determined by the value of g_b and the event kinematic distributions, with assumption of a narrow width, do not depend on its value. This model was implemented using FeynRules 2.1 [267] and imported as UFO model in Madgraph5. Samples of $t\bar{t}A$ events were generated for different A-boson masses, m_A=20, 30, 40, 60, 80 and 100 GeV, assuming $g_t = 1$.

A k-factor of 1.3, obtained as the ratio of the NLO to LO cross sections for $t\bar{t}h$ production, where h is a CP-even Higgs boson, is applied to the LO $t\bar{t}A$ signal cross section predicted by Madgraph5. It has been checked that this k-factor is rather constant as a function of m_h, varied between 20 and 125 GeV. The extra γ_5 factor present in the interaction between the CP-odd scalar and the top quark, compared to the case of a CP-even scalar, leads to two interesting features:

- a CP-odd scalar, at low mass, has harder p_{T} spectrum compared to a CP-even scalar (see figure A.1a), and
- the ratio $\sigma_{t\bar{t}h}/\sigma_{t\bar{t}A}$ varies significantly with mass, from about a factor of 20 at a mass of 20 GeV to only about a factor of two at a mass of 120 GeV (see figure A.1b).

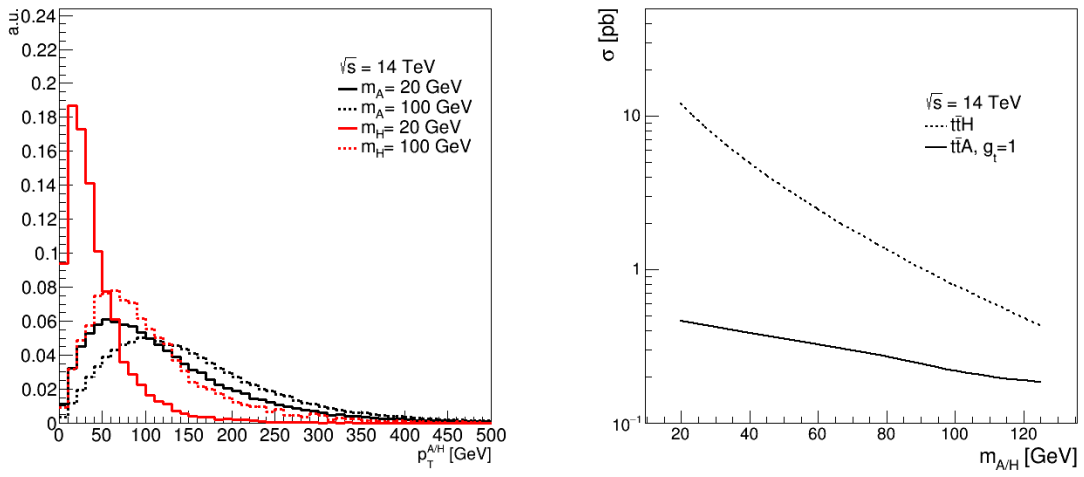

(a) (b)

Figure A.1: (a) Higgs-boson p_{T} distribution for $t\bar{t}h$ (red) and $t\bar{t}A$ (black) for two different mass hypotheses: 20 GeV (solid) and 100 GeV (dashed). (b) Comparison of the LO cross section for $t\bar{t}h$ (solid line) and $t\bar{t}A$ (dashed line) in pp collisions at $\sqrt{s}$= 14 TeV as a function of Higgs-boson mass. In both cases a value of $g_t = 1$ is assumed.

A.1.2 Background modelling

A sample of $t\bar{t}$+jets events is generated with up to two additional partons in the matrix element in the 5F scheme, and matched to the parton shower using the MLM prescription. The sample is normalized to to a cross section of 900 pb, computed at NNLO+NNLL cross section from TOP++ v2.0. The same procedure described in section 5.2.1 is used to categorise events according to the flavour content of extra jets in: $t\bar{t}$+light-jets, $t\bar{t}+\geq 1c$ and $t\bar{t}+\geq 1b$ (the latter two components together are usually referred as $t\bar{t}$+HF).

A sample of $t\bar{t}W$ events is generated requiring at least one W boson in the event to decay leptonically, and is normalised to the corresponding LO cross section, 0.404 pb, times a k-factor of 1.4.
A sample of $t\bar{t}Z$ events is generated requiring $Z \to q\bar{q}$ decays and is normalised to the corresponding LO cross section, 0.353 pb, times a k-factor of 1.3.
Finally, a sample of $t\bar{t}H$ events, with H being the SM Higgs boson, is generated assuming $m_H = 125$ GeVand requiring $H \to b\bar{b}$ decays. It is normalised to the NLO cross section, 0.611 pb, times the $H \to b\bar{b}$ branching ratio of 57.7%.

A.2 Experimental analysis

A.2.1 Event reconstruction

For this analysis a simplified simulation of detector response and object reconstruction is used. Objects are required not to overlap with each other. Leptons (electron and muons) are required to originate from a W-boson or τ-lepton decay and to have $p_{\mathrm{T}} > 25$ GeVand $|\eta| < 2.5$. To mimic the typical performance of an LHC detector, a reconstruction efficiency of 80% is assumed. A simplified simulation of a calorimeter is used to build jets. The four momenta of stable particles, except muons and neutrinos, falling within the same window in $\eta - \phi$ space of size $\Delta\eta \times \Delta\phi = 0.1 \times 0.1$ are added together to simulate the granularity of calorimeter cells. For each cell, the total three momentum is rescaled such as to make the cell massless. Cells with energy larger than 0.1 GeV and $|\eta| < 5.0$ become the inputs to the jet algorithm. Four jets collections are considered in this analysis. All jets contained in the four collections are required to satisfy $|\eta| < 2.5$. For those collections a semi-muonic energy correction is applied to recover the significant fraction of energy carried away by muons in b-hadron decays. This correction adds to to the calorimeter jet four momentum the four momenta of all reconstructed muons with $p_{\mathrm{T}} > 4$ GeV that are ghost-associated to a jet.

Two jet collections are built using the anti-k_T algorithm with two different radius paramenter, R=0.2 and R=0.4, referred to as AKT2 and AKT4 jets respectively. A minimum p_{T} requirement of 15 and 25 GeV is made for AKT2 and AKT4 respectively. AKT4 jets are used to define the jet multiplicity of the event, while AKT2 are chosen to define the b-tag multiplicity of the event since at low m_A values the b-quarks from the $A \to b\bar{b}$ decay emerge with small angular separation (see figure A.2). Heavy-flavour tagging is modelled in a probabilistic fashion by assigning a per-jet efficiency of 70% to b-jets, 20% to c-jets, and 0.7% to light jets. AKT2 jets are labelled as b-jet or c-jet if they are matched respectively to a b-hadron or a c-hadron (not originating from a b-hadron decay) within $\Delta R = 0.15$. The rest of the jets are taken to originate from the fragmentation of a light quark or gluon and are labelled as "light jets".

The other two jet collections are reconstructed with the Cambridge-Aachen (C/A) algorithm, which corresponds to the choice of $p = 0$ in the formulas 4.3 and 4.4. This algorithm clusters particles based exclusively on the spatial separation. The C/A algorithm is capable of discerning the components closest to the hard jet; it is therefore well-suited to discriminating softer subjets within harder jets.

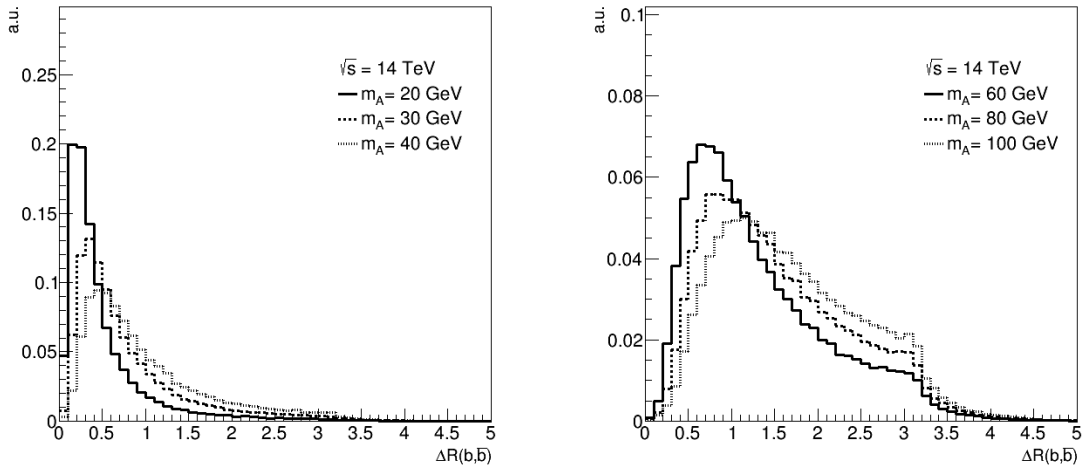

(a) (b)

Figure A.2: Distribution of ΔR between the two b-quarks from the $A \to b\bar{b}$ decay prior to any selection requirements, for different values of m_A: (a) m_A= 20, 30 and 40 GeV, and (b) m_A= 60, 80 and 100 GeV.

Thus, C/A jets are used to reconstruct the $A \to b\bar{b}$ decay, taking advantage of the boost with which A bosons are produced in the $t\bar{t}A$ process. Two radius parameters, R=0.6 and R=0.8 (referred to as CA6 and CA8 respectively), are chosen in order to optimise the reconstruction of the A boson depending on the value of the mass m_A. In order to minimise the impact of soft radiation and pileup (not modelled in this analysis), the mass-drop (a.k.a. BDRS) filtering algorithm [ref] with the following parameters, $\mu_{\text{frac}} = 0.67$ and $y_{\text{cut}} = 0.09$ is applied to the reconstructed C/A jets.

A.2.2 Analysis strategy

The final-state signature is characterised by one electron or muon and high jet and b-tag multiplicities. Therefore, events are required to satisfy the following requirements, referred to as "preselection": one electron or muon, $\geq$ 5 AKT4 jets and $\geq$ 3 AKT2 b-tagged jets (referred to as $\geq$5j, $\geq$3b). After the preselection $t\bar{t}$+jets is the dominant background. Following a similar strategy to those described in chapters 6 and 7, the events are categorised in two exclusive regions based on the number of b-tagged jets (3 and $\geq$4) in order to take advantage of the higher b-jet multiplicity of the signal process.

The $\geq$ 5j, $\geq$4b region is dominated by $t\bar{t}$+HF-jets events but it has the largest signal-to-background ratio and thus drives the sensitivity of the search. The $\geq$ 5j, 3b region instead has significantly lower signal-to-background ratio and the background is enriched in $t\bar{t}$+light-jets. The simultaneous analysis of both channels gives the possibility to measure in-situ the $t\bar{t}$+jets background (including its heavy-flavour content) and constrain the related systematic uncertainties.

After event categorisation this analysis, compared to the $t\bar{t}H$ search described in chapter 7, can make use of the boost of the A boson to further suppress the background. The two b-jets from the A-boson decay are collimated, particularly at low m_A mass, and can be reconstructed into a single fat jet, whose mass distribution would show a resonant structure peaked at the correct m_A value. Therefore, events are required to have at least one C/A BDRS-filtered jet with radius parameter R^{CA} and minimum p_{T} depending on the m_A hypothesis being tested. CA6 jets are used for $m_A < 40$ GeV, while CA8 jets are used for higher m_A values (up to 100 GeV). The minimum p_{T} requirements on the C/A jets are 60, 100, 120, 150, 200, and 250 GeV for m_A = 20, 30, 40, 60, 80, and 100 GeV, respectively.

The number of b-tags inside the C/A jet is determined by matching the b-tagged AKT2 jets within a cone of radius $R = 0.75R^{CA}$. Finally, it is required that the C/A jets have ≥ 2 b-tags inside. In case of more than one selected C/A jet, the leading p_{T} one is chosen. The final discriminating variable is the invariant mass of the selected C/A jet, referred to as "leading BDRS jet mass", shown in figure A.3 for signal and background in each of the analysis channels, for two different values of m_A.

The expected yields for signal and the SM backgrounds per fb^{-1} of integrated luminosity as a function of the selection cuts in the two analysis regions, ((5j, 3b), (≥5j, ≥4b)), are presented in table A.1.

	$t\bar{t}$+≥1b	$t\bar{t}$+≥1c	$t\bar{t}$+light-jets	$t\bar{t}+X$	Total bkg.	$t\bar{t}A$
$m_A = 30$ GeV						
1 lepton	4167	10958	155648	299	171072	377
≥5 jets	3109	7678	61866	215	72868	268
3 b-tags	766	765	2702	30.1	4263	72.4
≥1 CA6 jets	510	502	1485	21.4	2518	55.7
≥2 b-tags in selected CA6 jet	45.1	38.4	159	1.9	**245**	**14.6**
≥4 b-tags	234	100	128	10.6	474	28.7
≥1 CA6 jets	171	70.1	75.7	7.9	325	23.8
≥2 b-tags in selected CA6 jet	36.9	13.2	18.5	1.5	**70.2**	**11.7**
$m_A = 80$ GeV						
1 lepton	4167	10958	155648	299	171072	240
≥5 jets	3109	7678	61866	215	72868	198
3 b-tags	766	765	2702	30.1	4263	57.5
≥1 CA8 jets	252	246	646	11.5	1155	23.6
≥2 b-tags in selected CA8 jet	32.3	32.8	125	2.0	**192**	**6.1**
≥4 b-tags	234	100	128	10.6	474	25.0
≥1 CA8 jets	91.6	36.4	35.0	4.3	167	11.6
≥2 b-tags in selected CA8 jet	25.8	10.6	12.6	1.5	**50.4**	**5.3**

Table A.1: Expected signal and SM backgrounds at $\sqrt{s} = 14$ TeV per fb^{-1} of integrated luminosity as a function of the selection cuts applied in each of the analysis channels under consideration (see text for details): (≥5j, 3b) and (≥5j, ≥4b). The signal prediction is obtained under the assumptions of $g_t = 2$ and BR($A \to b\bar{b}$) = 1. Several background categories have been merged for readability. The sum of $t\bar{t}W$, $t\bar{t}Z$ and $t\bar{t}H$ is denoted as $t\bar{t}+X$. The yields shown correspond to the optimised selections for two different values of m_A, 30 GeV and 80 GeV. Shown in bold are the signal and backgrounds expectations after full selection in each of the analysis channels considered.

A.2.3 Systematic uncertainties

Several sources of systematic uncertainty are considered:

- $t\bar{t}$+light-jets normalisation uncertainty of 15% corresponding to the modelling of the jet multiplicity spectrum;
- $t\bar{t}$+HF-jets normalisation uncertainty of 30% uncorrelated across $t\bar{t}+b$, $t\bar{t}+b\bar{b}$, $t\bar{t}+B$, $t\bar{t}+c$, $t\bar{t}+c\bar{c}$, and $t\bar{t}+C$ components;
- $t\bar{t}+X$ normalisation uncertainty of 30% uncorrelated across $t\bar{t}W$, $t\bar{t}Z$, and $t\bar{t}H$ processes;
- uncertainties associated to jet energy and mass calibration are taken to be 5% per jet, fully correlated between energy and mass and across all jets;

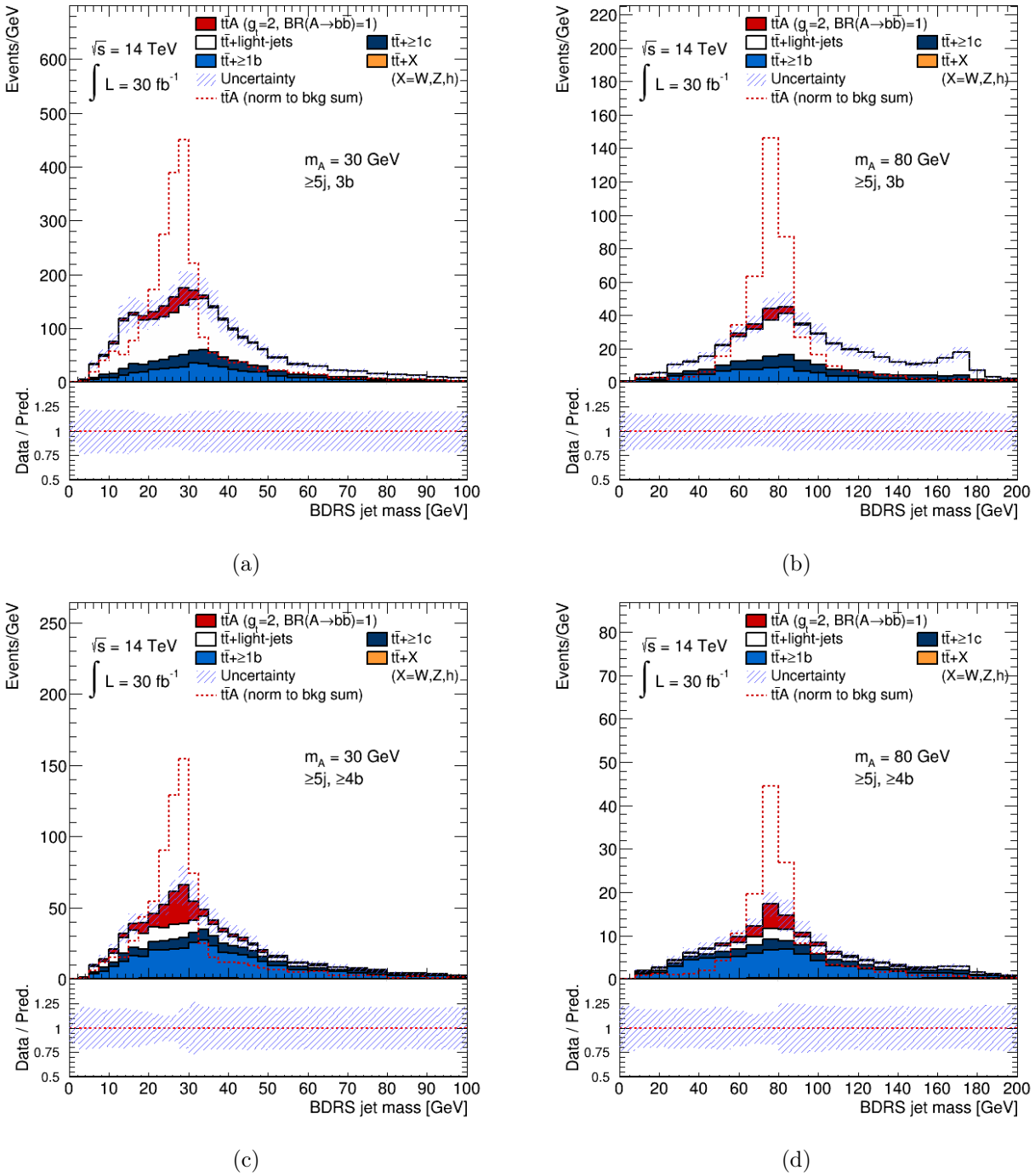

Figure A.3: Distribution of the leading BDRS jet mass in the two analysis channels considered after final selection: (top) ($\geq$ 5j, 3b) and (bottom) ($\geq$ 5j, $\geq$ 4b), for different values of m_A (30 and 80 GeV). The prediction corresponds to $\sqrt{s} = 14$ TeV and an integrated luminosity of 30 fb^{-1}. Contributions from $t\bar{t}W$, $t\bar{t}Z$ and $t\bar{t}H$ have been merged for visibility. The expected contribution from the $t\bar{t}A$ signal under the assumptions of $g_t = 2$ and BR($A \to b\bar{b}$) = 1 is also shown (red histogram), stacked on top of the SM background. The dashed red line shows the $t\bar{t}A$ signal distribution normalised to the background yield to better compare the shape to that of the background. The bottom panel displays the expected total systematic uncertainty on the total prediction prior to the fit to the pseudo-data

- uncertainties on the b-, c- and light-jet tagging efficiencies are taken to be 3%, 6% and 15% respectively, uncorrelated between b-jets, c-jets, and light-jets.

The resulting total background normalisation uncertainty is about 20%, although the different uncertainty components have different shape in the final distribution, as can be seen in figure A.3.

A.3 Limits on a light CP-odd scalar

For different values of the integrated luminosity, 95% CL upper limits on the $t\bar{t}A$ production cross section times branching ratio, $\sigma(t\bar{t}A) \times \mathrm{BR}(A \to b\bar{b})$, as a function of m_A (see figure A.4) are set using the CL_s method. Those limits can be translated onto upper limits on $|g_t|$ assuming $\mathrm{BR}(A \to b\bar{b}) = 1$, as shown in table A.2. This search can exclude a CP-odd scalar that couples with $g_t = 1$ for $20 \leq m_A \leq 90$ GeV with 30 fb^{-1} (the ATLAS detector in Run 2 has already collected 36.2 fb^{-1}); the scenario with 300 fb^{-1} can exclude a coupling g_t of order 0.5 in the mass range between 30 and 90 GeV.

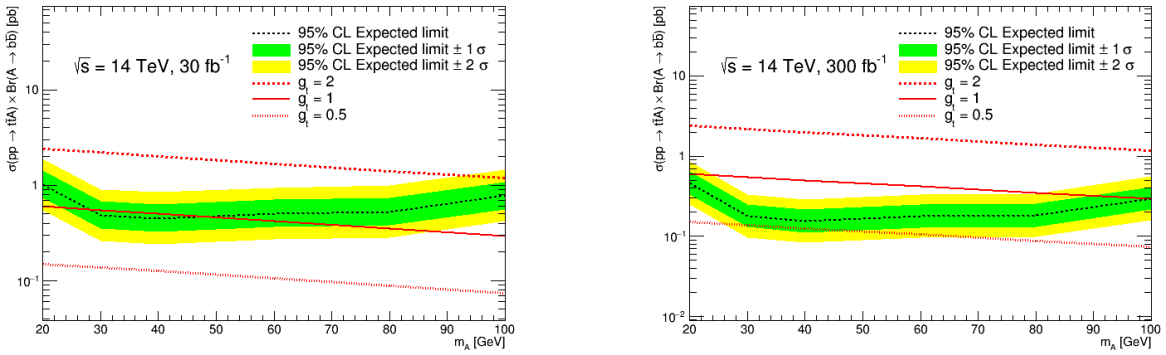

(a) (b)

Figure A.4: Expected 95% CL upper limits on $\sigma(t\bar{t}A) \times \mathrm{BR}(A \to b\bar{b})$ as a function of m_A in pp collisions at $\sqrt{s}$= 14 TeV for an integrated luminosity of (a) 30 fb^{-1} and (b) 300 fb^{-1}. The green and yellow bands correspond to 1 and 2 standard deviations respectively around the median expected limit under the background-only hypothesis. Also shown are the theoretical cross sections for $\sigma(t\bar{t}A)$ for different assumed values of g_t (0.5, 1.0, and 2.0) and $\mathrm{BR}(A \to b\bar{b}) = 1$.

	95% CL upper limits on $\sigma(t\bar{t}A) \times \mathrm{BR}(A \to b\bar{b})$ (pb)					
	m_A (GeV)					
$\mathcal{L}$ (fb^{-1})	20	30	40	60	80	100
30	1.02	0.48	0.45	0.51	0.53	0.78
300	0.46	0.18	0.16	0.18	0.18	0.30
3000	0.17	0.066	0.057	0.065	0.065	0.13

Table A.2: Expected 95% CL upper limits on $\sigma(t\bar{t}A) \times \mathrm{BR}(A \to b\bar{b})$ as a function of m_A in pp collisions at $\sqrt{s} = 14$ TeV for different integrated luminosities.

A.3.1 Interpretation of the limits

A light CP-odd Higgs boson ($m_A < 125$ GeV), which may or may not be related to global symmetries being present, exists in many extensions of the SM. This search is interpreted in several representative

BSM scenarios.

In the context of Type-I and Type-II 2HDM models, the $g_{t\bar{t}A}$ coupling is $\cot\beta$ enhanced and it can cover regions with $\tan\beta < 5$. The limits in the m_A vs. $\tan\beta$ plane are presented for this search and for a search that targets $b\bar{b}A$ production [268] in figure A.5. For a Type-I 2HDM, where both couplings are $\cot\beta$ enhanced, the $t\bar{t}A$ has a better sensitivity. Instead, for a Type-II 2HDM the $g_{b\bar{b}A}$ coupling is $\tan\beta$ enhanced and it leads to a complementarity of the two analysis on the plane, which can cover the whole parameter region except a corner with relatively large m_A and moderate $\tan\beta$. As shown in figure A.5 the green region of the plane, which can explain the gamma-ray excess in the Galactic Centre, can be effectively probed by the proposed $t\bar{t}A$ search.

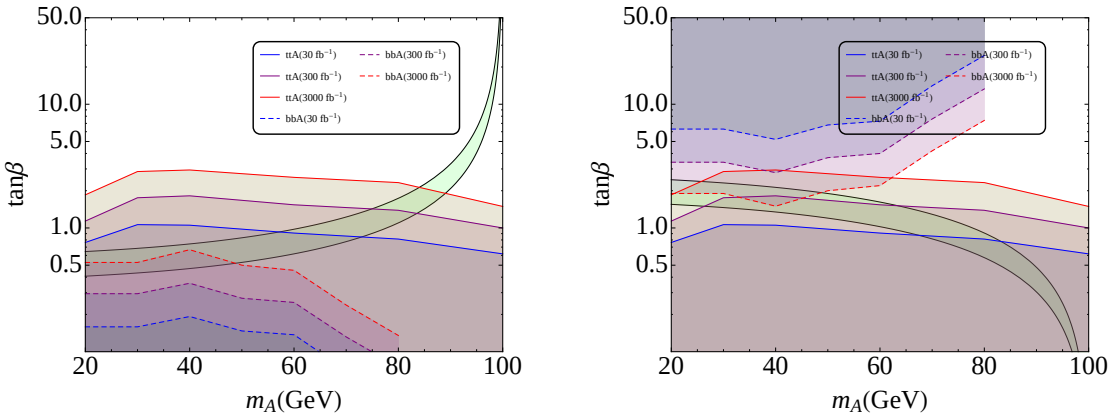

(a) (b)

Figure A.5: Sensitivity reach (at 95% CL) of the $b\bar{b}A$ and $t\bar{t}A$ channels within the (a) type-I 2HDM and (b) type-II 2HDM. The green bands represent a region where the recently observed gamma-ray excess from the Galactic Centre can be explained.

In the context of the NMSSM in the R-limit [269] and in the PQ-limit [270] this $t\bar{t}A$ search has very little sensitivity even at luminosity of 3 ab^{-1}, as shown in figure A.6.

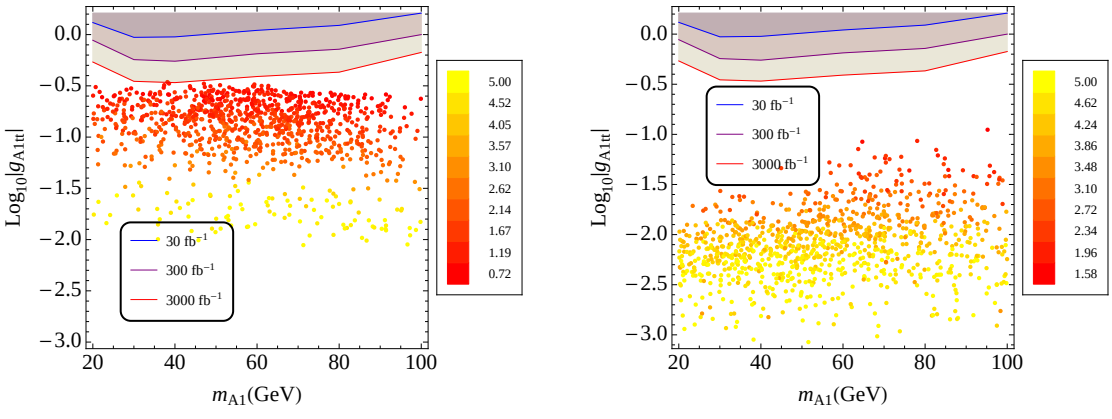

(a) (b)

Figure A.6: Sensitivity reach (at 95% CL) to the (a) R-limit and (b) PQ-limit scenarios in the NMSSM via the $t\bar{t}A$. The hue of the scatter points represents the corresponding $\tan\beta$ values.

B
Glossary

This glossary describes the naming of nuisance parameters corresponding to various systematic uncertainties in the fit output. Whenever two names are provided for a given uncertainty, separated by *or*, the first (second) name corresponds to that used in the search discussed in chapter 6 (chapter 7).

- Luminosity: Luminosity
- Pileup: Pile-up uncertainty *or* pileup modelling
- Electron:
  - identification: Electron ID *or* Electron ID efficiency
  - reconstruction: Electron reco.
  - isolation: Electron isol.
  - energy scale: Electron E_T scale *or* Electron energy scale
  - energy resolution: Electron E_T resolution *or* Electron energy resolution
  - trigger: Electron trig. eff.
- Muon:
  - identification: Muon ID (stat.), Muon ID (syst.)
  - reconstruction: Muon TTVA (stat.), Muon TTVA (syst.)
  - isolation: Muon Isol. (stat.), Muon (syst.)
  - momentum scale: Muon p_{T} scale
  - resolution in the tracker: Muon ID p_{T} res. *or* Muon energy resolution (ID)
  - resolution in the muon system: Muon MS p_{T} res *or* Muon energy resolution (MS)
  - trigger: Muon Trig. (stat.), Muon ID (syst.)
- Jet vertex tagger: JVT uncertainty *or* Jet vertex tagger efficiency
- Jet energy scale:
  17 independent components: Effective NP1 *or* JES effective NP 1, Effective NP2 *or* JES effective NP 2, Effective NP3 *or* JES effective NP 3, Effective NP4 *or* JES effective NP 4, Effective NP5 *or* JES effective NP 5, Effective NP6 *or* JES effective NP 6, η intercalib. (stat.) *or* JES η intercalibration total stat., η intercalib. (model) *or* JES η intercalibration modelling, η intercalib. (non-clos.) *or* JES η intercalibration non-closure, Flavour composition *or* JES flavour composition, Flavour response *or* JES flavour response, Pile-up offset mu term *or* JES

pileup offset μ, Pile-up offset NPV term *or* JES pileup offset NPV, Pile-up offset p_{T} term *or* JES pileup offset pT term, ρ topology *or* JES pileup ρ topology, bJES response *or* JES BJES, Punch-through correction

- Jet energy resolution: JER *or* Jet energy resolution
- Missing transverse momentum:
  - Soft term energy scale: MET TST scale
  - Soft term resolution: MET TST reso. para. *or* MET soft. reso (para.), MET TST reso. perp. *or* MET soft. reso (perp.)
- b-tagging uncertainties:
  5 eigenvectors corresponding to b-jet p_{T} bins ordered from the largest to the smallest: b-tag (B) EV1 *or* b-tag Eigenvar. 0, b-tag (B) EV2 *or* b-tag Eigenvar. 1, b-tag (B) EV3 *or* b-tag Eigenvar. 2, b-tag (B) EV4 *or* b-tag Eigenvar. 3, b-tag (B) EV5 *or* b-tag Eigenvar. 4
- c-tagging uncertainties:
  4 eigenvectors corresponding to c-jet p_{T} bins ordered from the largest to the smallest: b-tag (C) EV1 *or* c-tag Eigenvar. 0, b-tag (C) EV2 *or* c-tag Eigenvar. 1, b-tag (C) EV3 *or* c-tag Eigenvar. 2, b-tag (C) EV4 *or* c-tag Eigenvar. 3
- light-tagging uncertainties:
  14 eigenvectors corresponding to 7 light-jet p_T bins and two jet η regions ordered from the largest to the smallest: b-tag (L) EV1 *or* l-tag Eigenvar. 0, b-tag (L) EV2 *or* l-tag Eigenvar. 1, b-tag (L) EV3 *or* l-tag Eigenvar. 2, b-tag (L) EV4 *or* l-tag Eigenvar. 3, b-tag (L) EV5 *or* l-tag Eigenvar. 4, b-tag (L) EV6 *or* l-tag Eigenvar. 5, b-tag (L) EV7 *or* l-tag Eigenvar. 6, b-tag (L) EV8 *or* l-tag Eigenvar. 7, b-tag (L) EV9 *or* l-tag Eigenvar. 8, b-tag (L) EV10 *or* l-tag Eigenvar. 9, b-tag (L) EV11 *or* l-tag Eigenvar. 10, b-tag (L) EV12 *or* l-tag Eigenvar. 11, b-tag (L) EV13 *or* l-tag Eigenvar. 12, b-tag (L) EV14 *or* l-tag Eigenvar. 13
- high-p_{T} extrapolation uncertainty for b-, c- and light-tagging: b-tag extrap. *or* b-tag high pT extrap.
- τ-tagging extrapolation: b-tag extrap. from charm *or* b-tag $c \to \tau$ extrap.
- $t\bar{t}$ normalisation:
  - $t\bar{t}$ inclusive cross section: $t\bar{t}$ inclusive cross section *or* XS $t\bar{t}$ (inclusive)
  - $t\bar{t}+ \geq 1c$ normalisation: $t\bar{t}+ \geq 1c$ norm.
- $t\bar{t}$ and top p_{T} NNLO Rw:
  Uncertainties switching off the NNLO correction for $t\bar{t}$ and top p_{T} applied to MC:
  - For the search in chapter 6: $t\bar{t}$+light NNLO top-p_{T} correction, $t\bar{t}+ \geq 1c$ NNLO top-p_{T} correction.
  - For the search in chapter 7: $t\bar{t}$+light NNLO reweighting pT (tt), $t\bar{t}$+light NNLO reweighting pT (t), $t\bar{t}+ \geq 1c$ NNLO reweighting pT (tt), $t\bar{t}+ \geq 1c$ NNLO reweighting pT (t)
- $t\bar{t}$+light-jets modelling:
  - Radiation model: $t\bar{t}$+light rad. *or* $t\bar{t}$+light radiation

- Parton shower model: $t\bar{t}$+light parton shower *or* $t\bar{t}$+light PS & hadronisation
- Matrix element model: $t\bar{t}$+light generator *or* $t\bar{t}$+light NLO generator

- $t\bar{t}+ \geq 1c$-jets modelling:
  - Radiation model: $t\bar{t}+ \geq 1c$ rad. *or* $t\bar{t}+ \geq 1c$ radiation
  - Parton shower model: $t\bar{t}+ \geq 1c$ parton shower *or* $t\bar{t}+ \geq 1c$ PS & hadronisation
  - Matrix element model: $t\bar{t}+ \geq 1c$ generator *or* $t\bar{t}+ \geq 1c$ NLO generator
  - NLO modelling in MG5_aMC 3F sample: $t\bar{t}+ \geq 1c$ NLO reweighting
- $t\bar{t}+ \geq 1b$-jets modelling:
  - Radiation model: $t\bar{t}+ \geq 1b$ rad. (residual) *or* $t\bar{t}+ \geq 1b$ radiation (residual)
  - Parton shower model: $t\bar{t}+ \geq 1b$ parton shower (residual) *or* $t\bar{t}+ \geq 1b$ PS & had. (residual)
  - Matrix element model: $t\bar{t}+ \geq 1b$ generator (residual) *or* $t\bar{t}+ \geq 1b$ NLO gen. (residual)
  - NLO modelling in Sherpa 4F sample:
    - scale variations: $t\bar{t}+ \geq 1b$ scale *or* $t\bar{t}+ \geq 1b$ scale choice, $t\bar{t}+ \geq 1b$ glosoft *or* $t\bar{t}+ \geq 1b$ global scale, $t\bar{t}+ \geq 1b$ Q CMMPS *or* $t\bar{t}+ \geq 1b$ Q CMMPS
    - PDF uncertainties: $t\bar{t}+ \geq 1b$ NNPDF *or* $t\bar{t}+ \geq 1b$ NNPDF, $t\bar{t}+ \geq 1b$ MSTW *or* $t\bar{t}+ \geq 1b$ MSTW PDF
    - MPI modelling: $t\bar{t}+ \geq 1b$ MPI
    - UE modelling: $t\bar{t}+ \geq 1b$ UE modelling
  - NLO modelling in MG5_aMC 4F sample:
    - Parton shower model: $t\bar{t}+ \geq 1b$ PS (reweighting) *or* $t\bar{t}+ \geq 1b$ PS & had. (reweighting)
    - Matrix element model: $t\bar{t}+ \geq 1b$ GEN (reweightingl) *or* $t\bar{t}+ \geq 1b$ NLO gen. (reweighting)
- Small backgrounds:
  - Multijet uncertainty: QCD norm. *or* Fakes norm.
  - Diboson cross section uncertainty: Dibosons norm. *or* XS Diboson
  - W/Z+jets cross section uncertainty: V+bjets/cjets/jets norm. *or* W+jets/HF, Z+jets norm.
  - Single top cross section uncertainty:
    - For the search in chapter 6: Single-top norm.
    - For the search in chapter 7: Wt radiation, PS & hadronisation, diagram subtraction, XS single top (Wt), XS single top (t- & s-chan)
  - $t\bar{t}V$ cross section uncertainty: topEW norm. *or* XS ttZ QCD, XS ttZ PDF, ttZ generator, XS ttW QCD, XS ttW PDF, ttW generator
  - $t\bar{t}t\bar{t}$ cross section uncertainty: SM 4tops norm.
  - $t\bar{t}H$ modelling:
    - For the search in chapter 6 cross section uncertainty: $t\bar{t}H$ norm.
    - For the search in chapter 7 cross section uncertainty, scale choice, parton shower modelling, branching ratio, single tH: XS $t\bar{t}H$ QCD, XS $t\bar{t}H$ PDF, $t\bar{t}H$ scale choice (acceptance), $t\bar{t}H$ PS & hadronisation, BR($H \to bb$), BR($H \to WW$), BR($H \to other$), XS tHjb QCD, XS tHjbPDF, XS WtH QCD, XS WtH PDF

Bibliography

[1] S. Glashow, *Partial Symmetries of Weak Interactions*, Nucl. Phys. B **22** (1961) 579.

[2] S. Weinberg, *A Model of Leptons*, Phys. Rev. Lett. **19** (1967) 1264.

[3] A. Salam, *Gauge Unification of Fundamental Forces*, Rev. Mod. Phys. **52** (1980) 525.

[4] Particle Data Group Collaboration„ *Review of Particle Physics*, Chin. Phys. C **40** (2016) 100001.

[5] S. Bethke, G. Dissertori, and G. P. Salam, *World Summary of α_s (2015)*, EPJ Web Conf. **120** (2016) 07005.

[6] H. D. Politzer, *Reliable Perturbative Results for Strong Interactions?*, Phys. Rev. Lett. **30** (1973) 1346.

[7] D. J. Gross and F. Wilczek, *Ultraviolet Behavior of Nonabelian Gauge Theories*, Phys. Rev. Lett. **30** (1973) 1343.

[8] J. Maxwell, *A Treatise on Electricity and Magnetism*. Clarendon Press, 1873.

[9] W. Pauli, *Pauli letter collection: letter to Lise Meitner*, Handwritten copy.

[10] C. S. Wu, E. Ambler, R. W. Hayward, D. D. Hoppes, and R. P. Hudson, *Experimental Test of Parity Conservation in Beta Decay*, Phys. Rev. **105** (1957) 1413.

[11] L. Wolfenstein, *Violation of CP Invariance and the Possibility of Very Weak Interactions*, Phys. Rev. Lett. **13** (1964) 562.

[12] BaBar Collaboration„ *Observation of Time Reversal Violation in the B^0 Meson System*, Phys. Rev. Lett. **109** (2012) 211801, arXiv:1207.5832 [hep-ex].

[13] T. D. Lee and C. S. Wu, *Weak interactions*, Ann. Rev. Nucl. Part. Sci. **15** (1965) 381.

[14] N. Cabibbo, *Unitary Symmetry and Leptonic Decays*, Phys. Rev. Lett. **10** (1963) 531.

[15] M. Kobayashi and T. Maskawa, *CP Violation in the Renormalizable Theory of Weak Interaction*, Prog. Theor. Phys. **49** (1973) 652.

[16] F. Englert and R. Brout, *Broken Symmetry and the Mass of Gauge Vector Mesons*, Phys. Rev. Lett. **13** (1964) 321.

[17] P. W. Higgs, *Broken Symmetries and the Masses of Gauge Bosons*, Phys. Rev. Lett. **13** (1964) 508.

[18] J. Goldstone, A. Salam, and S. Weinberg, *Broken Symmetries*, Phys. Rev. **127** (1962) 965.

[19] LHC Higgs Cross Section Working Group, *Handbook of LHC Higgs Cross Sections: 1. Inclusive Observables*, arXiv:1101.0593 [hep-ph].

[20] Gargamelle Neutrino Collaboration„ *Observation of Neutrino Like Interactions Without Muon Or Electron in the Gargamelle Neutrino Experiment*, Phys. Lett. B **46** (1973) 138.

[21] SLAC Collaboration„ *Discovery of a Narrow Resonance in e^+e^- Annihilation*, Phys. Rev. Lett. **33** (1974) 1406.

[22] MIT Collaboration,, *Experimental Observation of a Heavy Particle J*, Phys. Rev. Lett. **33** (1974) 1404.

[23] S. Herb, D. Hom, L. Lederman, J. Sens, H. Snyder, et al., *Observation of a Dimuon Resonance at 9.5-GeV in 400-GeV Proton-Nucleus Collisions*, Phys. Rev. Lett. **39** (1977) 252.

[24] M. L. Perl, G. Abrams, A. Boyarski, M. Breidenbach, D. Briggs, et al., *Evidence for Anomalous Lepton Production in e+ - e- Annihilation*, Phys. Rev. Lett. **35** (1975) 1489.

[25] DONUT Collaboration,, *Observation of tau neutrino interactions*, Phys.Lett. B **504** (2001) 218, arXiv:hep-ex/0012035 [hep-ex].

[26] UA1 Collaboration,, *Experimental Observation of Isolated Large Transverse Energy Electrons with Associated Missing Energy at* $\sqrt{s} = 540$ *GeV*, Phys. Lett. B **122** (1983) 103.

[27] UA2 Collaboration,, *Observation of Single Isolated Electrons of High Transverse Momentum in Events with Missing Transverse Energy at the CERN anti-p p Collider*, Phys. Lett. B **122** (1983) 476.

[28] UA1 Collaboration,, *Experimental Observation of Lepton Pairs of Invariant Mass Around 95-GeV/c**2 at the CERN SPS Collider*, Phys. Lett. B **126** (1983) 398.

[29] UA2 Collaboration,, *Evidence for Z0 —> e+ e- at the CERN anti-p p Collider*, Phys. Lett. B **129** (1983) 130.

[30] CDF Collaboration,, *Observation of top quark production in* $\bar{p}p$ *collisions*, Phys. Rev. Lett. **74** (1995) 2626.

[31] D0 Collaboration,, *Observation of the top quark*, Phys. Rev. Lett. **74** (1995) 2632.

[32] ATLAS Collaboration,, *Observation of a new particle in the search for the Standard Model Higgs boson with the ATLAS detector at the LHC*, Phys. Lett. B **716** (2012) 1, arXiv:1207.7214 [hep-ex].

[33] CMS Collaboration,, *Observation of a new boson at a mass of 125 GeV with the CMS experiment at the LHC*, Phys. Lett. B **716** (2012) 30, arXiv:1207.7235 [hep-ex].

[34] ATLAS Collaboration and CMS Collaboration,, *Combined Measurement of the Higgs Boson Mass in pp Collisions at* $\sqrt{s} = 7$ *and 8 TeV with the ATLAS and CMS Experiments*, Phys. Rev. Lett. **114** (2015) 191803, arXiv:1503.07589 [hep-ex].

[35] ATLAS Collaboration,, *Evidence for the spin-0 nature of the Higgs boson using ATLAS data*, Phys. Lett. B **726** (2013) 120, arXiv:1307.1432 [hep-ex].

[36] CMS Collaboration,, *Constraints on the spin-parity and anomalous HVV couplings of the Higgs boson in proton collisions at 7 and 8 TeV*, Phys. Rev. D **92** (2015) 012004, arXiv:1411.3441 [hep-ex].

[37] ATLAS, CMS Collaboration,, *Measurements of the Higgs boson production and decay rates and constraints on its couplings from a combined ATLAS and CMS analysis of the LHC pp collision data at* $\sqrt{s} = 7$ *and 8 TeV*, JHEP **08** (2016) 045, arXiv:1606.02266 [hep-ex].

[38] M. Baak and R. Kogler, *The global electroweak Standard Model fit after the Higgs discovery*, arXiv:1306.0571 [hep-ph].

[39] A. D. Sakharov, *Violation of CP Invariance, c Asymmetry, and Baryon Asymmetry of the Universe*, Pisma Zh. Eksp. Teor. Fiz. **5** (1967) 32.

[40] K. Begeman, A. Broeils, and R. Sanders, *Extended rotation curves of spiral galaxies: Dark haloes and modified dynamics*, Mon. Not. Roy. Astron. Soc. **249** (1991) 523.

[41] Planck Collaboration,, *Planck 2013 results. XVI. Cosmological parameters*, Astron. Astrophys. **571** (2014) A16, arXiv:1303.5076 [astro-ph.CO].

[42] Super-Kamiokande Collaboration,, *Evidence for oscillation of atmospheric neutrinos*, Phys. Rev. Lett. **81** (1998) 1562, arXiv:hep-ex/9807003 [hep-ex].

[43] G. F. Giudice, *Naturally Speaking: The Naturalness Criterion and Physics at the LHC*, arXiv:0801.2562 [hep-ph].

[44] R. Haag, J. T. Lopuszanski, and M. Sohnius, *All Possible Generators of Supersymmetries of the S-Matrix*, **88** (1975) 257.

[45] M. Drees, *An Introduction to supersymmetry*, arXiv:hep-ph/9611409 [hep-ph].

[46] S. P. Martin, *A Supersymmetry primer*, Adv. Ser. Direct. High Energy Phys. **21** (2010) 1, arXiv:hep-ph/9709356 [hep-ph].

[47] E. Witten, *Dynamical Breaking of Supersymmetry*, **188** (1981) 513.

[48] G. C. Branco, P. M. Ferreira, L. Lavoura, M. N. Rebelo, M. Sher, and J. P. Silva, *Theory and phenomenology of two-Higgs-doublet models*, Phys. Rept. **516** (2012) 1, arXiv:1106.0034 [hep-ph].

[49] M. Trodden, *Electroweak baryogenesis: A Brief review*, arXiv:hep-ph/9805252 [hep-ph].

[50] D. Eriksson, J. Rathsman, and O. Stal, *2HDMC: Two-Higgs-Doublet Model Calculator Physics and Manual*, Comput. Phys. Commun. **181** (2010) 189, arXiv:0902.0851 [hep-ph].

[51] S. L. Glashow and S. Weinberg, *Natural Conservation Laws for Neutral Currents*, Phys. Rev. D **15** (1977) 1958.

[52] E. Ponton, *TASI 2011: Four Lectures on TeV Scale Extra Dimensions*, arXiv:1207.3827 [hep-ph].

[53] N. Arkani-Hamed, S. Dimopoulos, and G. Dvali, *The Hierarchy problem and new dimensions at a millimeter*, Phys. Lett. B **429** (1998) 263, arXiv:hep-ph/9803315 [hep-ph].

[54] ATLAS Collaboration,, *Search for new phenomena in final states with an energetic jet and large missing transverse momentum in pp collisions at $\sqrt{s}$=13 TeV using the ATLAS detector*, Phys. Rev. D **94** (2016) 032005, arXiv:1604.07773 [hep-ex].

[55] T. Appelquist, H.-C. Cheng, and B. A. Dobrescu, *Bounds on universal extra dimensions*, Phys. Rev. D **64** (2001) 035002, arXiv:hep-ph/0012100 [hep-ph].

[56] G. Burdman, B. A. Dobrescu, and E. Ponton, *Resonances from two universal extra dimensions*, Phys. Rev. D **74** (2006) 075008, arXiv:hep-ph/0601186.

[57] G. Cacciapaglia, A. Deandrea, and J. Llodra-Perez, *A Dark Matter candidate from Lorentz Invariance in 6D*, JHEP **1003** (2010) 083, arXiv:0907.4993 [hep-ph].

[58] L. Randall and R. Sundrum, *An Alternative to compactification*, Phys. Rev. Lett. **83** (1999) 4690, arXiv:hep-th/9906064 [hep-th].

[59] R. Contino, T. Kramer, M. Son, and R. Sundrum, *Warped/composite phenomenology simplified*, JHEP **0705** (2007) 074, arXiv:hep-ph/0612180 [hep-ph].

[60] L. Randall and R. Sundrum, *A Large mass hierarchy from a small extra dimension*, Phys. Rev. Lett. **83** (1999) 3370, arXiv:hep-ph/9905221 [hep-ph].

[61] K. Agashe, R. Contino, and A. Pomarol, *The Minimal composite Higgs model*, Nucl. Phys. B **719** (2005) 165, arXiv:hep-ph/0412089.

[62] D. B. Kaplan, H. Georgi, and S. Dimopoulos, *Composite Higgs scalars*, Phys. Lett. B **136** (1984) 187.

[63] H. S. Fukano, M. Kurachi, S. Matsuzaki, and K. Yamawaki, *Higgs boson as a top-mode pseudo-Nambu-Goldstone boson*, Phys. Rev. D **90** (2014) 055009, arXiv:1311.6629 [hep-ph].

[64] R. Contino, *The Higgs as a Composite Nambu-Goldstone Boson*, arXiv:1005.4269 [hep-ph].

[65] A. Pomarol and J. Serra, *Top Quark Compositeness: Feasibility and Implications*, Phys. Rev. D **78** (2008) 074026, arXiv:0806.3247 [hep-ph].

[66] B. Lillie, J. Shu, and T. M. Tait, *Top Compositeness at the Tevatron and LHC*, JHEP **0804** (2008) 087, arXiv:0712.3057 [hep-ph].

[67] K. Kumar, T. M. Tait, and R. Vega-Morales, *Manifestations of Top Compositeness at Colliders*, JHEP **0905** (2009) 022, arXiv:0901.3808 [hep-ph].

[68] J. Aguilar-Saavedra, R. Benbrik, S. Heinemeyer, and M. Perez-Victoria, *Handbook of vectorlike quarks: Mixing and single production*, Phys. Rev. D **88** (2013) 094010, arXiv:1306.0572 [hep-ph].

[69] Y. Okada and L. Panizzi, *LHC signatures of vector-like quarks*, Adv. High Energy Phys. **2013** (2013) 364936, arXiv:1207.5607 [hep-ph].

[70] J. Aguilar-Saavedra, *Mixing with vector-like quarks: constraints and expectations*, EPJ Web Conf. **60** (2013) 16012, arXiv:1306.4432 [hep-ph].

[71] J. A. Aguilar-Saavedra, *Identifying top partners at LHC*, JHEP **11** (2009) 030, arXiv:0907.3155 [hep-ph].

[72] F. del Aguila, J. A. Aguilar-Saavedra, and G. C. Branco, *CP violation from new quarks in the chiral limit*, **510** (1998) 39, arXiv:hep-ph/9703410 [hep-ph].

[73] D. Choudhury, T. M. P. Tait, and C. E. M. Wagner, *Beautiful mirrors and precision electroweak data*, Phys. Rev. D **65** (2002) 053002, arXiv:hep-ph/0109097 [hep-ph].

[74] K. Kumar, W. Shepherd, T. M. P. Tait, and R. Vega-Morales, *Beautiful Mirrors at the LHC*, JHEP **08** (2010) 052, arXiv:1004.4895 [hep-ph].

[75] M. Buchkremer, G. Cacciapaglia, A. Deandrea, and L. Panizzi, *Model Independent Framework for Searches of Top Partners*, **876** (2013) 376, arXiv:1305.4172 [hep-ph].

[76] V. D. Barger, A. Stange, and R. Phillips, *Four heavy quark hadroproduction*, Phys. Rev. D **44** (1991) 1987.

[77] S. Jung and J. D. Wells, *Low-scale warped extra dimension and its predilection for multiple top quarks*, JHEP **11** (2010) 001, arXiv:1008.0870 [hep-ph].

[78] G. Cacciapaglia, R. Chierici, A. Deandrea, L. Panizzi, S. Perries, et al., *Four tops on the real projective plane at LHC*, JHEP **1110** (2011) 042, arXiv:1107.4616 [hep-ph].

[79] L. Evans and P. Bryant, *LHC Machine*, JINST **3** (2008) S08001.

[80] H.T. Edwards, *The Tevatron Energy Doubler: A Superconducting Accelerator*, Ann. Rev. Nucl. Part. Sci. **35** (1985) 605.

[81] M. Benedikt, P. Collier, V. Mertens, J. Poole, and K. Schindl, *LHC Design Report. 3. The LHC injector chain*, CERN-2004-003-V-3 (2004).

[82] O. S. Bruning, P. Collier, P. Lebrun, S. Myers, R. Ostojic, J. Poole, and P. Proudlock, *LHC Design Report Vol.1: The LHC Main Ring*, CERN-2004-003-V1 (2004).

[83] ATLAS Collaboration,, *The ATLAS Experiment at the CERN Large Hadron Collider*, JINST **3** (2008) S08003.

[84] CMS Collaboration,, *The CMS experiment at the CERN LHC*, JINST **3** (2008) S08004.

[85] LHCb Collaboration,, *The LHCb experiment at the CERN LHC*, JINST **3** (2008) S08005.

[86] ALICE Collaboration,, *The ALICE experiment at the CERN LHC*, JINST **3** (2008) S08002.

[87] LHCf Collaboration,, *The LHCf detector at the CERN Large Hadron Collider*, JINST **3** (2008) S08006.

[88] TOTEM Collaboration,, *The TOTEM experiment at the CERN Large Hadron Collider*, JINST **3** (2008) S08007.

[89] MoEDAL Collaboration,, *Technical Design Report of the MoEDAL Experiment*, CERN-LHCC-2009-006, MoEDAL-TDR-001 (2009).

[90] ATLAS Collaboration,, *ATLAS detector and physics performance: Technical Design Report, 1*, CERN-LHCC-99-14, ATLAS-TDR-14 (1999).

[91] ATLAS Collaboration,, *ATLAS Insertable B-Layer Technical Design Report*, CERN-LHCC-2010-013 (2010).

[92] ATLAS Collaboration,, *Technical Design Report for the Phase-I Upgrade of the ATLAS TDAQ System*, CERN-LHCC-2013-018 (2013).

[93] I. Bejar Alonso and L. Rossi, *HiLumi LHC Technical Design Report: Deliverable: D1.10*, CERN-ACC-2015-0140 (2015).

[94] ATLAS Collaboration,, *New Small Wheel Technical Design Report*, CERN-LHCC-2013-006 (2013).

[95] ATLAS Collaboration,, *ATLAS Liquid Argon Calorimeter Phase-I Upgrade Technical Design Report*, CERN-LHCC-2013-017 (2013).

[96] ATLAS Collaboration,, *Fast TracKer (FTK) Technical Design Report*, CERN-LHCC-2013-007 (2013).

[97] ATLAS Collaboration,, *Performance Specifications of the Tracker Phase II Upgrade*, ATL-UPGRADE-PUB-2012-003 (2012).

[98] F. Siegert, *Monte-Carlo event generation for the LHC*, CERN-THESIS-2010-302 (2010).

[99] J. C. Collins, D. E. Soper, and G. F. Sterman, *Factorization of Hard Processes in QCD*, Adv. Ser. Direct. High Energy Phys. **5** (1989) 1, arXiv:hep-ph/0409313 [hep-ph].

[100] G. Altarelli and G. Parisi, *Asymptotic Freedom in Parton Language*, Nucl. Phys. B **126** (1977) 298.

[101] V.N. Gribov, L.N. Lipatov, *Deep inelastic e p scattering in perturbation theory*, Sov. J. Nucl. Phys. **15** (1972) 438.

[102] Yu.L. Dokshitzer, *Calculation of the Structure Functions for Deep Inelastic Scattering and e+ e- Annihilation by Perturbation Theory in Quantum Chromodynamics*, Sov. Phys. JETP **46** (1977) 641.

[103] H.-L. Lai et al., *New parton distributions for collider physics*, Phys. Rev. D **82** (2010) 074024, arXiv:1007.2241 [hep-ph].

[104] R. D. Ball, V. Bertone, S. Carrazza, C. S. Deans, L. Del Debbio, et al., *Parton distributions with LHC data*, Nucl. Phys. B **867** (2013) 244, arXiv:1207.1303 [hep-ph].

[105] A. D. Martin et al., *Parton distributions for the LHC*, Eur. Phys. J. C **63** (2009) 189, arXiv:0901.0002 [hep-ph].

[106] T. D. Lee and M. Nauenberg, *Degenerate Systems and Mass Singularities*, Phys. Rev. **133** (1964) 1549.

[107] T. Kinoshita, *Mass Singularities of Feynman Amplitudes*, Journal of Mathematical Physics **3** (1962) 650.

[108] P. Skands, *Introduction to QCD*, arXiv:1207.2389 [hep-ph].

[109] S. Catani, F. Krauss, R. Kuhn, and B. Webber, *QCD matrix elements + parton showers*, JHEP **0111** (2001) 063, arXiv:hep-ph/0109231 [hep-ph].

[110] M. L. Mangano, M. Moretti, F. Piccinini, and M. Treccani, *Matching matrix elements and shower evolution for top-quark production in hadronic collisions*, JHEP **0701** (2007) 013, arXiv:hep-ph/0611129 [hep-ph].

[111] S. Frixione, P. Nason, and C. Oleari, *Matching NLO QCD computations with Parton Shower simulations: the POWHEG method*, JHEP **11** (2007) 070, arXiv:0709.2092 [hep-ph].

[112] R. Frederix and S. Frixione, *Merging meets matching in MC@NLO*, JHEP **12** (2012) 061, arXiv:1209.6215 [hep-ph].

[113] B. Andersson, G. Gustafson, G. Ingelman, and T. Sjostrand, *Parton Fragmentation and String Dynamics*, Phys.Rept. **97** (1983) 31.

[114] T. Sjostrand, *Jet Fragmentation of Nearby Partons*, Nucl. Phys. B **248** (1984) 469.

[115] B. Webber, *A QCD Model for Jet Fragmentation Including Soft Gluon Interference*, Nucl. Phys. B **238** (1984) 492.

[116] G. Marchesini and B. Webber, *Monte Carlo Simulation of General Hard Processes with Coherent QCD Radiation*, Nucl. Phys. B **310** (1988) 461.

[117] T. Sjostrand and M. van Zijl, *A Multiple Interaction Model for the Event Structure in Hadron Collisions*, Phys. Rev. D **36** (1987) 2019.

[118] T. Sjöstrand, S. Mrenna, and P. Z. Skands, *PYTHIA 6.4 Physics and Manual*, JHEP **0605** (2006) 026, arXiv:hep-ph/0603175 [hep-ph].

[119] T. Sjöstrand and S. Mrenna and P. Skands, *A Brief Introduction to Pythia 8.1*, arXiv:0710.3820 [hep-ph].

[120] M. Bahr, S. Gieseke, M. Gigg, D. Grellscheid, K. Hamilton, et al., *Herwig++ Physics and Manual*, Eur. Phys. J. C **58** (2008) 639, arXiv:0803.0883 [hep-ph].

[121] J. Butterworth, J. Forshaw, and M. Seymour, *Multiparton interactions in photoproduction at HERA*, Z. Phys. C **72** (1996) 637, arXiv:9601371 [hep-ph].

[122] T. Gleisberg, S. Hoeche, F. Krauss, M. Schonherr, S. Schumann, et al., *Event generation with SHERPA 1.1*, JHEP **0902** (2009) 007, arXiv:0811.4622 [hep-ph].

[123] S. Schumann and F. Krauss, *A Parton shower algorithm based on Catani-Seymour dipole factorisation*, JHEP **0803** (2008) 038, arXiv:0709.1027 [hep-ph].

[124] F. Cascioli, P. Maierhofer, and S. Pozzorini, *Scattering Amplitudes with Open Loops*, Phys. Rev. Lett. **108** (2012) 111601, arXiv:1111.5206 [hep-ph].

[125] T. Gleisberg and S. Hoeche, *Comix, a new matrix element generator*, JHEP **12** (2008) 039, arXiv:0808.3674 [hep-ph].

[126] P. Nason, *A new method for combining NLO QCD with shower Monte Carlo algorithms*, JHEP **11** (2004) 040, arXiv:hep-ph/0409146.

[127] J. Alwall, R. Frederix, S. Frixione, V. Hirschi, F. Maltoni, et al., *The automated computation of tree-level and next-to-leading order differential cross sections, and their matching to parton shower simulations*, JHEP **1407** (2014) 079, arXiv:1405.0301 [hep-ph].

[128] S. Frixione and B. R. Webber, *Matching NLO QCD computations and parton shower simulations*, JHEP **06** (2002) 029, arXiv:0204244 [hep-ph].

[129] C. Degrande, C. Duhr, B. Fuks, D. Grellscheid, O. Mattelaer, and T. Reiter, *UFO - The Universal FeynRules Output*, Comput. Phys. Commun. **183** (2012) 1201, arXiv:1108.2040 [hep-ph].

[130] J. A. Aguilar-Saavedra, *PROTOS, a Program for Top Simulations*, http://jaguilar.web.cern.ch/jaguilar/protos/.

[131] P. Golonka and Z. Wąs, *PHOTOS Monte Carlo: a precision tool for QED corrections in Z and W decays*, Eur. Phys. J. C **45** (2006) 97, arXiv:0506026 [hep-ph].

[132] S. Jadach, J. H. Kühn, and Z. Waąs, *TAUOLA - a library of Monte Carlo programs to simulate decays of polarized τ leptons*, Comput. Phys. Commun. **64** (1991) 275.

[133] D. J. Lange, *The EvtGen particle decay simulation package*, Nucl. Instrum. Meth. A **462** (2001) 152.

[134] S. Agostinelli et al., *Geant4: a simulation toolkit*, Nucl. Instr. Meth. A **506** (2003) 250.

[135] ATLAS Collaboration,, *The simulation principle and performance of the ATLAS fast calorimeter simulation FastCaloSim*, ATL-PHYS-PUB-2010-013 (2010).

[136] A. Buckley, J. Butterworth, L. Lonnblad, D. Grellscheid, H. Hoeth, J. Monk, H. Schulz, and F. Siegert, *Rivet user manual*, Comput. Phys. Commun. **184** (2013) 2803–2819, arXiv:1003.0694 [hep-ph].

[137] C. Ay, S. Johnert, J. Katzy, and Z. Qin, *HepMCAnalyser: A tool for Monte Carlo generator validation*, Journal of Physics: Conference Series **219** (2010) 032029, http://stacks.iop.org/1742-6596/219/i=3/a=032029.

[138] M. Dobbs and J. B. Hansen, *The HepMC C++ Monte Carlo event record for High Energy Physics*, Comput. Phys. Commun. **134** (2001) 41.

[139] E. Ehses et al., *Job centric monitoring for ATLAS jobs in the LHC Computing Grid*, PoS ACAT **08** (2008) 042, http://inspirehep.net/record/858283/files/ACAT08_042.pdf.

[140] T. Cornelissen, M. Elsing, S. Fleischmann, W. Liebig, E. Moyse, and A. Salzburger, *Concepts, Design and Implementation of the ATLAS New Tracking (NEWT)*, ATL-SOFT-PUB-2007-007 (2007).

[141] ATLAS Collaboration,, *The Optimization of ATLAS Track Reconstruction in Dense Environments*, ATL-PHYS-PUB-2015-006 (2015).

[142] ATLAS Collaboration,, *Charged-particle distributions in $\sqrt{s}$=13 TeV pp interactions measured with the ATLAS detector at the LHC*, Phys. Lett. B **758** (2016) 67, arXiv:1602.01633 [hep-ex].

[143] ATLAS Collaboration,, *Performance of primary vertex reconstruction in proton-proton collisions at $\sqrt{s}$ =7 TeV in the ATLAS experiment*, ATLAS-CONF-2010-069 (2010).

[144] ATLAS Collaboration,, *Electron efficiency measurements with the ATLAS detector using the 2015 LHC proton-proton collision data*, ATLAS-CONF-2016-024 (2016).

[145] ATLAS Collaboration,, *Electron and photon energy calibration with the ATLAS detector using data collected in 2015 at $\sqrt{s}$ = 13 TeV*, ATL-PHYS-PUB-2016-015 (2016).

[146] ATLAS Collaboration,, *Muon reconstruction performance of the ATLAS detector in proton-proton collision data at $\sqrt{s}$=13 TeV*, Eur. Phys. J. C **76** (2016) 292, arXiv:1603.05598 [hep-ex].

[147] ATLAS Collaboration,, *Calorimeter clustering algorithms: Description and performance*, ATL-LARG-PUB-2008-002 (2008).

[148] G. P. Salam, *Towards Jetography*, Eur. Phys. J. C **67** (2010) 637, arXiv:0906.1833 [hep-ph].

[149] M. Cacciari, G. P. Salam, and G. Soyez, *The anti-k_t jet clustering algorithm*, JHEP **04** (2008) 063.

[150] ATLAS Collaboration,, *Monte Carlo Calibration and Combination of In-situ Measurements of Jet Energy Scale, Jet Energy Resolution and Jet Mass in ATLAS*, ATLAS-CONF-2015-037 (2015).

[151] ATLAS Collaboration,, *Pile-up subtraction and suppression for jets in ATLAS*, ATLAS-CONF-2013-083 (2013).

[152] M. Cacciari, G. P. Salam, and G. Soyez, *The Catchment Area of Jets*, JHEP **04** (2008) 005, arXiv:0802.1188.

[153] ATLAS Collaboration,, *Jet Calibration and Systematic Uncertainties for Jets Reconstructed in the ATLAS Detector at $\sqrt{s} = 13$ TeV*, ATL-PHYS-PUB-2015-015 (2015).

[154] ATLAS Collaboration,, *Determination of the jet energy scale and resolution at ATLAS using Z/γ–jet events in data at $\sqrt{s} = 8$ TeV*, ATLAS-CONF-2015-057 (2015).

[155] ATLAS Collaboration,, *Data-driven determination of the energy scale and resolution of jets reconstructed in the ATLAS calorimeters using dijet and multijet events at $\sqrt{s} = 8$ TeV*, ATLAS-CONF-2015-017 (2015).

[156] ATLAS Collaboration,, *Tagging and suppression of pileup jets with the ATLAS detector*, ATLAS-CONF-2014-018 (2014).

[157] A. Altheimer et al., *Boosted objects and jet substructure at the LHC. Report of BOOST2012, held at IFIC Valencia, 23rd-27th of July 2012*, Eur. Phys. J. C **74** (2014) 2792, arXiv:1311.2708 [hep-ex].

[158] D. Krohn, J. Thaler, and L.-T. Wang, *Jet Trimming*, JHEP **02** (2010) 084, arXiv:0912.1342 [hep-ph].

[159] J. M. Butterworth, A. R. Davison, M. Rubin, and G. P. Salam, *Jet substructure as a new Higgs search channel at the LHC*, Phys. Rev. Lett. **100** (2008) 242001, arXiv:0802.2470 [hep-ph].

[160] S. D. Ellis, C. K. Vermilion, and J. R. Walsh, *Techniques for improved heavy particle searches with jet substructure*, Phys. Rev. D **80** (2009) 051501, arXiv:0903.5081 [hep-ph].

[161] B. Nachman, P. Nef, A. Schwartzman, M. Swiatlowski, and C. Wanotayaroj, *Jets from Jets: Re-clustering as a tool for large radius jet reconstruction and grooming at the LHC*, JHEP **02** (2015) 075, arXiv:1407.2922 [hep-ph].

[162] ATLAS Collaboration,, *Commissioning of the ATLAS high-performance b-tagging algorithms in the 7 TeV collision data*, ATLAS-CONF-2011-102 (2011).

[163] ATLAS Collaboration,, *A new inclusive secondary vertex algorithm for b-jet tagging in ATLAS*, J. Phys. Conf. Ser. **119 032032** (2008).

[164] R. Fruhwirth, *Application of Kalman filtering to track and vertex fitting*, Nucl. Instrum. Meth. A **262** (1987) 444.

[165] ATLAS Collaboration,, *Optimisation of the ATLAS b-tagging performance for the 2016 LHC Run*, ATL-PHYS-PUB-2016-012 (2016).

[166] ATLAS Collaboration,, *Calibration of b-tagging using dileptonic top pair events in a combinatorial likelihood approach with the ATLAS experiment*, ATL-CONF-2014-004 (2014).

[167] ATLAS Collaboration,, *b-jet tagging calibration on c-jets containing D* mesons*, ATLAS-CONF-2012-039 (2012).

[168] ATLAS Collaboration,, *Measurement of the Mistag Rate of b-tagging algorithms with 5 fb^{-1} of Data Collected by the ATLAS Detector*, ATLAS-CONF-2012-040 (2012).

[169] ATLAS Collaboration,, *Expected performance of missing transverse momentum reconstruction for the ATLAS detector at $\sqrt{s} = 13$ TeV*, ATL-PHYS-PUB-2015-023 (2015).

[170] ATLAS Collaboration,, *2015 start-up trigger menu and initial performance assessment of the ATLAS trigger using Run-2 data*, ATL-DAQ-PUB-2016-001 (2016).

[171] ATLAS Collaboration,, *Measurement of top quark pair differential cross-sections in the dilepton channel in pp collisions at $\sqrt{s}$ = 7 and 8 TeV with ATLAS*, Phys. Rev. D **94** (2016) 092003, arXiv:1607.07281 [hep-ex].

[172] ATLAS Collaboration,, *Measurements of normalized differential cross sections for $t\bar{t}$ production in pp collisions at $\sqrt{s} = 7$ TeV using the ATLAS detector*, Phys. Rev. D **90** (2014) 072004, arXiv:1407.0371 [hep-ex].

[173] ATLAS Collaboration,, *Measurements of top-quark pair differential cross-sections in the lepton+jets channel in pp collisions at $\sqrt{s} = 8$ TeV using the ATLAS detector*, Eur. Phys. J. C **76** (2016) 538, arXiv:1511.04716 [hep-ex].

[174] J. Pumplin, D. R. Stump, J. Huston, H. L. Lai, P. M. Nadolsky, and W. K. Tung, *New generation of parton distributions with uncertainties from global QCD analysis*, JHEP **0207** (2002) 012, arXiv:hep-ph/0201195 [hep-ph].

[175] P. Skands, *Tuning Monte Carlo Generators: The Perugia Tunes*, Phys. Rev. D **82** (2010) 074018, arXiv:1005.3457 [hep-ph].

[176] M. Czakon and A. Mitov, *Top++: A Program for the Calculation of the Top-Pair Cross-Section at Hadron Colliders*, Computer Physics Communications **185** (2014) 2930, arXiv:1112.5675 [hep-ph].

[177] M. Czakon and A. Mitov, *NNLO corrections to top pair production at hadron colliders: the quark-gluon reaction*, JHEP **1301** (2013) 080, arXiv:1210.6832 [hep-ph].

[178] M. Czakon and A. Mitov, *NNLO corrections to top-pair production at hadron colliders: the all-fermionic scattering channels*, JHEP **1212** (2012) 054, arXiv:1207.0236 [hep-ph].

[179] P. Bärnreuther, M. Czakon, and A. Mitov, *Percent Level Precision Physics at the Tevatron: First Genuine NNLO QCD Corrections to $q\bar{q} \to t\bar{t} + X$*, Phys. Rev. Lett. **109** (2012) 132001, arXiv:1204.5201 [hep-ph].

[180] M. Cacciari, M. Czakon, M. Mangano, A. Mitov, and P. Nason, *Top-pair production at hadron colliders with next-to-next-to-leading logarithmic soft-gluon resummation*, Phys. Lett. B **710** (2012) 612, arXiv:1111.5869 [hep-ph].

[181] ATLAS Collaboration,, *Measurements of top-quark pair differential cross-sections in the eμ channel in pp collisions at $\sqrt{s} = 13$ TeV using the ATLAS detector*, arXiv:1612.05220 [hep-ex].

[182] ATLAS Collaboration,, *Measurements of top-quark pair differential cross-sections in the lepton+jets channel in pp collisions at $\sqrt{s} = 13$ TeV using the ATLAS detector*, ATLAS-CONF-2016-040 (2016).

[183] N. Kidonakis, *NNNLO soft-gluon corrections for the top-antitop pair production cross section*, PRD **90** (2014) 014006, arXiv:1405.7046 [hep-ph].

[184] M. Guzzi, K. Lipka, and S.-O. Moch, *Top-quark pair production at hadron colliders: differential cross section and phenomenological applications with DiffTop*, JHEP **01** (2015) 082, arXiv:1406.0386 [hep-ph].

[185] A. Bredenstein, A. Denner, S. Dittmaier, and S. Pozzorini, *NLO QCD Corrections to Top Anti-Top Bottom Anti-Bottom Production at the LHC: 2. full hadronic results*, JHEP **1003** (2010) 021, arXiv:1001.4006 [hep-ph].

[186] G. Bevilacqua, M. Czakon, C. Papadopoulos, R. Pittau, and M. Worek, *Assault on the NLO Wishlist: pp t anti-t b anti-b*, JHEP **0909** (2009) 109, arXiv:0907.4723 [hep-ph].

[187] A. Bredenstein, A. Denner, S. Dittmaier, and S. Pozzorini, *NLO QCD corrections to pp → t anti-t b anti-b + X at the LHC*, Phys. Rev. Lett. **103** (2009) 012002, arXiv:0905.0110 [hep-ph].

[188] F. Cascioli, P. Maierhofer, N. Moretti, S. Pozzorini, and F. Siegert, *NLO matching for $t\bar{t}b\bar{b}$ production with massive b-quarks*, Phys. Lett. B **734** (2014) 210, arXiv:1309.5912 [hep-ph].

[189] NNPDF Collaboration,, *Parton distributions for the LHC Run II*, JHEP **04** (2015) 040, arXiv:1410.8849 [hep-ph].

[190] ATLAS Collaboration,, *ATLAS Pythia 8 tunes to 7 TeV data*, ATL-PHYS-PUB-2014-021 (2014).

[191] S. Gieseke, C. Rohr, and A. Siodmok, *Colour reconnections in Herwig++*, Eur. Phys. J. C **72** (2012) 2225, arXiv:1206.0041 [hep-ph].

[192] ATLAS Collaboration,, *Studies of tt+cc production with MadGraph5_aMC@NLO and Herwig++ for the ATLAS experiment*, ATL-PHYS-PUB-2016-011 (2016).

[193] S. Höche, F. Krauss, M. Schönherr, and F. Siegert, *QCD matrix elements + parton showers: The NLO case*, JHEP **1304** (2013) 027, arXiv:1207.5030 [hep-ph].

[194] C. Anastasiou, L. J. Dixon, K. Melnikov, and F. Petriello, *High precision QCD at hadron colliders: Electroweak gauge boson rapidity distributions at NNLO*, Phys. Rev. D **69** (2004) 094008, arXiv:hep-ph/0312266 [hep-ph].

[195] S. Frixione, E. Laenen, P. Motylinski, and B. R. Webber, *Single-top production in MC@NLO*, JHEP **0603** (2006) 092, arXiv:hep-ph/0512250.

[196] N. Kidonakis, *Next-to-next-to-leading-order collinear and soft gluon corrections for t-channel single top quark production*, Phys. Rev. D **83** (2011) 091503, arXiv:1103.2792 [hep-ph].

[197] N. Kidonakis, *Two-loop soft anomalous dimensions for single top quark associated production with a W^- or H^-*, Phys. Rev. D **82** (2010) 054018, arXiv:1005.4451 [hep-ph].

[198] N. Kidonakis, *NNLL resummation for s-channel single top quark production*, Phys. Rev. D **81** (2010) 054028, arXiv:1001.5034 [hep-ph].

[199] F. Demartin, F. Maltoni, K. Mawatari, and M. Zaro, *Higgs production in association with a single top quark at the LHC*, Eur. Phys. J. C **75** (2015) 267, arXiv:1504.00611 [hep-ph].

[200] J. M. Campbell and R. K. Ellis, *$t\bar{t}W^{\pm}$ production and decay at NLO*, JHEP **1207** (2012) 052, arXiv:1204.5678 [hep-ph].

[201] M. V. Garzelli, A. Kardos, C. G. Papadopoulos, and Z. Trocsanyi, *$t\bar{t}W$ and $t\bar{t}Z$ Hadroproduction at NLO accuracy in QCD with Parton Shower and Hadronization effects*, JHEP **1211** (2012) 056, arXiv:1208.2665 [hep-ph].

[202] ATLAS Collaboration,, *Measurement of the top quark-pair production cross section with ATLAS in pp collisions at $\sqrt{s} = 7$ TeV*, Eur. Phys. J. C **71** (2011) 1577, arXiv:1012.1792 [hep-ex].

[203] P. Artoisenet, R. Frederix, O. Mattelaer, R. Rietkerk, *Automatic spin-entangled decays of heavy resonances in Monte Carlo simulations*, JHEP **2013** (2013) 15, arXiv:1212.3460 [hep-ph].

[204] W. Beenakker et al., *Higgs radiation off top quarks at the Tevatron and the LHC*, Phys. Rev. Lett. **87** (2001) 201805, arXiv:hep-ph/0107081.

[205] W. Beenakker et al., *NLO QCD corrections to ttH production in hadron collisions*, Nucl. Phys. B **653** (2003) 151, arXiv:hep-ph/0211352 [hep-ph].

[206] L. Reina and S. Dawson, *Next-to-leading order results for ttH production at the Tevatron*, Phys. Rev. Lett. **87** (2001) 201804, arXiv:hep-ph/0107101 [hep-ph].

[207] Y. Zhang, W.-G. Ma, R.-Y. Zhang, C. Chen, and L. Guo, *QCD NLO and EW NLO corrections to $t\bar{t}H$ production with top quark decays at hadron collider*, Phys. Lett. B **738** (2014) 1, arXiv:1407.1110 [hep-ph].

[208] S. Frixione, V. Hirschi, D. Pagani, H.-S. Shao, and M. Zaro, *Electroweak and QCD corrections to top-pair hadroproduction in association with heavy bosons*, JHEP **1506** (2015) 184, arXiv:1504.03446 [hep-ph].

[209] A. Djouadi, J. Kalinowski, and M. Spira, *HDECAY: a Program for Higgs Boson Decays in the Standard Model and its Supersymmetric Extension*, Comput. Phys. Commun. **108** (1998) 56, arXiv:9704448 [hep-ph].

[210] P. Meade and M. Reece, *BRIDGE: Branching ratio inquiry / decay generated events*, arXiv:hep-ph/0703031 [hep-ph].

[211] R. V. Harlander, S. Liebler, and H. Mantler, *SusHi: A program for the calculation of Higgs production in gluon fusion and bottom-quark annihilation in the Standard Model and the MSSM*, Comput. Phys. Commun. **184** (2013) 1605, arXiv:1212.3249 [hep-ph].

[212] R. V. Harlander and W. B. Kilgore, *Next-to-next-to-leading order Higgs production at hadron colliders*, Phys. Rev. Lett. **88** (2002) 201801, arXiv:hep-ph/0201206 [hep-ph].

[213] R. V. Harlander and W. B. Kilgore, *Higgs boson production in bottom quark fusion at next-to-next-to leading order*, Phys. Rev. D **68** (2003) 013001, arXiv:hep-ph/0304035 [hep-ph].

[214] U. Aglietti, R. Bonciani, G. Degrassi, and A. Vicini, *Two loop light fermion contribution to Higgs production and decays*, Phys. Lett. B **595** (2004) 432, arXiv:hep-ph/0404071 [hep-ph].

[215] R. Bonciani, G. Degrassi, and A. Vicini, *On the Generalized Harmonic Polylogarithms of One Complex Variable*, Comput. Phys. Commun. **182** (2011) 1253, arXiv:1007.1891 [hep-ph].

[216] R. Harlander and P. Kant, *Higgs production and decay: Analytic results at next-to-leading order QCD*, JHEP **0512** (2005) 015, arXiv:hep-ph/0509189 [hep-ph].

[217] R. Harlander, M. Kramer, and M. Schumacher, *Bottom-quark associated Higgs-boson production: reconciling the four- and five-flavour scheme approach*, arXiv:1112.3478 [hep-ph].

[218] C. Degrande, M. Ubiali, M. Wiesemann, and M. Zaro, *Heavy charged Higgs boson production at the LHC*, JHEP **1510** (2015) 145, arXiv:1507.02549 [hep-ph].

[219] M. Flechl, R. Klees, M. Kramer, M. Spira, and M. Ubiali, *Improved cross-section predictions for heavy charged Higgs boson production at the LHC*, Phys. Rev. D **91** (2015) 075015, arXiv:1409.5615 [hep-ph].

[220] LHC Higgs Cross Section Working Group, *Handbook of LHC Higgs Cross Sections: 3. Higgs Properties*, arXiv:1307.1347 [hep-ph].

[221] E. L. Berger, T. Han, J. Jiang, and T. Plehn, *Associated production of a top quark and a charged Higgs boson*, Phys. Rev. D **71** (2005) 115012, arXiv:hep-ph/0312286 [hep-ph].

[222] ATLAS Collaboration,, *Tagging Rate Function B-Tagging*, ATL-PHYS-PUB-2007-011 (2007).

[223] D0 Collaboration,, *Measurement of b-tagging efficiency and mis-tagging rates with CSIP method*, D0 Note 4432 (2004).

[224] T. Junk, *Confidence level computation for combining searches with small statistics*, Nucl. Instrum. Meth. A **434** (1999) 435, arXiv:hep-ex/9902006.

[225] G. Cowan, K. Cranmer, E. Gross, and O. Vitells, *Asymptotic formulae for likelihood-based tests of new physics*, Eur. Phys. J. C **71** (2011) 1554, arXiv:1007.1727 [physics.data-an].

[226] A. Wald, *Tests of Statistical Hypotheses Concerning Several Parameters When the Number of Observations is Large*, Transactions of the American Mathematical Society **54** (1943) 426.

[227] S. Frixione, E. Laenen, P. Motylinski, B. R. Webber and C. D. White, *Single-top hadroproduction in association with a W boson*, JHEP 07 (2008) 029, arXiv:0805.3067 [hep-ph].

[228] J. M. Campbell and R. K. Ellis, *An Update on vector boson pair production at hadron colliders*, Phys. Rev. D **60** (1999) 113006, arXiv:hep-ph/9905386.

[229] J. Alwall, S. Hoche, F. Krauss, N. Lavesson, L. Lonnblad, et al., *Comparative study of various algorithms for the merging of parton showers and matrix elements in hadronic collisions*, Eur. Phys. J. C **53** (2008) 473, arXiv:0706.2569 [hep-ph].

[230] J. M. Campbell and R. K. Ellis, $t\bar{t}W^{+-}$ *production and decay at NLO*, JHEP **1207** (2012) 052, arXiv:1204.5678 [hep-ph].

[231] M. V. Garzelli, A. Kardos, C. G. Papadopoulos, and Z. Trocsanyi, $t\bar{t}W$ *and* $t\bar{t}Z$ *Hadroproduction at NLO accuracy in QCD with Parton Shower and Hadronization effects*, JHEP **1211** (2012) 056, arXiv:1208.2665 [hep-ph].

[232] ATLAS Collaboration,, *Search for production of vector-like top quark pairs and of four top quarks in the lepton-plus-jets final state in pp collisions at* $\sqrt{s} = 13\,TeV$ *with the ATLAS detector*, ATLAS-CONF-2016-013 (2016).

[233] ATLAS Collaboration,, *Search for production of vector-like quark pairs and of four top quarks in the lepton-plus-jets final state in pp collisions at* $\sqrt{s} = 8$ *TeV with the ATLAS detector*, JHEP **1508** (2015) 105, arXiv:1505.04306 [hep-ex].

[234] ATLAS Collaboration,, *Search for pair production of heavy vector-like quarks decaying to high-*p_T *W bosons and b quarks in the lepton-plus-jets final state in pp collisions at* $\sqrt{s}$*=13 TeV with the ATLAS detector*, ATLAS-CONF-2016-102 (2016).

[235] ATLAS Collaboration,, *Search for pair production of vector-like top partners in events with exactly one lepton and large missing transverse momentum in* $\sqrt{s} = 13$ *TeV pp collisions with the ATLAS detector*, ATLAS-CONF-2016-101 (2016).

[236] ATLAS Collaboration,, *Search for new physics using events with b-jets and a pair of same charge leptons in 3.2* fb^{-1} *of pp collisions at* $\sqrt{s} = 13$ *TeV with the ATLAS detector*, ATLAS-CONF-2016-032 (2016).

[237] CMS Collaboration,, *Search for pair production of vector-like T quarks in the lepton plus jets final state*, CMS-PAS-B2G-16-002 (2016).

[238] CMS Collaboration,, *Search for vector-like quark pair production in final states with leptons and boosted Higgs bosons at* $\sqrt{s} = 13$ TeV, CMS-PAS-B2G-16-011 (2016).

[239] ATLAS Collaboration,, *Search for four-top-quark production in final states with one charged lepton and multiple jets using 3.2* fb^{-1} *of proton-proton collisions at* $\sqrt{s} = 13\,TeV$ *with the ATLAS detector at the LHC*, ATLAS-CONF-2016-020 (2016).

[240] CMS Collaboration,, *Search for standard model production of four top quarks in proton-proton collisions at 13 TeV*, CMS-PAS-TOP-16-016 (2016).

[241] ATLAS Collaboration,, *Search for charged Higgs bosons in the* τ*+jets final state using 14.7* fb^{-1} *of pp collision data recorded at* $\sqrt{s} = 13$ *TeV with the ATLAS experiment*, ATLAS-CONF-2016-088 (2016).

[242] TMVA Collaboration,, *TMVA - Toolkit for Multivariate Data Analysis*, arXiv:physics/0703039 [data-an].

[243] V. Barger, J. Ohnemus, and R. Phillips, *Event shape criteria for single lepton top signals*, Phys. Rev. D **48** (1993) 3953, arXiv:hep-ph/9308216.

[244] C. Bernaciak, M. S. A. Buschmann, A. Butter and T. Plehn, *Fox-Wolfram Moments in Higgs Physics*, Phys. Rev. D **87** (2013) 073014, arXiv:1212.4436 [hep-ph].

[245] S. Dawson, L. H. Orr, L. Reina, and D. Wackeroth, *Associated top quark Higgs boson production at the LHC*, Phys. Rev. D **67** (2003) 071503, arXiv:hep-ph/0211438 [hep-ph].

[246] ATLAS Collaboration,, *Search for the Standard Model Higgs boson produced in association with top quarks and decaying into $b\bar{b}$ in pp collisions at $\sqrt{s}$ = 13 TeV with the ATLAS detector*, ATLAS-CONF-2016-080 (2016).

[247] ATLAS Collaboration,, *Measurement of fiducial, differential and production cross sections in the $H \to \gamma\gamma$ decay channel with 13.3 fb^{-1} of 13 TeV proton-proton collision data with the ATLAS detector*, ATLAS-CONF-2016-067 (2016).

[248] ATLAS Collaboration,, *Search for the Associated Production of a Higgs Boson and a Top Quark Pair in Multilepton Final States with the ATLAS Detector*, ATLAS-CONF-2016-058 (2016).

[249] ATLAS Collaboration,, *Combination of the searches for Higgs boson production in association with top quarks in the $\gamma\gamma$, multilepton, and $b\bar{b}$ decay channels at $\sqrt{s}$=13 TeV with the ATLAS Detector*, ATLAS-CONF-2016-068 (2016).

[250] ATLAS Collaboration,, *Search for the Standard Model Higgs boson decaying into $b\bar{b}$ produced in association with top quarks decaying hadronically in pp collisions at $\sqrt{s} = 8$ TeV with the ATLAS detector*, JHEP **05** (2016) 160, arXiv:1604.03812 [hep-ex].

[251] CMS Collaboration,, *Search for associated production of Higgs bosons and top quarks in multilepton final states at $\sqrt{s} = 13$ TeV*, CMS-PAS-HIG-16-022 (2016).

[252] CMS Collaboration,, *Search for $\mathrm{t\bar{t}H}$ production in the $\mathrm{H} \to \mathrm{b\bar{b}}$ decay channel with 2016 pp collision data at $\sqrt{s} = 13$ TeV*, CMS-PAS-HIG-16-038 (2016).

[253] CMS Collaboration,, *Updated measurements of Higgs boson production in the diphoton decay channel at $\sqrt{s} = 13$ TeV in pp collisions at CMS.*, CMS-PAS-HIG-16-020 (2016).

[254] N. Moretti, P. Petrov, S. Pozzorini, and M. Spannowsky, *Measuring the signal strength in $t\bar{t}H$ with $H \to b\bar{b}$*, Phys. Rev. D **93** (2016) 014019, arXiv:1510.08468 [hep-ph].

[255] C. Degrande, J. M. Gerard, C. Grojean, F. Maltoni, and G. Servant, *Probing Top-Higgs Non-Standard Interactions at the LHC*, JHEP **07** (2012) 036, arXiv:1205.1065 [hep-ph], [Erratum: JHEP **03**, 032 (2013)].

[256] C. Arina, E. Del Nobile, and P. Panci, *Dark Matter with Pseudoscalar-Mediated Interactions Explains the DAMA Signal and the Galactic Center Excess*, Phys. Rev. Lett. **114** (2015) 011301, arXiv:1406.5542 [hep-ph].

[257] A. Hektor and L. Marzola, *Coy Dark Matter and the anomalous magnetic moment*, Phys. Rev. D **90** (2014) 053007, arXiv:1403.3401 [hep-ph].

[258] C. Boehm, M. J. Dolan, C. McCabe, M. Spannowsky, and C. J. Wallace, *Extended gamma-ray emission from Coy Dark Matter*, JCAP **1405** (2014) 009, arXiv:1401.6458 [hep-ph].

[259] L. Goodenough and D. Hooper, *Possible Evidence For Dark Matter Annihilation In The Inner Milky Way From The Fermi Gamma Ray Space Telescope*, arXiv:0910.2998 [hep-ph].

[260] D. Hooper and L. Goodenough, *Dark Matter Annihilation in The Galactic Center As Seen by the Fermi Gamma Ray Space Telescope*, Phys. Lett. B **697** (2011) 412, arXiv:1010.2752 [hep-ph].

[261] K. N. Abazajian and M. Kaplinghat, *Detection of a Gamma-Ray Source in the Galactic Center Consistent with Extended Emission from Dark Matter Annihilation and Concentrated Astrophysical Emission*, Phys. Rev. D **86** (2012) 083511, arXiv:1207.6047 [astro-ph.HE], [Erratum: Phys. Rev. D **87**, 129902 (2013)].

[262] T. Daylan, D. P. Finkbeiner, D. Hooper, T. Linden, S. K. N. Portillo, N. L. Rodd, and T. R. Slatyer, *The characterization of the gamma-ray signal from the central Milky Way: A case for annihilating dark matter*, Phys. Dark Univ. **12** (2016) 1, arXiv:1402.6703 [astro-ph.HE].

[263] N. Craig, F. D'Eramo, P. Draper, S. Thomas, and H. Zhang, *The Hunt for the Rest of the Higgs Bosons*, JHEP **06** (2015) 137, arXiv:1504.04630 [hep-ph].

[264] J. Hajer, Y.-Y. Li, T. Liu, and J. F. H. Shiu, *Heavy Higgs Bosons at 14 TeV and 100 TeV*, JHEP **11** (2015) 124, arXiv:1504.07617 [hep-ph].

[265] M. J. Dolan, F. Kahlhoefer, C. McCabe, and K. Schmidt-Hoberg, *A taste of dark matter: Flavour constraints on pseudoscalar mediators*, JHEP **03** (2015) 171, arXiv:1412.5174 [hep-ph], [Erratum: JHEP **07**,103 (2015)].

[266] M. Casolino, T. Farooque, A. Juste, T. Liu, and M. Spannowsky, *Probing a light CP-odd scalar in di-top-associated production at the LHC*, Eur. Phys. J. C **75** (2015) 498, arXiv:1507.07004 [hep-ph].

[267] A. Alloul, N. D. Christensen, C. Degrande, C. Duhr, and B. Fuks, *FeynRules 2.0 - A complete toolbox for tree-level phenomenology*, Comput. Phys. Commun. **185** (2014) 2250, arXiv:1310.1921 [hep-ph].

[268] J. Kozaczuk and T. A. W. Martin, *Extending LHC Coverage to Light Pseudoscalar Mediators and Coy Dark Sectors*, JHEP **04** (2015) 046, arXiv:1501.07275 [hep-ph].

[269] J. R. Espinosa and M. Quiros, *Higgs boson bounds in nonminimal supersymmetric standard models*, Phys. Lett. B **279** (1992) 92, arXiv:hep-ph/9208226 [hep-ph].

[270] P. C. Schuster and N. Toro, *Persistent fine-tuning in supersymmetry and the NMSSM*, arXiv:hep-ph/0512189 [hep-ph].